TECHNICAL UNIVERSITY OF MOLDOVA

AND KIEL UNIVERSITY

RAJAT

POROUS NETWORKS OF NANOSTRUCTURED HYBRID MATERIALS

134.03 PHYSICS OF NANOSYSTEMS AND NANOTECHNOLOGIES

Joint doctorate thesis in physical sciences (UTM)

and doctor of engineering (Kiel University)

Scientific advisors:

LUPAN Oleg
Dr. Hab. in Engineering,
University Professor

ADELUNG Rainer
Dr. rer. nat.,
University Professor

CHIȘINĂU, KIEL, 2026

UNIVERSITATEA TEHNICĂ A MOLDOVEI
ȘI UNIVERSITATEA DIN KIEL

RAJAT

REȚELE POROASE DE MATERIALE HIBRIDE NANOSTRUCTURATE

134.03 FIZICA NANOSISTEMELOR ȘI NANOTEHNOLOGIILOR

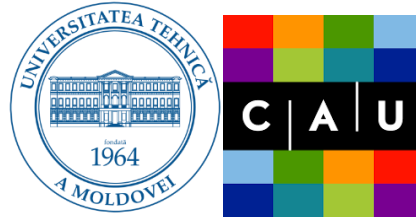**Teză de doctorat în științe fizice (UTM) și doctor în inginerie (Universitatea din Kiel)**

Conducători științifici:

LUPAN Oleg
Doctor habilitat în tehnică,
profesor universitar

ADELUNG Rainer
Doctor rer. nat.,
profesor universitar

CHIȘINĂU, KIEL, 2026

UNIVERSITATEA TEHNICĂ A MOLDOVEI
ȘI UNIVERSITATEA DIN KIEL

RAJAT

REȚELE POROASE DE MATERIALE HIBRIDE NANOSTRUCTURATE

134.03 FIZICA NANOSISTEMELOR ȘI NANOTEHNOLOGII

Teză de doctorat în științe fizice (UTM) și doctor în inginerie (Universitatea din Kiel)

Autor: RAJAT

Conducători științifici:

LUPAN Oleg
Dr. habilitat în tehnică,
profesor universitar

ADELUNG Rainer
Dr. rer. nat.,
profesor universitar

Membrii comitetului de îndrumare: BUZDUGAN Artur, dr. hab., prof. univ.

ABABII Nicolai, dr., conf. univ.

CREȚU Vasilii, dr., conf. univ.

CHIȘINĂU, KIEL, 2026

Contents

ABSTRACT

In the Ph.D. thesis entitled „**Porous Networks of Nanostructured Hybrid Materials**", submitted by **Rajat,** for conferring the scientific joint doctoral degree in physical sciences at Technical University of Moldova (UTM), in the speciality 134.03 „Physics of nanosystems and nanotechnologies", and in engineering at Kiel University, Germany.

Structure of the thesis: The thesis was carried out jointly at the UTM, Department of Microelectronics and Biomedical Engineering, Center for Nanotechnology and Nanosensors and Kiel University, Faculty of Engineering, Chair for Functional Nanomaterials, Germany. The thesis is written in English language and consists of an introduction, five chapters, general conclusions and recommendations, bibliography with 273 references, 104 pages of basic text, 40 figures, 7 tables, and 37 equations. The research results obtained were published in 25 scientific publications, 14 of which are directly related to the topic of the thesis, including one patent application; six peer-reviewed articles in international journals indexed in the ISI, WoS, and SCOPUS databases. All peer-reviewed articles were published open-access in journals with an impact factor greater than 3. One article in JES (Journal of Engineering Sciences) and six works were presented and published at National and International Conferences after review.

Keywords: MOFs, ZIFs, ZnO, CuO, synergistic, molecular sieving effect, hybrid materials, MOF/MO, sensor.

Research purpose: This PhD thesis aims to develop hybrid materials/systems based on metal-organic frameworks/metal oxide (MOF/MO) for improved functionality, advanced characterization for detailed investigation of their physicochemical properties and establishing their correlation with sensing performance. The main objectives include evaluating the performance of the developed MOF/MO hybrid systems and sensors for selective detection of target analytes (hydrogen and volatile organic compounds) under adverse environmental conditions, elucidating the corresponding detection mechanism and enabling differentiation of analytes.

Objectives: An extensive investigation of physicochemical properties of the ZIF/ZnO and ZIF/CuO based MOF/MO hybrid structures and their employment for gas sensing applications based on metal-organic framework (MOF)-metal oxide (MOF/MO) systems: (i) ZIF-71/CuO:Al, for the detection of hydrogen and n-butanol at different operating temperatures; (ii) ZIF-8/CuO:Al hybrid structures for hydrogen and VOCs sensing under adverse environmental conditions; (iii) development of multi-sensors arrays for complex analyte differentiation using ZIFs/ZnO and ZIFs/Cd-doped ZnO based MOF/MO hybrid structures.

Scientific originality and the novelty of the research: Hybrid structures based on metal-organic framework (MOF)-metal oxide (MOF/MO) systems, namely ZIF/ZnO structures, were developed using a simple and cost-effective approach. A detailed investigation of physicochemical properties of the ZIFs/ZnO and ZIFs/CuO-based hybrid materials and the establishment of a methodology to correlate structure-property-performance relationship for the selective detection of tested analytes, including volatile compounds VOCs and hydrogen gas in adverse environmental conditions is novel which makes it interesting for the scientific community. A methodology combining *in-situ* analysis at different temperatures with sequential detection for comprehensive gas differentiation using multiple sensors was established. The ZIF-8/CuO:Al-based hybrid structures exhibited appreciable gas response (75%) to 100 ppm hydrogen, even at a relative humidity of RH 81%, enabling their applications under adverse humid conditions for extended periods of investigations. The developed ZIF-71/CuO:Al hybrid sensor exhibited dual gas sensing for n-butanol and hydrogen at different operating temperatures of 200 ℃ and 250 ℃, respectively.

The scientific problem addressed: The research work established structure-property-performance correlations of hybrid structures based on metal-organic framework (MOF)-metal oxide (MOF/MO) systems−for example, ZIF-n (n = 67, 7, 71, 8) combined with metal oxides such as ZnO:Cd and CuO:Al. The synergistic effect of different metal oxides with MOFs on their gas sensing performance to VOCs and hydrogen under adverse conditions was identified. Highly sensitive and selective hydrogen gas detection, even in high-humidity conditions and at low detection limits, opens up new areas of applicability.

The theoretical significance and applications of the work: The theoretical significance lies in establishing structure-property-performance relationships by determining the thermal stability ranges and oxidative transformation pathways of metal-organic frameworks ZIF-n (n = 67, 7, 71, 8) and metal oxides (Co_3O_4/ZnO) through *in-situ* structural analysis at different temperatures, thus defining their fundamental operational limits and mechanistic contributions in gas sensing. Establishing a critical understanding of the radiolytic stability of halogenated MOFs by identifying X-ray-induced degradation in ZIF-71, thus elucidating how specific functional groups dictate structural integrity under ionizing radiation and defining the thresholds necessary for non-destructive characterization. The ZIF-8/CuO:Al-based hybrid structures exhibited selective detection of hydrogen compared to other tested analytes and a low detection limit of ~402 ppb was achieved, which is advantageous for various applications, including the detection of very small amounts of hydrogen gas leaks. ZIF-71/CuO:Al-based hybrid structures exhibited dual gas sensing performance for n-butanol and hydrogen at 200 ℃ and 250 ℃, respectively, where n-butanol sensing response at 200 ℃ is four times higher than response to hydrogen gas. ZIF-67/ZnO hybrid sensor exhibited ethanol selectivity at 250 ℃, where as selectivity to hydrogen was observed for other three hybrid structures (ZIF-7/ZnO, ZIF-71/ZnO, and ZIF-8/ZnO). The practical applications of the presented work in wearable device applications for the effective sensing performance of hydrogen and different VOCs in indoor and outdoor environment and possible radiolytic detection.

Implementation of scientific results: The obtained scientific results were partially implemented within the DMIB-FCIM at the UTM, as well as one patent application.

ADNOTARE

la teza de doctorat intitulată „**Rețele Poroase de Materiale Hibride Nanostructurate**", prezentată de **Rajat**, pentru conferirea titlului științific de doctor în științe fizice la Universitatea Tehnică a Moldovei (UTM), specialitatea 134.03 „Fizica nanosistemelor și nanotehnologiilor" și în inginerie la Universitatea din Kiel.

Structura tezei: Teza a fost realizată în comun la UTM, Centrul de Nanotehnologii și Nanosenzori, Departamentul Microelectronică și Inginerie Biomedicală și Universitatea din Kiel, Facultatea de Inginerie, Catedra Nanomateriale Funcționale, Germania. Teza este scrisă în limba engleză și constă dintr-o introducere, cinci capitole, concluzii generale și recomandări, o bibliografie cu 273 de referințe, 104 pagini de text de bază, 40 de figuri, 7 tabele și 37 de ecuații. Rezultatele obținute au fost diseminate în 25 lucrări științifice, dintre care 14 sunt direct corelate cu tema tezei, incluzând: o cerere de brevet de invenție; 6 articole recenzate în reviste internaționale indexate în bazele de date ISI (Web of Science) și Scopus. Toate articolele recenzate au fost publicate Open Access în reviste cu un factor de impact mai mare de 3, iar un articol în revista JES și 6 lucrări prezentate și publicate la conferințe.

Cuvinte-cheie: MOF, ZIF, ZnO, CuO, sinergic, efect de cernere moleculară, materiale hibride, MOF/MO, senzor.

Scopul cercetării: Teză de doctorat își propune să dezvolte sisteme hibride de tip oxid metalic-rețea metal-organică (MOF/MO) pentru o caracterizare avansată a proprietăților fizico-chimice și stabilirea corelației acestora cu performanța și funcționalitate îmbunătățită de detecție a gazelor. Evaluarea fizico-chimică avansată a sistemelor hibride oxid metalic-rețea metal-organică și a senzorilor pentru detectarea selectivă a analiților (hidrogen și compuși organici volatili) în diverse condiții de mediu, elucidarea mecanismului de detectare corespunzător pe baza răspunsurilor utilizând senzori multipli din MOF/MO.

Obiective: O investigație extinsă a proprietăților fizico-chimice ale structurilor hibride pe bază de ZIF/ZnO sau ZIF/CuO și utilizarea acestora în aplicații de senzor pe baza sistemelor de oxid metalic-rețele metalo-organic (MOF/MO): (i) ZIF-71/CuO:Al, pentru detecția hidrogenului și a n-butanolului la diferite temperaturi de operare; (ii) structuri hibride ZIF-8/CuO:Al pentru detectarea hidrogenului și a COV în diverse condiții; (iii) dezvoltarea matricelor multisenzori utilizând structuri hibride MOF/MO, în particular ZIFs/ZnO și ZIFs/ZnO:Cd.

Originalitate științifică și noutatea cercetării: Structurile hibride MOF/MO bazate pe rețele metal-organice (MOF)-oxid metalic, și anume heterostructuri ZIF/ZnO. O investigație detaliată a proprietăților fizico-chimice ale materialelor hibride pe bază de ZIF/ZnO și ZIF/CuO și stabilirea unei metodologii pentru corelarea relației structură-proprietate-performanță pentru detectarea selectivă a compușilor organici volatili COV și hidrogen, reprezintă o noutate pentru comunitatea științifică. A fost stabilită o metodologie care combină analiza *in-situ* cu detectarea secvențială pentru diferențierea completă a gazelor de test utilizând senzori multipli pe bază de MOF/MO. Structurile hibride pe bază de ZIF-8/CuO:Al au prezentat un răspuns înalt (75%) față de 100 ppm hidrogen chiar și la o umiditate relativă ridicată de 81%, permițând aplicațiile acestora în condiții de umiditate pentru perioade lungi de timp. Senzorul hibrid pe bază de ZIF-71/CuO:Al dezvoltat a demonstrat o detecție duală a gazelor (n-butanol și hidrogen) la temperaturi de operare diferite, 200 °C și 250 °C, respectiv.

Problema științifică abordată: Lucrarea a stabilit corelații structură-proprietăți-performanță ale structurilor hibride bazate pe rețele MOF/MO. A fost identificat efectul sinergic al diferiților oxizi metalici cu MOF asupra performanței lor de detectare a COV și a H_2. Detectarea H_2 cu răspuns și selectivitate ridicată, chiar și în condiții de umiditate înaltă și limite de detecție scăzute, deschide noi domenii de aplicabilitate.

Semnificația teoretică și aplicațiile lucrării: Semnificația teoretică rezidă în stabilirea relațiilor structură-proprietate-performanță prin determinarea intervalelor de stabilitate termică și a căilor de transformare oxidativă ale rețelelor metal-organice ZIF (ZIF-67, ZIF-7, ZIF-71 și ZIF-8) și a oxizilor metalici prin analiză structurală *in-situ*, definind astfel limitele operaționale fundamentale și contribuțiile la mecanismul senzor. Înțelegerea stabilității radiolitice a MOF prin identificarea degradării induse de razele X în ZIF-71, elucidând astfel modul în care grupele funcționale specifice dictează integritatea structurală sub acțiunea radiațiilor ionizante și definind pragurile necesare pentru o caracterizare non-distructivă. Structurile hibride pe bază de ZIF-8/CuO:Al au prezentat o detectare selectivă a H_2 în comparație cu alți analiți testați și s-a atins o limită de detecție de doar ~402 ppb, ceea ce este avantajos pentru diverse aplicații, inclusiv detectarea unor cantități foarte mici de scurgeri de H_2. Structurile hibride pe bază de ZIF-71/CuO:Al au prezentat performanțe duale de detectare a gazelor pentru n-butanol și H_2 la 200 °C și respectiv 250 °C, unde răspunsul de detectare a n-butanol la 200 °C este de patru ori mai mare decât răspunsul la H_2 gazos. Senzorul hibrid ZIF-67/ZnO a prezentat selectivitate pentru etanol la 250 °C, în timp ce selectivitatea față de H_2 a fost observată pentru alte structuri hibride (ZIF-7/ZnO, ZIF-71/ZnO și ZIF-8/ZnO). Aplicațiile practice pot fi pentru detectare eficientă a H_2 și a diferiților (COV) în medii interioare și exterioare și detecție radiolitică.

Implementarea rezultatelor științifice: Rezultatele științifice obținute au fost implementate parțial în cadrul DMIB-FCIM din cadrul UTM, fiind depusă, de asemenea, o cerere de brevet de invenție.

KURZFASSUNG

In der Dissertation mit dem Titel „**Porous Networks of Nanostructured Hybrid Materials**", eingereicht von **Rajat** zur Erlangung des gemeinsamen akademischen Grades eines Doktors der Naturwissenschaften an der Technischen Universität Moldau (UTM) im Fachbereich 134.03 „Physik von Nanosystemen und Nanotechnologien" sowie des Grades eines Doktors der Ingenieurwissenschaften an der Universität zu Kiel.

Struktur der Dissertation: Die Dissertation wurde gemeinsam an der UTM, DMBE, Zentrum für Nanotechnologie und Nanosensoren und der Universität zu Kiel, Technische Fakultät, Lehrstuhl für Funktionale Nanomaterialien. Die Arbeit ist in englischer Sprache verfasst und gliedert sich in eine Einleitung, fünf Kapitel, allgemeine Schlussfolgerungen und Empfehlungen, ein Literaturverzeichnis mit 273 Quellen, 104 Seiten Haupttext, 40 Abbildungen, 7 Tabellen und 37 Gleichungen. Die erzielten Ergebnisse wurden in 25 wissenschaftlichen Publikationen veröffentlicht, von denen 14 einen direkten Bezug zum Thema der Dissertation aufweisen. Dazu gehören: eine Patentanmeldung, 6 begutachtete Artikel (Peer-Review) in internationalen Fachzeitschriften, die in den Datenbanken ISI und Scopus indexiert sind. Sämtliche begutachteten Artikel wurden als Open-Access-Publikationen veröffentlicht. Zudem wurden ein Artikel im JES publiziert und 6 Beiträge auf nationalen sowie internationalen Konferenzen präsentiert.

Schlüsselwörter: MOFs, ZIFs, ZnO, CuO, Synergie, Molekularsiebeffekt, Hybridmaterialien, MOF/MO, der Sensor.

Forschungsziel: Diese Dissertation zielt auf die Entwicklung von Hybridsystemen auf Basis von Metalloxiden und MOFs zur Verbesserung der Funktionalität, die Anwendung fortschrittlicher Charakterisierungsmethoden zur detaillierten Untersuchung ihrer physikalisch-chemischen Eigenschaften sowie die Etablierung ihrer Korrelation mit den Detektionsmechanismen ab. Zu den Hauptzielen gehören die Leistungsbewertung der entwickelten Hybridsysteme und Sensoren zur selektiven Detektion von Zielanalyt-Gasen (Wasserstoff und VOCs) unter widrigen Umweltbedingungen, die Aufklärung der entsprechenden Detektionsmechanismen.

Zielsetzung: Eine umfassende Untersuchung der physikalisch-chemischen Eigenschaften von ZIF/ZnO- oder ZIF/CuO-Hybridstrukturen und deren Einsatz für Sensoranwendungen basierend auf: (i) ZIF-71/CuO:Al zur Detektion von Wasserstoff und n-Butanol bei verschiedenen Betriebstemperaturen; (ii) ZIF-8/CuO:Al-Hybridstrukturen für die Wasserstoff- und VOC-Sensorik unter widrigen Umweltbedingungen; (iii) Entwicklung von Multisensor-Arrays zur Differenzierung komplexer Analyten unter Verwendung von ZIFs/ZnO-Hybridstrukturen.

Wissenschaftliche Originalität und Neuheit der Forschung: Hybride Strukturen auf Basis von MOF-Metalloxid-Systemen, insbesondere ZIF/ZnO-Strukturen, wurden mittels eines einfachen und kostengünstigen Ansatzes entwickelt. Eine detaillierte Untersuchung der physikalisch-chemischen Eigenschaften der Hybridmaterialien auf ZIFs/ZnO- und ZIFs/CuO-Basis sowie die Etablierung einer Methodik zur Korrelation der Struktur-Eigenschaft-Leistungs-Beziehung für den selektiven Nachweis der getesteten Analyten – einschließlich VOCs und Wasserstoff unter widrigen Umweltbedingungen–stellt eine wissenschaftliche Neuerung dar, die für die Fachwelt von großem Interesse ist. Es wurde eine Methodik etabliert, die *In-situ*-Analysen mit sequenzieller Detektion zur umfassenden Gasdifferenzierung mittels mehrerer Sensoren kombiniert. Die Hybridstrukturen auf ZIF-8/CuO:Al-Basis zeigten eine beachtliche Sensitivität (75%) gegenüber 100 ppm Wasserstoff, selbst bei einer relativen Luftfeuchtigkeit von 81 %, was ihren Einsatz unter widrigen, feuchten Bedingungen über längere Zeiträume ermöglicht. Der entwickelte ZIF-71/CuO:Al-Hybridsensor wies eine duale Gasdetektion (n-Butanol und Wasserstoff) bei unterschiedlichen Betriebstemperaturen (200°C und 250°C) auf.

Die untersuchte wissenschaftliche Fragestellung: Die Forschungsarbeit etablierte Struktur-Eigenschaft-Leistungs-Korrelationen für Hybridstrukturen auf der Basis von metall-organischen Gerüstverbindungen (MOF) und Metalloxid-Systemen (MOF/MO), wie zum Beispiel ZIF-n (n = 67, 7, 71, 8) in Kombination mit Metalloxiden wie ZnO:Cd und CuO:Al. Dabei wurde der synergetische Effekt verschiedener Metalloxide in Kombination mit MOFs auf deren Gasdetektionsleistung gegenüber VOCs und Wasserstoff unter widrigen Bedingungen identifiziert. Die hochempfindliche und selektive Wasserstoffdetektion, selbst unter Bedingungen hoher Luftfeuchtigkeit und bei niedrigen Nachweisgrenzen, eröffnet neue Anwendungsbereiche.

Die theoretische Bedeutung und die Anwendungsgebiete der Arbeit: Die theoretische Bedeutung liegt in der Etablierung von Struktur-Eigenschaft-Leistungs-Beziehungen durch die Bestimmung der thermischen Stabilitätsbereiche und oxidativen Transformationspfade von metallorganischen ZIF-Gerüstverbindungen (ZIF-67, ZIF-7, ZIF-71 und ZIF-8) sowie Metalloxiden mittels *In-situ*-Strukturanalyse, wodurch deren fundamentale Betriebsgrenzen und mechanistische Beiträge zur Gassensorik definiert werden. Ebenso wurde ein kritisches Verständnis der radiolytischen Stabilität halogenierter MOFs durch die Identifizierung der röntgeninduzierten Degradation in ZIF-71 erarbeitet, wodurch aufgeklärt wurde, wie spezifische funktionelle Gruppen die strukturelle Integrität unter ionisierender Strahlung diktieren und welche Schwellenwerte für eine zerstörungsfreie Charakterisierung notwendig sind. Die Hybridstrukturen auf ZIF-8/CuO:Al-Basis zeigten eine selektive Detektion von Wasserstoff im Vergleich zu anderen getesteten Analyten, wobei eine niedrige Nachweisgrenze von ~402 ppb erreicht wurde, was für verschiedene Anwendungen, einschließlich der Detektion kleinster Wasserstofflecks, vorteilhaft ist. Hybridstrukturen auf ZIF-71/CuO:Al-Basis wiesen eine duale Gasdetektionsleistung für n-Butanol und Wasserstoff bei 200°C bzw. 250°C auf, wobei das Ansprechverhalten auf n-Butanol bei 200 °C viermal höher ist als auf Wasserstoffgas. Der ZIF-67/ZnO-Hybridsensor zeigte eine Ethanol-Selektivität bei 250°C, während bei den anderen drei Hybridstrukturen (ZIF-7/ZnO, ZIF-71/ZnO und ZIF-8/ZnO) eine Selektivität gegenüber Wasserstoff beobachtet wurde. Die praktischen Anwendungen der vorgestellten Arbeit liegen im Bereich der Wearable-Devices für die effektive Detektion von Wasserstoff und verschiedenen VOCs in Innen- und Außenbereichen und radiolytischer Detektion.

Umsetzung der wissenschaftlichen Ergebnisse: Die erzielten wissenschaftlichen Ergebnisse wurden teilweise am DMIB-FCIM der UTM implementiert; zudem wurde eine Patentanmeldung eingereicht.

LIST OF ABBREVIATIONS

MOF – Metal organic framework

MOF/MO – Metal organic framework/metal oxides

VOC – Volatile organic compound

TVOC – Total Volatile organic compound

UV – Ultraviolet

XRD – X-ray diffraction

SEM – Scanning electron microscopy

EDX – Energy dispersive X-ray

XPS – X-ray photoelectron spectroscopy

CuO – Cupric Oxide

t-ZnO – tetrapodal Zinc Oxide

Al – Aluminium

Eu – Europium

PB – parallel beam

Cu_2O – Copper Oxide

ZIF – Zeolitic imidazolate framework

TGA – Thermogravimetric analysis

STA – Simultaneous thermal analyzer

MO/MOH – metal oxides and metal hydroxides

ads./des. – adsorption/desorption

CuO:Al – Al-doped CuO

RH – relative humidity

MFCs – Mass flow controllers

sccm – standard cubic centimetres per minute

ABE – acetone, butanol, and ethanol

OSHA – Occupational safety and health administration

WHO – World health organization

ppm – parts per million

ppb – parts per billion

COVID-19 – Corona virus disease 2019

PM2.5 – particulate matter with a diameter of ≤ 2.5 μm

USEPA – United states environmental protection agency

LDL – Lowest detectable limit

IUPAC – International Union of Pure and Applied Chemistry

MERV – minimum efficiency reporting value

EC – Electrochemical

DFT – Density functional theory

IEA – International energy agency

VUV – Vacuum ultraviolet

CCD – Charge-coupled device

BET – Brunauer-Emmett-Teller

XPS – X-ray photoelectron spectroscopy

UHV – Ultra-high Vacuum

SCS – Synthesis from chemical solution

DI – Deionized

RTA – Rapid thermal annealing

IDE – Interdigitated electrode

INTRODUCTION

Description of the topic:

Metal-organic frameworks (MOFs) are among the most promising materials in the development of hybrid heterostructures and gas sensors due to their modular nature which facilitates the incorporation of specific functional groups for the customization of the structure of MOFs and the presence of flexible cavities which allows molecules of specific size to pass through due to the molecular sieving effect [1]. As the Nobel Prize foundation highlighted in 2025, designing and synthesis of materials at the molecular level (such as MOFs) is essential for addressing global challenges, from extracting CO_2 to extracting drinking water from desert air [2]. A continuous decline in the environmental quality can be observed due to a combination of human activities, wars and natural factors. To tackle this issue, researchers have been developing novel materials and studying their properties to employ them in the field of gas sensing. Continuous monitoring is required to limit the volatile organic compound (VOC) emissions. Real time monitoring to VOCs-exposure for individual humans, spatial monitoring for environment, and scientific research can help to mitigate its harmful effects. Since, in the ambient environment, the simultaneous presence of 50-300 VOCs [3], as well as extreme humidity variations, and temperature variations make accurate detection of target gas very challenging. Bare metal oxide-based gas sensors have limitations such as high operating temperature, poor selectivity, etc. The development of hybrid materials can improve the issue of selectivity and endurance against humidity. MOFs are porous framework materials that possess properties such as ultra-high specific surface area, preferential interaction sites, and structural flexibility. When used as an additional layer, they can act as concentrators, providing selective diffusion pathways that facilitate the transport of specific analytes to the sensing interface. Furthermore, with advances in technology and data analytics, different VOCs can be differentiated through the simultaneous or sequential detection of responses from individual sensors in sensor arrays. Thus, the synergistic effect of metal oxides and MOFs or other functionalized materials synthesized and deposited by the different techniques contribute to the development of more sensitive and selective materials, with high stability even under adverse environmental conditions.

The importance of the addressed problem:

The advancements in material design by employing hybrids combining metal oxides and zeolitic imidazolate frameworks (ZIFs), a special class of MOFs, for their synergistic effect has revolutionized modern materials science. The synergistic interaction between the metal oxide and MOF components in hybrid structures significantly enhances sensing performance by integrating

the complementary properties of each component and mitigating the limitations associated with bare metal oxide-based sensors. The development of robust hybrid structures based on metal-organic frameworks-metal oxide systems is of great significance in the field of gas sensing [4–8]. Numerous sensing materials have been employed in the field of gas sensing, including ZnO, CuO, mixed oxides such as tetrapodal ZnO (t-ZnO) and CuO nanostructures, etc [9, 10]. The primary problems with the metal-oxide-based gas sensors are non-withstanding against humidity, poor selectivity, and signal drift, etc [10]. An additional coating layer of hydrophobic MOFs on top of metal oxides can solve these issues of selectivity, stability, and humidity immunity by providing preferential interaction sites for the target analyte, utilizing the molecular sieving effect, or through the doping or functionalization of an appropriate material. The hydrophobic properties, as the name suggests keep the sample stable even in high humidity conditions. There are lot of other factors that influence the sensing properties such as the morphology, porosity, specific surface area, and particle size of the sensing material. The doping concentration influences both the optical and the electrical properties of the sensing material by altering the charge carrier concentration, modifying absorption efficiency, and by introducing new energy levels within the band structure. Partial surface conversion of metal oxides creates additional active sites at the interface for interaction with target analytes, thereby enhancing sensing performance. For example, complete coverage of CuO nanoplatelets on a single t-ZnO microrod provides preferential interaction sites for hydrogen molecules, while the branched arms of the t-ZnO microrods hinder the diffusion of large VOC molecules, limiting their interaction at the interface [10].

Sequential detection of target analytes using a sensor array enables the differentiation of multiple gases (multicomponent detection) by analysing various output parameters, such as the sensing response, response time, recovery time, and optimum operating temperature. By incorporating diverse tools such as principal component analysis (PCA), the classification of analytes into distinct groups becomes more reliable based on differences in their principal component scores.

The goal and objectives of the research:

The doctoral thesis aims to: (i) synthesize advanced hybrid materials based on metal-organic frameworks (MOF/ZIF) and nanostructured metal oxides (MOx), specifically MOF/MOX architectures; (ii) develop and optimize high-performance hybrid sensors based on ZIF-71/CuO:Al, ZIF-8/CuO:Al, ZIF-67/ZnO, ZIF-7/ZnO, ZIF-71/ZnO, and ZIF-8/ZnO structures capable of ensuring selective and stable detection of hydrogen and volatile organic compounds (VOCs) under variable environmental conditions; and (iii) elucidate the physicochemical

mechanisms governing gas-surface interactions to establish a predictive framework for the detection and discrimination of these analytes.

Proposed research objectives:

- Development of hybrid structures based on combinations of ZIF (ZIF-67, -7, -71, -8) and metal oxides (CuO:Al, ZnO:Cd) using a simple and cost-effective approaches, such as synthesis from chemical solutions (SCS) for oxides and room-temperature drop-casting of MOFs for the assembly of sensing structures.

- Advanced evaluation of the physicochemical properties of ZIF-8/CuO:Al hybrid structures and correlate them with sensing performance (sensitivity and selectivity) towards hydrogen and n-butanol (among VOCs), under adverse environmental conditions over an extended period.

- Comprehensive investigation of the physicochemical properties of ZIF-71/CuO:Al structures and establishment of structure-property-sensing performance correlations toward hydrogen and n-butanol at different operating temperatures over an extended period.

- Achieving selective detection and discrimination of various analytes (VOCs and hydrogen gas) with distinct sensitivity profiles, achieved through sequential detection using ZIF-67/ZnO, ZIF-7/ZnO, ZIF-8/ZnO și ZIF-71/ZnO-based sensor platforms.

- Elucidation of gas-surface interaction mechanisms was proposed by integrating ionosorption model, transport physics, and electronic-structure parameters (polarizability and dipole moments) to establish a predictive framework for the selective recognition of analytes using ZIF/metal-oxide hybrid structures.

Scientific research methodology:

To achieve the objectives of this work, the following technological and scientific research methods were employed:

- ZnO, CuO, Cd-doped ZnO, and Al-doped CuO were synthesized using a SCS approach, followed by heat treatment via conventional thermal annealing or rapid thermal annealing in air.

- ZIFs were synthesized at room temperature, and dispersions of ZIF particles were prepared in methanol/2-propanol. Subsequently, hybrid metal-organic framework/metal oxide (MOF/MO) structures, namely ZIF/ZnO- or ZIF/CuO-based hybrid structures were fabricated using a simple and cost-effective SCS technique followed by drop-casting.

- The morphology, grain size, and distribution of the synthesized metal oxides, as well as the distribution of ZIFs on the metal oxide surfaces, were investigated using scanning electron microscopy (SEM).

- The structural properties, phase transitions, phase transformations, and crystallinity of the developed hybrid materials were analyzed using X-ray diffraction (XRD) or temperature-dependent in-situ X-ray diffraction.

- Phonon modes associated with the different components of the hybrid materials were investigated using micro-Raman spectroscopy to elucidate their vibrational characteristics and structural interactions.

- Energy dispersive X-ray (EDX) and X-ray photoelectron spectroscopy (XPS) were used to determine the chemical composition, oxidation states, and bonding interactions of the different components of the developed MOF/MO hybrid material.

- The Keithley 2400 SourceMeter unit, controlled via a programable LabVIEW interface (National Instruments), was used to precisely characterize the electrical properties of the devices using a two-point probe configuration under different chemical environments for the evaluation of their sensing performance.

- Sensor characterization was performed using a custom-built apparatus integrated with a computer-controlled source meter (Keithley 2400 and 2450, Keithley, OH, USA). The gas-sensing performance was evaluated across various operating temperatures (OPTs). During the testing cycle, diverse analytes including hydrogen, n-butanol, 2-propanol, ethanol, acetone, ammonia, carbon dioxide, and methane were introduced into the test chamber at a fixed concentration of 100 ppm and different relative humidities.

Novelty of the obtained scientific results:

This work presents the development of hybrid materials based on nanostructured and microstructured metal-organic framework-metal oxide systems (MOF/MO), especially ZIF/ZnO and ZIF/CuO, were developed using a simple and cost-effective approach. The innovative contribution to the scientific community consists in the detailed investigation of the physicochemical properties of these hybrids and in the establishment of a rigorous methodology for correlating the structure-property-performance relationship for the selective detection of hydrogen and VOCs under adverse environmental conditions. (i) ZIF-8/CuO:Al-based hybrid structures are selective for hydrogen (>4 times) over other tested analytes (acetone, 2-propanol, n-butanol, and ethanol) at 350 °C. ZIF-8/CuO:Al-based hybrid structures exhibited an appreciable response (75%) to 100 ppm hydrogen even at a high relative humidity of 81%, enabling their

application under adverse humid conditions even for long periods of time. The developed hybrid structures demonstrated temporal stability and retains notable sensing performance for a long period of time, even after four weeks from the initial measurements. Furthermore, a very low detection limit of 402 ppb was achieved. (ii) ZIF-71/CuO:Al-based hybrid structures exhibited selectivity towards n-butanol at 200 °C, with the sensing response being approximately four times higher than the response to hydrogen gas and approximately five times higher than the response to acetone during the initial measurements. The developed hybrid sensor exhibited dual gas sensing (n-butanol and hydrogen) at different operating temperatures (200 °C and 250 °C, respectively), which can be attributed to the synergistic effect of ZIF-71 and CuO:Al. (iii) Temperature dependent in-situ XRD invesigation on four different ZIFs, including ZIF-n (n=67, 7, 71, and 8), provided detailed insights about the phase transitions, thermal degradation, and the transformation of ZIFs into their corresponding metal oxides (ZnO or Co_3O_4) at specific temperatures. The implementation of sequential gas detection of four studied ZIFs/ZnO hybrids and its Cd-doped ZnO counterparts demonstrated selectivity and optimal responses to 2-propanol, ethanol, n-butanol, and hydrogen under different operating conditions.

The scientific research problem solved:

The problem addressed in this work is to overcome the limitations of classical metal oxide-based sensors by developing advanced metal-organic framework/metal oxide (MOF/MO) hybrid materials. The synthesized hybrid materials-based on MOF/MO systems, including microstructures, nanostructures of metal oxides and ZIF-based hybrid structures, detect hydrogen, n-butanol, and 2-propanol under adverse environmental conditions. A fundamental understanding of the thermal degradation and phase transition mechanisms of the investigated ZIF-based MOFs was achieved by determining their thermal stability ranges, confirming stable operations of ZIF-67, ZIF-7, ZIF-71, and ZIF-8 structures. The ZIF-8/CuO:Al and ZIF-71/CuO:Al hybrid structure exhibited selectivity towards hydrogen gas even in the presence of extreme humidity conditions (RH 81%), with long-term temporal stability and detection of n-butanol and hydrogen at different operating temperatures. By combining *in-situ* analysis with sequential multi-sensor detection, the work established rigorous structure-property-performance correlations, enabling differentiation of analytes based on their distinct response signatures.

The theoretical significance:

The theoretical significance lies in establishing structure-property-performance relationships by determining the thermal stability ranges and oxidative transformation pathways of developed hybrid materials. These systems, based on ZIF-type metal-organic frameworks (ZIF-n (n=67, 7, 71, and 8)) and metal oxides through *in-situ* structural analysis, thus defining their

fundamental operational limits and mechanistic contributions in gas sensing. Similarly, this work brings a critical understanding of the radiolytic stability of halogenated MOFs by identifying X-ray-induced degradation in ZIF-71, thus elucidating how specific functional groups dictate structural integrity under ionizing radiation and defining the thresholds necessary for non-destructive characterization. Furthermore, physicochemical models were developed to explain the gas-sensing mechanisms, incorporating concepts such as adsorption/desorption, activation energy, modulation of the potential barrier at the heterojunction interface, analyte's electronic polarizability, dipole moment of analyte, transport physics, and molecular sieving effect through ZIF pores, for VOCs and hydrogen at the interface of the ZIF/CuO:Al hybrid structures. Consequently, these findings provide an underlying physical understanding of charge transport and molecular interactions at the hybrid interface, establishing a predictive framework for the optimization of selectivity in high-performance sensor technology. The work elucidates the role of charge transfer at the interface of heterostructures formed between metal oxides and ZIF phases, demonstrating how the modulation of the potential barrier and the depletion region contribute decisively to the sensor signal in the presence of target analytes.

The applicative values of the thesis consist of the following:

- The comparative analysis of thermal stability provided a fundamental roadmap for the thermal degradation of ZIFs within MOF/MOx systems, offering essential data for their integration into gas sensing devices. The research confirms the reliability of the materials by establishing safe operational limits: 250 °C (ZIF-67), 375 °C (ZIF-7), 350 °C (ZIF-71 and ZIF-8).

- The development of hybrid structures based on ZIF-8/CuO:Al, which demonstrated selective hydrogen gas detection with an extremely low limit of detection of approximately 402 ppb. This performance is essential for critical applications, such as detecting very small hydrogen leaks in energy infrastructures.

- The implementation of dual detection capability using ZIF-71/CuO:Al-based hybrid structures, which allow for the selective monitoring of n-butanol and hydrogen by modulating the operating temperature (200 °C and 250 °C, respectively). At 200 °C, the sensor exhibits a response to n-butanol four times higher than that for hydrogen gas, ensuring efficient discrimination of these analytes.

- The demonstration of the specific selectivity of the ZIF-67/ZnO hybrid sensor toward ethanol at 250 °C, whereas selectivity to hydrogen was observed for the other three hybrid structures: ZIF-7/ZnO, ZIF-71/ZnO, and ZIF-8/ZnO.

- The development and scalable fabrication of MOx and MOF/MOx systems based on synthesis from chemical solutions (SCS) and microdrop-casting techniques at room temperature, which requires low energy consumption and production cost compared to conventional methods, facilitating the integration of hybrid sensors into wearable devices.

Scientific thesis submitted for defense:

- Determination of the structural robustness, localization of defect states, and chemical configuration of metal organic frameworks ZIF-67, -7, -71, and -8 across various operating temperatures, achieved through complex characterization of the structural electrical, and chemical properties of the hybrid materials developed in this work.

- Establishment of the fundamental mechanisms of thermal degradation and phase transition for ZIF/MOx hybrids (ZIF-67, -7, -71, and -8 combined with ZnO:Cd) using in situ temperature-dependent XRD. This investigation identified thermal stability intervals and highlighted the transformation processes from ZIF-67, -7, -71, and -8 into their corresponding metal oxides (ZnO or Co_3O_4), confirming the viability of these materials for safe operation in sensory devices.

- Elucidation of the structural and physicochemical properties of ZIF-71/CuO:Al hybrid materials, correlated with the explanation of sensing mechanisms and underlying interfacial physical phenomena.

- Demonstration of the decisive role of hybridizing CuO:Al nanomaterials with ZIF-71 frameworks—forming the ZIF-71/CuO:Al structure—in enhancing dual-gas detection capabilities at different operating temperatures (200°C and 250°C). This phenomenon is attributed to the synergistic effect between these materials; specifically, selectivity toward n-butanol at 200°C is dictated by high polarizability, while at 250°C, the heterostructure exhibits superior hydrogen selectivity due to facilitated diffusion through the framework pores.

- Substantiation of selective hydrogen gas detection using ZIF-8/CuO:Al-based hybrid materials, a process governed by the molecular sieving effect. It was established that, among the tested analytes, n-butanol exhibits increased sensitivity due to superior electronic polarizability compared to acetone or ethanol.

The scientific results were partially obtained at the Technical University of Moldova, Moldova and the Kiel University, Germany within the framework of HORIZON SENNET project. Based on the obtained results and patent application, it is possible to further implement innovative research activities at UTM.

Approval of scientific results:

The basic results of the doctoral thesis were discussed and presented at the half-yearly and annual meetings at the Department of Microelectronics and Biomedical Engineering of Technical University of Moldova (2023-2026); periodic SENNET consortium meetings twice a year under HORIZON Europe project (2023-2026); scientific seminars of the Department of Microelectronics and Biomedical Engineering of Technical University of Moldova (2025, 2026); disseminating and presented among a wider audience in 4 national and international scientific conferences, including: International fair of innovation and creative education for youth (ICE-USV) Suceava, Romania, July 2023; MOFSIM 2024, Montpellier, France, April 2024; *IEEE 15th International Conference on "Nanomaterials: Applications & Properties",* Bratislava, Slovakia, Sept. 7-12, 2025, E-Health and Bioengineering Conference (EHB), Iasi, Romania, 2024; and International Conference on Nanotechnologies and Biomedical Engineering (ICNBME), 2025, Republic of Moldova.

The investigations in the thesis fall in the priority research and development directions of Europe including Moldova:

Publications related to the subject of the thesis

The obtained results were published in 25 scientific publications, 14 of which are directly related to the topic of the thesis. Scientific papers on the topic of the thesis includes one patent application; six peer-reviewed articles in international journals indexed in major academic databases such as SCOPUS and Web of Science (ISI). All scientific papers were published in peer-reviewed journals with a journal impact factor exceeding 3. One article was published in journals from the National Register of specialized journals (JES- Journal of Engineering Science), and six papers/posters were presented and published in National and International Conference Proceedings. A complete list of publications is listed at the end of the thesis.

h-index=5+; i-10 index=3+. Number of citations on Google Scholar=67+; SCOPUS=45+, 12 ISI papers in Scopus ID: 59194131400, Web of Science Researcher ID: KPA-8644-2024.

Thesis volume and structure

A joint doctorate thesis consists of an introduction, five chapters containing 104 pages of basic text, 40 figures, 7 tables, and 37 equations, general conclusions and recommendations, 4 annexures, and bibliography with 273 references.

Keywords: MOFs, ZIFs, ZnO, synergistic, CuO, mechanism, molecular sieving effect, hybrid materials, MOF/MO, hybrids, sensor.

The basic content of the paper:

The ***Introduction*** substantiates the description and the addressed problem of the research topic and importance to develop new MOF/MO heterostructured systems. It provides an analysis of current state of research on the subject, defines the purpose and objectives of the study, and outlines its scientific novelty. The introduction also summarizes the primary scientific thesis and supporting research for defense, justifies the reliability of the results, and lists the attended scientific conferences at which the principal findings of the conducted research on the topic of thesis were disseminated through oral presentations, poster presentations, and scientific discussions with the approval from the scientific community.

Chapter 1 includes the possible approaches to overcome the limitations of metal oxides and their applications in sensing field by employing variety of concepts, specifically metal-oxide/MOFs or MOF/MO heterostructured-based hybrid sensors. Followed by the detailed discussion on the stability of MOFs and key factors affecting their structural phases and corresponding structure-property relationship. Theoretical concepts of characterizations tools such as XPS, SEM, XRD, and micro-Raman spectroscopy, are also discussed in detail. In the final section of this chapter, the applications of developed hybrid structures for the sensing of VOCs and hydrogen are discussed thoroughly using recently published literature.

Chapter 2 outlines the experimental approaches including the simple and cost-effective synthesis methods employed for the growth of metal oxides (ZnO, CuO, or ZnO:Cd, CuO:Al), synthesis of ZIFs, and the development of corresponding MOF/MO heterostructured systems, namely ZIFs/ZnO or ZIFs/CuO-based hybrid structures. Followed by the section including the experimental methods used for the material, thermal, sorption, and electrical characterization of the hybrid structures.

Chapter 3 presents a detailed discussion on the physicochemical properties of MOF-metal oxide systems, namely ZIF-8/CuO:Al-based MOF/MO hybrid structures. This is followed by an elucidation of the surface and interfacial characteristics of the developed hybrids, as well as an evaluation of their electronic and charge-transport properties in the presence of tested analytes. The hybrid structures are applied to gas-sensing studies of the target analytes, and the corresponding sensing mechanisms are discussed based on the ionosorption model, transport physics, and molecular sieving effect.

Chapter 4 presents the physical and chemical properties of ZIF-71/CuO:Al-based MOF/MO hybrid structures, followed by an analysis of the thermal and sorption properties of ZIF-71 particles. The ZIF-71/CuO:Al hybrid structures demonstrate a synergistic effect of its individual components, enabling effective sensing of n-butanol and hydrogen at different operating

temperatures. The corresponding sensing mechanisms, based on ionosorption and transport physics, are discussed to explain the observed results and the underlying physical processes.

Chapter 5 is dedicated to a comprehensive discussion of the material, physicochemical, and sensing properties of ZIFs/ZnO-based MOF/MO hybrid structures. Particular emphasis is placed on temperature-dependent *in-situ* X-ray diffraction analysis of ZIFs (ZIF-n (n = 67, 7, 71, 8)), which provides insight into thermal degradation, phase transition, and structural transformations of ZIFs into the corresponding metal oxides, and correlates structure-property-performance relationships in the resulting hybrid materials. The chapter also addresses the applications of developed hybrid structures in gas-sensing devices and explains the corresponding chemoresistive sensing mechanisms using appropriate models, including the p-n heterostructure effect, ionosorption model, transport physics, and others.

1. RECENT PROGRESS IN PHYSICOCHEMICAL AND GAS SENSING STUDIES OF METAL OXIDES/MOF HYBRIDS

1.1 Synergistic effects in metal oxide and MOF based hybrid architectures

Metal oxides play an important role in various fields due to their unique electronic, optical, and chemical properties, which allow them to employ in catalysis, energy storage, sensing technologies, and drug-delivery, among others [11–13]. The most common metal oxides being employed are ZnO, CuO, NiO, Co_3O_4, and $ZnFe_2O_4$, due to their strong antimicrobial activity, catalytic activity, electrochemical activity, and magnetic behaviour [5].

Different morphologies influence the surface activity of metal oxides by changing the surface area, active site exposure, charge transport, and adsorption properties. For instance, by changing the synthesis temperature, the morphology of structures can be altered. Three different morphological structures, such as SnO_2 quantum dots, cauliflower, and kadam flower shows different physical properties. Due to increase in surface area of quantum dots, it offers more active sites for dye degradation, followed by cauliflower, and kadam structures [14].

In the field of gas sensing, metal oxides offer appreciable sensing response due to the modulation of surface properties such as electrical resistance, capacitance, and optical features. In case of chemoresistive gas sensing, the variation in resistance occurs due to the adsorption of different chemical species on the surface. Surface properties can be modified by functionalizing the surface with the noble metals, heterostructure-effect, mixed-metal compositions, and by doping the surface with the rare-earth metals.

By incorporating other metal dopants, their electronic and chemical properties can be modified for the desired applications. For instance, Eu-doped ZnO demonstrate enhancement in the presence of oxygen species on the surface, due to modification in electrical charge transfer by incorporation of additional Eu energy levels. This facilitates in the enhancement of hydrogen sensing response [15].

A formation of p-n heterostructure between two metal oxides, create a depletion region that significantly influence the gas sensing performance. For instance, a heterostructure between NiO and WO_3 exhibits tremendous gas sensing response (2184%) to 100 ppm of acetaldehyde at 250 °C [16]. Similarly, a p-n heterojunction between CuO and $ZnSnO_3$ exhibited good selectivity to 100 ppm of ethanol at 160 °C as compared to acetone, toluene, ammonia, and formaldehyde [17].

Despite these advantages, metal oxides have certain limitations. including poor selectivity, instability, and sensor drift in complex or humid environments. Additionally, they require high

operating temperatures and high-power consumption. These can be addressed using functionalized materials, specific doping additives, layered structures, and MOF materials.

When developing gas sensors for monitoring gaseous species under adverse conditions, long-term stability and selectivity are critical considerations. For example, the selectivity of individual nanostructures is often limited by variations in single-nanowire sensors. However, employing multi-nanowire sensors can average out these variations, leading to enhanced selectivity. Zhang et al. [18] reported that In_2O_3 multi-wire nanosensors exhibit enhanced selectivity toward NO_2 compared to NH_3, which was not observed in single wire nanosensors. The opposite sensing responses of individual nanowires cancels out in multiwire-configuration, resulting in a diminished response to NH_3, and consequently, improved selectivity for NO_2. Another study utilized a porous polymer filter (Cu(BTC)/PDMS) to improve the selectivity of a commercial SnO2-based sensor (MQ-5) for H_2 against CO [19]. After placing the porous filter at the gas inlet, the adsorption efficiency for H_2 remains almost same 98%, while the response toward CO was significantly reduced. This filter-integrated configuration not only enhances selectivity but also minimizes moisture adsorption, reducing it from approximately 76% to nearly zero.

Pristine semiconductor metal-oxide based gas sensors generally require high- temperatures to facilitate oxygen adsorption on the sensing surface by providing the necessary thermal activation energy. However, high power consumption remains a significant obstacle for integrating these sensors into wearable devices. To address these challenges, various strategies have been proposed, including self-powered gas sensors. For instance, a study based on p-n heterojunction effect in NiO/ZnO nanowires leveraged the piezoelectric effect to power the sensing element. This approach yielded an appreciable sensing response (31.5%) and remarkable selectivity to H_2S (100 ppm) at room temperature [20].

Another approach to classifying analytes more precisely is through machine learning (ML)-aided data analysis. When the figures of merit for similar gases are nearly identical, making differentiation difficult, advanced analytical tools such as machine-learning techniques are employed [21]. These models require large datasets to ensure high accuracy. Typically, the data is categorized into features (input variables) and labels (the target classes). The classification follows a systematic methodology. For instance, a study on ZnO decorated with noble metals (Ir, Ru, and IrRu alloys) utilized machine learning to evaluate sensing parameters [21]. In this approach, the dynamic response curve was treated as a combination of two distinct regions: the response region and the recovery region. An appropriate mathematical function, shown in Figure 1.1(a) I, was used to fit the curves in both regions. The exponential fitting function (F), defined in Equation 1.1, was then employed to classify the tested gases [21].

$$F = -a_{res/rec} \times e^{\left(-k_{res/rec} \times t\right)} + b_{res/rec} \tag{1.1}$$

where $a_{res/rec}$, $k_{res/rec}$, and $b_{res/rec}$ are the initaial constant, the time constant, and the offset between two curve regions, respectively.

The features were extracted from the fitting parameters, as shown in Figure 1.1(a) II, and subsequently evaluated in Figure 1.1(a) III.
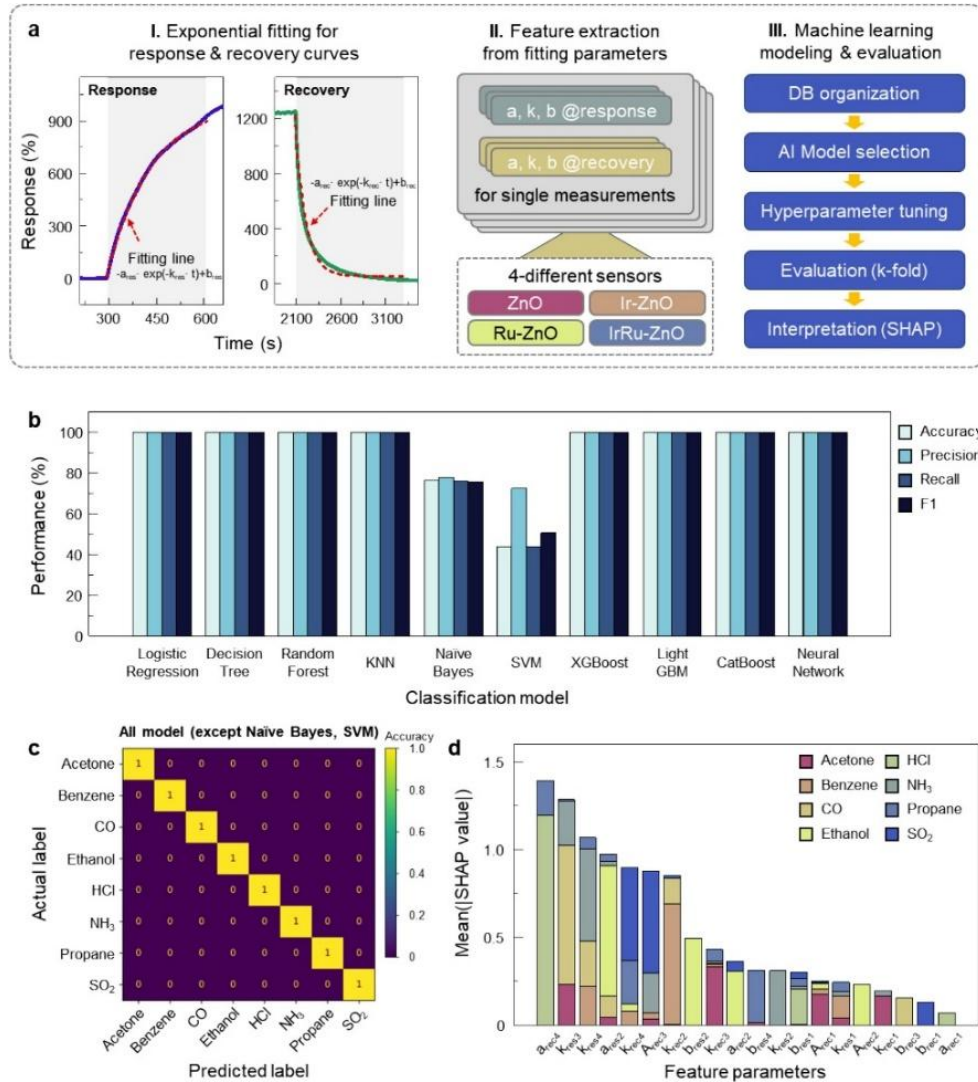
Fig. 1.1. (a). Schematic representation of machine-learning based classification, including data acquisition and feature extraction from mathematical functional of exponential fitting. (b) machine-learning models-based performance of different classification models. (c) Confusion matrix of obtained results except Naibe Bayes and SVM models-based results. (d) Mean SHAP value contribution plot of applied features for different target gas species using XGBoost model. Reproduced with permission from ref [21] from the Elsevier under a CC BY-NC-ND 4.0 licence.

The target gases were classified using a supervised machine learning approach, employing algorithms—such as logistic regression, k-Nearest Neighbours (kNN), Support Vector Machines (SVM), LightGBM, and neural networks. The performance of these training algorithms is presented in Figure 1.1(b). A confusion matrix (Figure 1.1(c)) was used to evaluate the overall classification performance from the trained models, excluding Naive Bayes and SVM. Finally, the impact of each feature on an individual prediction was assessed using the LightGBM model, as illustrated by the mean SHAP value rankings in Figure 1.1(d).

Highly advanced machine learning based classification models are useful when sensor responses are complex, multi-dimensional, or lack inherent selectivity. For direct analyte classification and in new environmental conditions for which diverse data are unavailable, hybrid materials can be employed to enhance selectivity, improve long-term stability in high humidity conditions, and lower the detection limit.

Hybrid structures composed of metal oxides and MOFs have emerged as advanced sensing platforms that overcome the limitations of metal oxide sensors. MOFs are recognized for their remarkable properties, such as high porosity, light weight, large specific surface area, high functionality, and good thermal and chemical stability [22, 23]. By incorporating MOFs with biomolecules, polymers, metal oxides, ceramics, or metal particles, novel hybrid materials with superior properties can be produced. This opens diverse possibilities for the employment of MOFs in fields such as photo sensing [24], gas sensing [25], gas storage and separation [26], drug-delivery [27], and catalysis [28].

The synergistic effect between MOFs and metal oxides significantly improves sensing performance by providing numerous interaction sites through unsaturated metal centers, surface functional groups, or the molecular sieving effect of the pores. For instance, Wu et al. presented a ZnO nanorod and ZIF-8 core-shell structure for the selective sensing of H_2 over CO, attributed to the molecular sieving effect of ZIF-8 [29]. In this study, the linker concentration controlled the grain size; a low linker concentration (0.12 mmol) resulted in large ZIF-8 nanoparticles (>400nm), whereas increasing the concentration to 0.48 mmol reduced the grain size to ~100 nm, ensuring uniform coverage on the ZnO nanorods.

The sensing performance of core-shell structure was enhanced by reducing CO sensitivity (from 1.3 to 1) and increasing H_2 sensitivity (from 1.8 to 2.8) for a 50 ppm concentration at 200 °C. This enhancement is attributed to increased surface area and the development of more oxygen vacancies following ZIF-8 growth. Furthermore, the synergistic effect of MOFs and metal oxides improves photodetection. Studies report that ligands absorb light, and photogenerated charge carriers are injected into the ligands to generate additional electron-hole pairs via ligand-to-cluster

charge transfer [30, 31]. It has been observed that the degree of conjugation affects the light-absorption properties of MOF linkers. MOFs are generally classified into two categories: those with azolate bases and those with carboxylate bases. Azolate linkers typically exhibit a high degree of conjugation than carboxylate linkers, which is inversely proportional to the band gap energy. For instance, while Kang et al. [32] reported poor charge separation in two-dimensional conductive MOFs, the use of a $Cu_3(HTTP)_2$/ZnO heterojunction significantly improved the separation of UV-generated charge carriers (Figure 1.2).

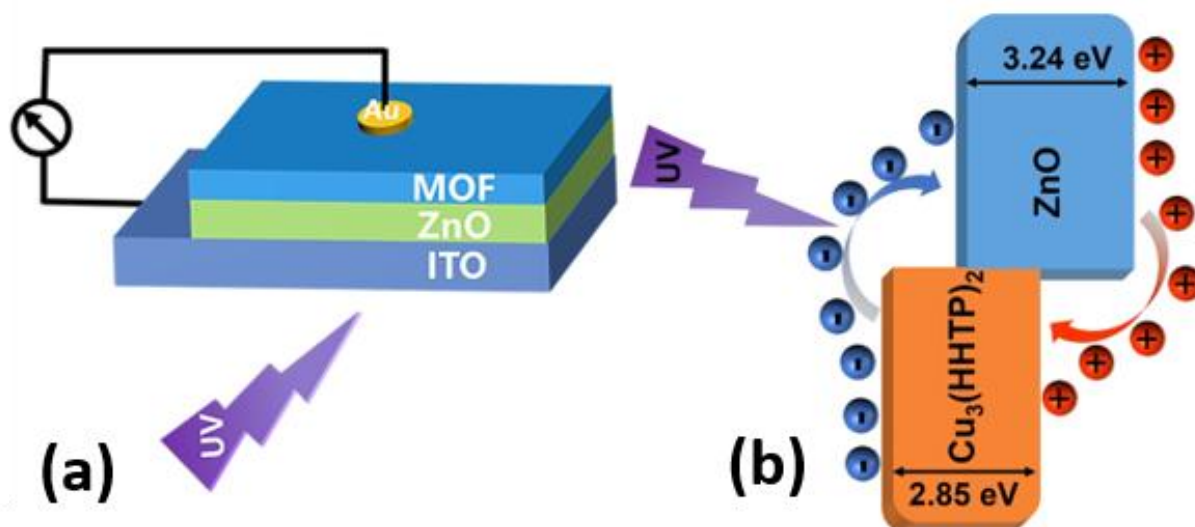**Fig. 1.2. (a) Schematic illustration of the $Cu_3(HHTP)_2$/ZnO structures on ITO substrate under the light illumination from the substrate side. (b) Energy band diagram of the $Cu_3(HHTP)_2$/ZnO heterojunction under UV illumination at a wavelength of 365 nm. Reproduced from ref** [32] **with permission. Copyright 2022, Wiley.**

It exhibited a responsivity of 78.2 A/W and a detectivity of approximately 3.8×10^9 Jones under a bias voltage of 1 V. In this study, charge separation is attributed to the heterojunction formation at the ZnO and conductive $Cu_3(HTTP)_2$ interface, as well as the pyroelectric effect of ZnO [32].

In other fields such as catalysis, the synergistic effect of PtO species and the Fe-based sulfonate organic cage MOF (Fe-soc-MOF) was presented for the photocatalytic CO_2 reduction reaction (Figure 1.3). An appropriate amount of Pt loading (1.5 wt%) in Fe-soc-MOF exhibited a selectivity of 94% to CO, with yields of 285.6 μmol/g for CO and 18.1 μmol/g for CH_4. The high CO_2 affinity of Fe-soc-MOF, combined with the decreased adsorption capacity of the CO intermediate, leads to high selectivity [33].

In the field of energy, the construction of an electrode using zinc ferrite and ferric oxide-based MOFs with a 2-methylimidazolate ligand was reported. It exhibited remarkable structural

stability and electrochemical performance. With the incorporation of ferric oxide, the migration energy of the lithium ion (Li^+) decreases, resulting in better kinetics for ion diffusion, which excels the performance of lithium-ion batteries [34].
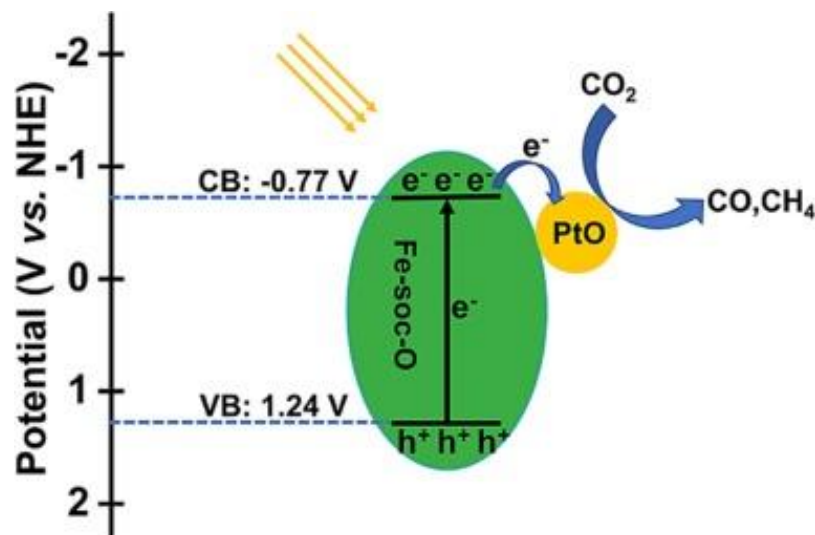

Fig. 1.3. Schematic representation of CO₂ reduction photocatalyzed using PtO on Fe-soc-O. Reproduced from ref [33] with permission. Copyright 2023, Elsevier.

1.2. Thermal and Chemical stability of metal-organic frameworks

The determination of chemical and thermal stability is crucial before employing MOFs in different fields. Since the discovery of MOFs in the 1990s, tailoring the properties of MOFs using the organic ligands has become much easier, which has led to their employment for compound-specific adsorption of analytes [35, 36]. Modifications of the framework network are possible using a combination of linkers and an appropriate metal node as per the requirements. However, in case of other porous networks such as silica gel and zeolites, modification of the assembly is limited to a small extent compared to the MOFs. Early complex coordination networks were inflexible and quite unstable; for instance, the complex compound Cu(tpp)CuBF₄ exhibited instability upon solvent extraction after activation [37]. With the advent of novel technologies, MOF synthesis has become more advanced, leading to the development of more stable and flexible MOFs−such as (Zn(BDC))−that retain porosity even after solvent extraction [38].

The stability of MOFs is affected by many factors such as the strength of the coordination bond, the strength of the acid, the modulator, and others [39, 40]. The strength of the coordination bond is affected by the oxidation state of the metal node, which impacts the coordination of organic ligands and metal nodes. It has been observed that the higher-valent metal centers exhibit stronger coordination with organic ligands that contain oxygen, resulting in better water stability compared

to organic compounds with lower-valent metal centers [41]. The water stability of MOFs is also affected by other factors such as the charge density of the metal center and the pK_a value of the linker. For example, a comparison of coordination of isoreticular structures of Mg-based frameworks and Zn-based frameworks with water molecules demonstrated that the Mg-based framework is more water-stable due to stronger coordination of the metal center (Mg) with the oxygen of water molecules, compared to the Zn counterpart [42]. The water stability of different classes of MOFs with azolate base and carboxylate base can be discussed with the help of Lewis acid-base coordination theory. It has been observed that the bond strength of the metal center is directly proportional to the pK_a value of the ligands. The classes of linkers with nitrogen that enable coordination with metal centers, such as pyrazole and imidazole, have higher pK_a values compared to carboxylate linkers, in which oxygen enables coordination bond to form with the metal center. So, the ZIFs consisting higher pK_a value linkers form stronger bonds with the metal centres, resisting water molecules or related entities that degrade its framework structure in alkaline conditions [39]. MOFs belonging to this class are ZIF-7, ZIF-8, ZIF-71, ZIF-67, PCN-601, and PCN-602, among others [39, 43]. In contrast, carboxylic group-based MOFs, especially Zr-MOFs are stable in acidic conditions but unstable in alkaline conditions due to weaker bond formation between Zr and carboxylic acid compared to OH^- [41]. This can be understood by the theory of natural bond orbitals.

The structural integrity of ZIFs has been explored in different environmental conditions, which is important for their combination with the metal oxides in the development of hybrid materials. For instance, temperature dependent *in-situ* FTIR measurements elucidate the transition of the ZIF-8 framework [44]. These measurements showed lattice expansion at temperatures less than 200 °C, and other reversible structural deformations in the temperature range of 200 to 350 °C, followed by then irreversible structural degradation at temperatures >350 °C. Similar studies have investigated other ZIFs such as ZIF-67 [45] and ZIF-7 [46], among others.

1.3. Overview of characterization fundamentals for MOF-MO systems

1.3.1. Synthesis from the chemical solutions

Synthesis via a chemical solution approach is an easy, low-cost, and repeatable method for the development of metal-oxide films on substrates [47]. In this process, the chemical reactants are mixed in a stoichiometric ratio according to the final film composition. The growth of the metal oxide film by this approach occurs through the appropriate selection of chemical precursors and their combination with a suitable solvent, followed by the thermal treatment to enhance the

crystallinity of the oxide film. To ensure homogeneous deposition and control the kinetics for the high-quality film formation, the selection of an appropriate solvent−and sometimes a complexing agent−helps to design the optimal formulation of the solution [48, 49].

1.3.2. Scanning electron spectroscopy (SEM)

SEM is a surface imaging tool used to produce high-resolution images of a specimen surface for the analysis of surface morphology and its composition. It uses high-energy electrons to complete this task. This advanced microscopic technique falls under the category of surface probe microscopy. Due to the short wavelength of focused and accelerated electrons, it can resolve features in the nm regime [50]. To reduce the number density of gas molecules inside the microscopic chamber and the collision probability between electrons and the gas molecules, a high vacuum (10^{-5} to 10^{-6} mbar regime) condition is vital [51]. Field emission guns and special SEM lenses need ultra-high vacuum (10^{-9}-10^{-10} mbar regime) to maintain a stable electron source tip.

High-energy primary electrons (in the keV range) [50] originating from the electron gun (thermionic filament or field emission) traverse through the lens column onto the specimen surface [52]. Following the scanning of the primary electron beam, a suitable detector quantifies the interaction signal from the specimen surface. The quantified signals provide depth information based on the interaction volume of the primary beam with the specimen. A secondary electron detector detects low-energy electrons from an interaction depth of approximately 100 nm, providing high-resolution morphological information [50]. Another detector detects high-energy backscattered electrons from an interaction depth of approximately 1 μm, which are elastically scattered back from deeper inside the sample; these provide compositional contrast [50]. An EDX spectroscopy detector detects characteristic X-rays emitted from the sample when the electron beam displaces inner-shell electrons, providing elemental composition and mapping [50].

1.3.3. X-ray diffraction (XRD)

Diffraction of X-rays at periodic crystal lattices is the necessity of the wavelength (0.5 Å $< \lambda < 2.5$ Å) [53] to be approximately of the order of the periodicity of the corresponding diffraction lattice [54]. Subsequently, a necessary condition for the diffraction is coherence between the waves passing through the lattice [55]. Moreover, the diffracted waves are assumed to be scattered elastically [54]. The necessary condition for constructive interferences among the diffracting waves is satisfied if the following condition holds [54]:

$$2d \sin \theta = n\lambda \qquad\qquad (1.2)$$

where d represents interplanar spacing, θ is the Bragg's angle, n is the diffraction order, and λ is the wavelength of the incident X-rays.

In this thesis, the parallel beam (PB) configuration of the Rigaku's SmartLab X-ray diffractometer is used to enable high-precision measurements, especially for thin films [56]. In principle, PB optics utilize multilayer mirrors optics, such as a PB collimator, to convert divergent X-rays into a parallel beam. This greatly improves angular resolution by reducing axial divergence and footprint errors caused by sample surface imperfections. In terms of the optical setup, a PB slit is inserted after the X-ray source to collimate the beam into a highly parallel state [56]. The incident optics typically include the X-ray tube (Cu Kα), multilayer mirrors, Soller slits, and PB slits. This system automatically aligns these components based on the chosen measurement package [56].

1.3.4. Raman spectroscopy

Raman spectroscopy is a non-destructive vibrational spectroscopic technique. When laser photons impinge on a sample surface, they cause inelastic scattering, leading to molecular vibration [57] and an energy shift that is quantized by a vibrational quantum number v_n [58].
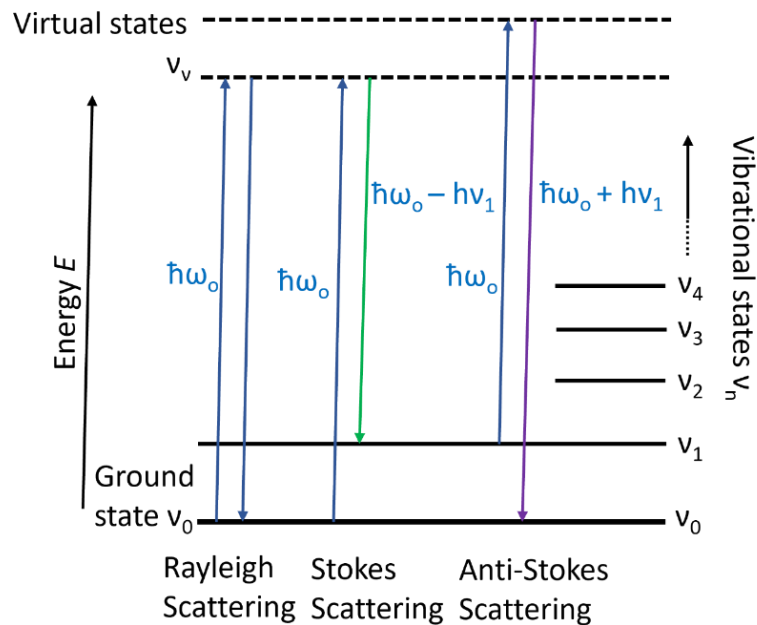

Fig. 1.4. Schematic for the energy transitions for different scattering modes.

When a monochromatic source of visible light is incident upon the specimen surface, it locally distorts the mobile surface charge carriers, resulting in excitation to a virtual state, v_v. When

the system relaxes from the virtual quantum state to the ground state (elastic scattering), it is known as Rayleigh scattering [58]. Contrary to this, there is a possibility of relaxation to a higher vibrational energy level, known as Stokes scattering [58]. In another case, if the molecule is already in an excited state before the absorption of photons and then relaxes back to the ground state, it is known as Anti-stokes scattering [58]. The whole concept is well illustrated in Figure 1.4.

1.3.5. X-ray photoelectron spectroscopy (XPS)

XPS is a surface sensitive spectroscopic technique that probes the binding energy of atomic core-hole states [59]. In this technique, the soft X-rays irradiated on the specimen surface, and the kinetic energy of emitted core-level electrons is analysed [59]. When the specimen surface is irradiated by the X-rays with energy *hv* sufficient to overcome the work function of the spectrometer (φ_{spect}), the rest is binding energy (E_{BE}) of an initial core-level electron bound to the atom and the kinetic energy (E_{KE}) of the electron, as shown in Equation 1.3 [60].

$$hv = \varphi_{spect} + E_{KE} + E_{BE} \qquad (1.3)$$

The kinetic energy of the core-level of electron is commonly analyzed by a hemispherical energy analyzer and φ_{spect} is included because the binding energy of the core-level electron is measured with respect to the Fermi level, rather than the vacuum level. To avoid the loss of binding energy of the core electrons due to scattering events caused by gas molecules at moderate pressure in the measurement chamber, an ultra-high vacuum condition is vital [61]. During analysis, the degradation of samples depends on the total X-rays exposure, the sensitivity of the material to the specific X-ray wavelength, the temperature of the surface and other related triggers.

1.4. Advances in VOCs and hydrogen sensing using hybrids

VOCs are organic species, which can easily evaporate at ambient conditions. Most common sources of VOCs are household products− such as furniture, paints, deodorants, cosmetics, cleansing products, and among others [62]. A prolonged exposure of these VOCs can cause serious health issues depending on their critical concentration limits set by different international regulatory authorities. For instance, Occupational Safety and Health Administration (OSHA) has set safe exposure limit for ethanol (<1000 ppm) and over exposure to this limit may cause temporary dizziness, problem in respiratory tract, but exceeding it to 10000-20000 ppm may cause serious problems such as paralyses or death due to respiratory failure [62, 63]. Similarly, other VOC species with their corresponding permissible limits− such as acetone (OSHA: 1000

ppm) [62], toluene (OSHA: 200 ppm for 8-hour work shift) [64], formaldehyde (WHO: 82 ppb) [65], xylene (OSHA: 100 ppm for 8-hour work shift) [64], and among others.

PM2.5 is a particulate matter with a mixture of solid particles (particle size ≤2.5 μm) and liquid present in environment. This component is very significant in the evaluation of air quality index. In 2024, U.S. environmental protection agency strengthened the standardization of PM2.5 concentration level and set its limit at 9 μgm^{-3} [66]. But a study conducted in Lucknow, a city in Uttar Pradesh, India [67], evaluated PM2.5 concentrations during contrasting seasons−monsoon and non-monsoon. The results revealed that PM2.5 levels ranged from 29 μgm^{-3} during the monsoon to 64 μgm^{-3} in the non-monsoon season. These concentrations significantly exceed standard safe value of PM2.5, clearly indicating a alarming situation in the region.

A lot of studies have been conducted across the globe to assess the impact of VOCs and total volatile organic compounds (TVOCs) on environment. Research investigated by Lai et al. for two days have demonstrated time spent by human for activities and their VOC exposure in different environments. It showed that human spend 90% of their daytime indoors−such as homes, offices, and shops-where VOC exposure levels were found to be 20% higher than outdoors [68]. Human exposure to VOCs varies significantly across different geographical regions. Studies on world's two most populous countries, India and China−which are under-developing and causing a lot of carbon emissions, facing significant air quality challenges. For instance, a pilot study conducted in India before COVID-19 tracked VOC sources in two cities of Gujarat−Ahmedabad and Gandhinagar [69]. By comparing contrasting seasons, the study found that total indoor VOC concentrations in winter (327 ± 224.2 μgm^{-3}) were significantly higher than in summer (150 ± 121.0 μgm^{-3}), with indoor levels consistently exceeding outdoor measurements. Similarly, a 35-day study in Beijing, China, across two contrasting seasons [70] reported that VOCs concentrations were higher in winter than in summer. The average TVOCs concentrations in summer was reported as 104.85 μgm^{-3} (converted from ppbv), using conversion relation [71].

During COVID-19, extensive measures−such as the widespread use of disinfecting solvents in homes, schools, and working places−were implemented to restrict the spread of COVID-19 cases. However, these actions led to a significant increase in TVOC concentrations. A study conducted in Tarragona, Spain by Ninyà et al. revealed that in 2021 [72], a sharp increase of TVOCs approximately three-times compared to its concentration in 2019 was observed. A major portion of this comes from solvents, which were present everywhere in schools at concentrations range from 272 to 423 μgm^{-3}, representing 68−83% of the TVOCs. Furthermore, indoor TVOC concentrations were found to be approximately twenty times higher than outdoor levels.

There is an urgent need for low-cost, high-performance sensors capable of selectively detecting VOCs with low power consumption for their real-time monitoring. Hybrid materials offer a sustainable and reliable solution by enhancing the sensitivity and selectivity of these sensors. Among these, a new class of materials known as ZIFs has proven effective as either pre-concentrators or porous sheath layers on metal oxides. These layers selectively adsorb target gas species from complex environments. Various hydrophobic ZIFs are currently available; these frameworks not only withstand against high RH but also provide numerous interaction sites through their metal centers and specific functional groups. For instance, a study by Malepe et al. demonstrated a highly sensitive sensor for toluene detection using these materials [73]. A composite sensor based on carbon soot and ZIF-71 exhibited notable toluene sensing (0.27 Ω) even at 80% RH, with only a slight deviation (from 0.27 to 0.20 Ω) when compared to 33% RH. The sensor demonstrated a stable response across varying humidity levels at room temperature. Moreover, Chen et al. reported the selective sensing of formaldehyde (S=14) at 150 °C, maintaining stability even at high RH (70%) [74]. In that study, the high surface area (1832.2 m^2/g) of ZIF-67 facilitated increased formaldehyde adsorption, resulting in a fast response speed until saturation. To investigate the sensing mechanism under high humidity, CO_2 infrared band measurements were performed; these showed an enhancement in intensity prolonged exposure time of the sensor to toluene. The recent developments in VOCs sensing technologies and their corresponding mechanisms are tabulated in Table 1.1.

In general, PM2.5 and VOCs are the two major class of pollutants that require effective mitigation. Classical filters−such as zeolites, activated carbon, and various polymer-based filters−often suffer from limitations, including low selectivity and poor affinity for polar gaseous molecules.

To address these challenges, a study reported on a composite electret filter (MERV-13) integrated with porous MIL-125-NH$_2$ [75]. This composite exhibited remarkable simultaneous removal efficiency for both PM2.5 and toluene. Though, its performance was limited to environments below 30% RH, as its hydrophobic nature caused removal efficiency to degrade at higher humidity levels. To overcome this issue, a PDMS layer was coated onto the composite to enhance its external hydrophobicity. Afterwards, the filter maintained significant simultaneous removal efficiency for PM2.5 and toluene at high humidity levels up to 60% RH.

Table 1.1. Summary of the hybrid sensors for VOC sensing.

Sensing material	Sensing mechanism	Target analyte	Interfering analytes	selectivity	Detection limit	Permissible limit of analyte	Ref.
s-Nb_2O_5@SnO_2	Resistance change	acetone	Isoprene, acetaldehyde, ammonia, hydrogen, toluene, paraxylene, and nitrogen dioxide	>2.8 times	40 ppt	< 1 ppm against diabetes	[76]
ZnO@ZIF-8 nanosheets	Heterostructure effect, inhibition of self-stacking of nanosheets, and resistance change	ethanol	Ammonia, methylbenzene, methanol, acetone, carbon monoxide, formaldehyde, and nitrogen dioxide	2.1 to 25.8	460 ppb	−	[77]
MOF derived heterostructures (WO_3/$ZnWO_4$/$CoWO_4$)	Poyoxometalates interaction with WO_3 and fast carrier transport, resistance change	n-butanol	Methanol, acetone, ethanol, TMA, TEA, NH_3, and DMF	>11 times	−	−	[78]
ZIF-8 derived ZnO/$Ni_{0.9}Zn_{0.1}O$	Heterojunction effect, selective contribution of Ni catalyst, and resistance change	xylene	Acetone, ammonia, methanol, toluene, ethanol, and NO_2	>2.7 times	0.12 ppm	100 ppm set by OSHA over an 8-hour work shift	[79]
Carbon soot@ZIF-71 nanoparticles	Using FTIR studies and LCR meter analysis, resistance change	toluene	Acetonitrile, mesitylene, ethanol, and diethyl ether	>1.47 times	518 ppb	200 ppm set by OSHA over an 8-hour work shift	[73]

VOC detection is also vital for non-invasive breathomics [80]. The effective detection of biomarkers within clinical limits using high-performance sensors is crucial for correlating

metabolic processes with overall health. Recently, a study reported on ferrocene-encapsulated ZIF-8 electrodes for the electrochemical (EC) sensing of four biomarkers: isopropanol, acetone, ethanol, and acetic acid [80]. While the developed EC sensor exhibited detection of all four biomarkers, only the detection of acetone fell within clinical limits. The detection levels for the remaining biomarkers were outside the required clinical ranges; however, the study serves as a significant proof-of-concept for this material platform.

Furthermore, a study was performed to design a bimetallic sensor for an effective detection of acetone as a biomarker for diagnosing lung cancer. A DFT-based study investigated different bimetallic combinations: (FeCoN$_5$P/fullerene), (FeNiN$_5$P/fullerene), (FeCuN$_5$P/fullerene), and (FeZnN$_5$P/fullerene) [81]. The study revealed that a composite with the Fe-Cu combination (FeCuN$_5$P/fullerene) exhibited increased adsorption energy for acetone. Moreover, an application of hollow ZIF-7 coated on stainless steel fibres was reported for the solid phase microextraction of five biomarkers (hexanal, decanal, isopropanol, acetone, and hexanol) [82]. The studied ZIF-coated fibre exhibited the highest extraction capacity and enhancement factor for acetone and isopropanol, followed by hexanol, hexanal, and decanal. It demonstrated good repeatability by maintaining notable extraction performance over 140 cycles of adsorption and desorption. This is attributed to the porous structure, large surface area, gate-opening effect, and hydrophobic interactions.

Preconcentrators have immense importance in state-of-the-art gas sensing technology. Their function is to mitigate the low detection limits of standalone gas sensors. A preconcentrator material should have a high adsorption capacity and an open structural form for the accumulation of adsorbates, quick diffusion, and desorption at low temperatures. Commercially available polymer-based preconcentrators have certain limitations; for example, their dense structures increase desorption times and lead to slower kinetics [83]. To mitigate this issue, researchers are focusing on developing adsorbent materials with open structural forms that enable the quick diffusion of adsorbates, leading to a faster adsorption/desorption process.

Traditional adsorbent materials for filtering applications, such as Tenax TA and activated carbon, remain in use, but research focuses on exploring alternative materials. For instance, a study on MOF-5 as a preconcentrator for benzene molecules demonstrated a higher preconcentration efficiency compared to the aliphatic ester series, due to better π-π interactions between benzene molecules and the MOF-5 framework [84]. Additionally, another study focused on enhancing preconcentration efficiency by adding a carbon-based preconcentrator to Carbopack-X adsorbent material [85]. It exhibited a notable preconcentration factor of about 352 using a copper-based preconcentrator for the detection of 10 ppb of isoprene. Moreover, a study investigated an NH$_2$-

UIO-66@PDMS adsorbent where the MOF was incorporated into a photoacoustic cell for the detection of acetone at sub-ppm levels in breath samples [86]. It revealed an 11-fold enhancement in signal intensity after the incorporation of the preconcentrator and an effective increase in selectivity against interfering analytes (ethanol, propanol, water vapor, and oxygen). The investigated adsorbent demonstrated notable reproducibility across five parallel adsorbents loadings and showed notable stability during a 30-day temporal stability test without appreciable degradation in sensing performance.

In the last five years, the world's population has grown tremendously at a rate of around 0.8 to 0.9% per year [87]. As per international energy agency (IEA), global energy demand rose by 2.2% in 2024, which is approximately double the annual average demand over the last decade [88]. The continuous use of fossil fuels for all energy requirements has been causing environmental degradation, leading to climate change that challenges human civilization [89]. Following this same trend in the future could increase emanation of green-house gases by 50% by 2050; this is predicted to increase the global air temperature to 6.4 °C in year 2100 from 1.1 °C in year 2000 [90]. Such a rise would have devastating effects on the climate. Currently, we can see the effects of climate change through irregular rainfall [91] and other uncontrolled natural hazards [92]. Thus, transforming global energy policy is an urgent need for today's world. Many countries in the world such as India and the European Union, have already taken strong action by adopting new energy policies and implementing renewable clean energy laws for a clean and safe future [93].

Hydrogen is emerging as a versatile carrier of energy which supports the integration of various energy systems, transforming them into more sustainable and low-carbon systems. It has the potential to fulfil energy requirements in different fields, such as the electronics and power industries. However, it is a flammable fuel with an explosion range of 4% to 75% in air [94]. Furthermore, it is colorless, tasteless, and odorless, which makes it difficult to monitor it using natural senses. Although it is non-toxic, a high-concentration (~52%) of asphyxiants (including hydrogen) can deplete the oxygen content in the air; which can cause death, because less than 10% of oxygen in air is lethal [95, 96]. Thus, efficient hydrogen sensors for the detection of leakage during transportation and storage are of great interest to researchers. Recent reports demonstrate advancement in hydrogen sensor technology. For instance, Gao et al. published a study on 5 at.% Pd-modified PdO/SnO_2 heterojunction-based sensors, which exhibited a magnificent sensing response (R_a/R_g) of around 35 at 162.5 °C for 1000 ppm of hydrogen [97]. In this study, integrated machine learning tools such as PCA and Random Forests, to extract features and assess models for predicting outcomes at a high relative humidity of 80%. It revealed a 91% accuracy in recognizing hydrogen concentrations. Such sensors, which maintain stable sensitivity in high-

humidity conditions, can be employed in semiconductor industries and battery manufacturing [98, 99], among others. Moreover, a review by Thokala et al. reported the preconcentrator effect of a MOF layer, which increases the concentration of hydrogen interacting with themetal oxide surface via redox reactions [100].

ZIFs are a special subclass of MOFs, comprising divalent metal ions coordinated with nitrogen atoms in the imidazolate linkers [101]. ZIFs have a porous framework, and integrating them with metal oxides can contribute to synergistic effects. For instance, ZnO@ZIF-8 nanowires using 10 wt% of ZIF-8 exhibited a selective sensing of hydrogen (50 ppm) with a response value (R_a/R_g=1.44) compared to C_6H_6 and C_7H_8 [102]. This can be attributed to the molecular sieving effect. Furthermore, another study on the integration of a polydopamine and ZIF-8 composite with In_2O_3 thin films showed an enrichment effect and improved the hydrogen sensing response by 900% compared to an In_2O_3 film [103]. A synergistic effect between noble metals and ZIFs was also observed; the catalytic effect of noble metals and the ultrahigh surface area of ZIFs provide selective sensing of the target analyte and increased oxygen vacancies, respectively, in metal oxide-based gas sensors. A reported study on ZnO@ZIF-71@Ag showed enhanced hydrogen detection compared to a ZnO@ZIF-71 composite-based sensor due to the catalytic action of Ag within the pores of ZIF-71 [103, 104]. The Ag-incorporated composite exhibited approximately 11 times higher sensitivity to 50 ppm hydrogen compared to the ZnO@ZIF-71 composite at 150 °C. This can be attributed to the molecular sieving effect of ZIF-71 and the catalytic action of the Ag nanoparticles.

A synergetic effect between ZnO and ZIF-8 has been widely recognized for improving hydrogen sensing properties. A study by Poschmann et al. has demonstrated the synergistic effect of tetrapodal ZnO and ZIF-8 by developing a surface-converted pinhole-free overlayer of ZIF-8 on ZnO [4]. This study explains the sensing mechanism through three different scenarios, as shown in Figure 1.6. Before gate-opening, the pore aperture (3.0 Å) allows only small molecules, such as hydrogen, to pass through the ZIF-8 and interact with the ZnO surface for chemoresistive sensing. After gate-opening, the flexible framework expands and the pore aperture increases to 3.5 Å, which allows other gas molecules, such as methane, to pass through the ZIF-8. This process of allowing gas molecules with a kinetic diameter less than or equal to the size of the pore aperture is known as the molecular sieving effect. Similar studies have investigated ultra-selective sensing of hydrogen using this approach [29, 105].
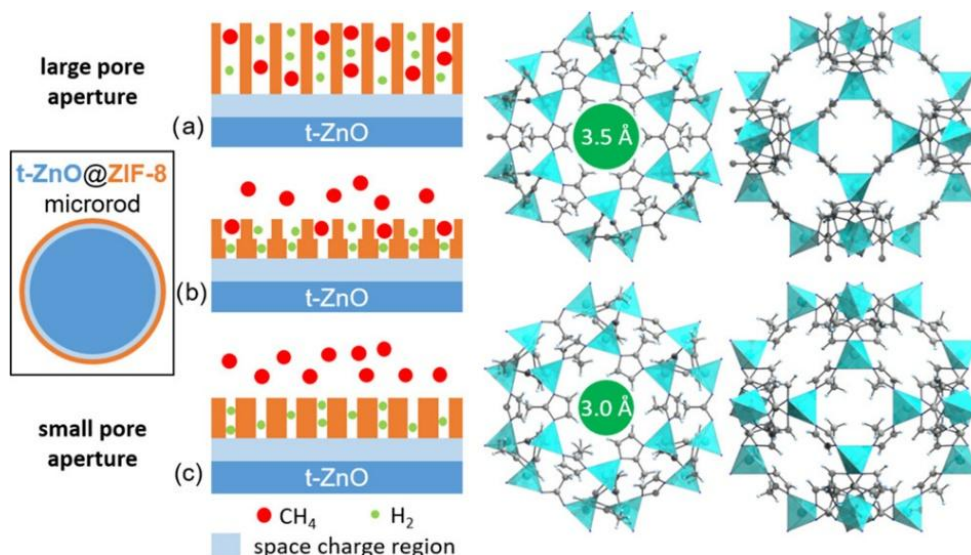
Fig. 1.6. Schematic illustration of the sensing mechanism of ZIF-8 coated tetrapodal ZnO with large pore aperture (a) 3.5 Å, (b) between 3.0 and 3.5 Å, and (c) 3.0 Å. Reproduced with permission from ref [4] from the American Chemical Society under a CC BY-NC-ND 4.0 licence.

The specific choice of a MOF as a sheath layer on metal oxides depends on several factors, including the required functionality, target analytes, and operating conditions. For instance, ZIF-8 and ZIF-67 have the same organic linker (2-methylimidazolate) and the same sodalite (SOD) topology, but they differ in their metal nodes−Zn and Co, respectively [106]. A comparison of the physicochemical properties of these two ZIFs clearly demonstrates the influence of the metal node. In contrast, two ZIFs (ZIF-8 and ZIF-7) possess the same metal nodes and SOD topology but differ in their organic linkers, resulting in variations in pore size, cage size, and other physicochemical properties [106, 107]. Furthermore, transitioning from ZIF-8 to ZIF-71−maintaining the same metal node while changing the topology (SOD to RHO) and organic linker−provides insights into thermal and chemical stability, even under exposure to acidic gases [108, 109]. Therefore, a comprehensive investigation of the physicochemical properties of these ZIFs integrated with the same metal-oxide-based hybrid structures enables the contribution of individual structural parameters to be isolated by keeping the other variables constant.

The demand for efficient hydrogen sensors is expanding in the aerospace industry and space missions [110, 111]. To reduce carbon emissions, hydrogen is being used as a fuel in aircraft, which requires hydrogen-based engines. At high flying altitudes, oxygen concentration decreases, leading to the requirement for efficient sensors whose sensing mechanism depends on factors other than oxygen. Technological developments in hydrogen-based fuel cells leads to the use of moisture

instead of oxygen for the hydrogen leak detection in aircraft systems [112]. For instance, Pd-alloy-based Schottky diodes do not require oxygen for their operation [113]. Pd catalyses the dissociation of hydrogen molecules into atoms, which then react with the oxide film. The resulting change in electrical properties reflects the change in hydrogen concentration.

1.5 Summary and Conclusions of Chapter 1

Metal oxides are widely explored materials that are sensitive to various gases. Generally, undoped and non-functionalized metal-oxide-based sensors exhibit limited selectivity to target analytes and intolerance to different environmental conditions. Moreover, bare metal oxides have certain limitations, such as limited light absorption, rapid electron-hole pairs recombination, and wide-bandgaps, among others. Thus, further modification of metal-oxide-based sensors is required to overcome these limitations.

Following the corresponding literature, it can be deduced that pristine metal oxides, such as SnO_2, ZnO, CuO, and among others, have been studied extensively for gas sensing applications. Though, the limitations of poor selectivity and sustainability in different environmental conditions, such as high RH conditions and high temperatures, remain a crucial challenge. Thus, new hybrid material combinations, such as MOF- or ZIF-coated metal-oxide-based layered structures, need to be developed using simple and cost-effective approaches. A comprehensive investigation of their physicochemical properties is required to correlate these properties with gas-sensing performance and to explain the underlying physics of the sensing mechanism.

The synergistic effect of MOFs and metal oxides in the field of gas sensing has been studied extensively, though an appropriate sensing mechanism is not discussed in detail. Although, the flexibility of MOFs and their corresponding molecular sieving effect have been widely discussed, a robust model to connect the chemical affinity of target analytes to MOFs− based on their adsorption energy, polarity, and interaction strength−still need to be developed.

The stability of ZIFs is discussed in different acidic and basic media. Moreover, only limited investigations using *in-situ* temperature-dependent measurements on variety of ZIFs, such as ZIF-71, ZIF-7, ZIF-67, and ZIF-8, have been conducted. An extensive study of these measurements provides information about the structural integrity and phase transitions of the ZIF framework.

2. DEVELOPMENT AND CHARACTERIZATION OF METAL OXIDES AND MOF SYSTEMS

2.1. Tools and methodologies for characterizing metal oxides and the MOF-MO hybrids

In this Chapter, the synthesis of bare metal oxides such as ZnO, CuO, and doped metal oxides such as CuO:Al, Cd-doped ZnO, was performed using the synthesis from chemical solution (SCS) approach. On the other hand, the synthesis process for ZIFs was carried out through a liquid solution approach at room temperature.

The morphological properties of metal oxides and the developed hybrid structures were investigated using SEM. The measurements were conducted using a Carl Zeiss SEM operated at 7 kV and 10 μA. The corresponding elemental mapping and the compositional analysis were conducted using Zeiss Gemini Ultra55 Plus EDX system attached to the SEM apparatus.

The structural investigation was performed using a Rigaku diffractometer equipped with a high flux X-ray source (9 kW), with a rotating anode Cu $K_{\alpha 1}$ (1.54 Å) operating at 45 kV and 200 mA. The measurements were performed within the 2θ range of 2-100˚, depending on the sample, with a step size of 0.05˚. The real-time structural evolution and phase degradation of ZIFs were measured using temperature-dependent *in-situ* XRD. *In-situ* measurements were performed using an Anton-Paar DHS 1100 temperature stage. The measurements were performed within the 2θ range of 4 to 40˚ at a step size of 0.04˚. All the *in-situ* measurements were performed at a scan speed of 11.48 degrees per minute; thereby, all the ZIFs were exposed to X-rays for 3.14 minutes at each temperature. A HyPix-3000 hybrid photon counting one-dimensional line detector was employed to acquire high resolution diffraction data.

To acquire the structural and chemical information in the specified region of the sample with high spatial resolution, the micro-Raman measurements were performed using a WITec 300 RA system. A solid-state Nd:YAG laser (8 mW) was used as the excitation source. For almost all the samples, a green laser line with a wavelength 532 nm from the Nd:YAG laser except ZIF-67 based samples. For ZIF-67-based samples, a red laser line with a wavelength of 633 nm was used at low intensity to avoid thermal degradation associated with strong-light absorption of cobalt (II) ions in the visible range. The inelastically scattered light was analyzed by a triple grating spectrometer equipped with a charge-coupled device (CCD) detector, optimized at a blaze wavelength of 500 nm. The choice of diffraction grating determined the accessible range and resolution. High-groove density gratings (1800 grooves/mm) offer superior spectral resolution but restrict the measurable range to ~900 cm^{-1} owing to the finite CCD dimensions. In contrast,

gratings with lower groove densities (1200 grooves/mm and 600 grooves/mm) extend the spectral coverage to ~1400-1600 cm^{-1} and ~3500 cm^{-1}, respectively, albeit with reduced resolution.

Nitrogen adsorption-desorption isotherms of ZIF particles were measured at 77 K using a Micromeritics 3Flex 3500 physisorption instrument to study the pore size distribution and Brunauer-Emmett-Teller (BET) surface area. Prior to measurements, the samples were degassed under vacuum at 140 °C for ZIF-8 and ZIF-67, or at 200 °C for ZIF-7 and ZIF-71 samples. The Flex software from Micromeritics was used to determine the BET surface area of the ZIF particles.

Thermogravimetric analysis (TGA) was performed on ZIF particles using a simultaneous thermal analyzer (STA) 449 F3 Jupiter® (Netzsch Germany). A small amount of ZIF particles was placed in alumina crucibles and heated from 25 °C to 800 °C at a constant rate of 5 °C/min under a continuous synthetic air flow of 50 ml/min during measurements.

XPS spectra of ZIF-coated CuO:Al films and ZIF-coated ZnO films were obtained using an XPS ultra-high vacuum (UHV) system (Prevac Sp. z o.o.). The base pressure in the analytical chamber was maintained in the range of $1×10^{-8}$ to $1×10^{-9}$ mbar range, which was achieved by a combination of a scroll backing pump and a turbomolecular pump. A non-monochromatic Al Kα excitation X-ray source (1486.6 eV) was operated at 300 W (15 kV, 20 mA). Survey scan spectra were obtained within the binding energy range of 0 to 1300 eV with three iterations for each scan at a pass energy of 200 eV. High-resolution spectra of the core levels (C 1s, Cu 2p, Co 2p, Zn 2p, O 1s, and N 1s) were obtained with twenty iterations at a pass energy of 50 eV. The obtained XPS spectra were analysed and processed using CasaXPS (2.3.23) software. The whole spectra were shifted by calibrating the binding energies against the Zn $2p_{3/2}$ line of the corresponding ZIF at 1021.7 eV. High-resolution XPS scan spectra were fitted using Gaussian-Lorentzian (1:1) functions, and the background was removed using the Shirley algorithm. Subsequently, relative sensitivity factors were applied after background subtraction to ensure the elimination of interfering signals and baseline noise. Finally, the chemical surface composition was determined by numerically integrating the peak areas.

For the gas sensing measurements, the prepared samples were exposed to a range of gases (n-butanol, hydrogen, 2-propanol, acetone, ethanol, and ammonia) at different test gas concentrations (10 ppm, 50 ppm, 100 ppm, and 1000 ppm) at different operating temperatures (20 °C, 150°C, 200 °C, 250 °C, and 300 °C). The sensing setup consisted of a gas flow system (carrier gas, target analyte, bubbler, and mass flow controllers (MFCs)), a closed chamber (sample platform, electrodes, temperature control, and inlet and outlet ports), and a Keithley 2400 source meter, controlled via a LabView interface.

The test gas was diluted to the desired concentration by mixing it with air using MFCs [114]. The final concentration (C_f) after dilution can be calculated using the formula:

$$C_f = \frac{C_t \times F_a}{F_m} \tag{2.1}$$

where C_t is the initial test gas concentration in the bottle, F_a is the flow rate of the analyte, and F_m is the flow rate of the mixture of the test gas and air.

Gas flow rates of the analyte (F_a) and the mixture of analyte and air (F_m) in the closed chamber were kept at 200 standard cubic centimetres per minute (sccm). Below the sample platform, a heater was placed to control the temperature using a microcontroller. Samples were tested in the presence of test gases at different RH levels of 11%, 50%, and 81%, measured using a hygrometer, as previously reported [115]. Using a bubbling system, by passing a carrier air through water at different temperatures depending on the desired RH% and then injected into the closed chamber. The two-probe measurement method was used to perform all the electrical measurements. As both a precision source and measuring instrument, the Keithley 2400 series sourcemeter® unit provides programmable voltage and current sourcing with integrated high-accuracy measuring capabilities.

The gas sensing response (S) was determined using the following relations depending on the type of the semiconducting material and the gas type, as shown in Table 2.1.

Table 2.1. Gas sensing response (S) for n-type and p-type semiconductors for reducing and oxidizing test gases [116, 117].

	Reducing gas	Oxidizing gas
n-type	$S(\%) = \dfrac{R_a - R_g}{R_g} \times 100\%$	$S(\%) = \dfrac{R_g - R_a}{R_a} \times 100\%$
p-type	$S(\%) = \dfrac{R_g - R_a}{R_a} \times 100\%$	$S(\%) = \dfrac{R_a - R_g}{R_g} \times 100\%$

where R_a is the resistance of the sample in air and R_g is the resistance of the sample in the presence of test gas.

The response and recovery times are defined as the time required to reach 90% of the total change in resistance of the sample after the gas exposure and the time required to return back to the 10% of the total resistance change after turning off the gas, as it approaches the baseline resistance, respectively.

2.2 Development of the ZIF-8/CuO:Al-based MOF/MO hybrids

Aluminium-doped CuO (CuO:Al) hybrid structures were deposited on glass substrates with dimensions 1.2 cm ×1.4 cm × 0.1 cm, using an SCS approach, as previously reported [115, 118]. Prior to deposition, the glass substrates were cleaned using a multi-step cleaning process. The substrates were immersed in a HNO_3 (30%) solution for 10 minutes, followed by rinsing in deionized (DI) water. Subsequently, the substrates were ultrasonically cleaned in ethanol and acetone for 5 minutes, followed by another rinse in DI water. Thereafter, the substrates were dried under a dry air flux. The deposition of the CuO:Al film was carried out by preparing cationic and anionic solutions in two different beakers separately. For the preparation of the cationic solution, a copper thiosulfate complex solution was used, comprising 1 mol/L of copper sulfate pentahydrate (purity 99%, Sigma-Aldrich) and 1 mol/L of sodium thiosulfate pentahydrate (purity 98.5%, Sigma-Aldrich). The cationic precursor solution was further diluted to 0.1 mol/L using DI water under continuous stirring at room temperature. The Al dopant precursor was obtained by adding 10 mg of $Al(NO_3)_3.9H_2O$ (Alfa Aesar) to 100 ml of DI water. The doping of Al was performed by mixing the Al precursor solution into the cationic precursor solution [114]. On the other hand, the anionic precursor solution consisted of NaOH (99%, Sigma-Aldrich) with a molar concentration of 2 mol/L in DI water. It was continuously stirred at 80 °C. The deposition process, involving the immersion of pre-cleaned substrates in precursor solutions, was carried out with the aid of an articulated robot to avoid human error in dipping times and the number of SCS cycles [118]. After multiple SCS cycles, the CuO:Al film was dried under a dry air flux, followed by the post-growth heat treatment. The samples were thermally treated at 600 °C for 60 seconds using rapid thermal annealing (RTA) to enhance the crystallinity of the thin film [115].

ZIF-8 was prepared by using a liquid solution approach at room temperature. For this purpose, 297.49 mg (1 mmol) of zinc nitrate hexahydrate (99%, Fisher Chemical) and 328.40 mg (4 mmol) of 2-methylimidazole (99%, Sigma-Aldrich) were separately dissolved in 20 mL of methanol (≥ 99%, Fisher Chemical). Consequently, the later solution was poured into the former solution and continuously stirred for 1 minute. After 24 h, the white solids were isolated from the dispersion by centrifugation, followed by washing it with methanol (two times) and 2-propanol (one time, ≥ 99%, Sigma-Aldrich). The obtained ZIF nanoparticles were kept in 2-propanol to prevent aggregation.

Prior to the ZIF-8 nanoparticles deposition on the CuO:Al structure, electrical Au contacts were fabricated on the CuO:Al film using an Al mask in a meander configuration with an electrode gap of 1 mm, following the established protocols [119]. The prepared ZIF-8 dispersion, with a concentration of 0.75 mg/mL in 2-propanol was ultrasonicated for 15 minutes, followed by a

deposition of 100 µL of the ZIF-8 dispersion on the CuO:Al structure in two iterations of 50 µL each by drop-casting using a micropipette. The schematic illustrating the fabrication process of the ZIF-8/CuO:Al-based hybrid structures on the glass substrate (Figure 2.1).
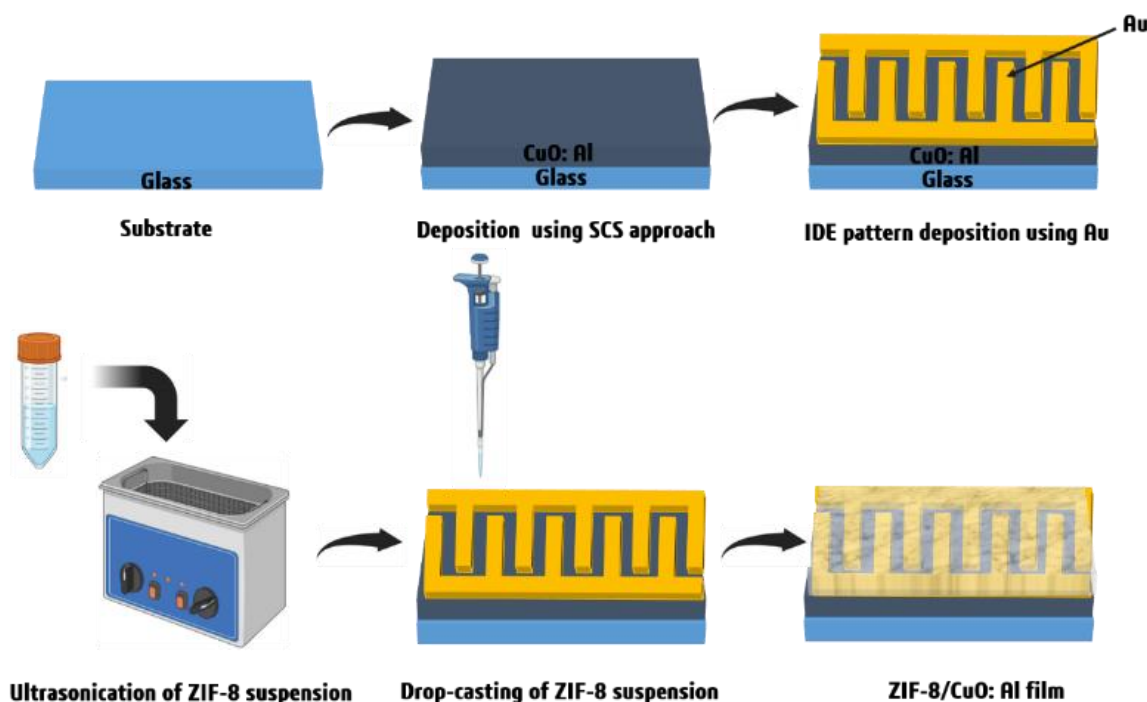

Fig. 2.1. Schematic illustration of the stepwise fabrication process of the ZIF-8/CuO:Al structures.

2.3. Synthesis and fabrication of the ZIF-71/CuO:Al-based MOF/MO hybrids

Al-doped CuO structures were deposited on glass substrates (1.2 cm×1.4 cm × 0.1 cm), using an SCS approach, as previously reported [115, 118]. Using a HNO_3(30%) solution, the glass substrates were cleaned for 10 minutes, followed by rinsing in DI water. Afterwards, the glass substrates were cleaned using ethanol and acetone mixture (1:1) for 5 minutes, followed by another rinse in DI water and dried under a dry air flux. Thereafter, a cationic precursor solution was prepared using a copper thiosulfate complex solution, comprising of 1 mol/L of copper sulfate pentahydrate (99%, Sigma-Aldrich) and 1 mol/L sodium thiosulfate pentahydrate (98.5%, Sigma-Aldrich). The prepared solution was diluted with DI water under continuous stirring at room temperature to obtain a 0.1 mol/L of copper concentration. Al doping was performed in a diluted cationic precursor solution, by adding 10 mg of aluminium nitrate hexahydrate (Alfa Aesar), previously dissolved to 100 ml of DI water [114]. The anionic precursor solution was prepared in DI water using 2 mol/L of sodium hydroxide (99%, Sigma-Aldrich) and was continuously stirred at 80 °C. Following the preparation of precursor solutions, the pre-cleaned glass substrates were immersed in the cationic and anionic precursor solutions using an articulated robot to avoid human

error in dipping times and the number of SCS cycles [118]. Following the deposition of CuO:Al films, the samples were dried under a dry air flux. Thereafter, the samples underwent post-thermal treatment by RTA at 650 °C for 60 s, as reported previously [115].

ZIF-71 particles were prepared by using a liquid solution approach at room temperature. Synthesis of ZIF-71 was carried out by using 1 mmol of zinc nitrate dihydrate (99%, Sigma-Aldrich) and 2 mmol of 4,5-dichloroimidazole (97%, Tokyo Chemical Industry Co., Ltd.) were dissolved separately in 20 ml of methanol (99.9%, Fisher Chemical) each. The later solution was rapidly added to the former solution under continuous stirring for 1 hour, followed by a centrifugation of dispersion solution, resulted in the separation of white solids from methanol. Afterwards, washing of obtained white solids was carried out using methanol and 2-propanol (99.5%, Sigma-Aldrich) separately. The obtained particles were kept in 2-propanol to prevent aggregation.

Before the deposition of the ZIF-71 particles on the CuO:Al films, Au IDE contacts (170 nm thick) were fabricated on the CuO:Al films using Al mask in a meander configuration, maintaining a interelectrode gap of 1 mm, as reported previously [119]. Following the ultrasonication, ZIF-71 dispersion was drop-cast onto the CuO:Al surface in two iterations, 50 µL each at an interval of 15 minutes. Figure 2.2 demonstrates the schematic fabrication of the ZIF-71/CuO:Al structures.
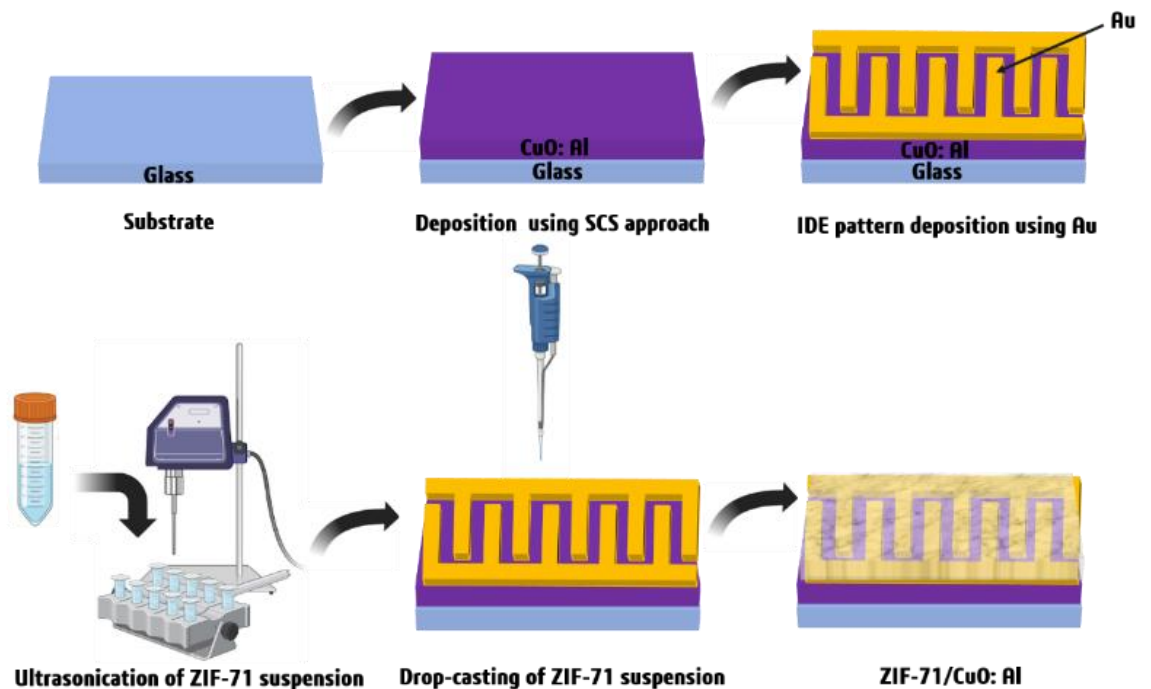

Fig. 2.2. Schematic illustration of the stepwise fabrication process of the ZIF-71/CuO:Al structures.

2.4. Fabrication protocols for ZIF-67, -7, -71, and -8 growth on ZnO-based templates

ZnO films were deposited on glass substrates (1.2 cm×1.4 cm×1 cm) using an SCS approach. Before the deposition of ZnO, the glass substrates were cleaned using a dilute HCl (20%) solution for 10 minutes, followed by rinsing in DI water. Thereafter, the substrates were ultrasonically cleaned for 5 minutes using a mixture of ethanol and acetone in equal proportions and then dried using an N_2 gas flux. The cleaned substrates exhibited hydrophilic properties. To ensure uniform coverage of ZnO films, the substrates were sensitized by dipping them into a $SnCl_2.2H_2O$/HCl solution.

Thereafter, a cationic precursor solution was prepared using a $Zn(SO_4).7H_2O$ (99%, Sigma-Aldrich) and NaOH (99%, Sigma-Aldrich). The prepared solution was diluted using DI water to obtain Zn concentrations ranging from 0.25 to 0.75 M, as reported previously [47]. For the synthesis of Cd-doped ZnO samples, 0.5 mg of $CdSO_4$ (≥99%, Sigma-Aldrich) was added to 500 ml of DI water, resulting in a Cd concentration of 5.46 µM. The solution was kept at room temperature. Subsequently, the anionic aqueous solution was kept at 95-98 °C during deposition.

The growth of ZnO films was carried out using four dip-coating steps with the aid of an articulated robot to avoid human error in dipping times and the number of SCS cycles. Firstly, the substrates were dipped into the cationic precursor solution for 3 s, followed by dipping the substrates into DI water to remove loosely attached cations. Subsequently, the substrates were dip-coated into the anionic solution kept at 95-98 °C for 2 s, followed by immersion in DI water to remove excess unreacted species. The deposition cycles were repeated multiple times to achieve the desired film thickness, depending on the growth kinetics, as previously reported [120]. Afterwards, the prepared samples were thermally annealed at 650 °C for 2 hours.

Four types of ZIFs were synthesized as follows; all reactions were carried out at room temperature. ZIF-67 dispersion was prepared by dissolving 1.35 g (4.6 mmol) of cobalt nitrate hexahydrate (≥98%, Sigma-Aldrich) and 16.35 g (199.1 mmol) of 2-methylimidazole (99%, Sigma-Aldrich) in 9 ml and 60 ml Milli-Q® water, respectively. Consequently, the 2-methylimidazole solution was poured into the cobalt nitrate hexahydrate solution. The mixture was stirred for 6 hours, followed by the separation of the purple solids from the solvent by centrifugation. Thereafter, the obtained solids were washed two times with Milli-Q® water and methanol (≥99.9%, Fisher Chemical) separately. The synthesis approach was carried out using the established protocol [121].

ZIF-7 dispersion was prepared using 892.47 mg (3 mmol) of zinc nitrate hexahydrate (99%, Fisher Chemical) in 60 mL of N, N-dimethylformamide (DMF, ≥99.5%, Fisher Chemical) and 1417.68 mg (12 mmol) of benzimidazole (≥99%, Sigma-Aldrich) in 60 mL of methanol (≥99.9%,

Fisher Chemical). Following the complete dissolution of the precursors, the linker solution was added to the zinc solution. The mixture was stirred for 1 minute. After 24 hours, the white solids were obtained from the solvent after centrifugation, followed by three times washing with methanol.

ZIF-71 dispersion was prepared by dissolving 351.22 mg (1.6 mmol) of zinc acetate dihydrate (≥99%, Sigma-Aldrich) in 40 mL of methanol (≥99.9%, Fisher Chemical) and 876.54 mg (6.4 mmol) of 4,5-dichloroimidazole (>97%, Tokyo Chemical Industry Co., Ltd.) in a mixture of methanol and DMF (methanol/DMF = 39.64/0.36, v/v). Following the complete dissolution of the prepared solutions, the linker solution was added to the zinc solution. The mixture was stirred for 4 hours, followed by the separation of white solids from the solvent by centrifugation. Afterwards, the obtained white solids were washed three times with methanol. The synthesis approach was carried out using the established protocol [122].

ZIF-8 dispersion was prepared by dissolving 892.47 mg (3 mmol) of zinc nitrate hexahydrate (99%, Fisher Chemical) and 985.20 mg (12 mmol) of 2-methylimidazole (99%, Sigma-Aldrich) in 60 mL of methanol (≥99.9%, Fisher Chemical), separately. Following the complete dissolution of solutions, the linker solution was added to the zinc solution and the mixture was stirred for 1 minute. After 24 hours, white solids were separated from the solvent by centrifugation and subsequently washed three times with methanol. Subsequently, the obtained ZIF-8 nanoparticles were kept in methanol.

The obtained ZIF dispersions were prepared in methanol at a concentration of 5 mg/ml. The obtained particles were found to have different sizes, depending on the synthesis conditions. The observed particle sizes for ZIF-67, ZIF-7, ZIF-71, and ZIF-8 were approximately 200 nm, 200 nm, 500 to 700 nm (broad-range distribution), and 70 nm, respectively. Prior to ZIF deposition, ZnO films and Cd-doped ZnO films were patterned with Au IDEs (170 nm) using an Al mask in a meander configuration with an interelectrode distance of 1 mm, as previously reported [119]. Following the electrical contacts patterning, ZIF dispersion was ultrasonicated for 15 minutes to ensure a homogeneous mixture, followed by drop-casting each ZIF on ZnO and Cd-doped ZnO films separately. The volume of the drop-casted dispersion differed for ZnO films (80 µl) and Cd-doped ZnO films (50 µl).

2.5. Conclusions of Chapter 2

Metal oxides, including Al-doped CuO or Cd-doped ZnO were synthesized using a simple and cost-effective SCS approach [6–8, 123], while all the ZIFs (ZIF-67, ZIF-7, ZIF-71, and ZIF-

8) were synthesized using a liquid solution approach at room temperature, which requires low energy consumption and offers good reproducibility [6, 7].

The development of ZIFs/CuO:Al and ZIFs/ZnO-based MOF/MO hybrid structures was carried out using a simple drop-casting approach, optimizing the concentration of the ZIF dispersion to achieve uniform coverage of the entire metal oxide surface [6, 7].

3. ADVANCED CHARACTERIZATION AND ELECTRON TRANSPORT ANALYSIS OF ZIF-8/CuO:Al HETEROSTRUCTURES FOR CHEMORESISTIVE SENSING

3.1. Morphological, Structural, and Vibrational analysis of ZIF-8/CuO:Al-based MOF/MO hybrids

In this chapter, the material properties of the ZIF-8/CuO:Al-based MOF/MO hybrid structures are studied. CuO:Al structures were synthesized using a simple and cost-effective SCS approach, followed by the drop-casting of ZIF-8 particles on top of the CuO:Al film. SEM images of the CuO:Al film prior to the ZIF-8 coating exhibited intergranular structures, as shown in Figure 3.1(a). These images reveal triangular-shaped CuO:Al grains within an approximate size range of 130 to 200 nm, distributed randomly without any orientation (Figure A1.1(a)). It was observed that the CuO:Al grains are homogeneously interconnected, which can be attributed to the thermal treatment (600 °C, 60 s). After the drop-casting of a well ultra-sonicated ZIF-8 dispersion on the CuO:Al surface, the particles exhibited a uniform distribution, as shown in Figure 3.1(b). SEM images revealed the rhombic-dodecahedral morphology of the ZIF-8 particles. The estimation of the ZIF-8 particle size on the Si substrate was carried out by scaling the respective SEM images, which revealed a particle size of approximately 70 nm, as shown in Figure A1.1(b).
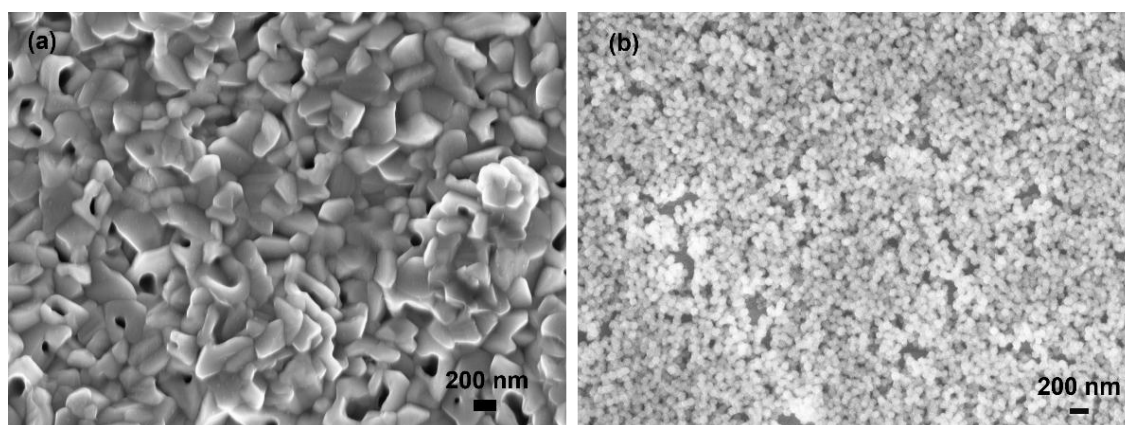

Fig. 3.1. SEM images of (a) CuO:Al structures. (b) ZIF-8/CuO:Al-based MOF/MO hybrid structures.

Elemental composition analysis of the CuO:Al film was carried out using EDX. The investigated region considered for the EDX analysis was approximately 11.3 µm×8.5 µm, as shown in Figure A1.2(a). Figures A1.2(b-c) shows the EDX mapping of the selected region reveals the presence of Cu, O, and Al, as expected. The analysis reveals a composition of 45.5 at% Cu, 54.3 at% O, and 0.2 at% Al, which confirms the low doping concentration of Al in the CuO film.

The structural features of the ZIF-8/CuO:Al hybrid structures were investigated using XRD. The XRD pattern of the investigated sample exhibited two primary peaks corresponding to CuO at 2θ angles of 38.81° and 35.56°, which correspond to the (1 1 1) and (1 1 $\bar{1}$) lattice planes of the monoloclinic phase of CuO. This was confirmed using the reference PDF map 1526990. There are several other peaks present in the diffractogram that correspond to the electrical Au connections, marked by #, as shown in Figure 3.2.

The peaks corresponding to Au were confirmed using reference pdf map no. 1100138. At the lower 2θ-range from 7° to 32°, multiple peaks were present, which correspond to ZIF-8. The most dominant peak with the highest intensity was observed at 2θ =7.20°, which corresponds to the (0 1 1) plane of ZIF-8. The positions of all ZIF-8 peaks were confirmed using a simulated reference pattern obtained from a crystallographic information file [124]. The presence of Al was not confirmed by XRD, which can be attributed to its low concentration.
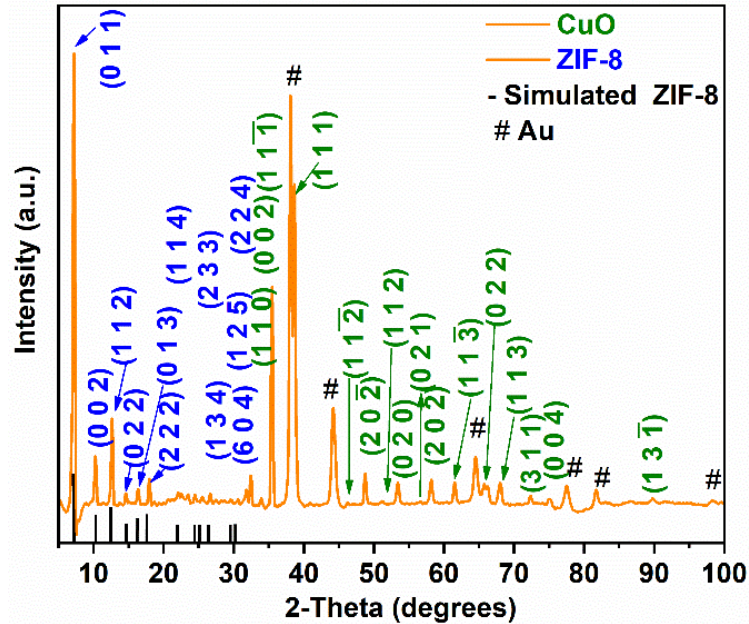

Fig. 3.2. XRD pattern of ZIF-8/CuO:Al-based MOF/MO hybrid structures. Our results: The diffraction peaks are indexed to CuO (green), ZIF-8 (blue), and Au used for electrical contacts (indicated by the symbol "#"). The black bars represent the simulated reference pattern corresponding to the ZIF-8 phase [124].

Using Scherrer equation, the crystallite size (*d*) of ZIF-8 particles can be investigated through XRD line profile [125]:

$$d = \frac{K \times \lambda}{\beta \times cos\theta} \qquad (3.1)$$

where K is the dimensionless shape factor, λ is the wavelength (0.154 nm) of Cu-Kα radiation, β is the full width at half maximum (in radians), and θ is the Bragg's angle.

On the primary peak of ZIF-8, three fitting functions were employed including the Gaussian profile, the Lorentzian profile, and the Voigt profile. The best fitting function was determined by comparing correlation coefficient of all three regression functions, resulting in the highest value of coefficient of determination (R^2) was observed for the Voigt function (0.98150). Orthogonal distance regression optimization was used for the peak deconvolution. The FWHM (β) of the primary XRD peak (0 1 1) was determined using the empirical approximation [126]:

$$\beta \approx 0.5346 \times w_L + \sqrt{0.2166 \times w_L^2 + w_G^2} \tag{3.2}$$

where w_L is the Lorentzian broadening and w_G is the Gaussian broadening.

The value of β was calculated to be 0.0049±0.02 radians. Using the Scherrer equation (Equation 3.1), the estimated crystallite size comes out to be approximately $d = 30$ nm, representing the coherent diffraction domains [127]. Although the ZIF-8 particle size estimated via SEM was observed to be 70 nm, this contrasts with the crystallite size determined using the Scherrer equation. This discrepancy indicates the polycrystallinity of the ZIF-8 particles, which are composed of smaller crystallites [127]. This results in the formation of the extensive grain boundaries, and the associated defect density provides active sites that offer optimization pathways for sensing applications. No Al phase was observed during the XRD analysis of the ZIF-8/CuO:Al hybrid structures, though its presence was confirmed by the EDX compositional analysis of the film.

The vibrational states of the CuO:Al structures and the ZIF-8/CuO:Al-based MOF/MO hybrid structures were studied using Raman spectrum (Figure 3.3). The spectrum of the CuO:Al structures exhibited the monoclinic phase and displayed three Raman-active modes: A_g (286 cm^{-1}), B_g^1 (327 cm^{-1}), and B_g^2 (614 cm^{-1}), which can be confirmed using the reported literature [128]. Similarly, the Raman spectrum of the ZIF-8/CuO:Al hybrid structures was tested in the range of 100 to 3500 cm^{-1}. The Raman shifts observed below 200 cm^{-1} (100.4 cm^{-1}, 146.2 cm^{-1}, and 186.6 cm^{-1}) can be attributed to the lattice framework of ZIF-8. Other Raman shifts observed at higher wavenumbers, such as 296.3 cm^{-1}, 688 cm^{-1}, 1146 cm^{-1}, and 1458 cm^{-1}, are attributed to the stretching (υ) of Zn-N bonds, the out-of-plane bending vibration of the imidazolate ring, the bending vibration of the C_5-N bond, and the methyl bending vibration, respectively. The assignment of these Raman shifts was confirmed by comparing the values for these vibrations with the reported literature, specifically at 278 cm^{-1}, 686 cm^{-1}, 1146 cm^{-1}, and 1458 cm^{-1}, respectively [129, 130]. All compared vibrational modes were confirmed except for the peak at 296.3 cm^{-1}, which showed a blue shift in

the Zn-N vibrational mode. This can be attributed to the localized defects, such as missing linker or uncoordinated metal sites [131]. Two additional modes were observed at 2932 cm^{-1} and 3135 cm^{-1}, which can be attributed to the antisymmetric stretching vibration (υ) of C-H in the methyl group and the imidazolate ring, respectively [132, 133]. These observations and the resulting implications confirmed that ZIF-8 retains its structure after deposition onto the CuO:Al structures.
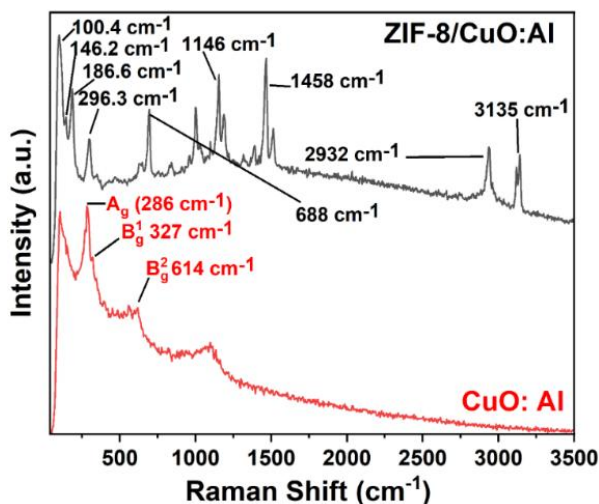

Fig. 3.3. Raman spectra of the ZIF-8/CuO:Al and CuO:Al structures.

3.2. Analysis of Thermal, Chemical, and Adsorptive properties of ZIF-8 and ZIF-8/CuO:Al hybrids

The thermal stability tests conducted on the ZIF-8 powder under a flow of synthetic air (50 ml/min) showed negligible weight loss up to 380 °C, indicating the absence of physiosorbed solvents or moisture content and confirming the structural integrity of the framework within the temperature range of 20 °C to 380 °C (Figure 3.4).
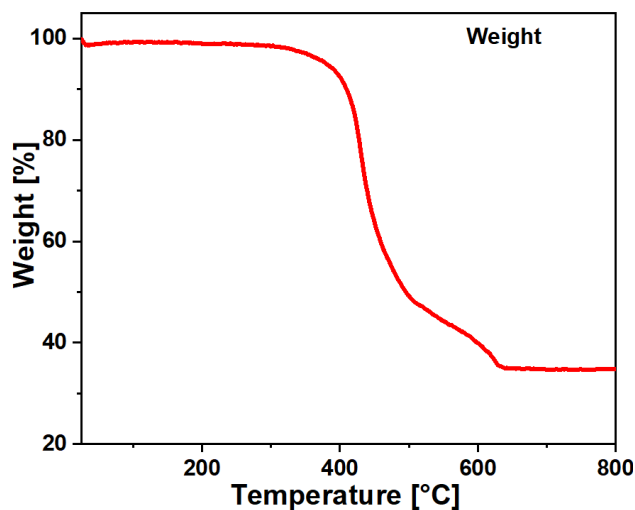

Fig. 3.4. TGA profile for ZIF-8 weight decomposition in the synthetic air.

Subsequently, by further increasing the temperature to 640 °C, a gradual weight loss of about 65.1% was observed, which is attributed to the collapse of the organic framework and the decomposition of the 2-methylimidazolate linkers [134]. Furthermore, upon reaching 800 °C, a relatively stable plateau was observed, which is attributed to the transformation of ZIF-8 into thermally stable ZnO, as confirmed using the previously reported literatures [44, 135].

XPS analysis of the CuO:Al (reference), partially covered ZIF-8/CuO:Al (low coverage), and almost fully covered ZIF-8/CuO:Al (high coverage) samples was conducted to analyze the surface chemistry. More details about the samples are given in Chapter 2. The survey spectra of all three samples, with respective photoemission lines corresponding to each species, are given in Figure 3.5(a). Low-resolution survey scan spectra of the CuO:Al film (reference) and ZIF-8/CuO:Al hybrid structures (low coverage) exhibited a small Na 1s peak, which may attribute to Na residual from the precursor solution (sodium thiosulfate pentahydrate) used in the synthesis process. For the CuO:Al (reference) sample, the photoelectron lines were observed for Cu, O, and C (Figure 3.5(a) (iii)). Moreover, the ZIF-8/CuO:Al (low coverage) sample exhibited Zn 2p, N 1s, and C 1s photoelectron lines (Figure 3.5(a) (ii)) similar to the ZIF-8/CuO:Al (high coverage) structures (Figure 3.5(a) (i)). Additionally, Cu-related photoelectron lines were also observed for the low-coverage sample due to the incomplete coverage of the CuO:Al film by ZIF-8. However, Cu-related photoelectron lines were not observed in the ZIF-8/CuO:Al (high coverage) sample. High-resolution spectra provided detailed information about the chemical states and the bonding of elements by focussing on the core-level electrons, which is not achievable using survey spectra alone.

High-resolution spectra for the ZIF-8/CuO:Al (high coverage) structures are illustrated in Figure 3.5(b-e). In this study, the photoelectron line corresponding to C 1s was deconvoluted into two components at binding energies of 287.0 eV (C 1) and 286.1 eV (C 2), as shown in Figure 3.5(b). To further analyze these deconvoluted components to derive bonding information, they can be compared to the existing literature. A variety of studies have reported on the deconvoluted components of C 1s at different line positions. For instance, Soliman et al. showed a C 1s deconvolution into three components positioned at 284.5 eV, 286.2 eV, and 288.8 eV [136], while Liu et al. demonstrated a C 1s line at 284.8 eV [137] and Awadalla et al. reported a C 1s component at 285.1 eV [138]. This shift in photoelectron lines observed in the literature makes the assignment of these deconvoluted components ambiguous. The C 1 component observed at 287.0 eV can be associated with the carbon atom linked to two nitrogen atoms in ZIF-8, as well as the carbon atom bonded to oxygen via oxidation, because a small O 1s photoelectron line was also observed in the survey spectra of the ZIF-8/CuO:Al (high coverage) structures (Figure 3.5(c)). The other

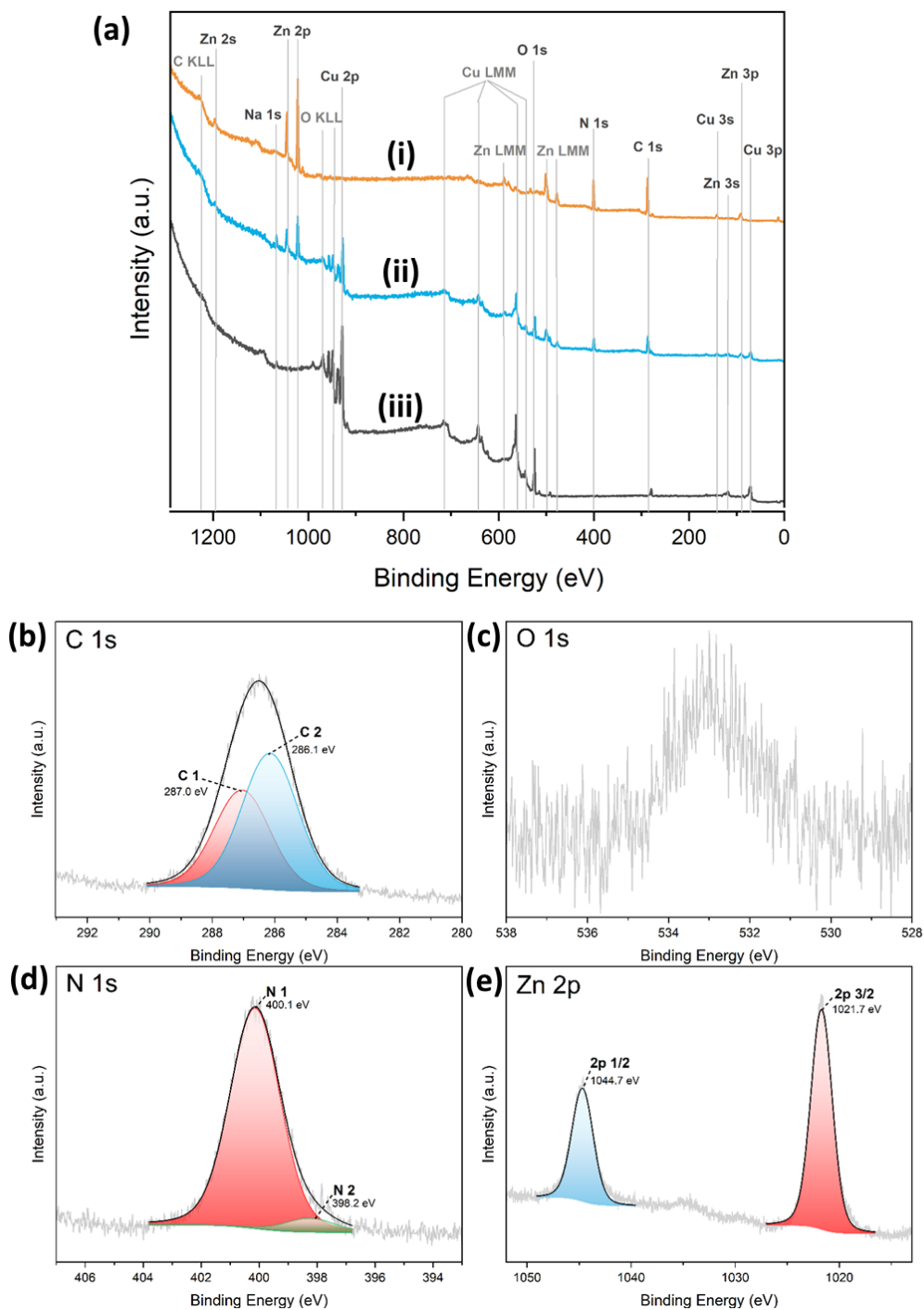component, C 2, can be associated with the carbon atom linked to one nitrogen atom in the imidazolate ring.

Fig. 3.5. XPS spectra of selected CuO:Al samples: (a) labelled survey spectra of: (i) ZIF-8/CuO:Al (high coverage), the spectrum shows the ZIF-8 characteristic XPS lines of Zn, N and C indicating complete coverage of the substrate. (ii) ZIF-8/CuO:Al (low coverage), the Cu specific substrate lines are still visible, and (iii) CuO:Al reference sample. (b – e) High-resolution spectra of the ZIF-8/CuO:Al (high coverage) sample: (b) C 1s, (c) O 1s, (d) N 1s, and (e) Zn 2p.

The photoelectron line observed corresponding to the N 1s spectra can be deconvoluted into two components N 1 and N 2, as shown in Figure 3.5(d). N 1 (more intense) at 400.1 eV can be assigned to the nitrogen atom linked to the Zn^{2+} in the ZIF-8 framework. On the other hand, the less intense component, N 2, at 398.2 eV can be assigned to the uncoordinated 2-methyimidazolate linker. The assignment of the deconvoluted N 1s components is according to the study by Tian et al. [139]. Furthermore, the deconvoluted components ($Zn\ 2p_{3/2}$ and $Zn\ 2p_{1/2}$) of the Zn 2p spectrum (Figure 3.5(e)) were observed at 1021.7 eV and 1044.7 eV, respectively. The difference in the binding energies of these two photoelectron lines is approximately 23 eV, which corresponds to the +2-oxidation state of Zn present in ZIF-8 [136, 139]. The high-resolution spectra of the ZIF-8/CuO:Al structures (low-coverage) are illustrated in Figure A1.3(a-d). A thorough analysis is complicated by differential charging from the CuO:Al film and the presence of an additional peak in the C 1s spectrum. Moreover, the presence of Cu 2p lines (specifically $Cu\ 2p_{3/2}$ and $Cu\ 2p_{1/2}$) at 928.2 eV and 948.0 eV, respectively, and X-ray satellites at 937 eV and 956.8 Ev were noted. Due to charge correction, the Cu 2p lines appear at binding energies 4.6 eV lower than reported in the literature [140]. However, the ZIF-8/CuO:Al (low coverage) structures also exhibited photoelectron lines corresponding to N 1s (Figure A1.3(c)) and Zn 2p (Figure A1.1(d)), which closely align with the ZIF-8/CuO:Al (high coverage) structures. This also indicates the presence of intact ZIF-8 on the surface of the low-coverage structures. Additionally, compositional analysis was carried out on the ZIF-8/CuO:Al (high coverage) sample using XPS. The composition was calculated to be approximately 56.2 at% C, 25.5 at% N, 16.3 at% Zn, as well as 2 at% O, which is consistent with the reported literature [138]. However, the exact chemical composition can be influenced by the preparation method employed for synthesis and deposition.
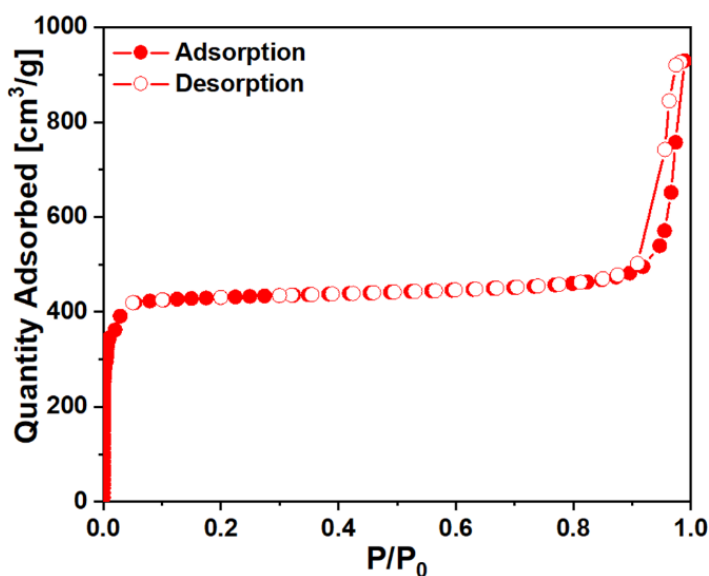

Fig. 3.6. N₂ adsorption-desorption isotherm curve of the ZIF-8 nanoparticles.

To further probe the surface area of ZIF-8 nanoparticles, N_2 adsorption-desorption isotherm measurements were undertaken at 77 K, with the results depicted in Figure 3.6. Intriguingly, the ZIF-8 isotherm displayed Type-I behavior, indicating a microporous structure. The obtained BET surface area was quantified to be 1647 m^2/g, which is in good agreement with the literature [141].

3.3. Gas sensing investigation and correlation with defect states of ZIF-8/CuO:Al-based MOF/MO hybrids

The gas sensing behavior of the CuO:Al film was assessed against various reducing gases: hydrogen, n-butanol, 2-propanol, ethanol, acetone, and ammonia−across operating temperatures (OPTs) ranging from room temperature to 350 °C. No detectable response was recorded below 250 °C. Sensing responses of 84% for hydrogen, 80% for 2-propanol, and 54% for n-butanol were achieved at 300 °C. When the temperature was increased to 350 °C, the corresponding responses were 90%, 70%, and 60% for hydrogen, 2-propanol, and n-butanol, respectively. These results suggest that the selectivity between n-butanol and 2-propanol is more prominent at 300 °C than at 350 °C, as shown in Figure A1.4(a). Figure A1.4(b) presents the dynamic response to 100 ppm hydrogen over three test cycles at an operating temperature of 350 °C. The baseline drift observed in the hydrogen response (Figure A1.4(b) and (c)) was likely due to reaction by-products accumulating on the sensing surface [142]. The hydrogen response and recovery times at 350 °C were 17.1 s and 37.1 s, respectively, with an estimated uncertainty of ±0.5 s. Figure A1.4(c) displays the dynamic responses to 100 ppm of the tested gases at 350 °C. Consistent with the above discussion, hydrogen yielded the highest sensing response (~90%), followed by 2-propanol (~70%) and n-butanol (~60%). Figure A1.4(d) shows the current–voltage (I–V) characteristics of the CuO:Al film, exhibiting typical Ohmic behavior. As the temperature increased from room temperature to 350 °C, thermal excitation enhanced the number of charge carriers in the semiconductor, leading to an increased current [145]. However, at 350 °C, slight deviations from linearity occurred in the I–V curves at low and high voltage ranges, as corroborated by earlier studies [144].

Figure 3.7(a) depicts the gas sensing behavior of the ZIF-8/CuO:Al hybrid sensor toward 100 ppm of a series of relevant reducing gases: hydrogen, n-butanol, 2-propanol, ethanol, acetone, and ammonia, at operating temperatures ranging from 150 °C to 350 °C. The operating temperature significantly affects gas sensing by altering the electrical conductivity and charge mobility of the sensing layer. At lower operating temperatures of 150 °C and 200 °C, no measurable gas response was obtained, likely because slow reaction kinetics and insufficient thermal energy hindered the activation process between the analyte and the sensor surface [145]. By increasing the temperature

from 250 °C to 350 °C, the hydrogen response steadily increased, and a maximum response of 170% was observed at 350 °C. Conversely, other gases exhibited bell-shaped response curves with maxima at 250 °C, followed by declines in the sensing response at higher temperatures due to accelerated desorption [146]. The strongest response was observed for n-butanol among the ABE (acetone–butanol–ethanol) molecules at all tested operating temperatures, indicating a greater adsorption affinity than acetone and ethanol, in accordance with competitive adsorption isotherms in ternary ABE systems [147]. The prepared sensor demonstrated approximately 1.3 and 1.6 times higher selectivity toward n-butanol relative to ethanol and acetone, respectively. The hydrogen response at 350 °C exceeded those of the other gases by a factor greater than four. Figure 3.7(b) presents the transient response to 100 ppm hydrogen for three cycles at 350 °C, showing response and recovery times of 11.1 s and 27.0 s, with an estimated uncertainty of ±0.5 s. Figure 3.7(c) illustrates the dynamic responses to 100 ppm of each gas at 350 °C. The enhanced hydrogen response is attributed to improved gas diffusion at elevated temperatures.

Baseline drift observed in hydrogen sensing (Figure 3.7(b) and (c)) is likely due to surface residues from reaction products, as explained by Equations 3.3–3.5 [142].

$$H_2 + 2CuO \rightarrow H_2O + Cu_2O \qquad (3.3)$$

$$H_2 + Cu_2O \rightarrow H_2O + 2Cu \qquad (3.4)$$

$$H_2 + CuO \rightarrow H_2O + Cu \qquad (3.5)$$

Some of the H_2O molecules generated as per the equations above may form strong bonds with active sites on the CuO, resulting in the creation of hydroxyl-adsorbed species. This phenomenon can significantly impede hydrogen desorption, contributing to a baseline drift observed in subsequent cycles [148], as illustrated in Figure 3.7(b). The observed modest increase in the sensing response during later cycles may be ascribed to the sensor's annealing history, specifically the repetitive high-temperature measurements, documented in the literature [149].

The current-voltage (I-V) characteristics of the ZIF-8/CuO:Al hybrid sensor display standard Ohmic behavior, as presented in the Figure 3.7(d). As the temperature increased from ambient conditions to 350 °C, thermal excitation induced an increase in the carrier concentration within the sensing layer, resulting in a corresponding rise in current [150]. However, at 350 °C, a deviation from linearity in the I-V characteristics became evident at both low and high voltage extremes, as corroborated by previous findings. CuO is characterized as a p-type semiconductor. Under constant operating parameters, the resistance of this gas sensor is contingent upon the amount of O_2 adsorbed on its sensing surface [9].
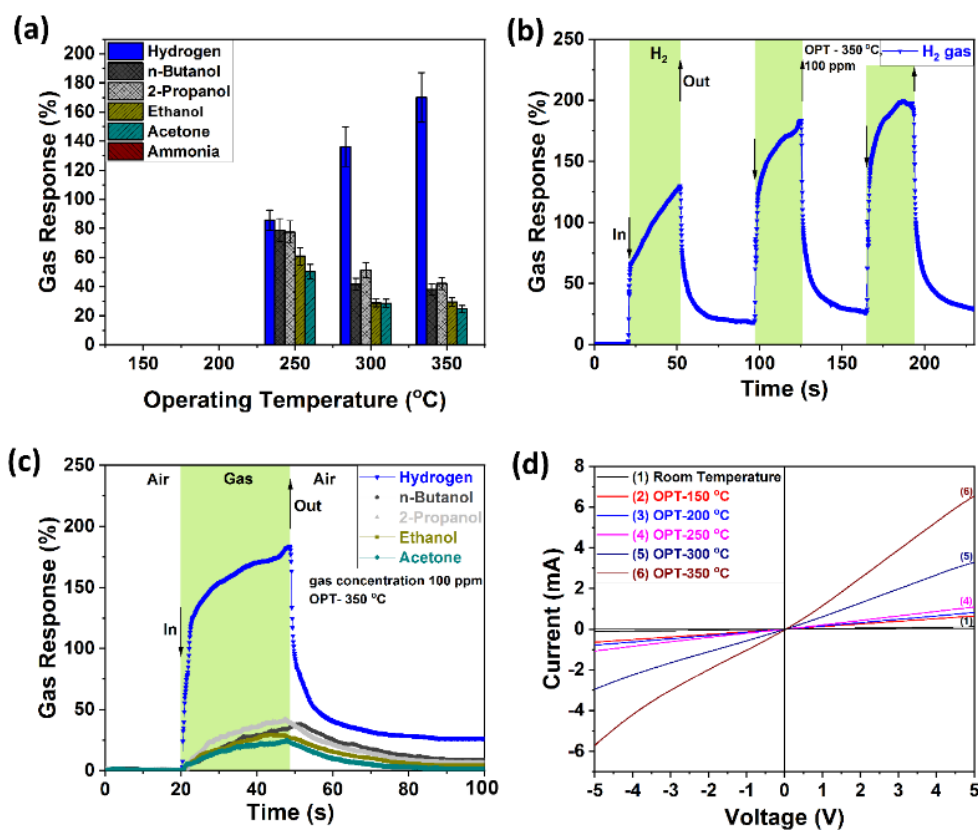
Fig. 3.7. Gas response of the ZIF-8/CuO:Al-based MOF/MO hybrid sensor: (a) to a series of gases with a concentration of 100 ppm, (b) dynamic response to hydrogen at 350 °C, (c) dynamic characteristic of all the tested gases at 350 °C; and (d). current-voltage (I-V) characteristics at different OPTs.

The sensing responses of the ZIF-8/CuO:Al and CuO:Al sensors are visualized in Figure A1.5, demonstrating sensing responses to various gases (including hydrogen, n-butanol, 2-propanol, ethanol, acetone, and ammonia), derived from the data in Figures A1.4 and 3.7. The CuO:Al sensor exhibited approximately 1.5 times greater selectivity for hydrogen in comparison to n-butanol at 350 °C. Post-ZIF-8 deposition, the ZIF-8/CuO:Al sensor exhibited over a fourfold enhancement in selectivity for hydrogen over n-butanol. This improved selectivity can be attributed to the molecular sieving effect of ZIF-8, which selectively permits the diffusion of smaller hydrogen molecules (2.89 Å) [151] through its pores to reach the CuO:Al surface.

Sensing performance is significantly impacted by the operating temperature. Figure A1.5 illustrates the sensing performance of both the CuO:Al and ZIF-8/CuO:Al structures as a function of operating temperature for 100 ppm of the gases. Prior to ZIF-8 coating, no significant variation in response was noted for the ABE molecules across different operating temperatures. Conversely, the sensing response of the ZIF-8/CuO:Al film to ABE molecules initially increased as the temperature escalated from 150 °C to 250 °C. A further increase in operating temperature to 350

°C led to a decline in the sensing response. This behavior can be attributed to thermal effects that influence the adsorption-desorption processes of ABE molecules on the sensing surface [152]. Consequently, 250 °C emerges as the most favorable or critical temperature for sensing ABE molecules using the ZIF-8/CuO:Al sensor. The increase in sensing response after ZIF-8 coating may be attributed to the accumulation of the target analyte, facilitated by the high porosity of ZIF-8, which also acts as a concentrator [153].

To investigate the position of the defect states above the valence band, the activation energy (E_a) of the ZIF-8/CuO:Al hybrid structures was evaluated by measuring the current (I) in an ambient environment across a temperature range from room temperature (25 °C) to 350 °C. The slope of the linear regression was calculated using a plot of ln(I) against 1/T (as shown in Figure 3.8), which relates to the activation energy (E_a) divided by the Boltzmann constant (k_B) in accordance with the Arrhenius Equation [123] (Equation 3.6).

$$Slope = -\frac{E_a}{k_B} \tag{3.6}$$

The slope of the plotted curve is approximately -2.4×10^3 K, leading to an estimated activation energy of around 0.2 eV from the valence band to the defect state. This activation energy aligns with the trap levels or defect states (V_{Cu}) reported in the literature [154–156]. These trap levels serve as acceptor states and are integral to the p-type conductivity exhibited by CuO. Positioned just above the valence band, these shallow trap levels facilitate the thermal excitation of electrons from the valence band to the acceptor level, subsequently generating holes in the valence band that contribute to hole conduction.
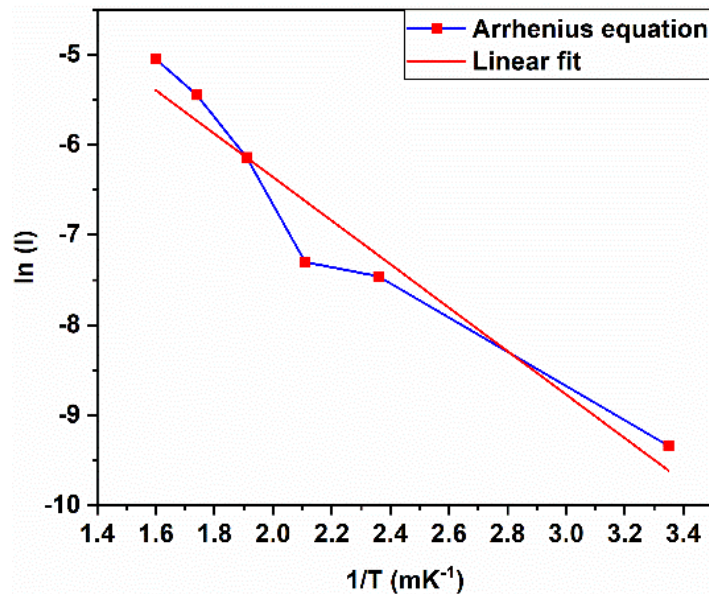

Fig. 3.8. Arrhenius plot of ln (I) vs 1/T with the corresponding linear fit for the calculation of activation energy of the ZIF-8/CuO:Al-based MOF/MO hybrid structures.

Figure 3.9(a) presents the gas response characteristics of the ZIF-8/CuO:Al hybrid structures when exposed to varying hydrogen concentrations ranging from 10 to 1000 ppm, under operational conditions of RH 11% at 350°C. The sensor demonstrates the capability to detect hydrogen concentrations as low as 10 ppm, yielding a response of approximately 50%. As hydrogen concentration increases, a corresponding rise in response is observed, attaining nearly 400% at 1000 ppm.

In a similar way, Figure 3.9(b) illustrates the gas response of the ZIF-8/CuO:Al hybrid structures to hydrogen concentrations between 10 and 1000 ppm at RH 50%. Notably, the response at 10 ppm remains consistent across both humidity levels, yet significant variations are observed at concentrations of 100 ppm and 1000 ppm. Transitioning from RH 11% to 50% induces only a minor reduction in the hydrogen sensing response. Specifically, at 100 ppm, the response diminishes from approximately 170% to 152% as the relative humidity increases from 11% to 50%. This slight variation can be attributed to the hydrophobic nature of the ZIF-8 layer on the CuO:Al film [157].
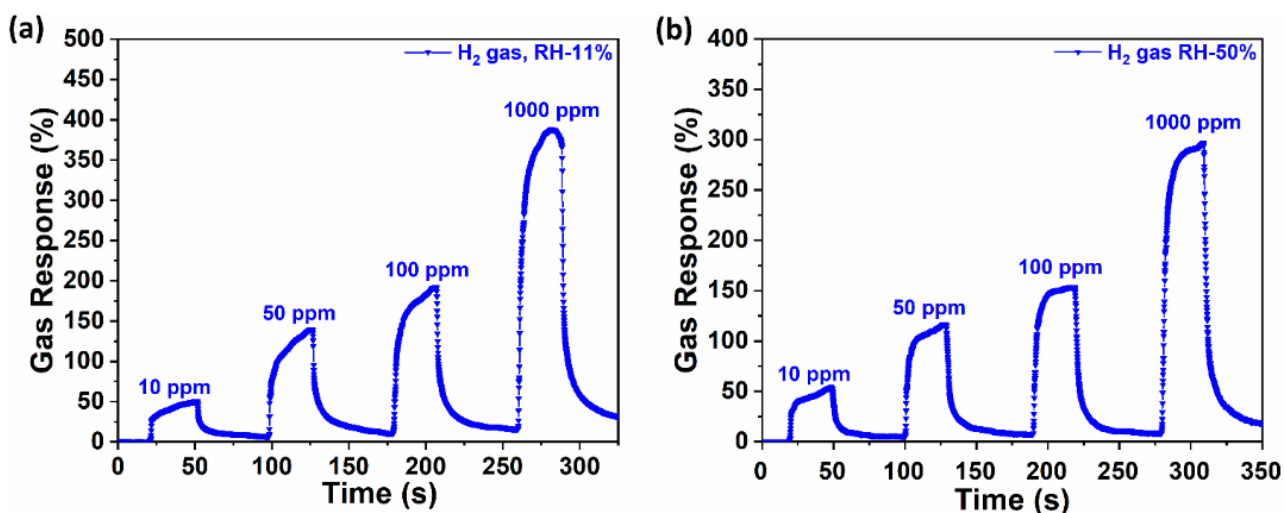

Fig. 3.9. Gas response of the ZIF-8/CuO:Al-based MOF/MO hybrid sensor to different hydrogen concentrations and RH values (a) RH 11%, and (b) RH 50%.

Furthermore, an increase in relative humidity to 81% results in a further decrease in the gas sensing response to about 75% at a concentration of 100 ppm, as depicted in Figure 3.10.

The theoretical lowest detectable limit (*LDL*) of the sensor is defined as the minimal concentration of an analyte that can be reliably detected. According to the International Union of Pure and Applied Chemistry (IUPAC), the LDL represents the smallest distinguishable signal from background noise that a sensor can detect following exposure to the minimum amount of the tested analyte [158]. This parameter is critical for assessing the sensing performance and can be expressed in parts per million (ppm) or parts per billion (ppb).
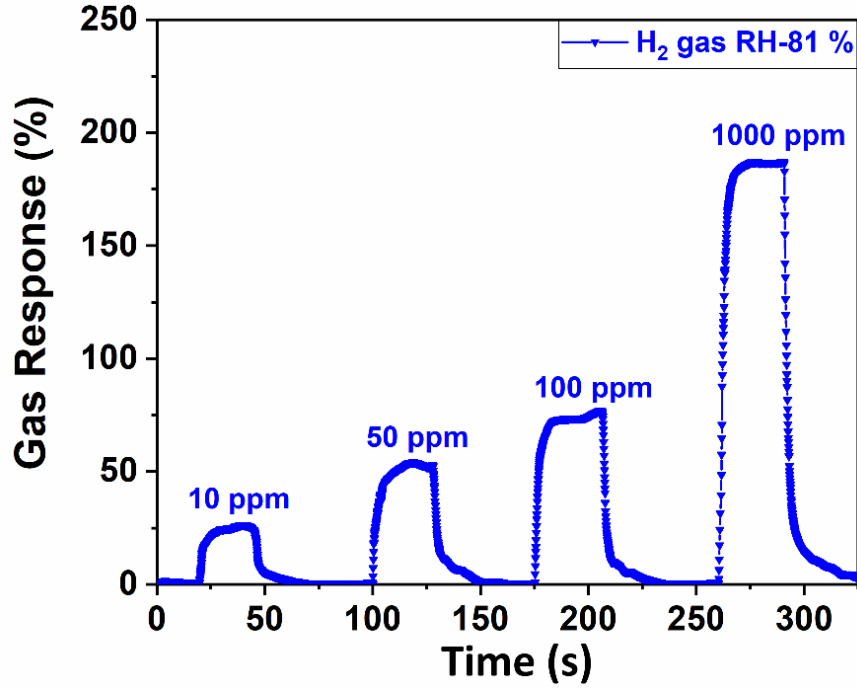
Fig. 3.10. The effect of operating temperature on the gas sensing response of the ZIF-8/CuO:Al -based MOF/MO hybrid sensor at the relative humidity (RH) of 81%.

Figure 3.11 illustrates the relationship between gas sensing response (S) and hydrogen concentration. The LDL and root mean square noise (rms_{noise}) are quantified in Equations 3.7 and 3.8, respectively.

The LDL can be articulated mathematically as [159]:

$$LDL = \frac{3 \times rms_{noise}}{s} \tag{3.7}$$

and rms_{noise} can be mathematically represented as:[160]

$$rms_{noise} = \sqrt{\frac{\sum_i (R_i - R)^2}{n}} \tag{3.8}$$

where, s represents the slope of the linear fit of sensing response (%) plotted against the analyte concentration (ppm), derived from linear fitting at lower concentrations (up to 100 ppm). R_i's denotes the experimental data points of the baseline prior to gas exposure, while R is the average of these consecutive baseline data points. The variable n indicates the number of baseline data points collected before gas exposure.

The rms_{noise} is determined to be 0.18%, and the slope (s) of the sensing response as a function of analyte concentration is 1.34%/ppm. Consequently, the LDL for the ZIF-8/CuO:Al-based hybrid sensor is approximately 402 ppb.
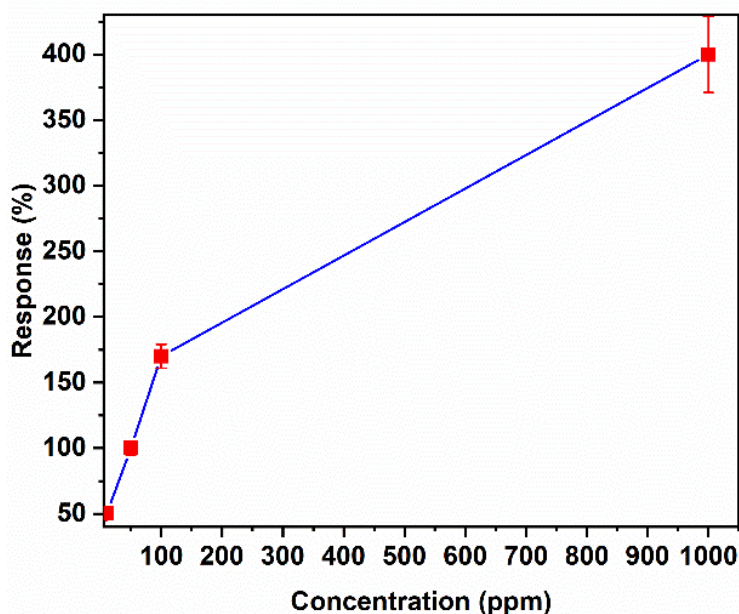
Fig. 3.11. Sensing response (%) of the ZIF-8/CuO:Al -based MOF/MO hybrids as a function of the hydrogen concentration (ppm).

To assess the temporal stability of the ZIF-8/CuO:Al hybrid structures, the dynamic response to varying hydrogen concentrations was evaluated at RH levels of 11% and 50% after three and four weeks. Figures A1.6 and A1.7 illustrate the dynamic gas sensing responses for hydrogen concentrations ranging from 10 ppm to 1000 ppm, documented three and four weeks post-initial measurements, respectively. The data indicate a slight decrease in the sensing response under elevated humidity conditions (RH 50%) relative to lower humidity (RH 11%), particularly at higher hydrogen concentrations. Notably, the sensor exhibited a consistent response at 10 ppm across both humidity levels and durations, demonstrating robust detection efficiency even after four weeks. This finding underscores the exceptional temporal stability of the fabricated sensor.

A comparative analysis with the existing literature is provided in Table A1.1. The current study corroborates the sensor's good temporal stability, which maintained its performance over a four-week period while attaining a low detection limit of 402 ppb. Defect characterization, derived from the Arrhenius equation ($\sim$0.2 eV, V_{Cu}), provides insights into the electronic properties of the material. Furthermore, the sensor demonstrated substantial sensitivity retention even at a high RH level (RH 50%), affirming its suitability for practical applications in real-world environments.

3.4. Mechanistic insights into the gas sensing process of ZIF-8/CuO:Al hybrids

CuO functions predominantly as a p-type semiconductor, primarily due to copper interstitial defects that facilitate the formation of an acceptor state located just above the valence band, as illustrated in Figure 3.12.
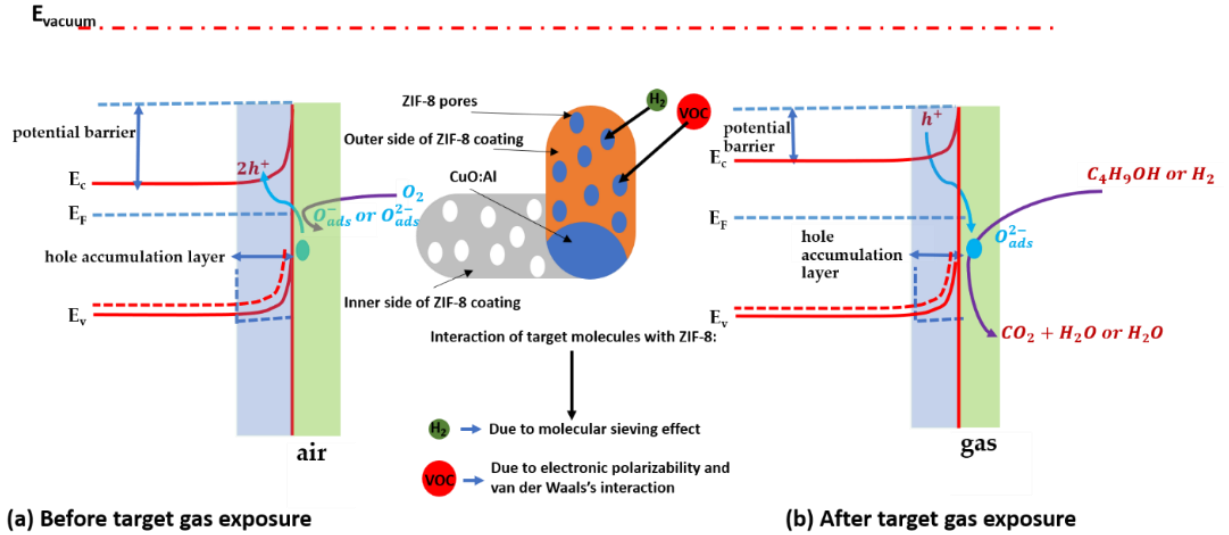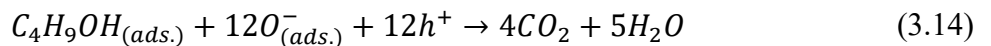
Fig. 3.12. Schematic diagram illustrating the gas sensing mechanism of the CuO:Al film: (a) surface state in air before target gas exposure, (b) surface state during target gas exposure. In the middle of (a) and (b), a schematic demonstrating molecular interaction mechanism showing target gases (H₂: green spheres; VOCs: red spheres) diffusing through the ZIF-8 layer to the CuO:Al sensing surface.

Upon exposure to ambient conditions, oxygen molecules adsorbed on the sensor surface are ionized into various oxygen ionic species, dependent on the operating temperature, as delineated in Equations 3.9-3.14 [161].

$$O_{2(gas)} \leftrightarrow O_{2(ads.)} \tag{3.9}$$

$$O_{2(ads.)} \leftrightarrow O_{2(ads.)}^- + h^+ \tag{3.10}$$

$$O_{2(ads.)}^- \leftrightarrow 2O_{(ads.)}^- + h^+ \tag{3.11}$$

$$O_{2(ads.)} \leftrightarrow O_{(ads.)}^{2-} + h^+ \tag{3.12}$$

$$H_2 + O_{(ads.)}^- + h^+ \rightarrow H_2O_{(vap.)} \tag{3.13}$$

$$C_4H_9OH_{(ads.)} + 12O_{(ads.)}^- + 12h^+ \rightarrow 4CO_2 + 5H_2O \tag{3.14}$$

Various oxygen ionic species are adsorbed onto the surface of the sensing material. As indicated in Equation 3.10, molecular oxygen ions (O_2^-) are formed at temperatures below 100°C. The origin of monoionic oxygen (O^-) and bi-ionic oxygen (O^{2-}) species is detailed in Equations

3.11 and 3.12, corresponding to temperature ranges of 100°C < T < 300°C and T > 300°C, respectively. The generation of holes (h$^+$) occurs as electrons are transferred to the surface acceptor level situated just above the valence band, as illustrated in Figure 3.12. When exposed to hydrogen (H$_2$), the hole accumulation layer (HAL) on the surface of CuO:Al decreases in width, as described in Equation 3.13 [162]. In a similar manner, exposure to n-butanol (C$_4$H$_9$OH) leads to a reduction in the HAL width on the CuO:Al surface, as indicated in Equation 3.14 [9]. The interaction of target gases with adsorbed oxygen ionic species, through adsorption and desorption processes, alters the sensor's electrical resistance, resulting in a quantifiable response. After exposure of the ZIF-8/CuO:Al hybrid sensor to hydrogen and n-butanol, the energy band representation is illustrated in Figure 3.12. The mechanism of gas sensing in the chemoresistive ZIF-8/CuO:Al hybrid sensor is fundamentally tied to the adsorption processes of hydrogen and other gases on the sensor surface. The ZIF-8 coating significantly improves the adsorption capacity owing to its highly porous structure, which promotes hydrogen diffusion through the coating and enhances its interaction with the CuO:Al sensing surface [163]. Following the adsorption of hydrogen on the vacant copper atom sites, the electronic properties of the CuO:Al surface experience notable alterations. The dissociation of the H-H bond, succeeded by the formation of two O-H bonds, may necessitate increased energy input due to the elevated concentration of oxygen vacancies, thus complicating the reaction between hydrogen and CuO [142]. The reaction between CuO and hydrogen molecules is represented in Equation 3.5 [164].

The mean free path of the gas molecules can be determined using standard kinetic theory, as represented in the following relation [165]:

$$\lambda = \frac{k_B T}{\sqrt{2}\pi r_{uv}^2 p}$$
(3.15)

where λ is the mean free path of gas molecules, T is the operating temperature, r_{uv} is the collision diameter, and p is the atmospheric pressure.

Due to significantly lower concentration of target gas molecules (e.g., 100 ppm) in comparison to the background gas, the number density of background molecules predominates. Therefore, the value of λ becomes independent of the small mole fraction, and atmospheric pressure is incorporated into Equation 3.15.

At a temperature of 350°C, the mean free paths for all test gases (hydrogen, acetone, 2-propanol, n-butanol, and ethanol) were calculated, yielding values of 164.9 nm, 94.5 nm, 94.2 nm, 75.7 nm, and 115 nm, respectively.

The transport behavior of gas molecules can be categorized into three regimes based on their Knudsen number (K_n), which is defined as follows [165]:

$$K_n = \frac{\lambda}{p_s} \tag{3.16}$$

where p_s (0.34 nm) [166] is the pore size of the ZIF-8 nanoparticle.

Using Equation 3.16, the Knudsen number can be calculated for each tested analyte at an operating temperature of 350°C. In all instances, the Knudsen number exceeds 10, indicating that gas transport occurs within the Knudsen diffusion regime. For example, the Knudsen numbers for hydrogen and n-butanol at this temperature are approximately 485 and 223, respectively. If all target analyte molecules passed solely through the intrinsic pores of ZIF-8, diffusion would proceed strictly via Knudsen diffusion. SEM analysis reveals that the CuO:Al film is predominantly covered by the ZIF-8 layer; nevertheless, the ZIF-8 film is not entirely free of pinholes, as grain boundaries and small defects are present. These structural imperfections may locally enlarge the effective pore size, permitting contributions from transitional or even molecular diffusion in certain regions. Consequently, while Knudsen diffusion serves as the primary transport mechanism through the intrinsic ZIF-8 pores, transitional or molecular diffusion may also have localized effects at grain boundaries and defects.

Figure 3.12 presents a schematic representation of hydrogen sensing (2.89 Å) [151] through the ZIF-8 layer, highlighting its smaller kinetic diameter compared to other VOCs, such as ethanol (4.53 Å) [151], 2-propanol (4.7 Å) [167], n-butanol (5.0 Å) [168], and acetone (4.6 Å) [151]. Even though the nominal pore size of ZIF-8 is 3.4 Å [166], it does not serve as a sharp molecular sieve due to its flexible framework. The larger cavity diameter of ZIF-8 (11.6 Å) [166] has been shown to allow access to various VOCs with kinetic diameters ranging from 4.3 to 5.85 Å, significantly larger than its nominal aperture size [166]. The interaction of VOCs with ZIF-8 may be influenced by their electronic polarizability and van der Waals interactions with the ZIF-8 framework. Among the VOCs, n-butanol (~8.57) [169] exhibited the highest electronic polarizability, followed by 2-propanol (~6.67) [169], acetone (~6.27) [169], and ethanol (~4.92) [169]. This leads to the heightened adsorption of n-butanol on ZIF-8 due to its strong van der Waals interactions with the framework. According to research by Remi et al. [170], liquid-phase adsorption profiles of VOCs on ZIF-8 conducted at room temperature demonstrated the highest uptake for n-butanol, followed by 2-propanol, acetone, and ethanol. In the present study, the diffused molecules interacting with the CuO:Al sensing surface exhibited a bell-shaped response curve, peaking at 250°C, followed by a decrease at elevated temperatures due to the predominance of desorption. The gas sensing

responses for n-butanol and 2-propanol are nearly equivalent within the margin of error, with n-butanol displaying a marginally higher response at 250°C.

3.5. Conclusions of Chapter 3

The crystallite size of the ZIF-8 nanoparticles was estimated at approximately 30 nm, determined using the Scherrer equation, which reflects the coherent diffraction domain size. SEM provided comprehensive insights into the surface morphology, revealing a densely packed arrangement of triangular-shaped CuO:Al grains along with a uniform distribution of rhombic dodecahedral ZIF-8 particles on the CuO:Al film. The estimated particle size of ZIF-8 stood at approximately 70 nm based on SEM imagery [6].

TGA demonstrated that ZIF-8 retains thermal stability up to approximately 380°C. XPS offered detailed insights into the chemical states and elemental composition of the films, affirming the integrity of the ZIF-8 layer following its deposition on the CuO:Al films [6].

The nitrogen adsorption isotherm quantified a BET surface area of approximately 1647 m²/g [6] and exhibited type-I isotherm behavior, which is characteristic of ZIF-8. Moreover, Raman spectroscopy corroborated the structural analysis by identifying key vibrational modes associated with both the ZIF-8 and CuO phases.

The ZIF-8/CuO:Al hybrid sensor demonstrated exceptional sensing performance, exhibiting temporal stability, a significant sensing response (75%) at low concentrations (10 ppm), and durability in high relative humidity (81%) conditions [6]. Current measurements across varying operating temperatures provided insights into the location of defect states by enabling the calculation of the sensor's activation energy.

Notably, the fabricated sensor displayed considerable selectivity to hydrogen, exhibiting over four times higher sensitivity compared to other tested analytes such as acetone, 2-propanol, n-butanol, and ethanol at elevated temperatures (350°C) [6]. The sensor showed approximately 1.3- and 1.6-times greater selectivity to n-butanol when compared to ethanol and acetone, respectively [6]. These notable characteristics establish the ZIF-8/CuO:Al-based MOF/MO hybrid structures as formidable candidates for effective hydrogen sensing across diverse environmental conditions.

4. PHYSICOCHEMICAL EVOLUTION AND DEVICE INTEGRATION OF ZIF-71/CuO:Al-BASED MOF/MO HYBRIDS FOR HIGH-PERFORMANCE CHEMORESISTIVE SENSING

4.1. Multi-scale characterization of ZIF-71/CuO:Al hybrids: From Vibrational dynamics to Adsorption properties

The ZIF-71 dispersion was prepared in 2-propanol following the procedure outlined in the experimental section of Chapter 2. The prepared dispersion, illustrated in Figure 4.1(a), was subsequently drop-cast onto the CuO:Al structures featuring Au IDEs on the glass substrate, as depicted in Figure 4.1(b). Initial investigations into the surface morphology of the CuO:Al structures and the ZIF-71/CuO:Al composite-based hybrid structures were conducted using SEM. The SEM image in Figure 4.1(c) reveals uniform intergranular structures covering the entire glass slide substrate, with the CuO:Al film characterized by densely packed, triangular-shaped nanograins that were likely formed through RTA at 650°C for 60 s. These grains exhibited random orientations, indicative of isotropic growth during the annealing process [118]. In addition, SEM analysis of the ZIF-71/CuO:Al hybrid structures was performed (refer to Figures 4.1(d), 4.1(f), and 4.1(g)). The low-magnification SEM image in Figure 4.1(d) displays partial coverage of the CuO:Al surface with ZIF-71 particles exhibiting a rhombic dodecahedron morphology following the deposition of 50 µL of the ZIF-71 dispersion.

A corresponding high-resolution SEM image in Figure A2.1 further confirms these particles while retaining features of the underlying CuO:Al film, suggesting that they are primarily ZIF-71 particles adhering to the CuO:Al surface. This image facilitates a preliminary particle size assessment, estimating sizes in the range of 500 nm to 750 nm.

Comparatively, Figures 4.1(f) and 4.1(g) illustrate both high- (200 nm) and low-magnification (2 µm) images of the sample surface after a total deposition of 100 µL of ZIF-71 dispersion, which shows enhanced coverage of the CuO:Al surface with ZIF-71 particles compared to the 50 µL sample in Figure 4.1(d). Compositional analysis of the CuO:Al film was performed using EDX characterization, detailed in Figure A2.2. The bright-field SEM image in Figure A2.2(a) indicates the analyzed region of approximately 5 µm × 4 µm, with compositional data derived from Cu Lα1,2, O Kα1,2, and Al Kα1 signal images (Figure A2.2(b-d)). The measured composition was found to be O (43.6 at%), Al (0.1 at%), and Cu (56.3 at%), collectively providing insights into the structural and compositional characteristics of the ZIF-71 dispersion on the CuO:Al film.
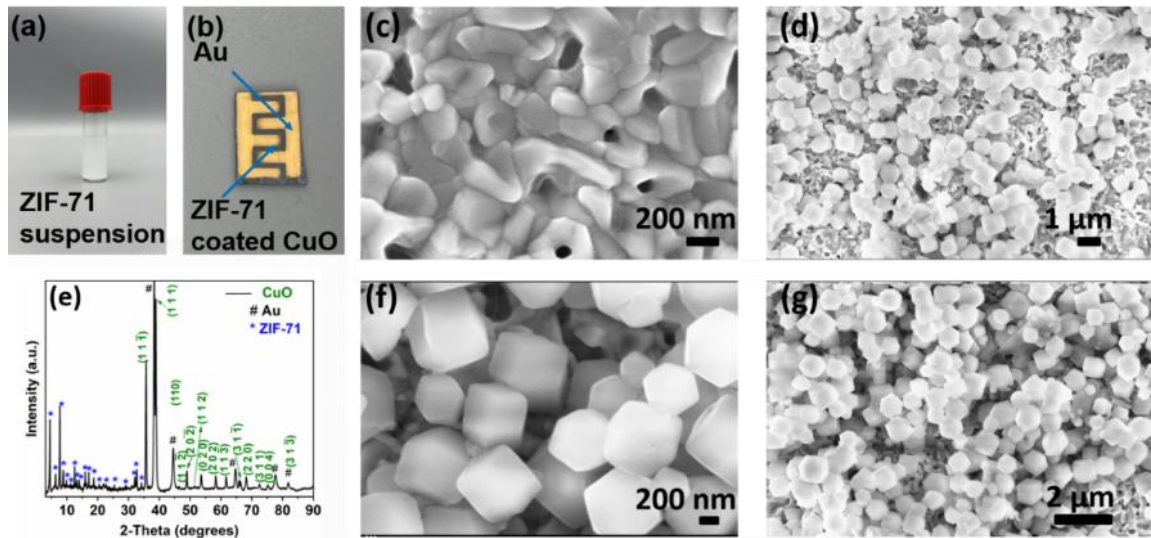
Fig. 4.1.(a) A photograph image of ZIF-71 dispersion in 2-propanol. (b) Representative photographic image of fabricated gas sensor device with ZIF-71 dispersion drop-cast onto the CuO:Al metal oxide sensing layer and Au IDEs. (c) Scanning electron microscopy (SEM) image of the CuO:Al structures. (d) SEM image of the ZIF-71/CuO:Al hybrid structures after the initial 50 μL ZIF-71 dispersion deposition. (f) and (g) High and low magnification SEM images of the ZIF-71/CuO:Al film after a complete cumulative 100 μL ZIF-71 dispersion deposition. (e) XRD pattern of the ZIF-71/CuO:Al hybrid structures with Au contacts.

All subsequent experiments were conducted on CuO:Al films exhibiting nearly complete coverage by ZIF-71 particles, achieved through a cumulative dispersion volume of 100 μL. The labelled XRD pattern of the ZIF-71/CuO:Al hybrid structures is depicted in Figure 4.1(e). Prominent reflections of CuO were detected at 38.83° and 35.67°, corresponding to the (1 1 1) and (1 1 $\bar{1}$) lattice planes of CuO (PDF card no. 1526990). Well-resolved Bragg reflections throughout the measurement range of 2θ (2° to 90°) were labelled, which can be attributed to CuO (PDF card no. 1526990), Au (PDF card no. 1100138), and ZIF-71 [171, 172]. Additional significant reflections associated with Au, evident in Figure 4.1(e), arise from the Au interdigitated electrodes (IDEs) utilized for electrical characterization.

Figure A2.3 illustrates the XRD pattern of the CuO:Al film containing only Au IDEs, revealing clear reflections corresponding to CuO that support the initial hypothesis of a crystalline CuO phase within the CuO:Al matrix. Notably, no reflections associated with Al or its oxides (PDF card nos. 1000059, 1512488, and 1534642) were observed, likely due to the minimal doping concentration of Al (0.1 at %). In addition, the XRD pattern for the ZIF-71/CuO:Al hybrid structures presented in Figure 4.1(e) showcases multiple characteristic reflections of ZIF-71 within

the 2θ range of 4° to 35°. The more clearly distinguished positions of diffraction peaks corresponding to ZIF-71 are illustrated in Figure A2.4, which displays the XRD pattern for the ZIF-71 particles.

The primary characteristic diffraction peaks of ZIF-71 are located at approximately 2θ values of 4.42° and 7.67°, corresponding to the (1 1 0) and (2 1 1) planes, respectively [171]. The crystallite size of the ZIF-71 particles was calculated employing the Scherrer equation (Equation 3.1). The FWHM was determined for the most prominent XRD reflection−(2 1 1) of ZIF-71 at approximately 2θ = 7.67°. Peak fitting was performed using a Voigt function with the orthogonal distance regression pro iteration algorithm. The FWHM was computed using an empirical approximation formula for the Voigt function (Equation 3.2).

The FWHM of the XRD reflection−(2 1 1) was determined to be 0.002 radians using Equation 3.2. Subsequently, the crystallite size was calculated using Equation 3.1, resulting in an estimated value of approximately 57.28 nm. Crystallites are defined as the smallest ordered regions within a material, parted by grain boundaries that may exhibit partial amorphous characteristics. The Scherrer equation specifically quantifies the size of these coherent diffracting domains [127]. A notable discrepancy was observed between the particle size (approximately 500 nm to 750 nm, as estimated from SEM images) and the crystallite size (approximately 57.28 nm, calculated via the Scherrer equation). This indicates that ZIF-71 particles are comprised of multiple smaller crystallites. These results clearly indicate the polycrystalline nature of ZIF-71 particles [127]. The increased number of grain boundaries suggests a higher density of active sites, which could enhance the material's efficacy in sensing applications.

Figure 4.2(a) presents the Raman spectrum of the ZIF-71/CuO:Al film, revealing several characteristic peaks indicating that the structural integrity of the ZIF-71 framework is preserved. Peaks below 200 cm^{-1} are assigned to the ZIF-71 lattice framework, aligning with prior studies [173]. The peak at 443 cm^{-1} corresponds to the stretching vibration of the Zn-N bond [174]. Peaks at 667 cm^{-1}, 1009 cm^{-1}, and 1063 cm^{-1} are associated with the in-plane deformation of the imidazolate ligand linker rings, as previously reported [175]. In addition, peaks near 295 cm^{-1}, 343 cm^{-1}, and 629 cm^{-1} correspond to the A_g, B_{1g}, and B_{2g} vibrational modes of the CuO film, respectively [176]. The Raman bands at 1290 cm^{-1} and 1240 cm^{-1} are due to C-H vibrations, while the peak at 1331 cm^{-1} is associated with C═N stretching within the imidazolate ring, as verified by earlier investigations [177].

The thermal stability of ZIF-71 particles was assessed using TGA. The weight loss (TG) and the derivative weight loss (DTG) are illustrated in Figure 4.2(b). The TGA demonstrated negligible weight loss up to 400 °C, confirming that ZIF-71 is thermally stable in that temperature range. A significant weight loss around 415 °C is attributed to the decomposition of the ZIF-71

structure, leading to the formation of ZnO. The total weight loss observed from 400 °C to 700 °C was 88%, exceeding the theoretical mass loss of 76% expected when ZIF-71 converts to ZnO. This discrepancy between theoretical and experimental weight loss may be explained by the presence of 4,5-dichloroimidazolate linkers coordinated to terminal zinc atoms at the crystal surface [178].
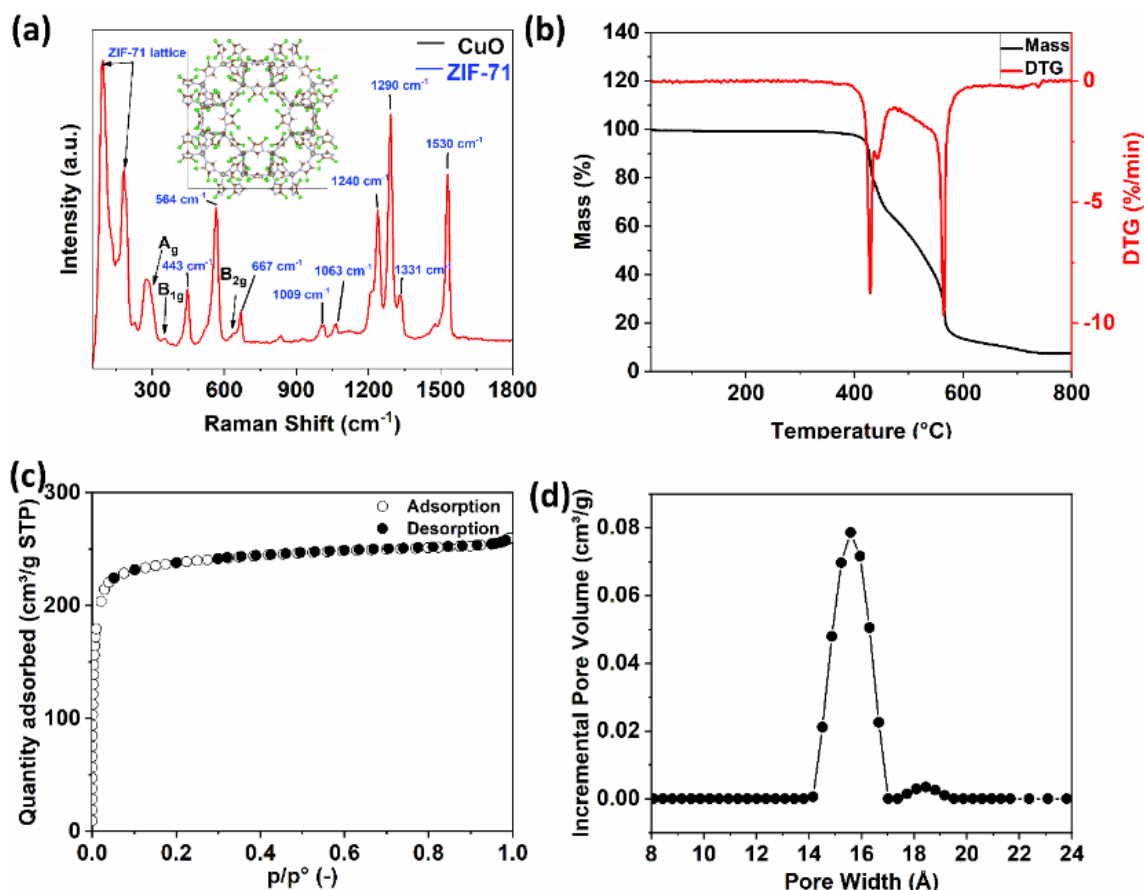

Fig. 4.2. (a) Raman spectra for the ZIF-71/CuO:Al film. (b) TGA and DTG profiles for ZIF-71. (c) N₂ adsorption−desorption isotherm curves for ZIF-71. STP stands for standard temperature and pressure, *p* is the monitored pressure and *p₀* is the saturated pressure. (d) Incremental pore volume curve as a function of pore width.

The surface area and pore size distribution of the ZIF-71 particles were analyzed by measuring a nitrogen adsorption-desorption isotherm at 77 K. The isotherm presented in Figure 4.2(c) displayed a distinct inflection at low relative pressures (P/Po < 0.1), characteristic of a Type-I isotherm according to IUPAC classification, confirming a microporous structure with pore diameters less than 2 nm. Figure 4.2(d) illustrates the BET pore size distribution, revealing a calculated surface area of 969.9 ± 6.3 m²/g with an average pore size of 16.3 Å, which is in close agreement with the literature findings [179].

The surface chemistry of the ZIF-71/CuO:Al structures, including elemental chemical states and bonding environments, was characterized using XPS. The survey spectrum in Figure 4.3(a) reveals signals attributed to carbon and nitrogen from imidazolate units, zinc cations, and chlorine anions from the organic ligand. The absence of copper and aluminum signals confirms near-complete surface coverage by ZIF-71. A minor O 1s peak suggests minimal surface oxidation, despite the sample's prolonged air storage prior to measurement.

High-resolution XPS spectra, presented in Figures 4.3(b)−(g), provide detailed insights. The Zn 2p spectrum (Figure 4.3(b)) exhibited characteristic spin-orbit split peaks at 1021.7 eV (Zn $2p_{3/2}$) and 1044.7 eV (Zn $2p_{1/2}$) with a 23.0 eV splitting [73], indicative of a single zinc species. The C 1s spectrum (Figure 4.3(c)) was deconvoluted into two components: a dominant peak at 286.8 eV (79%) corresponding to C-N/C=N and C-Cl bonds [180], consistent with intact ZIF-71, and a smaller peak at 285.2 eV (21%) attributed to carbon not bonded to electronegative partners, which is unexpected for pristine ZIF-71. The N 1s spectrum (Figure 4.3(d)) features three components: N 1 at 397.6 eV (5%) assigned to C-N bonds, N 2 at 399.7 eV (80%) linked to H-N bonding [180], and N 3 at 401.5 eV (15%), consistent with Zn-N species and indicating partial degradation.

The higher binding energy component aligns with previous synchrotron X-ray studies revealing ZIF-71 degradation [181], while Zn 2p remained stable, validating its role as a binding energy reference. The Cl 2p region (Figure 4.3(e)) displays four peaks corresponding to two spin-orbit doublets: Cl 2 and Cl 2′ at 201.3 and 202.9 eV assigned to C-Cl bonds [182], and Cl 1 and Cl 1′ at 199.1 and 200.7 eV [181], respectively, associated with Zn-Cl bonds formed during X-ray-induced degradation [181]. The C-Cl doublets constitute 71% of the Cl intensity, whereas Zn-Cl degradation products represent 21% of the total Cl intensity. The C 1 species at 285.2 eV is thus linked to degradation products characterized by C-C or C-H bonds not bonded to chlorine or nitrogen. Repeated measurements (Figure 4.3(g)) showed an increase in Zn-Cl doublet intensity from 21% to 42%, indicating progressive X-ray-induced degradation during XPS acquisition. This rapid degradation appears primarily driven by secondary electrons rather than direct X-ray exposure, given similar effects observed under laboratory XPS conditions and the much higher photon flux at synchrotron sources. Raman analysis prior to XPS confirmed the intactness of the ZIF-71 layer without X-ray or electron exposure, supporting the conclusion that degradation occurs during XPS measurement.
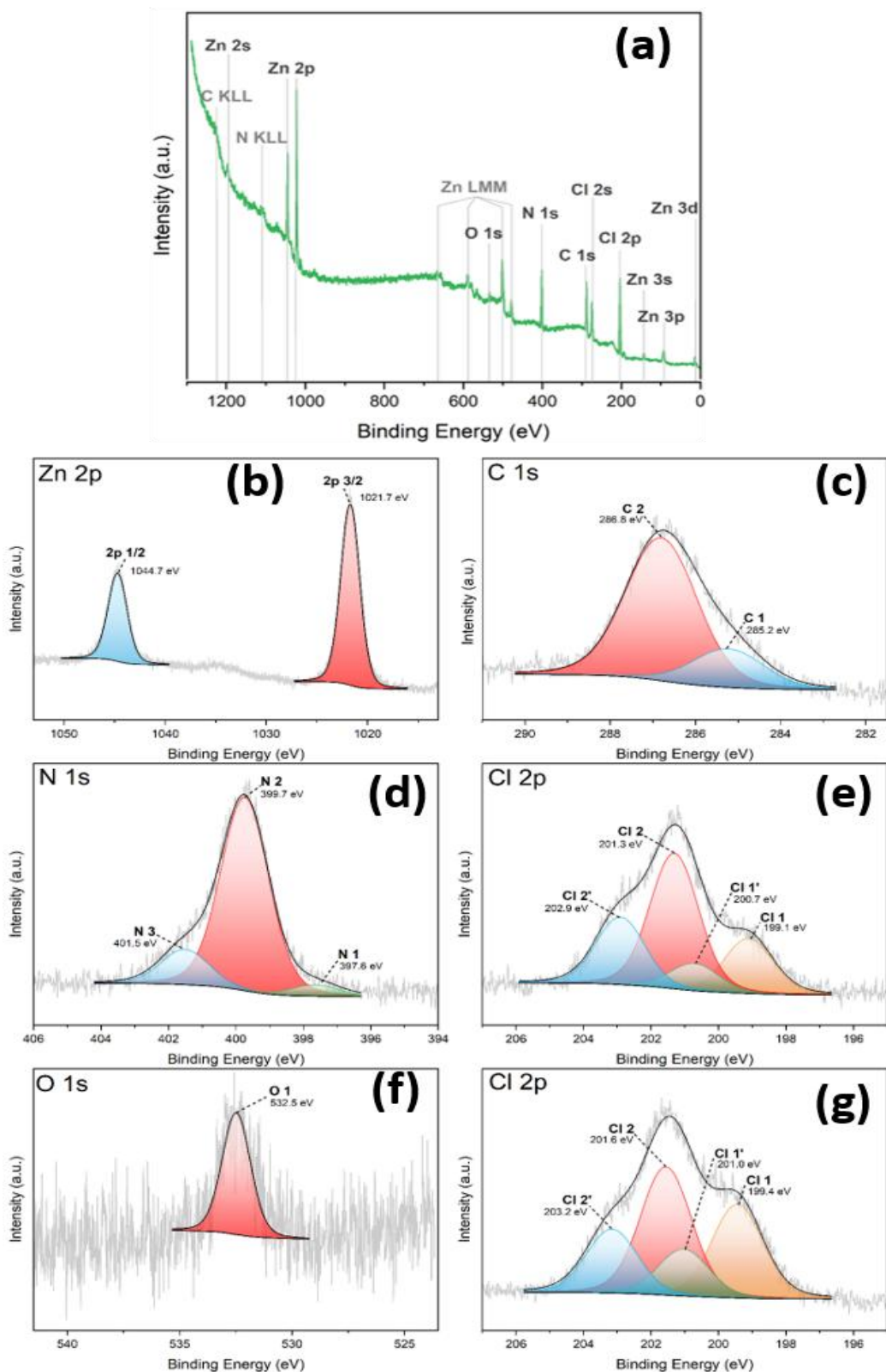
Fig. 4.3. XPS spectra of the ZIF-71/CuO:Al-based MOF/MO hybrids: (a) survey spectra showing XPS lines of all elements present. High-resolution (b) Zn 2p region. (c) C 1s region. (d) N 1s region. (e) Cl 2p region. (f) O 1s region. (g) Cl 2p region, second measurement.

The susceptibility of ZIF-71 to X-ray damage is attributed to the fact that the halogen (-Cl) facilitates radical formation from C-Cl bonds, promoting C-H and C-N bond activation and linker fragmentation [183]. The O 1s spectrum (Figure 4.3(f)) shows a broad peak at 532.5 eV, consistent with slight oxidation possibly forming alcohols, ketones, oxidized nitrogen species, or zinc hydroxides− while the formation of ZnO (530.7 eV) is ruled out [184].

Elemental quantification from XPS yields approximately 36.7 at% C, 23.8 at% Cl, 21.8 at% N, 15.7 at% Zn, and 2.1 at% O. The C:Cl and C:N ratios (~3:2), and N:Cl ratio (~1:1), align with the stoichiometry of 4,5-dichloroimidazolate units in ZIF-71. The relatively lower Zn content suggests excess 4,5-dichloroimidazolate species at the surface, consistent with the larger weight loss observed during TGA.

The location of the defect states can be determined using the Arrhenius plot by calculating the corresponding activation energy (E_a). The activation energy (E_a) of the CuO:Al film was assessed by plotting the logarithmic current (ln I) versus the inverse of the corresponding temperature (1/T) (Figure 4.4). The slope of the resulting curve provides the activation energy (E_a) using the following relation:

$$Slope = -\frac{E_a}{k}$$
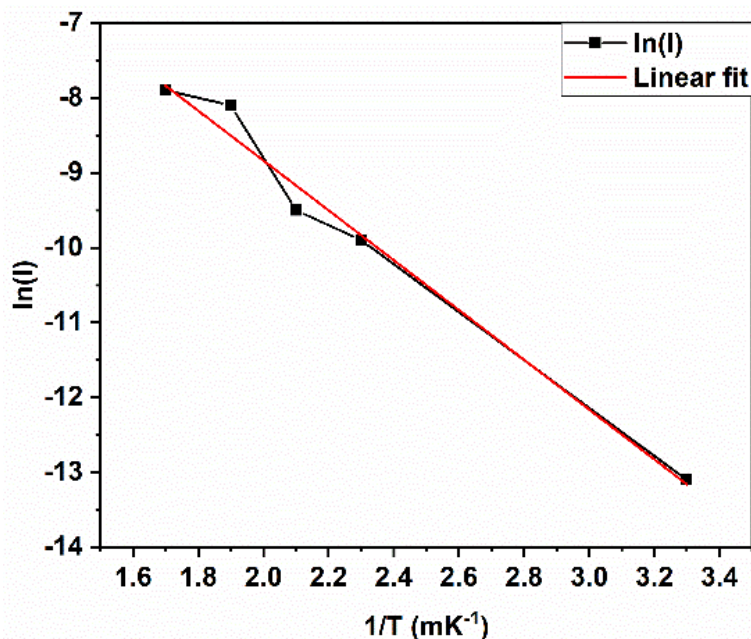
(4.1)

where k (eV/k) is the Boltzmann's constant.

Fig. 4.4. The Arrhenius plot of ln (I) vs 1/T for the calculation of activation energy.

The slope of the plotted curve is approximately 3.32×10^3 K. Using Equation 4.1, the activation energy (E_a) was calculated to be approximately 0.28 eV. The determined activation

energy (E_a) corresponds to defect levels or hole trap states (V_{Cu}) [154, 185]. Specifically, it corresponds to copper's shallow acceptor states, in contrast to the deep acceptor states observed in other metal oxides (e.g., MgO) [185].

Band bending at the metal–semiconductor interface originates from the difference in work functions, which drives charge transfer across the junction. For Au contacts formed on p-type CuO:Al, this results in upward band bending near the interface (Figure 4.5(a,b)). This effect causes electron depletion and hole accumulation, effectively reducing the injection barrier for holes and establishing an Ohmic contact with the p-type semiconductor oxide.
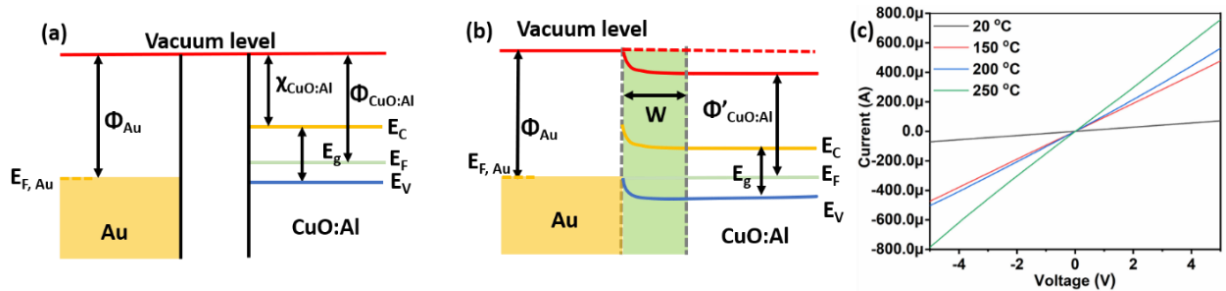

Fig. 4.5. The energy band diagrams of Zn and CuO (a) before, and (b) after Ohmic contact. (c) Current-Voltage measurement of Au IDE (170 nm thick) contacts to p-type CuO:Al sample.

The magnitude of band bending depends on the disparity between the metal's work function and the semiconductor's electron affinity [186]. This bending alters the effective work function and induces a depletion region of width (W) at the interface. The space charge region thus formed thus facilitates low-resistance charge transport. The linear current–voltage characteristics observed in Figure 4.5(c) confirm the presence of Ohmic contacts between the Au IDEs and the CuO:Al structures.

4.2. Evaluation of the sensing performance of ZIF-71/CuO:Al hybrids

The gas sensing performance of the CuO:Al structures without and with ZIF-71 coating, was tested and evaluated for a series of analytes (n-butanol, ethanol, 2-propanol, hydrogen gas, ammonia gas, and methane gas) at a concentration of 100 ppm at different operating temperatures ranging from 20 to 250 °C. The transient gas sensing measurement of the CuO:Al film (without coating) towards hydrogen at 250 °C exhibited 45% response (Figure 4.6). The corresponding response and recovery times were calculated and the approximate values were 11 s and 15 s, respectively.
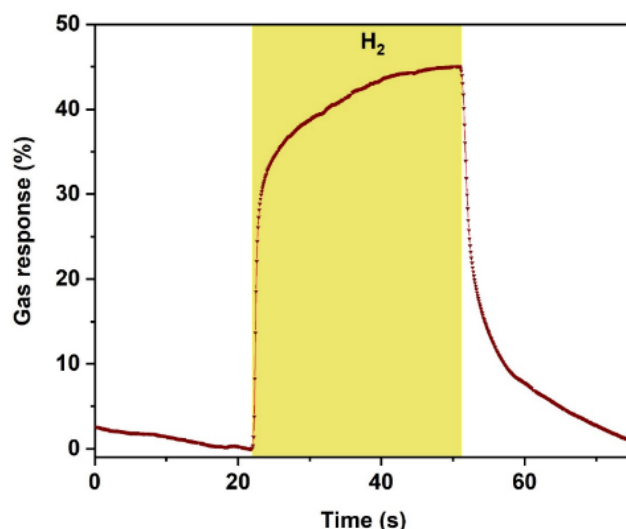
Fig. 4.6. Transient gas sensing response of the CuO:Al sensor (without ZIF-71 coating) to 100 ppm of hydrogen at 250°C operating temperature.

The comparative results for the gas sensing response of the CuO:Al film, both without and with the ZIF-71 coating, for a series of analytes at different tested temperatures are demonstrated in Figure 4.7 (a) and (b). The application of a ZIF-71 coating on CuO:Al films significantly improves gas-sensing responses to hydrogen, n-butanol, 2-propanol, and acetone at operating temperatures of 200°C and above. Notably, at 200°C, the ZIF-71-coated sensor exhibited a markedly improved response compared to the uncoated CuO:Al sensor. This enhancement is attributed to synergistic interactions at the ZIF-71/CuO:Al interface, where selective adsorption of target gases at ZIF-71's active sites increases sensitivity and selectivity, particularly toward n-butanol and hydrogen at their optimal operating temperatures [170, 187]. For n-butanol sensing, the gas response (S) increases dramatically from approximately 0.1% in the bare CuO:Al sensor to 11% for the ZIF-71/CuO:Al-based hybrid sensor at 200 °C, highlighting the pivotal role of ZIF-71 in enhancing detection.

Figure 4.7(b) shows gas sensing responses of the CuO:Al films (with ZIF-71 coating) to a series of test gases, with the highest sensitivity to hydrogen (~60%) observed at 250°C. No detectable response occurred at 20 °C or 150 °C for any analyte, likely due to adsorption of non-reactive molecular oxygen ionic species (O_2^-) on the sensor surface, causing slow analyte reaction kinetics at these lower temperatures [188]. Within the 200-250 °C range, the sensor responded distinctly to VOCs and hydrogen, whereas a gas sensing response for methane and ammonia was not observed across all tested temperatures, likely because these gases lack oxygen-containing functional groups, resulting in only weak physisorption on the sensor surface [189]. The strongest sensing response was observed for n-butanol at 200°C and hydrogen at 250°C. At 200°C,

selectivity toward n-butanol was approximately four times that of hydrogen and five times that of acetone, underscoring the preferential interaction of the sensor with specific analytes in this temperature regime.
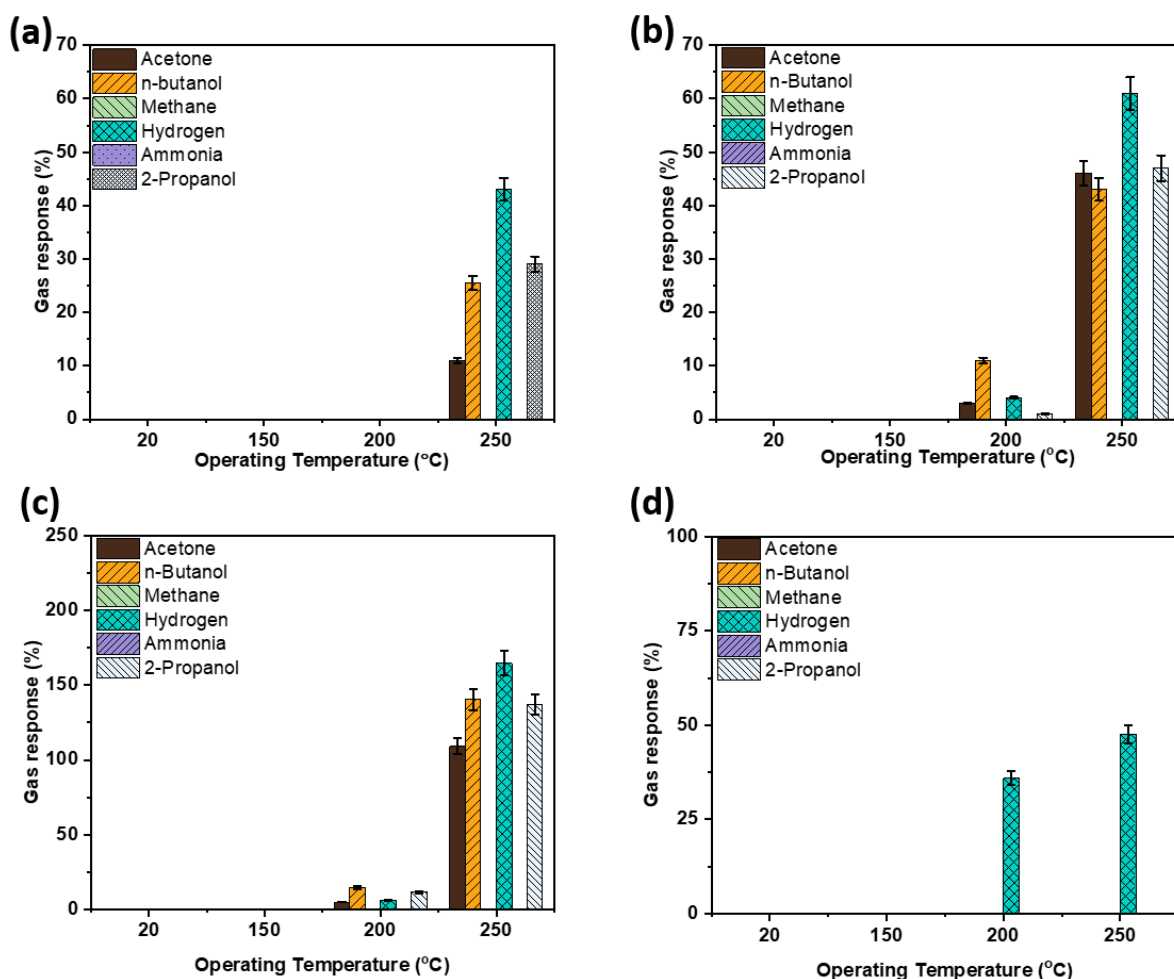

Fig. 4.7. Gas response to a series of gases with concentration of 100 ppm at different operating temperature for CuO:Al sample: (a) Without ZIF-71 coating, RH10%. (b) With metal-organic frameworks ZIF-71 coating initial test, RH10%. (c) With metal-organic frameworks ZIF-71 coating after 21 days, RH10%. (d) With metal-organic frameworks ZIF-71 coating after 21 days, RH50%.

To elucidate the sensor's interaction with n-butanol, Gao et al. [168] studied the desorption kinetics of n-butanol across three different ZIFs: ZIF-8 (pore aperture 3.4 Å), MAF-6 (7.6 Å), and TIF-1 Zn (11.7 Å). They observed that smaller pore apertures correspond to slower desorption rates, with desorption temperatures measured at 230°C for ZIF-8 and 130°C for TIF-1 Zn, clearly demonstrating the crucial role of pore size in desorption behavior. Accordingly, the desorption temperature for ZIF-71, possessing a 5.1 Å pore aperture, is expected to range between those of ZIF-8 and MAF-6, approximately 200–230°C [187]. Additionally, Wang et al. [187] demonstrated

that ZIFs with larger pore windows exhibit higher adsorption affinities for n-butanol relative to acetone and smaller-chain alcohols. This finding supports the enhanced adsorption of n-butanol by ZIF-71 compared to acetone or 2-propanol prior to desorption.

To evaluate the stability of the ZIF-71/CuO:Al hybrid sensor, gas sensing measurements were conducted 21 days and subsequently 42 days after the initial test. Figure 4.7(c) presents the gas sensing response (S) at 10% RH after 21 days, showing an overall increase in response compared to the original measurements. At 200°C, response values remained comparable to initial results, whereas at 250°C, all test gases exhibited enhanced responses. The most notable increase was observed for n-butanol, where the response rose significantly from ~43% to ~141% at 250°C. This enhancement likely arises from repeated thermal cycling during initial measurements that annealed the sensor material, thereby improving sensitivity. Figure 4.7(d) illustrates the sensor's response to various target analytes at 50% RH, measured 21 days post-initial testing. Between 200°C and 250°C, the hybrid sensor demonstrated increased selectivity toward 100 ppm hydrogen gas. Comparing Figures 4.7(c) and 4.7(d) highlights the effect of humidity: increasing RH from 10% to 50% substantially degraded the sensor's response to n-butanol across all operating temperatures. A more pronounced decline in response for all analytes except hydrogen was also evident at elevated RH levels. This behavior is attributed to incomplete ZIF-71 surface coverage and competitive adsorption between hydroxyl ions and oxygen molecules.

Figure 4.8 demonstrates hydrogen sensing dynamics at 250°C under varying humidity, showing maximum responses of approximately 164% at 10% RH and approximately 47% at 50% RH.
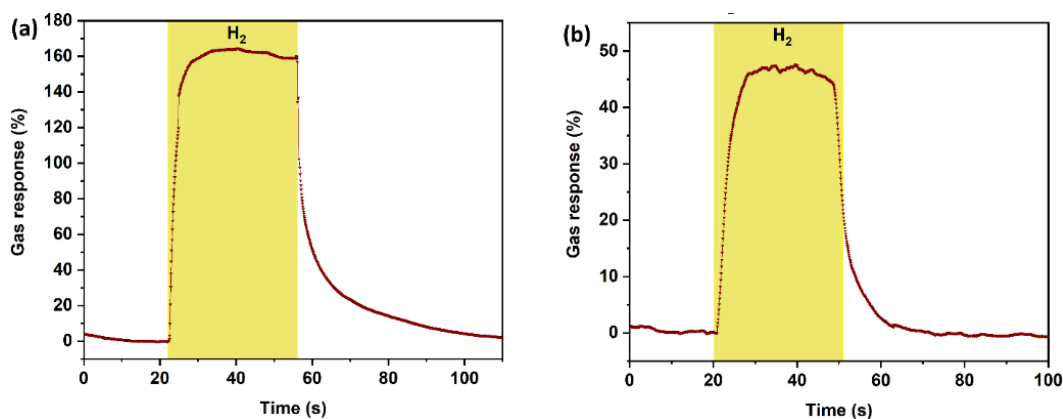

Fig. 4.8. Transient gas sensing response of the metal-organic frameworks ZIF-71/CuO:Al - based MOF/MO hybrid sensor to hydrogen gas at 250°C, measured 21 days after the initial measurements at different relative humidities: (a) RH=10%. (b) RH=50%.

Figure 4.9 presents the transient sensing response to n-butanol at 250°C, with a peak response of approximately 141% and response/recovery times of 19 s and 105 s, respectively. The relatively slower kinetics for 2-propanol and n-butanol are ascribed to hindered gas diffusion through the ZIF-71 layer to the CuO:Al sensing interface [190].
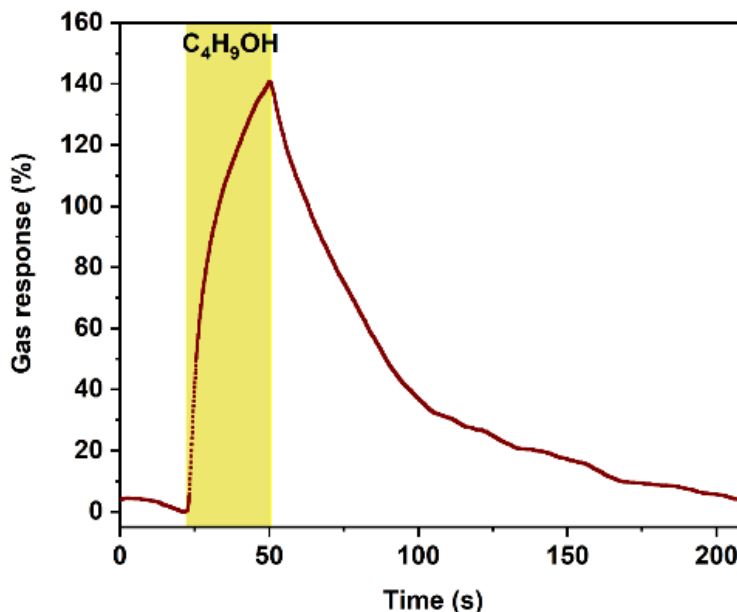

Fig. 4.9. Transient gas sensing response of the ZIF-71/CuO:Al-based MOF/MO hybrid sensor to n-butanol at 250°C, measured 21 days after the initial measurements.

Transient gas sensing responses of the ZIF-71/CuO:Al hybrid sensor were also recorded 21 days after the initial measurements for acetone, 2-propanol, hydrogen gas, and n-butanol.

As tabulated in Table 4.1, the developed hybrid sensors showed fast adsorption and desorption kinetics for hydrogen gas, whereas VOCs exhibited slower kinetics.

Table 4.1 The extracted response and recovery times at 250 °C at RH 10%, 21-days post-initial measurements.

Test analyte	Operating temperature, °C	Response time, s	Recovery time, s
Acetone	250	14	52
2-Propanol	250	18	73
Hydrogen	250	2	11
n-Butanol	250	19	105

Figure A2.5 demonstrates the transient response to acetone at 250°C and 10% RH, showing a stable baseline resistance (approximately 4 kΩ) at a low bias voltage of 6 mV. Multiple exposure

cycles (~30 s each) yielded reproducible responses (approximately 109%), demonstrating remarkable repeatability and sensor reliability over this interval. Figure A2.6 presents the transient response to 2-propanol at 250°C, with a peak response of approximately 138% and response/recovery times of 18 s and 73 s, respectively.

By applying the Boltzmann distribution together with the Poisson equation, an analytical expression describing the resistance dependence on surface band bending in p-type CuO:Al sensing layers is derived. This emphasizes that charge transport is dominated by surface processes involving adsorbed species, as presented in Equation (4.2) [191].

$$R_{air} \approx e^{-\frac{qV_{air}}{2kT}} \tag{4.2}$$

where V_{air} is the baseline surface potential or electric potential in air.

For p-type semiconductor, the ratio of the resistance of the CuO:Al surface when exposed to the target analyte (R_{gas}) to the resistance measured in the absence of the target analyte (R_{air}) define the gas sensing response. The correlation between the sensor signal and resistance variation in terms of band bending is described as follows:

$$\text{Sensing response, } S = \frac{R_{gas} - R_{air}}{R_{air}} \approx \frac{e^{-\frac{qV^{gas}}{2kT}} e^{-\frac{qV^{air}}{2kT}}}{e^{-\frac{qV^{air}}{2kT}}} \approx e^{\frac{-q\Delta V}{2kT}} - 1 \tag{4.3}$$

In terms of band bending ($q\Delta V$), this equation can be modified by using Equation 4.6. The change in affinity and band bending also impact the sensing response, which can be easily understood using Equations 4.4 and 4.5, respectively.

$$\Delta \chi = \Delta \emptyset - q\Delta V \tag{4.4}$$

where $\Delta\chi$ represents change in electron affinity and $\Delta\Phi$ represents the change in the work function of the CuO:Al sample by changing the gaseous environment.

The influence of relative humidity on sensor performance can be interpreted using Equation (4.5). When the CuO:Al sensor is exposed to a target gas such as n-butanol in the presence of humidity, the interaction results in complex effects. It is generally assumed that the band bending at the sensor surface decreases, resulting in an increase in surface resistance due to a reduction in ionosorbed oxygen species, which are replaced by hydroxyl groups [191]. Specifically, water vapor interacts with adsorbed oxygen on the CuO surface, leading to the formation of dipoles through a surface chemical process. This dipole formation alters the surface charge distribution and modifies the electronic properties of the sensing layer, thereby affecting the overall gas sensing response.

$$O^-_{(ads)} + H_2O_{(vap)} + 2Cu_{(site)} + h^+ \leftrightharpoons 2(Cu^+_{(site)} - OH^-) + S \tag{4.5}$$
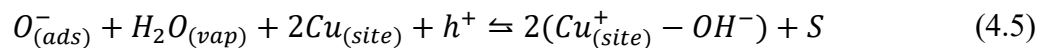
where $O^-_{(ads)}$ represents an ionosorbed oxygen species, $H_2O_{(vap)}$ represents the water vapor in the atmosphere, Cu_{site} represents an atomic Cu site on the CuO:Al surface, h^+ represents the consumed hole, $(Cu^+_{(site)} - OH^-)$ represents the formed terminal hydroxyl groups (electric dipole) on the surface, and S represents a surface site for oxygen chemisorption on the CuO:Al surface.

The contribution of electric dipoles to the work function enhances electron affinity by increasing the energy barrier for electron emission from the sensor surface [191]. Consequently, with rising relative humidity, the predominant electron-trapping species shifts from ionosorbed oxygen to water vapor [192, 193], causing an increase in surface resistance and a corresponding decrease in the gas sensing response. Figure 4.7(d) demonstrates a pronounced selectivity toward hydrogen gas at an elevated 50% RH, measured 21 days post-initial testing.

After 42 days from the initial measurements, a subsequent gas sensing evaluation of the ZIF-71/CuO:Al-based hybrid sensor was conducted at 10% RH, with the results shown in Figure A2.7. At 200°C, the sensor's response closely resembled previous measurements, while at 250°C, the VOC responses remained stable compared to the results 21 days post-initial testing. A slight reduction in the hydrogen gas response was noted at 250°C. Overall, consistent response trends across measurements at 21 and 42 days indicate stable sensor performance over this period, likely aided by thermal annealing during the initial testing [194].

Figure A2.8 compares gas sensing responses at 21 and 42 days after initial testing at 250°C for hydrogen and VOCs under 10% RH. The observed increase in sensor response−roughly twofold to threefold at 21 days−is attributed to the thermal aging and preheating effect on the sensor [194].

A detailed comparison with similar studies on ZIF-coated semiconducting oxide sensors of various morphologies is presented in Table A2.1. The present sensor exhibited superior performance, including rapid response and recovery times (2 s and 11 s) for hydrogen, and an approximately 110-fold sensitivity enhancement for n-butanol. Furthermore, it maintains repeatable, temporally stable, and selective detection of hydrogen even under high RH conditions (50% RH), demonstrating its practical robustness and efficiency in adverse environmental conditions.

4.3. Assessment of gas sensing selectivity in ZIF-71/CuO:Al-based MOF/MO hybrids

The identification of the gas flow regime is important for understanding the transport mechanism of gas molecules through the ZIF-71 layer at the CuO:Al interface. The mean free path (λ) of the gas molecules is defined in Equation 3.15.

Since the concentration of the test gas is negligible compared to the background air, the number density of the background air dominates. This makes the mean free path effectively independent of the small mole fraction of the test gas. The mean free paths of n-butanol and hydrogen gases were calculated at 200°C and 250°C, yielding values of 62.5 nm and 136 nm at 200°C, and 69 nm and 150 nm at 250°C, respectively (using Equation 3.15).

The transport regime of these target gases can be categorized into three types-Knudsen diffusion, transitional diffusion, and molecular diffusion-based on the Knudsen number (K_n), which is determined using the Equation 3.16. Furthermore, using Equation 3.16, the K_n was calculated for n-butanol and hydrogen at two different operating temperatures (200 °C and 250 °C) where temperature-dependent selectivity was observed. The calculated values of K_n at 200 °C (n-butanol: 122 and hydrogen: 267) and 250 °C (n-butanol: 135 and hydrogen: 294) clearly indicate that both gases fall within the Knudsen diffusion regime ($K_n > 10$) at all the mentioned temperatures.

SEM images of the ZIF-71/CuO:Al-based MOF/MO hybrids showed that ZIF-71 particles almost completely cover the CuO:Al surface, forming a continuous layer. However, the ZIF-71 film is not entirely free of pinhole defects. Transport through grain boundaries and other minor defects may locally decrease the Knudsen number (K_n) in certain areas. Therefore, it can be concluded that the intrinsic transport of n-butanol and hydrogen through the ZIF-71 pores at both temperatures predominantly occurs via Knudsen diffusion, although localized contributions from transitional or molecular diffusion may arise at grain boundaries and defects.

The competitive diffusion of tested molecules through the ZIF-71 pores was enabled because the large pore aperture of ZIF-71 (~5.1 Å) [187] closely matches the kinetic diameters of VOCs such as 2-propanol (~4.7 Å) [167], n-butanol (~5.0 Å) [168], and acetone (~4.6 Å) [195]. The molecular sizes of n-butanol, acetone, and 2-propanol are comparable to the pore size, facilitating access via a molecular sieving effect. However, n-butanol shows a stronger affinity for ZIF-71 adsorption sites compared to smaller molecules like acetone and 2-propanol, due to its longer carbon chain, which enhances van der Waals interactions within the ZIF-71 framework [196]. Wang et al. [187] calculated adsorption energies indicating higher adsorption strength for n-butanol over acetone on ZIF-71. Moreover, polarizability significantly affects the interaction strength between the adsorbate and adsorbent. n-Butanol, with a higher polarizability (~8.57) [169] than acetone (~6.27) [169] and 2-propanol (~6.67) [169], exhibits stronger van der Waals interactions with the ZIF-71 structure, leading to increased adsorption facilitated by effective surface interactions [168].

As a result, n-butanol proceeds easily toward the interface, leading to greater sensitivity compared to the other two tested analytes (acetone and 2-propanol). At lower temperatures (~200°C), the sensor performs well due to strong van der Waals forces and hydrogen bonding between the hydroxyl group of n-butanol and the chlorine functional groups (-Cl) in the MOF, promoting high adsorption and an enhanced sensing response. The relatively low kinetic energy of n-butanol at this temperature allows it to interact effectively with the ZIF-71 framework and to reach the heterostructure interface easily. In contrast, hydrogen's smaller size enables rapid diffusion at higher temperatures, which increases its sensing response at higher temperature (250 °C). Figure A2.9(a) illustrates a schematic of ZIF-71's relevant structural features and properties for gas sensing. These characteristics synergistically improve the selective adsorption and diffusion of target gases, thus enhancing gas selectivity and sensor performance. Figure A2.9(b) depicts the crystal structure of ZIF-71 exhibiting an RHO topology, composed of Zn ions tetrahedrally coordinated with 4,5-dichloroimidazolate linkers.

4.4. Proposed sensing mechanism of ZIF-71/CuO:Al-based MOF/MO hybrids

The ZIF-71 coating layer on top of the CuO:Al film significantly influences gas-sensing performance toward VOCs such as acetone, n-butanol, and 2-propanol, as well as gases like hydrogen. To elucidate the mechanism behind the enhanced selectivity for target analytes at different operating temperatures− specifically n-butanol at a low temperature (200 °C) and hydrogen at a higher temperature (250 °C)−the interaction model between the analytes and the sensing surface is presented in Figure 4.10. For gas sensing on CuO, the model involves three key processes: sorption, diffusion, and desorption. As reported by Wei et al., variations during the adsorption and desorption of tested analytes are critical factors influencing the gas-sensing response [197]. As discussed earlier, n-butanol shows a stronger affinity for the ZIF-71 framework compared to acetone and 2-propanol, attributed to its longer carbon chain, higher polarizability, and greater adsorption energy. The incorporation of ZIF-71 particle dispersion onto the CuO:Al film enhances the interaction of n-butanol at their interface due to this strong molecular affinity. Studies analyzing analyte affinity on ZIFs have reported superior n-butanol adsorption on ZIF-71 relative to acetone and other short-chain alcohols [187]. The higher dipole moment of acetone compared to n-butanol results in a weaker interaction with the weakly polar ZIF-71 framework, which also possesses a larger cavity size relative to the acetone molecule [170, 198]. Consequently, n-butanol is expected to exhibit the highest affinity toward ZIF-71. Thus, the selective detection of n-butanol at 200 °C (i.e., just below its desorption temperature) can be attributed to the

synergistic effect arising from CuO:Al's chemoresistive contribution with ZIF-71's strong adsorption affinity.

Metal oxide semiconductors like ZnO and TiO$_2$, in their undoped form, typically display n-type behavior due to inherent oxygen vacancies [199, 200]. Conversely, certain metal oxides such as CuO show p-type semiconductor characteristics owing to inherent defects−specifically Cu interstitial defects that generate acceptor states above the valence band. Generally, gas sensing in metal oxide semiconductors originates from the adsorption of oxygen molecules from the atmosphere, which activates these inherent defect states [201]. According to the ionosorption-desorption model, the sensing mechanism for reducing gases−such as n-butanol, 2-propanol, and hydrogen−can be explained. Upon exposure to atmospheric air, oxygen molecules adsorb on the sensor surface and ionize into different oxygen species depending on the operating temperature, as outlined in Equations (3.9) – (3.12) and (3.14) from Chapter 3.
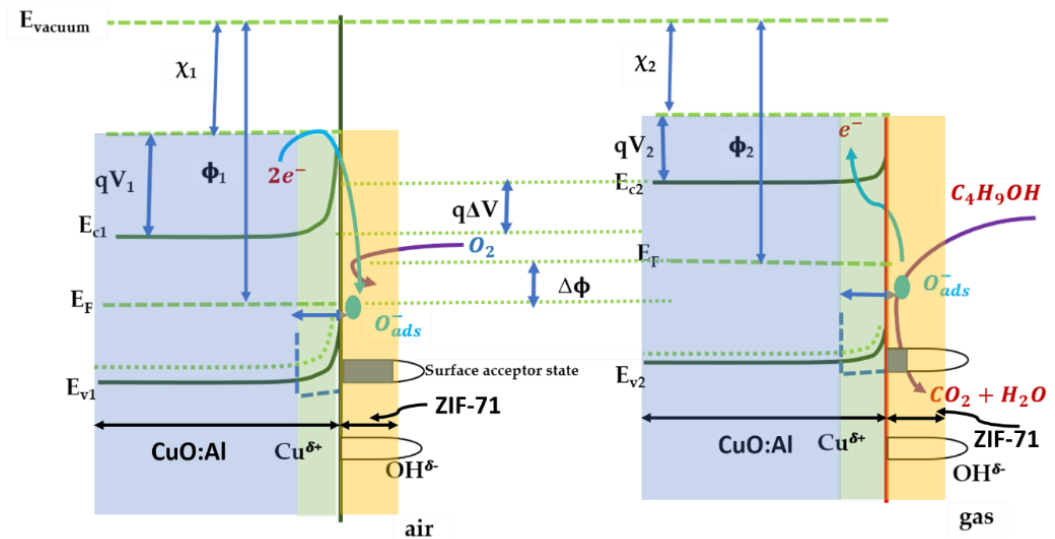

Fig. 4.10. Sensing mechanism of the CuO:Al illustrated energy band diagrams toward n-butanol and other reducing gases; the adsorption of oxygen species from ambient air; and in the presence of target analytes (n-butanol).

As shown in Figure 4.10, the adsorption of oxygen ions on the sensor surface via surface traps creates a high potential barrier and a hole accumulation layer, causing an upward band bending and a consequent decrease in the resistance of the accumulation layer. Upon exposure to n-butanol at 200°C, the corresponding adsorbed oxygen species react with the analyte, releasing electrons that recombine with holes in the bulk material, as detailed in Equation 3.14. This recombination led to decrease in the hole concentration in the accumulation layer, resulting in downward band bending ($q\Delta V = \Delta\Phi$) and an increase in the resistance of the accumulation layer [9].

4.5. Conclusions of Chapter 4

The physicochemical properties of organic/inorganic hybrid structures were investigated in detail using advanced characterization techniques. Detailed materials characterization was performed for structural evaluation using XRD analysis, confirming the crystalline structure of the CuO:Al film and ZIF-71 particles. Surface morphology and related insights were provided by analyzing SEM images, revealing intergranular features of the CuO:Al film and triangular crystallites formed as a result of thermal annealing [7].

Surface-sensitive measurements were carried out using XPS, confirming the effective intactness of ZIF-71 on the CuO:Al film. XPS provided information regarding the elemental composition−36.7 at% C, 23.8 at% Cl, 21.8 at% N, 15.7 at% Zn, and 2.1 at% O−indicating a C-to-Cl ratio of 3:2 and an 1:1 N-to-Cl ratio, consistent with the linker stoichiometry and a lower presence of Zn in ZIF-71 [7].

The ZIF-71/CuO:Al structures demonstrated a notable enhancement in sensitivity to n-butanol (110 times) while maintaining sensitivity to hydrogen compared to bare CuO:Al structures at different operating temperatures of 200°C and 250°C, respectively. The hybrid structures exhibited good repeatability of sensing results, along with notable temporal and chemical stability under ambient conditions [7].

The drop-casting of a ZIF-71 particles dispersion on the CuO:Al film provided ideal active sites for n-butanol, outperforming smaller carbon chain alcohols and acetone. The strong affinity for ZIF-71 adsorption sites just prior to the desorption temperature resulted in high selectivity toward n-butanol. During initial measurements, the selectivity for n-butanol at 200°C was approximately five times greater than that for acetone and about four times higher than that for hydrogen [7].

A comparative study between the CuO:Al film with and without the ZIF-71 coating indicates a significant enhancement in sensitivity to the target analytes at their respective temperatures. Transient sensing results exhibited fast response and recovery times for hydrogen of 2 seconds and 11 seconds, respectively [7].

The interactions between target analytes and ZIF-71, emphasizing the diffusion of analyte molecules onto the CuO:Al surface, are explained by the proposed gas sensing mechanism. These findings underscore the pivotal role of ZIF-71 active sites in facilitating interactions with target analytes, thus improving the gas-sensing performance of this chemoresistive hybrid sensor. Further research is required to explore the effects of varying ZIF-71 concentrations under different conditions [7].

5. PHYSICOCHEMICAL PROPERTIES AND STRUCTURE-PROPERTY-PERFROMANCE CORRELATIONS IN ZIF-n (n = 67, 7, 71, 8)/ZnO HYBRIDS

5.1. Systematic Morphological and Structural characterization of ZIF-n (n = 67, 7, 71, 8)/Metal Oxide (ZnO, ZnO:Cd) hybrids

In this section, a detailed investigation of the morphological and structural properties of hybrid structures−including, ZIF-67/ZnO, ZIF-7/ZnO, ZIF-71/ZnO, and ZIF-8/ZnO structures, as well as Cd-doped ZnO-based hybrid structures−is elucidated. The surface morphology of the hybrid structures was investigated using SEM. For all studied samples, SEM micrographs were acquired at different magnifications to capture coarse and fine details. SEM images at lower magnifications revealed compactly dense and uniformly distributed grains of ZnO and Cd-doped ZnO (Figure A3.1(a) and (c)), respectively. This can be attributed to the thermal annealing effect. More detailed information was revealed by higher-magnification images, illustrating columnar morphologies for the ZnO (Figure A3.1(b)) and Cd-doped ZnO-based samples.
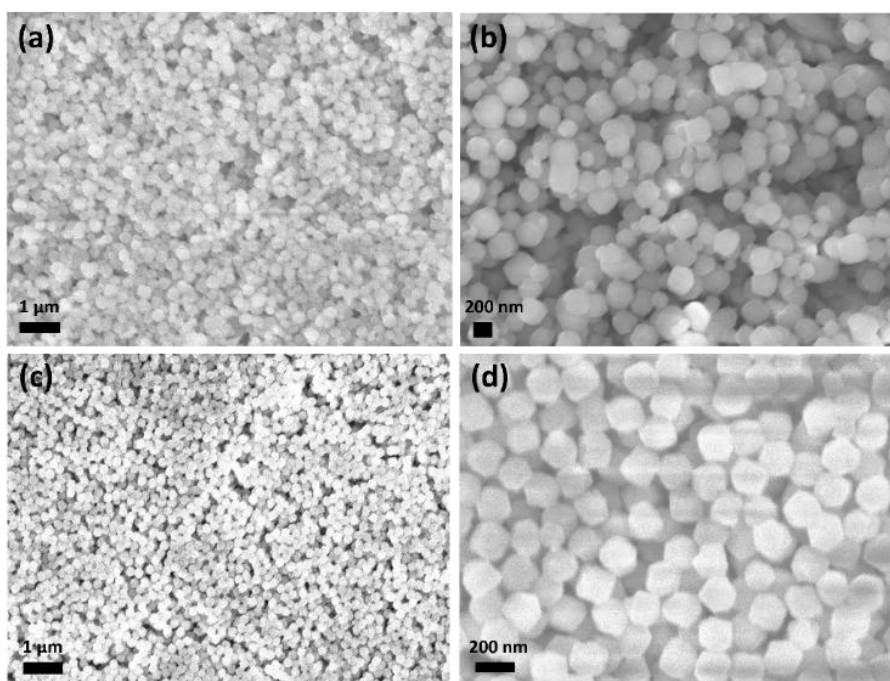

Fig. 5.1. SEM micrographs of ZIF-67/ZnO hybrid structures at: (a) lower magnification (1 μm) and (b) higher magnification (200 nm); and SEM micrographs of ZIF-7/ZnO based hybrid structures at: (c) lower magnification (1 μm) and (d) higher magnification (200 nm).

Additionally, for the Cd-doped ZnO samples, new columns growing out of the existing columns were observed (Figure A3.1(d)). Following ZIFs deposition, SEM images were acquired

for the ZIF/ZnO structures at lower and higher magnifications. SEM micrographs of ZIF-67/ZnO and ZIF-7/ZnO structures revealed dodecahedral morphologies with ZIF particle sizes of 200 nm for both ZIFs, in their respective images, as shown in Figure 5.1(a)-(d).

Furthermore, SEM micrographs corresponding to ZIF-71/ZnO and ZIF-8/ZnO structures revealed particle sizes in the range of 500 to 700 nm and approximately 70 nm, respectively (Figure 5.2(a)-(d)). Moreover, the ZIF-71 and ZIF-8 particles also exhibited dodecahedral morphologies. Additionally, EDX measurements were carried out on the Cd-doped ZnO sample to estimate the elemental composition. The compositional analysis and elemental mapping confirm the presence of Cd in the ZnO film, with a Cd composition of approximately 0.18 at%.
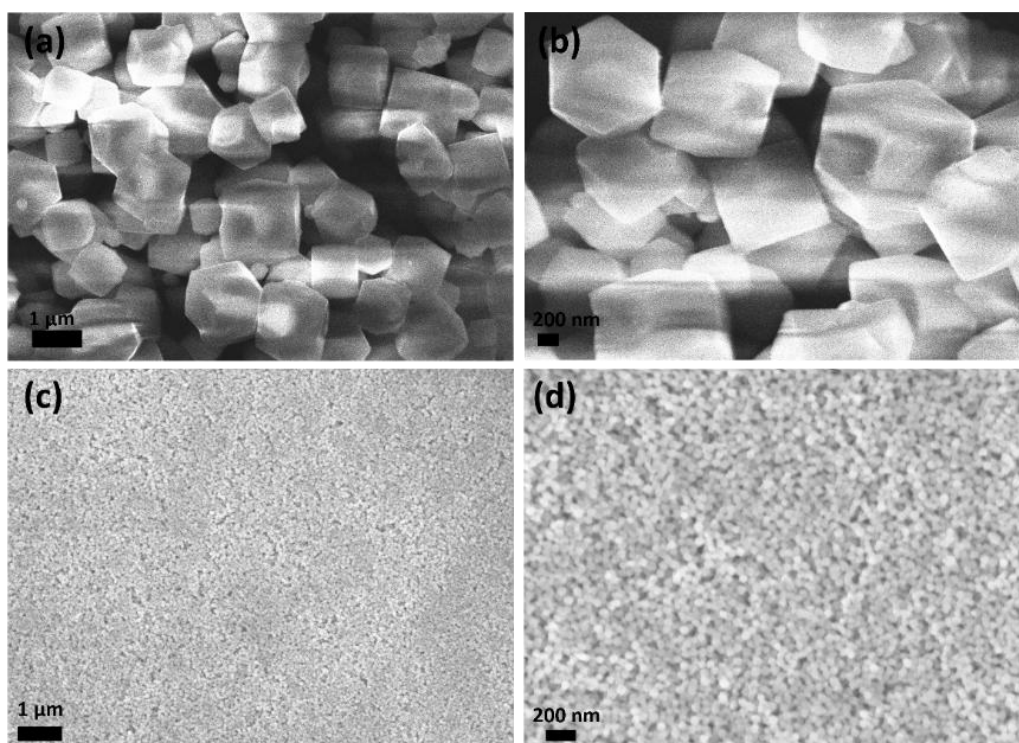

Fig. 5.2. SEM micrographs of ZIF-71/ZnO based hybrid structures at: (a) lower magnification (1 µm) and (b) higher magnification (200 nm); and SEM micrographs of ZIF-8/ZnO based hybrid structures at: (c) lower magnification (1 µm) and (d) higher magnification (200 nm).

To study the structural properties of the prepared samples, XRD investigations were carried out for two sample series: one comprising ZIF/ZnO based hybrid structures and the other consisting of ZIF/Cd-doped ZnO based hybrid structures. A discussion of these two series, involving ten samples in total, would require repeating similar names multiple times. To avoid this repetition, a codification scheme is proposed as tabulated in Table 5.1.

The structural features of both series were examined using XRD. Structural investigations of all the studied hybrid structures elucidated distinct diffraction peaks, indicating high crystallinity (Figure 5.3(a) and (b)).

Table 5.1. Codification scheme for all the ten samples ZIF/ZnO and ZIF/Cd-doped ZnO-based MOF/MO hybrids.

Sample name	Sample codification
ZnO	0A
ZIF-67/ZnO	1A
ZIF-7/ZnO	2A
ZIF-71/ZnO	3A
ZIF-8/ZnO	4A
Cd-doped-ZnO	M0
ZIF-67/Cd-doped ZnO	M1
ZIF-7/Cd-doped ZnO	M2
ZIF-71/Cd-doped ZnO	M3
ZIF-8/Cd-doped ZnO	M4

The XRD pattern corresponding to ZnO matches well with the hexagonal wurtzite structure (PDF 2300112). In ZnO, the dominant reflection was observed at 34.43˚, which corresponds to the (0 0 2) plane, indicating preferential growth along the c-axis, perpendicular to the substrate. The presence of highly crystalline reflections corresponding to ZIF-67 [202], ZIF-7 [203], ZIF-71 [171], and ZIF-8 [204] has been marked, as shown in both Figure 5.3(a) and (b). The patterns reveal that the dominant reflection from all ZIFs corresponds to the [1 1 0] family of planes.
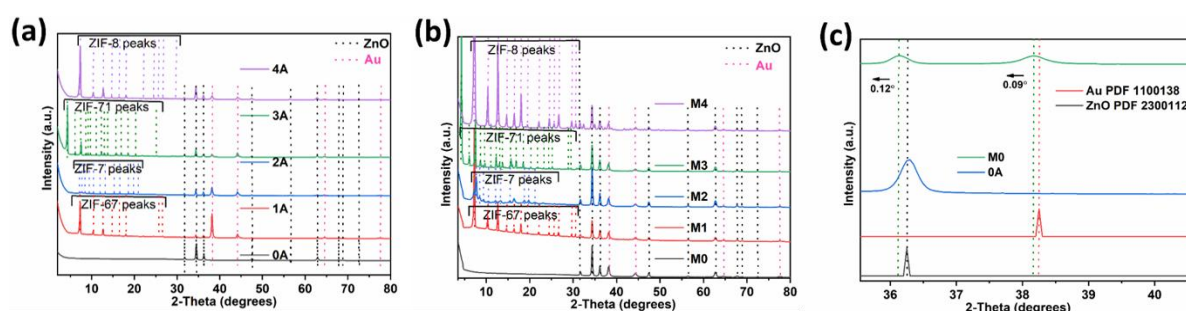

Fig. 5.3. XRD patterns of two series of samples: (a) 0A, 1A, 2A, 3A, and 4A and (b) M0 to M4, (c) comparison of 0A and M0 sample to show the crystallographic peak shift due to Cd doping.

By comparing the XRD reflections of the 0A and M0 samples, a clear shift of approximately 0.12˚ can be observed for the (1 0 1) plane (Figure 5.3(c)). Au IDEs were used for making electrical contacts on the samples, and the observed Au reflections matched those of Au (PDF 1100138). Similarly, after Cd doping, a shift in the Au reflection to lower 2θ values was

observed for the (1 1 1) Au reflection (Figure 5.3(c)). Cd incorporation leads to shift in lower 2θ values was also reported in previous studies [205–207]. This can be attributed to the presence of larger ionic radius of Cd^{2+} (~0.92 Å) substituting Zn^{2+} ions (~0.74 Å) at crystallographic positions [205]. As discussed previously in the same section, the presence of Cd in the ZnO film has already been confirmed using EDX analysis, which is further supported by the corresponding XRD shifts in the XRD patterns.

From the XRD data presented in Figure 5.3, the crystallite size (D) of each ZIF was calculated for the most prominent reflection, using the Scherrer equation (Equation 3.1). For all four studied ZIF particles, the shape factor was taken as approximately 0.94, which is standard for cubic-like crystallite geometries. The most dominant reflection in each XRD pattern was selected for peak fitting to determine the FWHM. Peak profiles were fitted using a Voigt function and optimized with the Orthogonal Distance Regression (Pro) iteration algorithm. The FWHM (β in radians) was then calculated using the two-step empirical approximation formula for the Voigt profile (Equation 3.2).

The FWHM of the most prominent reflection for all ZIF particles was calculated using Equation 3.2. For ZIF-67, the most prominent reflection corresponds to the (0 1 1) plane was observed at $\theta = 0.063873$ radians, where the values of w_L and w_G were found to be 0.001948 and 0.002211 radians. This resulted in a calculated value of $\beta = 0.003431$ radians. Similarly, the corresponding values of w_L and w_G, and the resulting β were calculated for all other ZIFs. Using Equation 3.1, the crystallite size (D) can be calculated for all four studied ZIFs, as summarized in Table 5.2.

Table 5.2. Calculated value of all the parameters required for calculating the crystallite size (D).

Name of the ZIF	Reflection with the highest intensity	w_L (radians)	w_G (radians)	β (radians)	θ (radians)	D (nm)
ZIF-7	(1 1 0)	0.002635	0.002293	0.004069	0.068067	~35.67
ZIF-67	(0 1 1)	0.001948	0.002211	0.003431	0.063873	~42.30
ZIF-71	(1 1 0)	0.001402	0.001447	0.002339	0.038034	~61.97
ZIF-8	(0 1 1)	0.002248	0.002450	0.003870	0.064232	~37.50

It was observed that the calculated crystallite sizes for the ZIFs, using the Scherrer equation, were smaller than the particle sizes estimated by scaling the SEM images. This

discrepancy in values can be attributed to coherent scattering, resulted in the broadening of the FWHM and the exclusion of surface-related domains [127].

5.2. Thermally induced phase dynamics of ZIF structures: An *in-situ* XRD investigation

Dispersion of all four studied ZIFs was drop-cast onto Si substrates to understand the structural changes due to the thermal effects. In situ temperature-dependent XRD measurements were carried out within a temperature range of 30 °C to ≥500 °C for all studied ZIF-based samples (Figure 5.4 (a)-(f)).
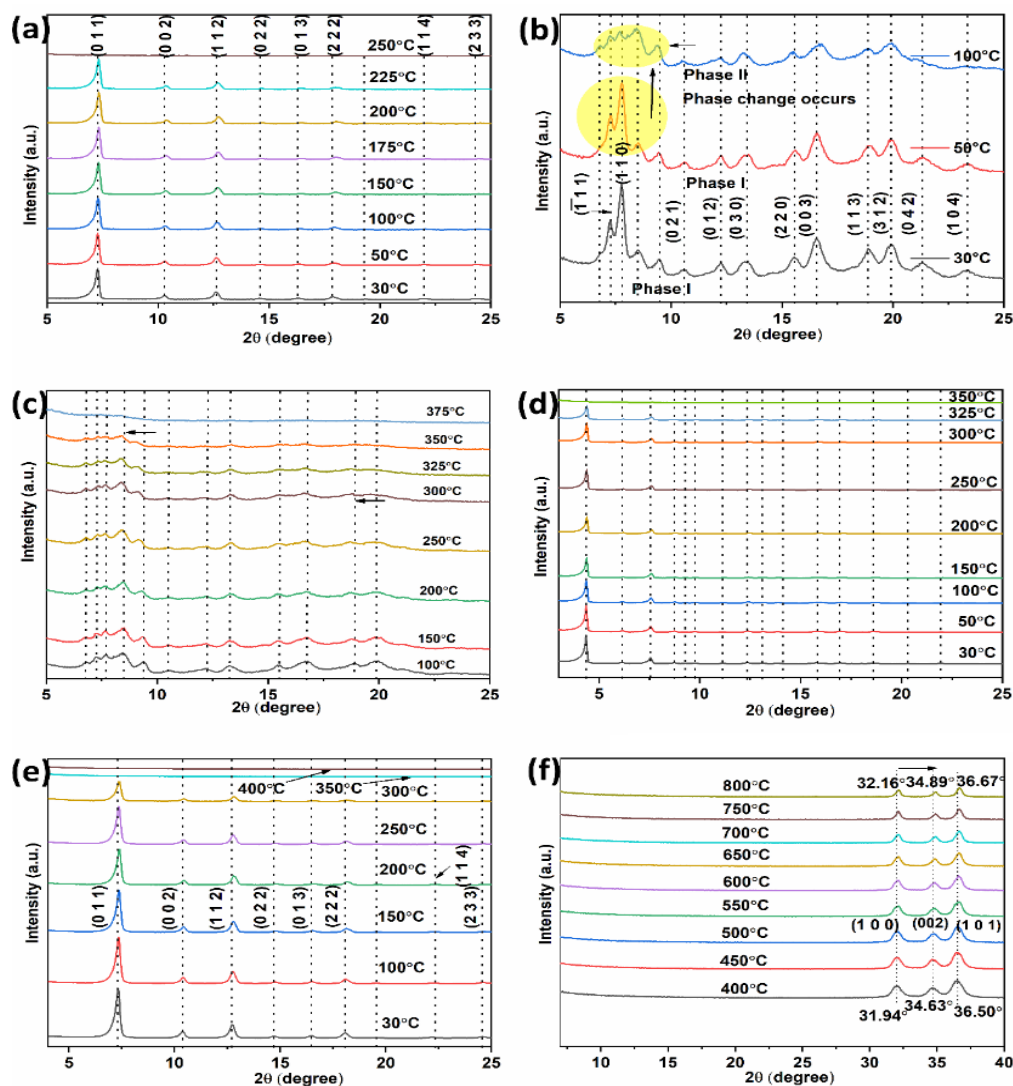

Fig. 5.4. *In-situ* temperature dependent XRD study of all the four studied ZIFs: (a) ZIF-67, (b, c) ZIF-7, (d) ZIF-71, and (e, f) ZIF-8 particles.

XRD investigation at room temperature for all four ZIFs was demonstrated in the previous section. Observing structural changes in ZIFs by changing the operating temperature is a key aspect of this study. For ZIF-67, as the temperature increased from 30 °C to 500 °C, significant transformations in the structural framework were observed. Miller indices (h k l) were assigned to

the corresponding XRD reflections according to the literature [202]. Within the temperature range of 30 °C to 250 °C, the spectral intensity of the XRD reflections diminished, indicating a loss in crystallinity in the ZIF-67 framework (Figure 5.4(a)), which can be attributed to thermal stress. At higher temperatures (500 °C), the complete transformation of the ZIF-67 framework into Co_3O_4 was observed. At 250 °C, a coexistence of both ZIF-67 and transformed Co_3O_4 reflections was noted. Increasing the temperature from 30 °C to 225 °C caused a slight rightward shift in the XRD reflections (within 0.04˚ to 0.12˚), suggesting framework shrinkage. However, a rightward shift due to thermal stress is not standard behaviour [45]. This peculiar observation is known as negative thermal expansion, which may be attributed to the soft or low-frequency transverse vibrational modes of the organic framework [208]. These modes can cause the organic framework to hinge, resulting in a slight contraction rather than expansion upon heating. At higher temperatures ($\geq$275 °C), ZIF-67 transformation into Co_3O_4 is evident (Figure A3.2(a)).

XRD investigations of ZIF-7 demonstrated a phase change as the temperature increased from 50 °C to 100 °C. At lower temperatures (30 °C and 50 °C), the diffraction refletions correspond to phase-I, and can be assigned to the (-1 1 1), (1 1 0), (0 2 1), (0 1 2), (0 3 0), (2 2 0), (0 0 3), (1 1 3), (3 1 2), (0 4 2), and (1 0 4) planes, at 7.23˚, 7.77˚, 10.58˚, 12.24˚, 13.4˚, 15.55˚, 16.57˚, 18.9˚, 19.92˚, 21.33˚, and 23.37˚, respectively, as confirmed by reported results [203]. At 100 °C, significant changes occurred: an emerging reflection at $2\theta = 6.77$˚ appeared, accompanied by a slight shift in other lower angle peaks (Figure 5.4(b)). These changes represent the transformation of initial phase (phase-I) into phase-II, which may be attributed to the release of synthesis solvent or dispersion solvent molecules (DMF or methanol), followed by a rearrangement of the ZIF-7 framework. A further temperature increases to 325 °C resulted in a loss of diffraction intensity for the main reflection at $2\theta = 8.36$˚, as shown in Figure 5.4(c). This reveals slow decomposition and a loss of long-range order, attributed to thermal stress. By going from phase-I to phase-II resulted in a loss of symmetry. At 375 °C, ZIF-7 and ZnO phases coexisted, with complete dissociation of the ZIF-7 framework occurring at 400 °C (Figure A3.2(b)).

As the temperature from 30 °C to 350 °C, a slight shift in diffraction reflexes was observed from 9.47˚ to 9.04˚. This can be attributed to the thermal expansion of the framework. At higher temperatures (500 °C), the ZnO phase was clearly observed; it retained its phase even after cooling back to room temperature (30 °C), as shown in Figure A3.2(b). This phenomenon has been reported in previous studies [209]. Moreover, the rightward shift was also observed (Figure 5.4(b)), which can be attributed to thermal stress. The effect of temperature on structural changes

has also been noted using TGA analysis [107]. Moreover, phase changes in the ZIF-7 framework have been reported at higher temperatures in previous results [203, 210].

The effect of increasing temperature was also clearly observed in the diffraction intensity of ZIF-71 (Figure 5.4(d)). Increasing the temperature from 30 °C to 325 °C led to a gradual loss in crystallinity and the sluggish decomposition of the ZIF-71 framework, which is attributed to thermal stress. Furthermore, increasing the temperature to 350 °C resulted in the emergence of ZnO reflections and almost entirely diminished intensity of ZIF-71 reflections. The effect of temperature was also observed on the FWHM of the XRD reflections; by increasing the temperature from 30 °C to 325 °C, significant amorphization and broadening of XRD reflection were observed. With the emergence of ZnO reflections, crystallinity improves at higher temperatures (Figure A3.2(c)). Additionally, a slight shift in XRD reflections was observed from 4.36˚ to 4.40˚ as the temperature increased from 30 °C to 325 °C. This peculiar behaviour can be attributed to the negative thermal expansion caused by soft lattice vibrations within the organic framework [208]. By increasing the temperature from 375 °C to 500 °C, the positive thermal expansion was observed in the XRD reflections of the transformed ZnO.

Similarly, the effect of an increased temperature was observed on the structural features of the ZIF-8 framework. From 30 °C to 300 °C, a gradual loss in diffraction intensity was observed; the sluggish decomposition in the ZIF-8 framework can be attributed to thermal stress. With a further increase in temperature to 325 °C, an incremental loss of long-range order for Miller indices above 13˚ (2θ) was noticed, and a coexistence of ZIF-8 and ZnO reflections was observed. Additionally, the effect of increasing temperature from 30 °C to 325 °C was noted on the FWHM of the XRD peaks. However, the complete transformation of ZIF-8 into ZnO was observed at 350 °C. A further increase in temperature from 325 °C to 500 °C elucidated an improvement in crystallinity and a decrease in peak broadening. Moreover, an increase in temperature from 30 °C to 325 °C showed a slight shift (~0.12˚) in diffraction peaks at higher 2θ (Figure 5.4(e)). This caused a shrinkage in the ZIF-8 framework due to the release of guest molecules. By further increasing the temperature from 400 °C to 800 °C, a shift in the XRD peak was observed by 0.2˚ at higher 2θ angles (Figure 5.4(f)). Detailed analysis revealed that a significant deterioration in XRD intensity occurred for the most dominant plane (0 1 1) by increasing the temperature from 30 °C to 300 °C. This elucidates the weakening of the Zn-N bond, leaving behind the 2-methylimidazolate linker at 350 °C, which is corroborated by previously reported literature [45]. Similarly, the effect of temperature on Raman shifts and the effect of pressure on *in-situ* XRD reflections were reported previously [44, 211–213]. However, in our study, we observed a

complete transformation of the ZIF-8 framework into ZnO at 350 °C, which is significantly higher than in previously reported studies [214].

Table 5.3 summarizes the thermal decomposition processes for all four ZIFs, outlining the sequence of events, including the transition from the pristine ZIF phase to the corresponding metal oxides at four distinct temperatures (T1−T4).

Table 5.3. Sequence of events during the *in-situ* temperature dependent XRD measurements.

S. No.	Material	Temperature 1, T1 (°C)	Temperature 2, T2 (°C)	Temperature 3, T3 (°C)	Temperature 4, T4 (°C)	Comments
1.	ZIF-8	300	-	325	350	Single phase of ZIF-8 exists and rightward peak shift was observed at higher temperatures, implying shrinking frame.
2.	ZIF-7	50	100	375	400	Two phases of ZIF-7 exists and by increasing the temperature, the leftward shift at smaller angle shows thermal expansion of porous structure. On contrary, at higher angles the rightward shift shows thermal stress.
3.	ZIF-71	325	-	350	375	Single phase of ZIF exists. Significant amorphization and peak broadening was observed by increasing a temperature, from 30-325 °C.
4.	ZIF-67	225	-	250	275	Single phase of ZIF-67 exists. Slight shift in ZIF-67 peaks in rightward direction within the range of 0.04-0.12˚, while going from the temperature of 30-225 °C. This small rightward shift, implying a shrinking frame of ZIF-67.

1. T1 is the temperature up to which, good intensity of ZIF reflections exists for phase-I.
2. T2 is the temperature at which another phase of ZIF emerged.
3. T3 is the temperature, where both ZIF and metal oxide phase co-exist, i.e., the transition temperature.
4. T4 is the temperature at which complete degradation of ZIF framework and the emergence of metal oxide phase is clearly visible.

Overall, a detailed temperature-dependent in situ analysis of four different varieties of ZIF particles provides comprehensive insights into phase transitions, thermal degradation, and the transformation of ZIFs into their corresponding metal oxides, which are corroborated by TGA results. A detailed comparison of two similar frameworks (ZIF-8 and ZIF-67) revealed thorough information about their bonding environment. Both ZIF-8 and ZIF-67 use the same organic linker, but the difference lies in the central atom: ZIF-67 contains Co, while the ZIF-8 contains Zn. It has been observed that the thermal decomposition occurs in ZIF-67 and ZIF-8 at 250 °C and 325 °C, respectively. Moreover, it has been reported that the metal-ligand bond in ZIF-8 is more easily broken compared to ZIF-67 under constant heating, due to the higher bond energy of Co-N (2.834 eV) compared to Zn-N (2.075 eV), which can be attributed to the higher electronegativity of Co compared to Zn [215].

On the contrary, *in-situ* temperature dependent XRD results revealed that the ZIF-8 framework deteriorates at a higher temperature (325 °C) compared to ZIF-67 (250 °C), which cannot be understood only by considering the bond energy concept alone. Diving deeper into the realm of the coordination chemistry of Co and Zn with N provides significant insights. It is well known that the outermost shell configuration of Zn ($3d_{10}4s_2$) is completely filled, whereas it is incomplete for Co ($3d_7 4s_2$). This demonstrates that Zn forms a saturated coordination with N, whereas Co forms an unsaturated coordination with N, making it more prone to oxygenation. This results in the faster thermal decomposition of the ZIF-67 at 250 °C. This is also supported by the TGA results. A fundamental understanding of the thermal degradation and phase transition mechanisms of the investigated ZIF-based MOFs was achieved by determining their thermal stability ranges, confirming the stable operation of ZIF-67, ZIF-7, ZIF-71, and ZIF-8 up to 250 °C, 375 °C, 350 °C, and 350 °C, respectively.

5.3. Spectroscopic elucidation of Vibrational modes in ZIF/ZnO and ZIF/ZnO:Cd-based MOF/MO hybrids

The Raman spectra of the 0A sample (ZnO) were measured in a limited spectral range (0 to 900 cm^{-1}), as shown in Figure A3.3(a). ZnO possesses a hexagonal wurtzite structure with no

center of symmetry [216]. Two polar components of A_1 mode– the transverse optical and longitudinal optical components, i.e., A_1(TO) and A_1(LO)–were observed at 381.56 cm^{-1} and 582.9 cm^{-1}, respectively [217]. This mode represents the stretching of Zn-O along the c-axis. Specifically, A_1(TO) and A_1(LO) are associated with lattice vibration symmetry and the electron-phonon interactions, respectively. Additionally, three more vibrational modes (non-polar) were observed for the 0A sample, which were E_2^{low} (98.28 cm^{-1}), E_2^{high} (438.62 cm^{-1}), and the difference mode $E_2^{high} - E_2^{low}$ (331.81 cm^{-1}). All these components vibrate perpendicular to the c-axis. E_2^{low} mode is associated with the low-frequency vibrations of heavier Zn sublattice, whereas the E_2^{high} mode is associated with the high-frequency vibrations of the lighter O sublattice.

Moreover, the Raman spectra of the sample M0 (Cd-doped ZnO) were also measured in the same spectral range of 0 to 900 cm^{-1} (Figure A3.3(b)). By comparing the characteristic modes of samples 0A and M0, it was concluded that there was a rightward shift in vibrational modes towards higher wavenumbers for the Cd-doped ZnO sample compared to the bare ZnO sample. This can be attributed to the incorporation of the Cd atoms into the ZnO lattice, which causes enhanced lattice stress due to the larger dopant atom, as supported by the previously published literature [207]. The Raman spectra of ZnO-based samples (1A, 2A, 3A, and 4A) with four different ZIF coatings such as ZIF-67, ZIF-7, ZIF-71, and ZIF-8, respectively were investigated in detail.
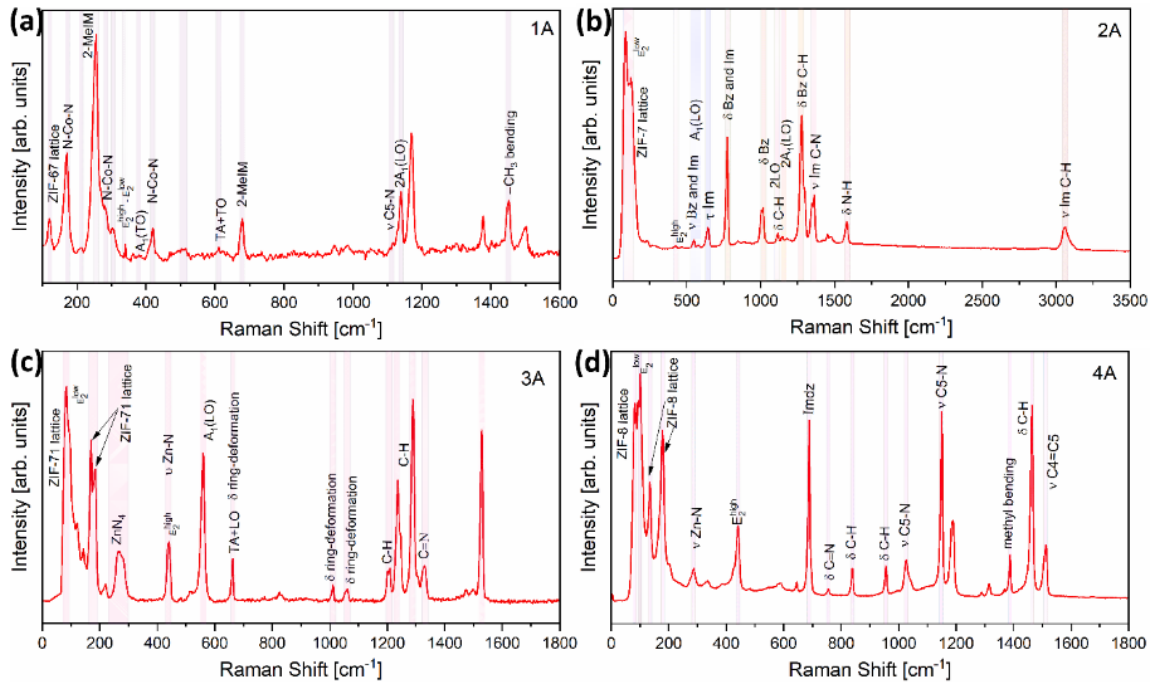

Fig. 5.5. Raman spectra of the ZIF/ZnO samples: (a) 1A, (b) 2A, (c) 3A, and (d) 4A.

In 1A sample, the vibrational modes corresponding to both the ZnO and ZIF-67 frameworks were observed. The vibrational modes corresponding to ZnO, such as E_2^{high}-E_2^{low} (339 cm^{-1}), $A_1(TO)$ (379 cm^{-1}), TA+TO (611 cm^{-1}), and 2A$_1$(LO) (1140 cm^{-1}), were observed (Figure 5.5(a)). These represent the second-order acoustic mode, polar transverse optical, simultaneous interaction of transverse acoustic and transverse optical modes, and the optical overtone mode of the ZnO lattice, respectively [218, 219]. These modes provide insights into the lattice dynamics of the ZnO.

Similarly, the vibrational modes corresponding to ZIF-67 framework were also observed at 120 cm^{-1}, 171 cm^{-1}, 256 cm^{-1}, 281 cm^{-1}, 419 cm^{-1}, 679 cm^{-1}, 1110 cm^{-1}, and 1452 cm^{-1}. These correspond to its lattice vibrations, N-Co-N bending, linker vibrations, N-Co-N bending, N-Co-N bending, linker vibrations, υ-C$_5$-N stretching, and methyl bending vibrations, respectively, as corroborated by previously published results [133]. Diving deeper into the realm provides more insights about the observed vibrational modes. The lattice vibration mode, which is highly significant and provides insights into structural transitions, breathing modes, and related instabilities of the lattice, was observed at 120 cm^{-1}, corroborated with earlier studies [133]. Linker vibrations (2-methylimidazolate) corresponding to ZIF-67 were observed at 256 cm^{-1} and 679 cm^{-1}, in line with prior studies [220]. The vibrational modes corresponding to metal-ligand (N-Co-N) coordination in the ZIF-67 framework were observed at 171 cm^{-1}, 281 cm^{-1}, and 419 cm^{-1}, which is supported by the literature [220]. These vibrational modes are significant, as small shifts in these modes suggests changes in the coordination environment. Moreover, other vibrational modes corresponding to the stretching modes (υ) of the C$_5$-N bond and methyl bending vibrations in the imidazolate ring were observed at 1110 cm^{-1} and 1452 cm^{-1}, respectively, which is also corroborated with earlier research [133]. These modes may affect the adsorption capacity of the framework for guest molecules.

For sample 2A, the characteristic vibrational modes corresponding to ZnO were observed at 99 cm^{-1}, 429 cm^{-1}, 576 cm^{-1}, 1115 cm^{-1}, and 1156 cm^{-1} (Figure 5.5(b)). These modes are associated with the E_2^{low}, E_2^{high}, $A_1(LO)$, 2LO, and 2A$_1(LO)$, respectively [218]. Moreover, vibrational modes corresponding to the ZIF-7 framework were observed at 83.9 cm^{-1}, 121.6 cm^{-1}, 547.3 cm^{-1}, 644.3 cm^{-1}, and 1345 cm^{-1} (Figure 5.5(b)). These are associated with the lattice framework (83.9 cm^{-1} and 121.6 cm^{-1}), and bond stretching in the linker rings (547.3 cm^{-1} and 1345 cm^{-1}) for the benzimidazolate (Bz) and imidazolate (Im) rings, respectively [210, 221]. Phonons associated with the lattice frameworks are sensitive to structural changes and phase changes. Another phonon mode associated with ZIF-7 was observed at 644.3 cm^{-1}, which

corresponds to the torsion mode, involving twisting and rotational movements of ligands bonded with the metal center [210].

Characteristic phonon modes for sample 3A include ZnO and ZIF-71 based modes (Figure 5.5(c)). Vibration modes corresponding to ZnO were observed at 96 cm^{-1}, 439 cm^{-1}, 560 cm^{-1}, and 662 cm^{-1}, which are assigned to E_2^{low}, E_2^{high}, $A_1(LO)$, and $TA+LO$, respectively, corroborated with the prior research [222]. Moreover, the phonon modes corresponding to ZIF-71 framework were observed at 84 cm^{-1}, 169.7 cm^{-1}, 183.9 cm^{-1}, 266.6 cm^{-1}, 422.3 cm^{-1}, 660.9 cm^{-1}, 1011.3 cm^{-1}, 1054.9 cm^{-1}, 1209.4 cm^{-1}, 1236 cm^{-1}, 1288 cm^{-1}, and 1328 cm^{-1}. These modes are associated with the ZIF-71 lattice framework (84 cm^{-1}, 169.7 cm^{-1}, and 183.9 cm^{-1}) [173], tetrahedra configuration of ZnN$_4$ (266.6 cm^{-1}) [173], Zn-N bond stretching (422.3 cm^{-1}) [173], in-plane dichloroimidazolate ring deformation (660.9 cm^{-1}, 1011.3 cm^{-1}, and 1054.9 cm^{-1}) [175], and C-H and C=N bending and stretching vibrations (1209.4 cm^{-1}, 1236 cm^{-1}, 1288 cm^{-1}, and 1328 cm^{-1}) [173, 177, 223], respectively.

Phonon modes corresponding for sample 4A include ZnO- and ZIF-8-based modes (Figure 5.5(d)). For ZnO, the phonon modes were observed at 102 cm^{-1} and 442 cm^{-1}, which can be assigned to non-polar E_2^{low} and E_2^{high} modes, respectively [222]. Moreover, phonon modes corresponding to the ZIF-8 lattice framework were observed at 82 cm^{-1}, 135 cm^{-1}, and 179 cm^{-1}, corroborating prior results [133]. These observed modes can be attributed to the structural changes and phase transitions in the lattice [133]. Other phonon modes at 285 cm^{-1}, 1025 cm^{-1}, 1146 cm^{-1}, and 1512 cm^{-1} can be assigned to the stretching of Zn-N, C$_5$-N, C$_5$-N, and C$_4$=C$_5$ in the imidazolate ring, respectively [130]. Rest of the observed phonon modes correspond to in-plane or out-of-plane bending vibrations. For instance, one of the most intense phonon modes observed at 685 cm^{-1} is assigned to out-of-plane bending vibrations of the imidazolate ring, while in-plane bending modes were observed at 754 cm^{-1}, 839 cm^{-1}, 957 cm^{-1}, and 1463 cm^{-1}, which can be assigned to C=N, C-H, C-H, and C-H vibrational modes in the imidazolate ring, respectively [132]. Moreover, another phonon mode at 1388 cm^{-1} is assigned to methyl bending vibrations [132].

In a similar way, considering an evaluation of another batch of samples (M1 to M4 sample series), where the only difference was Cd incorporation into the ZnO lattice, demonstrated similar phonon modes to the undoped sample series (1A to 4A), as shown in Figure A3.4. Following the analysis of obtained results from both sample series, it can be concluded that a slight shift in phonon modes occurred after Cd incorporation into the ZnO lattice. Specifically considering an example of comparative study of sample M1 and 1A (Figure A3.5(a)), which demonstrated Raman shift spectral range of both samples within a range 0-1600 cm^{-1}. For a better understanding of the

Cd incorporation effect in ZnO, zoomed-in view of the spectrum in a range 1070 cm^{-1} to 1230 cm^{-1} was considered for comparing the Raman shift of vibrational mode *2A$_1$(LO)* (Figure A3.5(b)). A clear shift in the corresponding phonon mode was observed from 1139.87 cm^{-1} to 1141.55 cm^{-1} (a shift of 1.68 cm^{-1} at higher wavenumbers) for sample M1. The observation corroborates published results [207], which attribute this shift to the large ionic radius of the Cd ion compared to the Zn ion, leading to increased lattice stress and providing insights into electron-phonon interactions.

5.4. X-ray photoelectron spectroscopic analysis of surface chemistry in ZIF/ZnO:Cd-based MOF/MO hybrids

To examine the surface chemistry of the developed ZIF-coated Cd-doped ZnO based hybrid structures, XPS measurements (a surface-sensitive technique) were performed on a set of samples (marked as M1−M4). As inferred from the survey scan spectra of the measured samples (Figure 5.6), the photoelectron lines and Auger electron peaks were labelled from the core-levels and LMM levels, respectively.
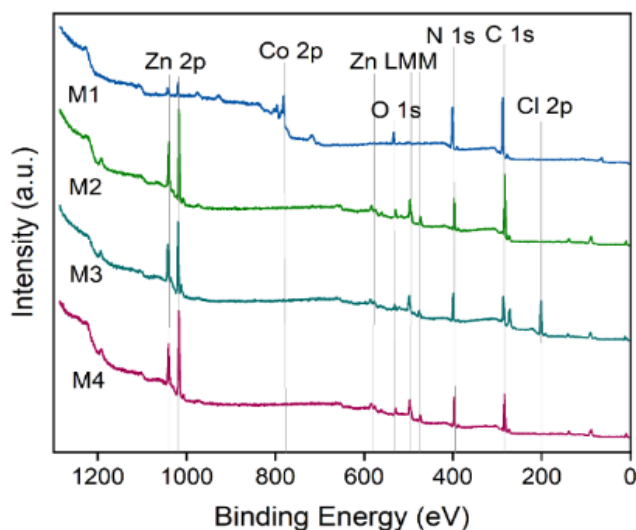

Fig. 5.6. XPS survey spectra of ZIF-coated Cd-doped ZnO samples: M1 (ZIF-67), M2 (ZIF-7), M3 (ZIF-71), and M4 (ZIF-8).

All the sample spectra contain core-levels lines such as C 1s, N 1s, O 1s, and Zn 2p, which confirm the presence of C, N, O, and Zn in each measured sample. Moreover, the presence of Co 2p core-level was observed in sample M1, which corresponds to the central metal of ZIF-67 [224]. In sample M3, the presence of Cl was confirmed by two distinct photoelectron lines from Cl 2s and Cl 2p, which were associated with the presence of the 4,5-dichloroimidazolate linker in the ZIF-71 framework [73]. Overall, the elemental composition of all the measured samples is summarized in Table A3.1. The presence of the Zn 2p core-level in samples M2−M4 was expected due to the presence of the Zn as the central metal in the framework [108, 225, 226]. However, the

presence of Zn 2p core-levels (low intensity) was also observed in sample M1, which is not present in ZIF-67 but originates from the ZnO. This indicates that the ZIF-67 does not cover the whole ZnO surface, which can be attributed to the inhomogeneous thickness and the presence of potential voids due to drop-casting approach. Moreover, the influence of substrate was also observed in sample M3 via a distinct side peak in the Zn 2p signal, which can be associated with the ZnO surface at a different surface charge. The effect of doping (the presence of Cd) was not observed in the survey spectra of any sample due to the low doping concentration in the ZnO.

Furthermore, for a detailed investigation of the surface chemistry of the ZIF coatings, a high-resolution XPS scans were carried out on each sample. The corresponding core-levels of Zn 2p, N 1s, C 1s, and Cl 2p spectra of related samples were fitted (Figure 5.7). Comparing the photoemission peaks of N 1s, O 1s, and C 1s for each sample (and Cl 2p from the sample M3) with the previously reported binding energies reported in Chapter 4 [7], it showed a shift towards higher binding energies, even after applying the charge correction as described in detail in Chapter 2 [6, 7]. Figure A3.6 demonstrates a comparison of the high-resolution XPS spectra of the sample M3 with the corresponding charge corrected high-resolution scans of the CuO-based sample discussed in Chapter 4 [7]. Comparing the explicit core-levels of C 1s and O 1s photoemission peaks of the studied sample with the similarly reported high-resolution scans in Chapter 4, a clear shift in binding energies was observed toward higher binding energies with a shift of $\Delta E_b \approx + 1.9\ \mathbf{eV}$ for the C 1s peak to $\Delta E_b \approx + 1.1\ \mathbf{eV}$ for the O 1s peak. This can be attributed to differential surface charging (i.e., inhomogeneous surface charging of the sample); further analysis of its origin and effects is still under investigation. Regardless of these shifts, we assume that the spectra for the measured samples can still be subjected to consistent analysis because peak shapes allow for a direct comparison. Therefore, the following analysis focuses on the relative positions of the fitted components within a peak rather than absolute binding energy positions. In spite of this, the absolute positions of binding energies of all fitted functions are presented in Table A3.2.

A high-resolution spectrum of the sample M1 demonstrated the individual components of the core-levels of ZIF-67 (Figure 5.7M1a-M1c). The Co 2p core-level spectrum corresponding to the central metal exhibited characteristic spin-orbit splitting into Co $2p_{1/2}$ and Co $2p_{3/2}$ components at binding energies, Co 1' and Co 1, respectively (Figure 5.7M1a). In addition to these main photoemission peaks, two additional peaks were observed, which are attributed to satellite peaks associated with shape-up processes [227]. Moreover, the N 1s core-level spectrum was fitted with a single component N 1 (Figure 5.7M1b). This indicates that the nitrogen in sample M1 exists predominantly in a single bonding environment. It is, therefore, highly likely that this dominant component corresponds to nitrogen atoms originating from the imidazolate linkers of ZIF-67,

which coordinate to cobalt through the nitrogen sites. The C 1s core-level spectrum was also fitted with a single component that was associated with the C-N/C=N bonds of the imidazolate linker. Consequently, the high-resolution C 1s, N 1s, and Co 2p spectra indicate the presence of an intact layer of ZIF-67 on the Cd-doped ZnO surface.

In a similar way, the high-resolution spectra of the sample M2 demonstrated the individual components of the core-levels of ZIF-7 overlayer (Figure 5.7M2a-M2c). In the ZIF-7 framework, the central metal is Zinc, and the corresponding core-level is Zinc is Zn 2p. The spectrum exhibited a characteristic spin-orbit splitting into a Zn $2p_{3/2}$ lower binding energy component (Zn 1) and a Zn $2p_{1/2}$ higher binding energy component (Zn 1'), as shown in Figure 5.7M2a. Since the surface oxidation state of Zn^{2+} ions is the same in both ZIF-7 and ZnO (i.e. +2 oxidation state), it is difficult to distinguish whether the Zn 2p peak arises from ZIF-7 or ZnO [228]. However, as observed in the survey scan of sample M3 (Figure 5.6) and high-resolution spectra in Figure 5.7M3a, the photoelectron line of the Zn 2p core-level of ZnO is located at shifted position compared to the Zn 2p core-level of ZIF-71, which can be attributed to the differential charging. In the case of sample M2, only a single photoelectron line was observed for the Zn 2p core-level; unlike sample M3, the influence of ZnO surface is most likely negligible. To further confirm the presence of ZIF-7, the N 1s and C 1s spectra were analyzed. N 1s spectra in sample M2 exhibited single component (N 1), which is most likely a characteristic of the C-N/C=N bonds of the imidazolate linker (Figure 5.7M2b). Furthermore, the C 1s core-level was deconvoluted into two components, C 1 and C 2: a low binding energy component at higher intensity and relatively a high binding energy component at lower intensity, respectively. These components are attributed to the C-C/C=C bonds and the C-N/C=N bonds in the benzimidazole linkers present in ZIF-7. An observed bond (C/C=C) corresponding to an additional aromatic ring in benzimidazole linker [225], exhibited higher intensity compared to the C-N/C=N bonds, in accordance with the expectations. Thus, the C 1s and N 1s spectra validated the presence of intact ZIF-7 layer on the sample M2 surface.

The high-resolution photoelectron spectrum of the sample M3 demonstrated the individual components of the core-levels (Figure 5.7M3a-M3d). As discussed above, sample M3 exhibited an additional photoelectron line between the binding energies of spin-orbit splitted components Zn $2p_{1/2}$ (Zn 1') and Zn $2p_{3/2}$ (Zn 1) for the Zn 2p core-level corresponding to the ZIF-71 (Figure 5.7M3a). An additional photoelectron line corresponds to the Zn $2p_{1/2}$ signal from the ZnO surface. This shift in binding energy of the Zn 2p of ZnO components is likely due to the differential charging effect caused by pin-holes or non-uniform thickness in the ZIF-71 layer. To further evaluate the ZIF-71 layer on ZnO, other core-levels were investigated in high-resolution spectra. In a similar way to the ZIF-71/CuO:Al as discussed in Chapter 4, the N 1s spectrum exhibited

three components corresponding to three different bonding environments, such as C-N (N 1), H-N (N 2), and Zn-N (N 3) [7, 183], as shown in Figure 5.7M3b. The highest intensity was observed for N 3 component, followed by low intensities of other two components. The highly intense component (N 3) degrades under X-rays, as corroborated by previously reported research [7, 181, 183]. The other two low-intensity components likely originate from fragmented imidazolate linkers due to X-ray degradation [183]. To further examine the possible degradation of ZIF-71, other core-levels, such as Cl 2p and the C 1s spectrum were evaluated. The C 1s spectrum was deconvoluted into three components, including C 1, C2, and C 3 (Figure 5.7M3c).
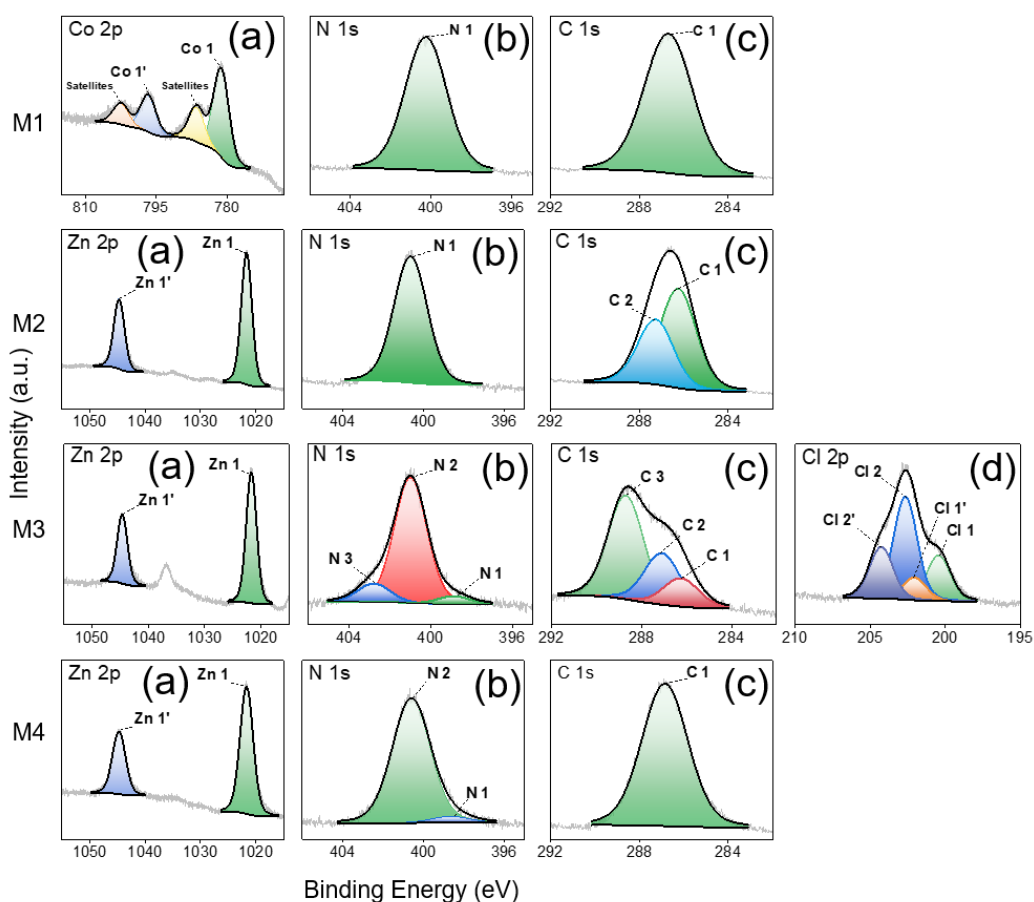

Fig. 5.7. XPS high-resolution spectra of the ZIF-coated Cd-doped ZnO samples: M1a – M1c: ZIF-67, M2a – M2c: ZIF-7, M3a – M3d: ZIF-71, and M4a – M4c: ZIF-8.

Due to differential charging, a shifted C 1 component can be attributed to the carbon species on the ZnO surface, while the C 2 component can be associated with the carbon which is not bonded to the electron withdrawing species, which is most likely arises due to the ZIF-71 degradation. Highly intense component C 2 can be associated with the intact ZIF-71 in non-degraded ZIF-71. Moreover, the interpretation of the Cl 2p core-level spectrum further supports this degradation. As shown in Figure 5.7M3d, two spin-orbit doublets were observed, (Cl 2', Cl

2) and (Cl 1', Cl 1). The observed doublets arose from spin-orbit splitting into Cl $2p_{3/2}$ at higher binding energies and Cl $2p_{1/2}$ at lower binding energies, corroborated with the deconvolutions of the Cl 2p core-level spectrum reported previously on ZIF-71 degradation [7, 181, 183]. The higher binding energy doublet (Cl 2', Cl 2) was attributed to C-Cl bonds characteristic of the intact ZIF-71, whereas the lower binding energy doublet (Cl 1', Cl 1) was assigned to Zn-Cl bonds formed upon framework degradation [7, 181, 183]. These bonding configurations originate from linker fragmentation initiated by Cl radicals from the ZIF-71 linker, as reported previously [183]. It can be summarized that a detailed investigation of high-resolution spectra of the sample M3 strongly elucidated a significant degradation of ZIF-71 and highlighted the influence of the ZnO.

Similarly, the core-level high-resolution XPS spectra of sample M4 demonstrated the individual components of ZIF-8 (Figure 5.7M4a-M4c). Since zinc is the central metal of ZIF-8, the Zn 2p spectrum was split into spin-orbit components, including Zn $2p_{1/2}$ (Zn 1') and Zn $2p_{3/2}$ (Zn 1), as shown in Figure 5.7M4a. As observed in the case of sample M2, the influence of ZnO was negligible, as no additional zinc peaks were observed. The C1 s spectrum was deconvoluted into a single component (C 1), which was assigned to the C-N/C=N bonds present in the imidazolate linkers of ZIF-8 (Figure 5.7M4b). Furthermore, the N 1s spectrum exhibited a dominant N 2 component at higher binding energies and a comparatively low-intensity N 1 component at lower binding energy (Figure 5.7M4c). The N 1 component was most likely associated with uncoordinated 2-methylimidazole linkers, whereas the N 2 component was attributed to nitrogen atoms coordinated to Zn^{2+} in the ZIF-8 structure [6, 139].

Moreover, in addition to the high-resolution spectra presented in Figure 5.7M4a-M4c, the O 1s core-level spectrum was observed for all four measured samples (M1 to M4), as shown in Figure A3.7. The spectra indicated the presence of a small amount of oxygen in all samples, which was attributed to minor surface oxidation and the adsorption of oxygen-containing carbon species resulting from exposure to air during fabrication and storage. Owing to the low oxygen concentration (i.e., less than 4.0 at%, as summarized in Table A1.1), the influence of oxygen on the sensing properties of the measured samples was considered negligible.

5.5. Thermal stability and Electrophysical properties of ZIF/ZnO and ZIF/ZnO:Cd-based MOF/MO hybrids

Thermal stability profile was evaluated for all four ZIFs using TGA test. Figure 5.8 illustrates weight decomposition and temperature ramp-up profiles of the measured samples. This demonstrated the thermal stability of ZIF-67, ZIF-7, ZIF-71, and ZIF-8 particles up to temperatures of 330 °C, 480 °C, 410 °C, and 370 °C, respectively, at which point weight reduction

increased up to 360 °C, 540 °C, 580 °C, and 610 °C. At a final temperature of 800 °C, the remaining mass residues were 34.5%, 34.1%, and 25.6% for ZIF-67, ZIF-7, and ZIF-8, respectively. These values corroborate the theoretical residue masses of 36.3%, 35.4%, and 25.4%, which correspond to the formation of the respective metal oxides: Co_3O_4 for ZIF-67 and ZnO for ZIF-7 and ZIF-8.
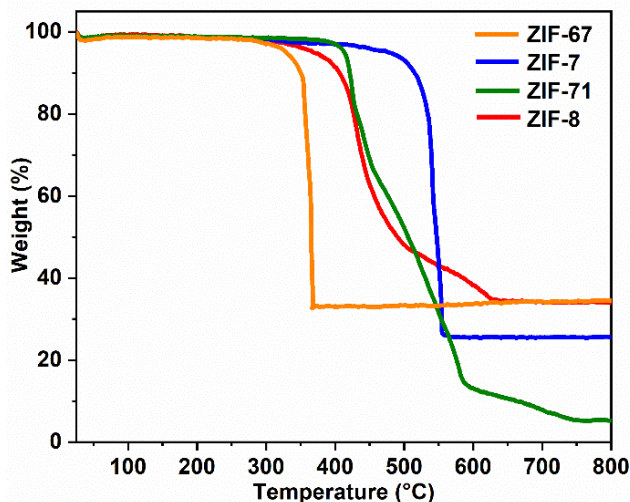

Fig. 5.8. Thermal stability test of different ZIFs: ZIF-n (n=-67, 7, 71, and 8) using TGA analysis.

On the contrary, the residue mass for ZIF-71 was observed to be 5.2%, which is significantly less than the theoretical mass residue of 23.4%. Regardless, the observed weight reduction was still in accordance with the previously reported results [229, 230]. The observed difference between the theoretical and experimental values of weight reduction was attributed to the presence of extra 4,5-dichloroimidazolate linkers bonded to zinc in the ZIF-71 framework [231]. The thermal stability limits of ZIF-n (n=67, 7, 71, and 8) were evaluated by correlating TGA data with temperature dependent *in-situ* XRD patterns. The observed deviations in the upper stability thresholds between the two techniques are likely due to the higher ramping rates in TGA, which contrasts with the prolonged thermal exposure times required for *in-situ* XRD measurements at equivalent temperatures. Consequently, these stability ranges define the permissible operational temperature range for gas sensing applications, ensuring the structural integrity of the ZIF-n frameworks during device operation.

The current-voltage characteristics were evaluated for the measured samples 0A and M0, as shown in Figures A3.8(a) and (b), as well as for two separate batch of samples (1A to 4A) and (M1 to M4), as illustrated in Figures 5.9 and A3.9, respectively.

For all measured samples, the current-voltage characteristics of the Au IDEs and ZIF-coated ZnO exhibited linear-behaviour, except at elevated temperatures (300 °C). At 300 °C, a clear deviation from linearity was observed for sample 0A, which was attributed to the thermal

release of trapped charge carriers from defect states such as interstitial Zinc (Zn_i) and Zinc vacancies (V_{Zn}), as corroborated by published results [144]. Similarly, for the M-series samples (M1 to M4), forward and reverse voltage sweeps revealed an inversted hysterisis in the current-volatge curves for all measured samples (Figure A3.9(a)-(d)). This behaviour was associated with capacitive hysterisis, which indicated that trapped charges slowed down the return path of the current [232, 233]. The extent of this effect was also found to depend on the voltage sweep rate.
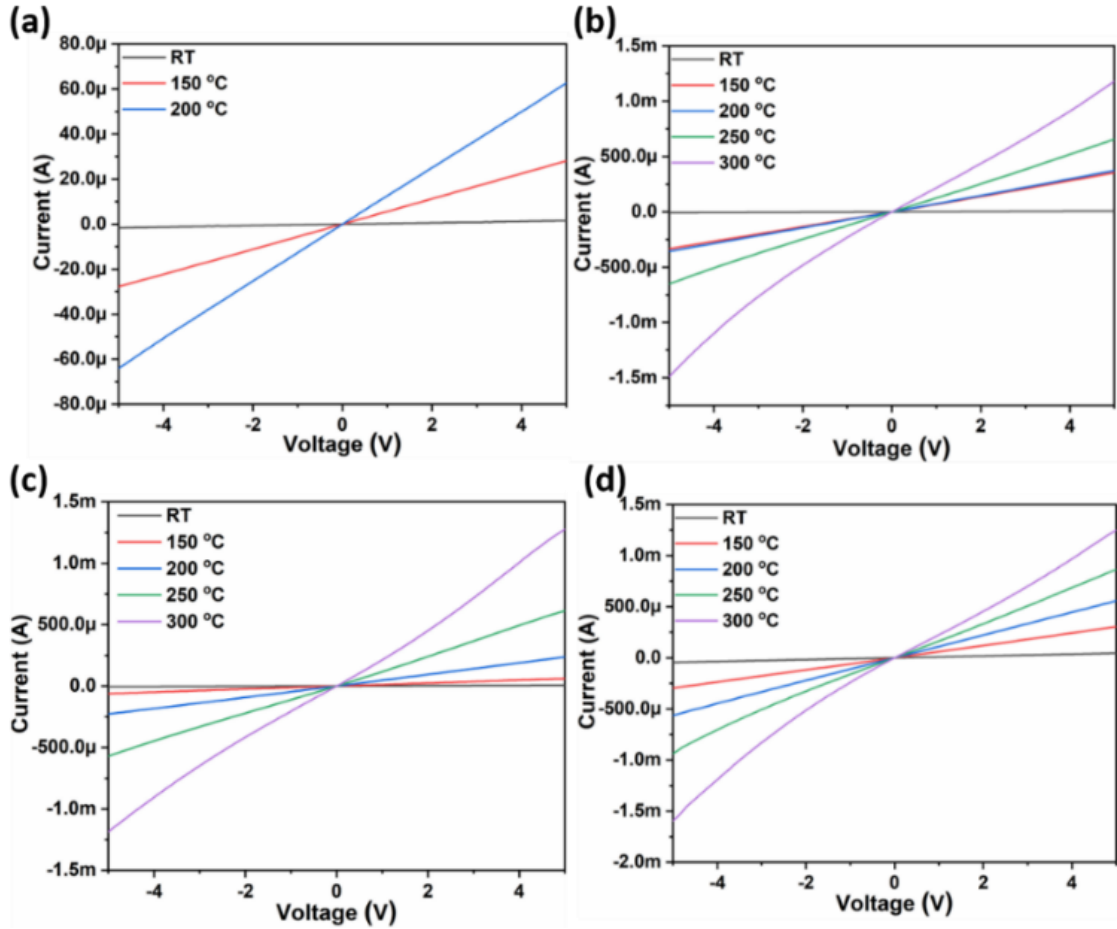

Fig. 5.9. Current-voltage characteristics of (a) 1A, (b) 2A, (c) 3A, and (d) 4A samples at different temperatures.

For sample series A, the Arrhenius plot derived from the current-volatge characteristics is illustrated in Figure A3.10(a). Similarly, for sample series M, the corresponding current-volatge characteristics are illustrated in Figure A3.10(b). In the Arrhenius equation, the relationship between the temperature and the corresponding current is established using the concept of activation energy (E_a) (Equation (5.1)).

$$I(T) = I_o e^{\frac{-E_a}{k_B T}} \tag{5.1}$$

or reorganized form of Equation 5.1 is represented in Equation 5.2,

$$\ln \left(I(T) \right) = \left(\frac{-E_a}{k_B} \times \frac{1}{T} \right) + \ln I_o \tag{5.2}$$

where $I(T)$ is the measured current at temperature T, I_0 is the pre-exponent factor, and k_B is the Boltzmann's constant (8.617 eV/K).

Equation 5.2 is in the form of straight-line equation, where E_a/k_B represents the slope of straight line, and I_o is the intercept of vertical axis.

The slopes and activation energies of all measured samples in series A and M were extracted using linear regression of the data in Figure A3.11(a) and (b). The results of these analyses and the corresponding calculations are summarized in Table A3.3.

As summarized in Table A3, the extracted activation energies for all tested samples in both the A series and M series were in good agreement with previously reported values associated with defect levels in ZnO [234]. Minor variations in activation energies among the samples were observed due to the presence of different ZIFs on ZnO. For sample series A, the calculated positions of the defect levels are listed in Table A3.3 and well-illustrated in Figure A3.11(a). The associated defects for samples 1A, 2A, and 4A were identified as interstitial zinc (Zn_i), while the associated defect level for sample 3A was determined to be zinc vacancies (V_{Zn}).

Similarly for sample series M, the defect levels associated with samples M1, M3, and M4 were intrinsic zinc vacancies (V_{Zn}), while the defect levels associated with sample M2 was determined to be interstitial Zn (Zn_i) level (Figure A3.11(b)). The calculated values for sample series M, as shown in Table A3.3, corroborate well with the published results [235–237].

5.6. Analysis of gas sensing performance in ZIF/ZnO and ZIF/ZnO:Cd-based MOF/MO hybrids

The gas sensing properties of the reference samples (0A and M0) were evaluated in the temperature range of 20 °C to 300 °C (Figure A3.12(a) and (b)). In the case of 0A sample, the maximum sensing responses were observed for the alcohol series, including n-butanol and 2-propanol at low temperatures (200 °C and 250 °C) and ethanol at higher temperatures (300 °C). The obtained results for the ZnO structures toward alcohol series are well-corroborated with published literature [238–240].

Generally, the selective detection of homologous alcohol series using single sensor involves a variety of challenges; though, the developed ZnO structures exhibited the possibility of

employing temperature modulation. For example, a reported study on selective detection of homologous alcohols using three ZnO-based gas sensors by modulating the operating temperature attributed this behavior to the temperature-dependent regulation of oxygen vacancy concentration [241].

Cd doping was observed to enhance hydrogen sensing performance, as evidenced in previous studies [242]. At a lower operating temperature of 150˚C, M0 sample exhibited the highest sensing response to n-butanol (~3.7%), exceeding the responses toward the other investigated analytes. This selective response is consistent with earlier reports showing that ZnO nanoparticles preferentially detect *n*-butanol over ethanol, 2-propanol, and acetone [243].

At an elevated operating temperature of 300 °C, the sensor exhibited a maximum response toward hydrogen gas (~15%). Similar enhancements in hydrogen sensitivity at higher temperatures have been widely reported in the literature [244–246]. The pronounced *n*-butanol sensitivity at a low temperature (150°C), together with the substantially enhanced hydrogen response at temperatures ≥150 °C, can be ascribed to Cd-induced modifications of the ZnO surface chemistry and defect structure. These interpretations are further corroborated by previously reported studies [242, 247].

In ZIFs, adsorption of target molecules typically occurs via pore channels or specific active sites. In the case of ZIF-67, however, the lack of functional groups restricts adsorption exclusively to its pore architecture. The ZIF-67 framework contains two distinct diffusion pathways defined by its window apertures: a four-membered ring (4R) and a six-membered ring (6R). The corresponding pore window sizes are approximately 0.8 Å for the 4R aperture and 3.4 Å for the 6R aperture, as depicted in Figure 5.10.

The passage of target molecules through the window apertures of ZIFs involves interactions between the target molecules and the walls of the window aperture, which can be analyzed using Derouane's theory [250]. Using this theory, an effective Van der Waals physisorption energy can be described by Equation 5.3 [250]:

$$F(f) = -\left(\frac{k}{4r^3}\right)\left(1 - \frac{1}{2f}\right)^{-3} \tag{5.3}$$

where *F(f)* represents the Van der Waals physisorption energy between a framework pore and target molecule, k represents a molecular constant which is directly related to the polarizability of the adsorbate, r represents an effective interaction distance or adsorption distance between the pore wall and the center of molecule, *f (r/s)* represents the curvature factor, and s represents the pore window size.
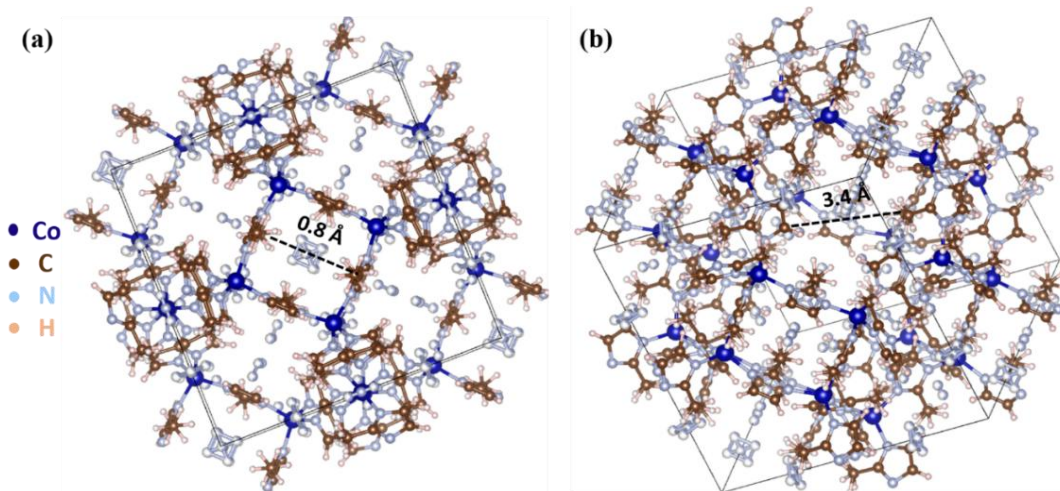
Fig. 5.10. Pore window size of ZIF-67 framework through two different membered rings (a) four-membered (4R) ring and (b) six-membered (6R) ring. Crystal structure of ZIF-67 visualized using VESTA [248]. Adapted with permission from ref [249]. Copyright 2008 Royal Society of Chemistry.

Using this model, three cases arose depending on the target molecule's size. If the molecular size of the target analyte (r) is much smaller than the size of pore window (s), the effective van der Waals interaction reaches zero. In the second case, if the molecular size becomes comparable to the pore window size, the van der Waals interaction is maximized, attaining values up to eight times higher than the first case (when s=0). In the third scenario, when the molecular size exceeds the pore window size, a substantial energy barrier is formed, preventing the molecule from passing through the pores. Consequently, optimal adsorption occurs when the molecular size closely matches the pore window dimensions.

The passage of tested molecules through the window apertures (either the 4R or 6R apertures of ZIF-67) depends on the kinetic diameters of the investigated molecules, including acetone (4.6 Å) [195], n-butanol (5.0 Å) [168], hydrogen (2.89 Å) [151], ethanol (4.53 Å) [168], and 2-propanol (4.7 Å) [167]. The passage through 4R aperture, the pore window size is approximately 0.8 Å, which is too small to allow the diffusion of any tested analytes. Similarly, the passage through 6R aperture of window size (3.4 Å), all analyte molecules are larger than the pore opening, with the exception of hydrogen. Temperature-dependent *in situ* XRD results indicated that the phase transformation from ZIF-67 to Co_3O_4 initiated at 250°C, where both phases coexist. At temperatures below 250°C, the sensing behaviour was dominated by ZIF-67, leading to the exclusion of larger molecules while permitting the diffusion of smaller species such as hydrogen. However, at temperatures ≥250 °C, it was observed that the ZIF-67 transformed into Co_3O_4, resulting in the formation of a Co_3O_4/ZnO p-n heterostructure. Sample 1A exhibited a

substantial increase in sensitivity to ethanol at 250 °C compared to sample 0A, attributed to the p-n heterostructure effect. These results corroborate the reported literature [251]. The p-n heterostructure behaviour included the localized transfer of electrons from ZnO to Co_3O_4 and transfer of holes from Co_3O_4 to ZnO at the particle-film interface—driven by the higher Fermi level of ZnO relative to Co_3O_4—until equilibrium is established. According to the chemisorption model, since the ethanol sensing was observed at 250 °C (a temperature where monoionic oxygen species dominate and primarily adsorb on the surface), a hole accumulation layer formed on Co_3O_4 and an electron depletion layer on the ZnO surface, as shown in Figure A3.14(a). Upon exposure to ethanol, trapped electrons in the adsorbed oxygen ionic species were released back into the conduction band. This process reduces the thickness of the accumulation layer and depletion layers on Co_3O_4 and ZnO, respectively (Figure A3.14(b)). As a result, the electrical resistance of the heterostructure increased after exposure to ethanol. The heterostructure exhibited a higher sensing response to ethanol compared to bare ZnO. Therefore, a selective detection of ethanol was achieved at 250 °C (Figure A3.13(a)). The dynamic electrical resistance variations and the corresponding gas-sensing response of sample 1A upon ethanol exposure at 250 °C presented in Figure A3.15(a) and Figure A17(b), respectively.

Similarly, for the case of series-M, sample M1 exhibited the highest sensing responses for n-butanol and 2-propanol at 300 °C (Figure A3.16(a)). This behaviour can be attributed to Cd doping, which enhances electron affinity at this operating temperature, thereby enabling selectivity of these analytes. Prior studies have similarly reported that Cd doping in ZnO improves n-butanol sensing performance [247]. The dynamic sensing responses for sample M1 to n-butanol and 2-propanol at 300 °C, as illustrated in Figure A3.17(a) and (b), respectively.

Another important flexible ZIF (ZIF-7) that undergoes phase transition due to its interactions with adsorbates, attributed to the gate-opening effect. This flexibility arises from the rotational motion of the benzene rings in the benzimidazole linkers, which enables the framework to switch between a closed phase (~3 Å) and an open phase (~5 Å) to accommodate guest molecule [252]. The diffusion of guest species within ZIF-7 is governed by both their kinetic diameter and their interactions with the pore aperture before its entry. Even at equilibrium, diffusion remains dependent on the molecular size and the framework-guest interactions. Subsequently, due to small kinetic diameter of hydrogen, it exhibited the highest diffusion coefficient among the investigated analytes [253], leading to the high hydrogen selectivity of ZIF-7 observed in Figure A3.13(b). The more symmetric state of ZIF-7, characterized by a larger accessible pore volume, is favoured at higher temperatures, as corroborated with the prior research [254]. At higher temperatures (300°C), sensing responses toward n-butanol and ethanol were observed, attributed to dipolar

interactions between the hydrogen atomic sites of the alcohol molecules and the nitrogen sites of the benzimidazole linkers, reported in prior research [255]. For sample M2, the gas sensing performance was evaluated, as illustrated in (Figure A3.16(b)).

The gas sensing results were evaluated for samples M3 and 3A, these samples exhibited hydrogen selectivity attributed to the ZIF-71 coating and the Cd-doping effect (Figures A3.13(c) and A3.16(c)). This resulted in the elimination of interference effects from other analytes, which was consistent with prior research [242, 256].

For the case of sample 4A and M4, they exhibited high hydrogen sensing response even at lower temperatures, attributed to the molecular sieving effect through the ZIF-8 framework (Figure A3.13(d)). However, among the VOCs, the studied samples exhibited n-butanol selectivity compared to ethanol or 2-propanol (Figure A3.16(d)). This can be attributed to the abundance of non-polar aliphatic sites in ZIF-8, making it more favourable for the adsorption of the longer carbon chain of n-butanol compared to other interfering VOCs [255], including ethanol or 2-propanol. The obtained results are supported by Grand Canonical Monte Carlo and Molecular Dynamics simulations, which demonstrate that alcohols with longer carbon chains are more readily adsorbed on ZIF-8, due to its hydrophobic nature. Prior research has demonstrated that apolar molecules like n-butanol can easily adsorbed on ZIF-8, while 2-propanol adsorption is hindered by its molecular geometry [257].

5.7. Proposed sensing model: Synergistic effects and Electronic modulation in ZIF/ZnO and ZIF/ZnO:Cd-based MOF/MO hybrids

The sensing mechanism of the chemisresistive sensors toward the tested analytes is explained using the adsorption-desorption model, which consists of three processes: sorption, diffusion, and desorption. The role of ZIF particles overlayer on ZnO or Cd-doped ZnO played a significant role in all three processes. The interaction of the tested analytes with the ZIF pore walls varied depending on their physicochemical properties, as discussed in the section 5.6.

A trend of adsorption of tested analytes on ZIFs greatly influenced the electrical properties of the hybrid material [197]. Moreover, the diffusion of the adsorbed analytes through ZIFs, their interaction with the pore walls, and their behaviour at the hybrid material (ZIF/ZnO) interface modulate the electrical properties. In case of hybrid materials, multiple factors affect the electrical properties, including molecular sieving, affinity for functional groups, polarity differences, diffusion coefficients, and gate-opening mechanisms due to aromatic ring rotation, among others.

Following the adsorption process, the diffusion of the sorbed analyte through the pore channels is greatly dependent on operating conditions and their geometrical configuration. The

determination of the flow regime was carried out at a temperature (T=300 °C) and atmospheric pressure (p). To evaluate this, the Knudsen number (K) was calculated, using an Equation 3.16 from Chapter 3.

Comparing the concentration of the tested analytes (100 ppm) with that of the background air, the effect of analyte concentration was neglected due to its relatively small concentration. As a result, the background air dominated the gas mixture, rendering the mean free path (λ) of the tested analytes independent of their small mole fraction. Consequently, the λ of the tested analytes depended solely on differences in their respective collision diameters. Using this information, the λ of the tested analytes was determined to be 52 nm, 63 nm, and 148 nm for n-butanol, ethanol, and hydrogen, respectively, at 300 °C.

For the classification of the flow regime, the Knudsen number (K) was determined for the tested sensor in the presence of each tested analyte under particular operational conditions and categorized into three regimes: the Knudsen diffusion regime, the transitional diffusion regime, and the molecular diffusion regime, using the Equation 3.16, mentioned in Chapter 3.

The pore aperture sizes of ZIF-67 (t_{11}), ZIF-7 (t_{22}), ZIF-71 (t_{33}), and ZIF-8 (t_{44}) were represented by t_{kl}. The calculated Knudsen number (K) for all the studied ZIFs toward the tested analytes, including n-butanol, ethanol, and hydrogen, are summarized in Table 5.4.

Table 5.4. Knudsen number (K) of tested analytes for all the studied ZIFs.

ZIF names	Hydrogen	N-butanol	Ethanol
ZIF-67	435	153	185
ZIF-7	493-296	173-104	210-126
ZIF-71	290	102	124
ZIF-8	435	153	185

Using the quantitative analysis in Table 5.4, it was concluded that the value of K is greater than 10 in all cases, which clearly indicated the dominance of Knudsen diffusion regime. ZIF particles almost completely cover the whole ZnO film, however, it was not continuous as observed in SEM images. In addition, the ZIF layers may contain pinhole defects, allowing gas transport through grain boundaries and other structural imperfections, which may locally decrease the value of K. Overall, transport of n-butanol, hydrogen, and ethanol through the studied ZIFs predominantly occurred via Knudsen diffusion. Nevertheless, localized contributions from molecular and transitional diffusion could occur at grain boundaries and defect sites.

The reference material used was ZnO, which is an n-type semiconductor due to the presence of intrinsic defects that generate donor states just below the conduction band [258]. Upon exposure of the ZnO surface to atmospheric oxygen molecules, electrons from the conduction band

are trapped, and the adsorbed oxygen molecules were transformed into a variety of oxygen ionic species, including molecular ionic, monoionic atomic, and bionic species, depending on the temperature, as illustrated in Equations 5.4 to 5.7 [259].

$$O_{2\,(gas)} \leftrightarrow O_{2(ads.)} \tag{5.4}$$

$$O_{2(ads.)} + e^- \leftrightarrow O_{2(ads.)}^- \tag{5.5}$$

$$O_{2(ads.)} + 2e^- \leftrightarrow 2O_{(ads.)}^- \tag{5.6}$$

$$O_{(ads.)}^- + e^- \leftrightarrow O_{(ads.)}^{2-} \tag{5.7}$$

where $O_{2(gas)}$, $O_{2(ads.)}$, and e^- represent the oxygen gaseous molecule in the atmosphere, adsorbed oxygen molecule on the sensing surface, and transferred electron from the conduction band of the ZnO, respectively.

It was observed that, for all studied samples, sensing responses occured in the temperature range of 150-300 °C, which clearly indicated the dominance of monoionic oxygen species (O^-) [259]. The trapping of electrons from the ZnO conduction band by the adsorbed monoionic oxygen species resulted in an increase in the surface work function and upward band bending in ZnO (Figure 5.11). This, in turn, led to an increase in the electrical resistance of ZnO surface.
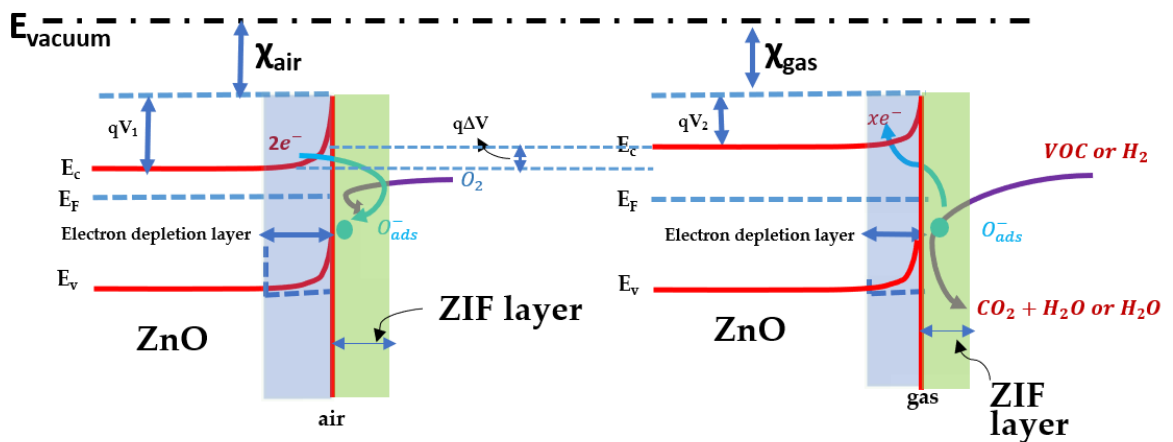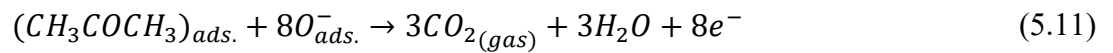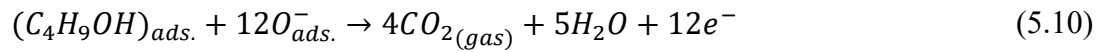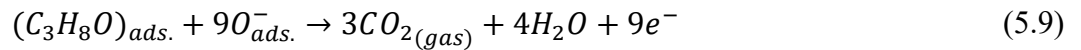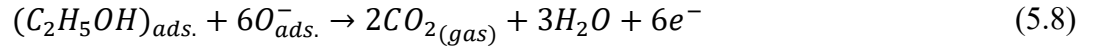

Fig. 5.11. Schematic of the gas sensing mechanism of ZIF-coated ZnO, illustrating energy band diagrams upon exposure to reducing gases (VOCs and H₂).

Following the exposure of reducing gases (n-butanol, ethanol, 2-propanol, hydrogen, and acetone), the trapped electrons were released back into the ZnO conduction band (Equations 5.8 to 5.12) [9, 260–262] by reacting with the adsorbed monoionic oxygen species, which contributed to a decrease in the electrical resistance of ZnO. This led to a reduction in the upward band bending ($q\Delta V = qV_1 - qV_2$), and the EDL becomes thinner [263], as illustrated in Figure 5.11.

$$(C_2H_5OH)_{ads.} + 6O^-_{ads.} \rightarrow 2CO_{2(gas)} + 3H_2O + 6e^- \tag{5.8}$$

$$(C_3H_8O)_{ads.} + 9O^-_{ads.} \rightarrow 3CO_{2(gas)} + 4H_2O + 9e^- \tag{5.9}$$

$$(C_4H_9OH)_{ads.} + 12O^-_{ads.} \rightarrow 4CO_{2(gas)} + 5H_2O + 12e^- \tag{5.10}$$

$$(CH_3COCH_3)_{ads.} + 8O^-_{ads.} \rightarrow 3CO_{2(gas)} + 3H_2O + 8e^- \tag{5.11}$$

$$(H_2)_{ads.} + O^-_{ads.} \rightarrow H_2O + e^- \tag{5.12}$$

where $(C_2H_5OH)_{ads.}$, $(C_3H_8O)_{ads.}$, $(C_4H_9OH)_{ads.}$, $(CH_3COCH_3)_{ads.}$, $CO_{2(gas)}$, $H_{2(ads.)}$, and H_2O, represent adsorbed ethanol, 2-propanol, n-butanol, acetone, released carbon dioxide, adsorbed hydrogen, and released water molecules, respectively.

5.8. Conclusion of Chapter 5

Using XRD, a preferential growth of ZnO was observed along the c-axis corresponding to (0 0 2) plane; meanwhile, for the various ZIF-n (n= 67, 7, 71, and 8), the most prominent XRD reflections were observed along the family of planes {0 1 1}. By employing the Scherrer equation on the most prominent XRD reflections, crystallite sizes were determined to be approximately 35.67 nm, 42.30 nm, 61.97 nm, and 37.50 nm for ZIF-67, ZIF-7, ZIF-71, and ZIF-8, respectively.

Moreover, temperature-dependent in situ XRD measurements on all ZIFs from a temperature of 30 °C to ≥500 °C provided comprehensive insights into the phase transitions, thermal degradation, and their transformation into respective metal oxides (ZnO or Co_3O_4), which were well-corroborated with the TGA results. Specifically, for ZIF-67, increasing the temperature from 30 °C to 225 °C resulted in a slight shift of the XRD reflections by 0.04˚ to 0.12˚ toward higher 2θ values, which was attributed to the shrinkage of the ZIF-67 framework. In the case of ZIF-7, a transformation of ZIF-framework from the open phase (phase I) to the closed phase (phase

II) due to the release of solvent molecules. Additionally, a slight shift in XRD reflections from 9.47˚ to 9.04˚ toward lower 2θ was observed when increasing the temperature from 30 °C to 350 °C, which was attributed to the thermal expansion of the ZIF-7 framework. In a similar manner, for ZIF-8 framework, increasing the temperature from 30 °C to 325 °C resulted in a slight shift in XRD reflections by 0.12˚ toward higher 2θ and a deterioration in the intensity of the most prominent XRD peak (0 1 1), which can be attributed to the degradation of the Zn-N bond.

Furthermore, distribution of ZIF particles and morphology analysis provided insights about the dodecahedral morphology of the ZIF particles covering almost whole surface of the ZnO or Cd-doped ZnO. EDX analysis of the Cd-doped ZnO structures confirmed the presence of Cd in Zn sublattice, which was also supported by the shift in XRD reflections toward lower 2θ following Cd incorporation.

To support this claim, a shift in the Raman peak was observed toward higher wavenumbers by 1.68 cm^{-1} after Cd doping, which was attributed to increased lattice stress. Additionally, distinct phonon modes─including methyl bending, N─(Co or Zn)─N stretching, linker stretching and torsional modes (τ), linker bending, and δ-ring deformation─ were identified in the hybrid structures.

XPS analysis provided detailed information on the surface chemistry of the hybrid structures and confirmed the structural intactness of the ZIFs on the ZnO surface. In addition, it revealed the extent of degradation of the ZIF-71 framework under X-ray exposure due to the presence of special functional sites (-Cl). By employing forward and reverse voltage sweeps during current-voltage characteristics measurements, an inverted hysteresis was observed. This behaviour corresponds to capacitive hysteresis and was attributed to charge traps, which slowed the return path.

Gas sensing results of the developed hybrid sensors exhibited appreciable selectivity to ethanol (sample 1A), 2-propanol and n-butanol (samples M1, 1A, 4A, M2, and M4), and hydrogen (samples 2A, 3A, 4A, M2, M3, and M4). The effect of Cd doping was observed in the gas sensing results; samples in the M-series exhibited selectivity toward n-butanol and hydrogen at 150 °C and 300 °C, respectively. The transport mechanism demonstrated that the passage of tested analytes predominantly followed the Knudsen diffusion regime; however, due to the presence of pinholes and grain boundaries, molecular and transitional flows also contributed in localized regions.

GENERAL CONCLUSIONS AND RECOMMENDATIONS

The proposed research aimed to develop hybrid structures, namely nanostructured and microstructured Metal-Organic Framework (MOF)-metal oxide systems, based on ZIF/CuO:Al or ZIF/ZnO for the enhancement of functionality. They were accompanied by an advanced characterization for their structural and chemical analysis, in order to correlate the physicochemical properties with sensing mechanisms under adverse environmental conditions. Through the synergistic integration of ZIF metal-organic networks with doped metal oxides, hybrid sensors with high thermal stability and superior performance of selective detection of hydrogen and VOCs have been developed, demonstrating a remarkable potential for environmental monitoring under extreme humidity conditions. Thus, based on the obtained results, the following general conclusions can be formulated:

1. A fundamental understanding of the thermal degradation and phase transition mechanisms of the investigated ZIF-based MOFs was achieved by determining their thermal stability ranges, confirming stable operations of ZIF-67, ZIF-7, ZIF-71, and ZIF-8 up to 250 °C, 375 °C, 350 °C, and 350 °C, respectively [6-7] [274].

2. The ZIF-8/CuO:Al-based hybrid sensor exhibited well defined structural integrity, high surface area, and stable morphology, with strong confirmation from XRD, SEM, XPS, Raman, and BET analysis. Thermal stability up to 380 °C and selective gas sensing performance, particularly for hydrogen and n-butanol, highlight their application potential [6].

3. The ZIF-71/CuO:Al-based MOF/MO hybrid sensor demonstrated a stable monoclinic CuO structure with uniform ZIF-71 deposition, as confirmed by XRD, SEM, XPS, and Raman analysis. The films exhibited nanoscale crystallite size (approx. 57 nm) with larger dimensions (500-700 nm), reflecting coherent growth and surface uniformity [7].

4. ZIFs/ZnO-based study confirmed preferential crystallographic orientations and nanoscale crystallite sizes of all ZIF-n (n= 67, 7, 71, and 8), with *in-situ* temperature dependent XRD and TGA revealing thermal stability and phase transformations into corresponding oxides. Raman spectroscopy provided detailed vibrational insights, while Cd doping in ZnO induced lattice stress evidenced by Raman peak shifts. Sequential gas-sensing demonstrated selective responses toward alcohols and hydrogen gas, recommending further optimization of doping levels and film architecture for enhanced sensitivity and long-term stability [6-7] [274].

5. The ZIF-8/CuO:Al-based MOF/MO hybrid sensor exhibited appreciable sensitivity (75%) for 100 ppm hydrogen gas even at a high RH of 81%, enabling its application under adverse conditions. Furthermore, a very low detection limit of 402 ppb was achieved, which is advantageous for various applications, including the detection of very small amount of hydrogen leaks [6, 8].

6. The ZIF-8/CuO:Al-based MOF/MO hybrid sensor exhibited appreciable selectivity to hydrogen (>4 times) over other tested analytes such as acetone, 2-propanol, n-butanol, and ethanol at higher temperature (350 °C) [6, 8].

7. ZIF-71/CuO:Al-based MOF/MO hybrid sensor exhibited the selectivity for n-butanol at 200 °C, which was approximately four times higher than hydrogen gas and about five times higher than acetone during the initial measurements [7].

8. Dual gas sensing (n-butanol and hydrogen) at different operating temperatures (200 °C and 250°C) exhibited by the ZIF-71/CuO:Al can be attributed to the synergistic effect of ZIF-71 and CuO:Al. At lower temperatures (200 °C), n-butanol selectivity over other tested analytes was observed due to the high polarizability of n-butanol as compared to acetone, it affects the strength of interaction of tested analyte with ZIF-71 framework. At higher temperatures, hydrogen can easily diffuse through pores and shows higher selectivity at 250 °C. Further optimization of coating thickness, and device-label testing are recommended to enhance practical sensing performance [7].

Based on the obtained general conclusions, following recommendations can be formulated:

1. In order to prevent thermal degradation and phase transitions in ZIF-based MOFs and MOF-metal oxide hybrid structures, operation must be maintained below their respective thermal stability limits: 250 °C (ZIF-67), 375 °C (ZIF-7), 350 °C (ZIF-7), and 350 °C (ZIF-8).

2. It is recommended to use simple and cost-effective techniques, such as SCS and microdrop-casting to obtain hybrid structures of ZIF/ZnO or ZIF/CuO.

3. It is recommended to comprehensively characterize material and other physicochemical properties of ZIF-based hybrid structures for their employment in adverse environmental conditions. Thermal test and sorption tests of ZIF-8 particles exhibited its thermal stability up to 380 °C and microporous structure, which is advantageous for sensing applications. XPS analysis revealed an intactness of ZIF-8 layer on CuO:Al film, which confirmed a successful development of hybrid structures.

4. Hydrophobic nature and thermal stability of ZIF-8 retains its structural framework in adverse environmental conditions. ZIF-8/CuO:Al-based hybrid sensor exhibited appreciable sensitivity (75%) toward 100 ppm hydrogen even at a RH of 81% at 350 °C. This configuration of hybrid sensor exhibited >4 times hydrogen selectivity compared to other tested analytes, including VOCs (ethanol, acetone, 2-propanol, and n-butanol).

5. It is recommended that uniformly complete coverage of ZIF-71 or ZIF-8 particles on ZnO or CuO enables the employment of hybrid structures in sensing applications. ZIF-71/CuO:Al-based MOF/MO hybrid sensor exhibited four-times higher sensitivity for n-butanol compared to hydrogen and five-times compared to acetone at 200 °C. At higher temperature (250 °C), hydrogen selectivity was observed for ZIF-71/CuO:Al-based hybrid sensor.

6. It is recommended to tune the selectivity of alcohol series using an appropriate doping (Cd) in ZIF-67/ZnO based hybrid sensors. ZIF-67/ZnO exhibited higher sensitivity (>1.5 times) for ethanol compared to other alcohols, but in case of ZIF-67/ZnO:Cd hybrid structures, highest sensitivity was observed for n-butanol or 2-propanol (>2.5 times) at 300 °C.

BIBLIOGRAPHY

1. NGUYEN, L.H.T., MIRZAEI, A., KIM, J.Y., PHAN, T.B., TRAN, L.D., WU, K.C.W., KIM, H.W., KIM, S.S., DOAN, T.L.H.: Advancements in MOF-based resistive gas sensors: synthesis methods and applications for toxic gas detection. Nanoscale Horiz. 10, 1025–1053 (2025). https://doi.org/10.1039/d4nh00662c

2. Nobel Foundation: Press release of Nobel prize in Chemistry 2025. (2025)

3. GALLEGO, E., PERALES, J.F., CALAF, J.M.: Continuous monitoring of volatile organic compounds through sensorization. Automatic sampling during pollution/odour/nuisance episodic events. Atmos. Environ. 299, 119657 (2023). https://doi.org/https://doi.org/10.1016/j.atmosenv.2023.119657

4. POSCHMANN, M.P.M., SIEBERT, L., LUPAN, C., LUPAN, O., SCHÜTT, F., ADELUNG, R., STOCK, N.: Surface Conversion of ZnO Tetrapods Produces Pinhole-Free ZIF-8 Layers for Selective and Sensitive H2 Sensing Even in Pure Methane. ACS Appl. Mater. Interfaces. 15, 38674–38681 (2023). https://doi.org/10.1021/acsami.3c06317

5. NAGPAL, R., ABABII, N., LUPAN, O.: Comprehensive Advances in Gas Sensing: Mechanisms, Material Innovations, and Applications in Environmental and Health Monitoring. Materials Today Electronics. 100192 (2025). https://doi.org/https://doi.org/10.1016/j.mtelec.2025.100192

6. NAGPAL, R., SUGIHARA, M., MAGARIU, N., TJARDTS, T., MELING-LIZARDE, N., STRUNSKUS, T., AMERI, T., AMELOOT, R., ADELUNG, R., LUPAN, O.: Humidity-tolerant selective sensing of hydrogen and n-butanol using ZIF-8 coated CuO:Al film. Mater. Chem. Front. 9, 3425–3442 (2025). https://doi.org/10.1039/D5QM00565E

7. NAGPAL, R., SUGIHARA, M., LUPAN, C., TJARDTS, T., MELING-LIZARDE, N., STRUNSKUS, T., QIU, H., ADELUNG, R., AMELOOT, R., LUPAN, O.: ZIF-71-Coated CuO:Al with Enhanced Gas-Sensing Performance for n-Butanol and Hydrogen. ACS Appl. Electron. Mater. 7, 10198–10215 (2025). https://doi.org/10.1021/acsaelm.5c01659

8. LUPAN, O., NAGPAL, R., LITRA, D., BRINZA, M., SUGIHARA, M., AMELOOT, R., RAILEAN, S., AMERI, T., ADELUNG, R., SCHRÖDER, S., FAUPEL, F.: Hybrid Nanomaterials for Biomedical Sensors. In: Sontea, V., Tiginyanu, I., and Railean, S. (eds.) 7th International Conference on Nanotechnologies and Biomedical Engineering. pp. 162–176. Springer Nature Switzerland, Cham (2025)

9. NAGPAL, R., LUPAN, C., BÎRNAZ, A., SEREACOV, A., GREVE, E., GRONENBERG, M., SIEBERT, L., ADELUNG, R., LUPAN, O.: Multifunctional Three-in-One Sensor on t-ZnO for Ultraviolet and VOC Sensing for Bioengineering Applications. Biosensors (Basel). 14, 293 (2024). https://doi.org/10.3390/bios14060293

10. CHAKRABORTY, B., LITRA, D., MISHRA, A.K., LUPAN, C., NAGPAL, R., MISHRA, S., QIU, H., RAILEAN, S., LUPAN, O., DE LEEUW, N.H., ADELUNG, R., SIEBERT, L.: Ultra-selective hydrogen sensors based on CuO - ZnO hetero-structures grown by surface conversion. J. Alloys Compd. 1002, 175385 (2024). https://doi.org/https://doi.org/10.1016/j.jallcom.2024.175385

11. LIU, L., WANG, Y., LIU, Y., WANG, S., LI, T., FENG, S., QIN, S., ZHANG, T.: Heteronanostructural metal oxide-based gas microsensors. Microsyst. Nanoeng. 8, 85 (2022). https://doi.org/10.1038/s41378-022-00410-1

12. HEIGHT, M.J., PRATSINIS, S.E., MEKASUWANDUMRONG, O., PRASERTHDAM, P.: Ag-ZnO catalysts for UV-photodegradation of methylene blue. Appl. Catal. B. 63, 305–312 (2006). https://doi.org/https://doi.org/10.1016/j.apcatb.2005.10.018

13. GARCÍA, M.C., TORRES, J., DAN CÓRDOBA, A. V, LONGHI, M., UBERMAN, P.M.: 2 - Drug delivery using metal oxide nanoparticles. In: Mondal, K. (ed.) Metal Oxides for Biomedical and Biosensor Applications. pp. 35–83. Elsevier (2022)

14. DUTTA PATHAK, D.: Impact of morphology on defect related properties and photocatalytic activity of tin oxide structures. Materials Science and Engineering: B. 311, 117803 (2025). https://doi.org/https://doi.org/10.1016/j.mseb.2024.117803

15. LUPAN, C., MISHRA, A.K., WOLFF, N., DREWES, J., KRÜGER, H., VAHL, A., LUPAN, O., PAUPORTÉ, T., VIANA, B., KIENLE, L., ADELUNG, R., DE LEEUW, N.H., HANSEN, S.: Nanosensors Based on a Single ZnO:Eu Nanowire for Hydrogen Gas Sensing. ACS Appl. Mater. Interfaces. 14, 41196–41207 (2022). https://doi.org/10.1021/acsami.2c10975

16. NAKATE, U.T., YU, Y.T., PARK, S.: High performance acetaldehyde gas sensor based on p-n heterojunction interface of NiO nanosheets and WO3 nanorods. Sens. Actuators B Chem. 344, 130264 (2021). https://doi.org/https://doi.org/10.1016/j.snb.2021.130264

17. YU, S., JIA, X., YANG, J., WANG, S., LI, Y., SONG, H.: Highly sensitive ethanol gas sensor based on CuO/ZnSnO3 heterojunction composites. Mater. Lett. 291, 129531 (2021). https://doi.org/https://doi.org/10.1016/j.matlet.2021.129531

18. ZHANG, D., LIU, Z., LI, C., TANG, T., LIU, X., HAN, S., LEI, B., ZHOU, C.: Detection of NO2 down to ppb Levels Using Individual and Multiple In2O3 Nanowire Devices. Nano Lett. 4, 1919–1924 (2004). https://doi.org/10.1021/nl0489283

19. HWANG, K., AHN, J., CHO, I., KANG, K., KIM, K., CHOI, J., POLYCHRONOPOULOU, K., PARK, I.: Microporous Elastomer Filter Coated with Metal Organic Frameworks for Improved Selectivity and Stability of Metal Oxide Gas Sensors. ACS Appl. Mater. Interfaces. 12, 13338–13347 (2020). https://doi.org/10.1021/acsami.0c00143

20. QU, Z., FU, Y., YU, B., DENG, P., XING, L., XUE, X.: High and fast H_2S response of NiO/ZnO nanowire nanogenerator as a self-powered gas sensor. Sens. Actuators B Chem. 222, 78–86 (2016). https://doi.org/https://doi.org/10.1016/j.snb.2015.08.058

21. KWON, Y.M., SON, Y., LEE, D.H., LIM, M.H., HAN, J.K., JANG, M., PARK, S., KANG, S., YIM, S., MYUNG, S., LIM, J., LEE, S.S., BAE, G., KIM, S.-H., SONG, W.: Enhancing selectivity and sensitivity in gas sensors through noble metal-decorated ZnO and machine learning. Appl. Surf. Sci. 693, 162750 (2025). https://doi.org/https://doi.org/10.1016/j.apsusc.2025.162750

22. SALEHI ROZVEH, Z., POORIRAJ, M., RAD, M., SAFARIFARD, V., MORADI, M.: Synergistic effect of metal node engineering and mixed-linker-architected on the energy storage activities of pillar-layered Cu2(L)2(DABCO) metal-organic frameworks. Mater. Chem. Phys. 292, 126761 (2022). https://doi.org/https://doi.org/10.1016/j.matchemphys.2022.126761

23. NASEER, M., SIYAL, S.H., NAJAM, T., AFZAL, S., IQBAL, R., ISMAIL, M.A., RAUF, A., SHAH, S.S.A., NAZIR, M.A.: Engineering of metal oxide integrated metal organic frameworks (MO@ MOF) composites for energy and environment sector. Materials Science and Engineering: B. 313, 117909 (2025). https://doi.org/https://doi.org/10.1016/j.mseb.2024.117909

24. ZHANG, J.-B., TIAN, Y.-B., GU, Z.-G., ZHANG, J.: Metal–Organic Framework-Based Photodetectors. Nanomicro Lett. 16, 253 (2024). https://doi.org/10.1007/s40820-024-01465-7

25. KRENO, L.E., LEONG, K., FARHA, O.K., ALLENDORF, M., VAN DUYNE, R.P., HUPP, J.T.: Metal–Organic Framework Materials as Chemical Sensors. Chem. Rev. 112, 1105–1125 (2012). https://doi.org/10.1021/cr200324t

26. GAO, Y., WANG, J., YANG, Y., WANG, J., ZHANG, C., WANG, X., YAO, J.: Engineering Spin States of Isolated Copper Species in a Metal–Organic Framework Improves Urea Electrosynthesis. Nanomicro Lett. 15, 158 (2023). https://doi.org/10.1007/s40820-023-01127-0

27. WANG, L., ZHENG, M., XIE, Z.: Nanoscale metal–organic frameworks for drug delivery: a conventional platform with new promise. J. Mater. Chem. B. 6, 707–717 (2018). https://doi.org/10.1039/C7TB02970E

28. GADZIKWA, T., MATSEKETSA, P.: The post-synthesis modification (PSM) of MOFs for catalysis. Dalton Trans. 53, 7659–7668 (2024). https://doi.org/10.1039/D4DT00514G

29. WU, X., XIONG, S., MAO, Z., HU, S., LONG, X.: A Designed ZnO@ZIF-8 Core–Shell Nanorod Film as a Gas Sensor with Excellent Selectivity for H2 over CO. Chemistry – A European Journal. 23, 7969–7975 (2017). https://doi.org/https://doi.org/10.1002/chem.201700320

30. LIU, H., XU, C., LI, D., JIANG, H.-L.: Photocatalytic Hydrogen Production Coupled with Selective Benzylamine Oxidation over MOF Composites. Angewandte Chemie International Edition. 57, 5379–5383 (2018). https://doi.org/https://doi.org/10.1002/anie.201800320

31. LI, M.-J., WANG, H.-J., YUAN, R., CHAI, Y.-Q.: A zirconium-based metal–organic framework sensitized by thioflavin-T for sensitive photoelectrochemical detection of C-reactive protein. Chem. Commun. 55, 10772–10775 (2019). https://doi.org/10.1039/C9CC05086H

32. KANG, C., AHSAN IQBAL, M., ZHANG, S., WENG, X., SUN, Y., QI, L., TANG, W., RUAN, S., ZENG, Y.-J.: $Cu_3(HHTP)_2$ c-MOF/ZnO Ultrafast Ultraviolet Photodetector for Wearable Optoelectronics. Chemistry – A European Journal. 28, e202201705 (2022). https://doi.org/https://doi.org/10.1002/chem.202201705

33. ZHANG, X.-Y., WANG, P., LU, X.-Y., ZHANG, Y., SUN, W.-Y.: Synergistic effect on photocatalytic CO2 reduction of facet-engineered Fe-soc-MOFs with photo-deposited PtO species. Chemical Engineering Journal. 476, 146560 (2023). https://doi.org/https://doi.org/10.1016/j.cej.2023.146560

34. FU, Y., QIU, W., HUANG, H., HUANG, Q., GUO, Y., MAI, W., LUO, Y., XU, Z., WU, Y., LIN, X.: Bimetal-organic framework-templated Zn-Fe-based transition metal oxide composites through heterostructure optimization to boost lithium storage. J. Colloid Interface Sci. 683, 507–520 (2025). https://doi.org/https://doi.org/10.1016/j.jcis.2024.12.213

35. EVANS, J.D., GARAI, B., REINSCH, H., LI, W., DISSEGNA, S., BON, V., SENKOVSKA, I., FISCHER, R.A., KASKEL, S., JANIAK, C., STOCK, N., VOLKMER, D.: Metal–organic frameworks in Germany: From synthesis to function. Coord. Chem. Rev. 380, 378–418 (2019). https://doi.org/https://doi.org/10.1016/j.ccr.2018.10.002

36. SCHOEDEL, A., RAJEH, S.: Why Design Matters: From Decorated Metal Oxide Clusters to Functional Metal–Organic Frameworks. Top. Curr. Chem. 378, 19 (2020). https://doi.org/10.1007/s41061-020-0281-0

37. ABRAHAMS, B.F., HOSKINS, B.F., MICHAIL, D.M., ROBSON, R.: Assembly of porphyrin building blocks into network structures with large channels. Nature. 369, 727–729 (1994). https://doi.org/10.1038/369727a0

38. LI, H., EDDAOUDI, M., GROY, T.L., YAGHI, O.M.: Establishing Microporosity in Open Metal−Organic Frameworks: Gas Sorption Isotherms for Zn(BDC) (BDC = 1,4-Benzenedicarboxylate). J. Am. Chem. Soc. 120, 8571–8572 (1998). https://doi.org/10.1021/ja981669x

39. YUAN, S., FENG, L., WANG, K., PANG, J., BOSCH, M., LOLLAR, C., SUN, Y., QIN, J., YANG, X., ZHANG, P., WANG, Q., ZOU, L., ZHANG, Y., ZHANG, L., FANG, Y.,

LI, J., ZHOU, H.-C.: Stable Metal–Organic Frameworks: Design, Synthesis, and Applications. Advanced Materials. 30, 1704303 (2018). https://doi.org/https://doi.org/10.1002/adma.201704303

40. ISLAMOGLU, T., RAY, D., LI, P., MAJEWSKI, M.B., AKPINAR, I., ZHANG, X., CRAMER, C.J., GAGLIARDI, L., FARHA, O.K.: From Transition Metals to Lanthanides to Actinides: Metal-Mediated Tuning of Electronic Properties of Isostructural Metal–Organic Frameworks. Inorg. Chem. 57, 13246–13251 (2018). https://doi.org/10.1021/acs.inorgchem.8b01748

41. AN, Y., LV, X., JIANG, W., WANG, L., SHI, Y., HANG, X., PANG, H.: The stability of MOFs in aqueous solutions—research progress and prospects. Green Chemical Engineering. 5, 187–204 (2024). https://doi.org/https://doi.org/10.1016/j.gce.2023.07.004

42. YU, Z., CAO, X., WANG, S., CUI, H., LI, C., ZHU, G.: Research Progress on the Water Stability of a Metal-Organic Framework in Advanced Oxidation Processes. Water Air Soil Pollut. 232, 18 (2021). https://doi.org/10.1007/s11270-020-04953-9

43. PARK, K.S., NI, Z., CÔTÉ, A.P., CHOI, J.Y., HUANG, R., URIBE-ROMO, F.J., CHAE, H.K., O'KEEFFE, M., YAGHI, O.M.: Exceptional chemical and thermal stability of zeolitic imidazolate frameworks. Proceedings of the National Academy of Sciences. 103, 10186–10191 (2006). https://doi.org/10.1073/pnas.0602439103

44. XU, B., MEI, Y., XIAO, Z., KANG, Z., WANG, R., SUN, D.: Monitoring thermally induced structural deformation and framework decomposition of ZIF-8 through in situ temperature dependent measurements. Phys. Chem. Chem. Phys. 19, 27178–27183 (2017). https://doi.org/10.1039/C7CP04694D

45. WU, C., XIE, D., MEI, Y., XIU, Z., PODUSKA, K.M., LI, D., XU, B., SUN, D.: Unveiling the thermolysis natures of ZIF-8 and ZIF-67 by employing in situ structural characterization studies. Phys. Chem. Chem. Phys. 21, 17571–17577 (2019). https://doi.org/10.1039/C9CP02582K

46. CUADRADO-COLLADOS, C., FERNÁNDEZ-CATALÀ, J., FAUTH, F., CHENG, Y.Q., DAEMEN, L.L., RAMIREZ-CUESTA, A.J., SILVESTRE-ALBERO, J.: Understanding the breathing phenomena in nano-ZIF-7 upon gas adsorption. J. Mater. Chem. A. 5, 20938–20946 (2017). https://doi.org/10.1039/C7TA05922A

47. LUPAN, O., SHISHIYANU, S., CHOW, L., SHISHIYANU, T.: Nanostructured zinc oxide gas sensors by successive ionic layer adsorption and reaction method and rapid photothermal processing. Thin Solid Films. 516, 3338–3345 (2008). https://doi.org/https://doi.org/10.1016/j.tsf.2007.10.104

48. SALLES, P., MACHADO, P., YU, P., COLL, M.: Chemical synthesis of complex oxide thin films and freestanding membranes. Chem. Commun. 59, 13820–13830 (2023). https://doi.org/10.1039/D3CC03030J

49. SCHWARTZ, R.W.: Chemical Solution Deposition of Perovskite Thin Films. Chemistry of Materials. 9, 2325–2340 (1997). https://doi.org/10.1021/cm970286f

50. Ludwig Reimer: Scanning Electron Microscopy, Physics of image formation and microanalysis. Springer, Berlin (1998)

51. UL-HAMID, A.: A Beginners' Guide to Scanning Electron Microscopy. (2018)

52. AMELINCKX, S..: Handbook of microscopy : applications in materials science, solid-state physics, and chemistry. VCH (1997)

53. B.D. CULLITY: Elements of X-ray Diffracation. , Phillippines (1978)

54. R. GROSS AND A. MARX: Festkörperphysik. De Gruyter (2018)

55. DEMTRÖDER, W.: INTERFERENZ, BEUGUNG UND STREUUNG. In: Experimentalphysik 2: Elektrizität und Optik. pp. 285–329. Springer Berlin Heidelberg, Berlin, Heidelberg (2017)

56. OMORI, M.: Powder X-ray Diffraction Basic Course Second installment: Selection of equipment configuration to obtain high-quality data.

57. SMITH, E., DENT, G.: Modern Raman Spectroscopy-A Practical Approach. Presented at the (2005)

58. RICHARD L. McCREERY: Raman Spectroscopy for Chemical Analysis. A JOHN WILEY & SONS, INC., Ohio (2000)

59. J. F. MOULDER, W. F. STICKLE, P. E. SOBOL, K. D. Bomben: Handbook of X-ray Photoelectron Spectroscopy. Perkin-Elmer Corporation. (1992)

60. RUDOLF GROSS, ACHIM MARX: Festkörperphysik. De Gruyter (2018)

61. BRIGGS, D., SEAH, M.P.: Practical surface analysis : by Auger and x-ray photoelectron spectroscopy . Wiley, Chichester (1983)

62. Volatile Organic Compounds' Impact on Indoor Air Quality, https://www.epa.gov/indoor-air-quality-iaq/volatile-organic-compounds-impact-indoor-air-quality

63. Fisher Scientific Corporation: Material Safety Datasheet of Ethyl alcohol. (1996)

64. BRAUER, R.L.: Appendix A: Osha Permissible Exposure Limits. In: Safety and Health for Engineers. pp. 723–728. Wiley (2005)

65. ALLOUCH, A., GUGLIELMINO, M., BERNHARDT, P., SERRA, C.A., LE CALVÉ, S.: Transportable, fast and high sensitive near real-time analyzers: Formaldehyde detection. Sens. Actuators B Chem. 181, 551–558 (2013). https://doi.org/https://doi.org/10.1016/j.snb.2013.02.043

66. USEPA: National Ambient Air Quality Standards for PM by USEPA, https://www.epa.gov/pm-pollution/national-ambient-air-quality-standards-naaqs-pm#:~:text=On%20February%207%2C%202024%2C%20EPA,with%20the%20available%20health%20science.

67. MADHWAL, S., TRIPATHI, S.N., BERGIN, M.H., BHAVE, P., DE FOY, B., REDDY, T.V.R., CHAUDHRY, S.K., JAIN, V., GARG, N., LALWANI, P.: Evaluation of PM2.5 spatio-temporal variability and hotspot formation using low-cost sensors across urban-rural landscape in lucknow, India. Atmos. Environ. 319, 120302 (2024). https://doi.org/https://doi.org/10.1016/j.atmosenv.2023.120302

68. LAI, H.K., KENDALL, M., FERRIER, H., LINDUP, I., ALM, S., HÄNNINEN, O., JANTUNEN, M., MATHYS, P., COLVILE, R., ASHMORE, M.R., CULLINAN, P., NIEUWENHUIJSEN, M.J.: Personal exposures and microenvironment concentrations of PM2.5, VOC, NO2 and CO in Oxford, UK. Atmos. Environ. 38, 6399–6410 (2004). https://doi.org/https://doi.org/10.1016/j.atmosenv.2004.07.013

69. NORRIS, C.L., EDWARDS, R., GHOROI, C., SCHAUER, J.J., BLACK, M., BERGIN, M.H.: A Pilot Study to Quantify Volatile Organic Compounds and Their Sources Inside and Outside Homes in Urban India in Summer and Winter during Normal Daily Activities. Environments. 9, (2022). https://doi.org/10.3390/environments9070075

70. MOZAFFAR, A., ZHANG, Y.-L.: Atmospheric Volatile Organic Compounds (VOCs) in China: a Review. Curr. Pollut. Rep. 6, 250–263 (2020). https://doi.org/10.1007/s40726-020-00149-1

71. SENSIRION: Beurteilung von Innenraumluftkontaminationen Mittels Referenz- und Richtwerten : Handreichung der Ad-hoc-Arbeitsgruppe der Innenraumlufthygiene-Kommission des Umweltbundesamtes und der Obersten Landesgesundheitsbehörden. (2007)

72. NINYÀ, N., VALLECILLOS, L., MARCÉ, R.M., BORRULL, F.: Evaluation of air quality in indoor and outdoor environments: Impact of anti-COVID-19 measures. Science of The Total Environment. 836, 155611 (2022). https://doi.org/https://doi.org/10.1016/j.scitotenv.2022.155611

73. MALEPE, L., NDINTEH, T.D., NDUNGU, P., MAMO, M.A.: A humidity tolerance and room temperature carbon soot@ZIF-71 sensor for toluene vapour detection. Mater. Res. Bull. 181, 113076 (2025). https://doi.org/https://doi.org/10.1016/j.materresbull.2024.113076

74. CHEN, E.-X., YANG, H., ZHANG, J.: Zeolitic Imidazolate Framework as Formaldehyde Gas Sensor. Inorg. Chem. 53, 5411–5413 (2014). https://doi.org/10.1021/ic500474j

75. ZHANG, Y., ZHU, Z., WANG, W.-N., CHEN, S.-C.: Mitigating the relative humidity effects on the simultaneous removal of VOCs and PM2.5 of a metal–organic framework

coated electret filter. Sep. Purif. Technol. 285, 120309 (2022). https://doi.org/https://doi.org/10.1016/j.seppur.2021.120309

76. LI, C., KIM, K., FUCHIGAMI, T., ASAKA, T., KAKIMOTO, K., MASUDA, Y.: Acetone gas sensor based on Nb2O5 @SnO2 hybrid structure with high selectivity and ppt-level sensitivity. Sens. Actuators B Chem. 393, 134144 (2023). https://doi.org/https://doi.org/10.1016/j.snb.2023.134144

77. LIU, T., JIA, X., ZHANG, J., YANG, J., WANG, S., LI, Y., SHAO, D., FENG, L., SONG, H.: Selective detection of ethanol at low concentration by ZnO@ZIF-8 porous nanosheets. Sens. Actuators B Chem. 372, 132661 (2022). https://doi.org/https://doi.org/10.1016/j.snb.2022.132661

78. WANG, X., MA, Q., WANG, Y., LI, L., ZHAO, D., ZHANG, H., LI, B.: Bimetallic MOFs-derived hierarchical WO3/ZnWO4/CoWO4 heterostructures for enhanced n-butanol gas-sensing performance. Chem. Phys. Lett. 844, 141260 (2024). https://doi.org/https://doi.org/10.1016/j.cplett.2024.141260

79. QU, F., ZHANG, B., ZHOU, X., JIANG, H., WANG, C., FENG, X., JIANG, C., YANG, M.: Metal-organic frameworks-derived porous ZnO/Ni0.9Zn0.1O double-shelled nanocages as gas sensing material for selective detection of xylene. Sens. Actuators B Chem. 252, 649–656 (2017). https://doi.org/https://doi.org/10.1016/j.snb.2017.06.060

80. SUBAWICKRAMA MALLIKA WIDANAARACHCHIGE, N., PAUL, A., MUTHUKUMAR, S., PRASAD, S.: Fc@ZeNose platform for the detection of four physiologically relevant breath biomarkers: a case study using ethanol, isopropanol, acetic acid, and acetone. Sens. Diagn. 4, 723–735 (2025). https://doi.org/10.1039/D5SD00038F

81. OMIDVAR, A., SOLEYMANI, H.: Designing Bimetallic Sensors for Acetone Biomarker Detection. ACS Omega. 10, 12953–12960 (2025). https://doi.org/10.1021/acsomega.4c09037

82. JIANG, X.-X., YU, L.-Q., SUN, Y.-N., LI, Y., LI, H.-M., LV, Y.-K.: Hollow zeolitic imidazolate framework-7 coated stainless steel fiber for solid phase microextraction of volatile biomarkers in headspace gas of breast cancer cell lines. Anal. Chim. Acta. 1181, 338901 (2021). https://doi.org/https://doi.org/10.1016/j.aca.2021.338901

83. LEIDINGER, M., RIEGER, M., SAUERWALD, T., ALÉPÉE, C., SCHÜTZE, A.: Integrated pre-concentrator gas sensor microsystem for ppb level benzene detection. Sens. Actuators B Chem. 236, 988–996 (2016). https://doi.org/https://doi.org/10.1016/j.snb.2016.04.064

84. LV, Y., YU, H., XU, P., XU, J., LI, X.: Metal organic framework of MOF-5 with hierarchical nanopores as micro-gravimetric sensing material for aniline detection. Sens. Actuators B Chem. 256, 639–647 (2018). https://doi.org/https://doi.org/10.1016/j.snb.2017.09.195

85. HAN, B., WANG, H., HUANG, H., LIU, T., WU, G., WANG, J.: Micro-fabricated packed metal gas preconcentrator for enhanced monitoring of ultralow concentration of isoprene. J. Chromatogr. A. 1572, 27–36 (2018). https://doi.org/https://doi.org/10.1016/j.chroma.2018.08.058

86. HUANG, Y., ZHANG, T., XU, T., PENG, Z., XU, Y., HE, S.: Monitoring Acetone with Photoacoustic Spectroscopy Using a Metal–Organic Framework. Adv. Opt. Mater. 12, 2302280 (2024). https://doi.org/https://doi.org/10.1002/adom.202302280

87. United Nations, D. of E. and S.A.P.D.: World Population meter, https://www.worldometers.info/world-population/world-population-by-year/

88. Growth in global energy demand surged in 2024 to almost twice its recent average. (2025)

89. CHOUDHURY, T., KAYANI, U.N., GUL, A., HAIDER, S.A., AHMAD, S.: Carbon emissions, environmental distortions, and impact on growth. Energy Econ. 126, 107040 (2023). https://doi.org/https://doi.org/10.1016/j.eneco.2023.107040

90. PACHAURI, R.K.., REISINGER, ANDY., BERNSTEIN, LENNY.: Climate change 2007 : synthesis report. Intergovernmental Panel on Climate Change (2013)

91. Directorate-General for Climate Action: How climate change is disrupting rainfall patterns and putting our health at risk, https://climate.ec.europa.eu/news-your-voice/news/how-climate-change-disrupting-rainfall-patterns-and-putting-our-health-risk-2023-08-03_en#:~:text=Where%20water%20is%20scarce%2C%20land,water%20in%20a%20changing%20climate, (2023)

92. United States Government Officials: How can climate change affect natural disasters. United States Geological Survey. (2025)

93. Directorate-General for Energy: EU-INDIA JOINT STATEMENT ON CLEAN ENERGY AND CLIMATE CHANGE. (2017)

94. WADELL, C., NUGROHO, F.A.A., LIDSTRÖM, E., IANDOLO, B., WAGNER, J.B., LANGHAMMER, C.: Hysteresis-Free Nanoplasmonic Pd–Au Alloy Hydrogen Sensors. Nano Lett. 15, 3563–3570 (2015). https://doi.org/10.1021/acs.nanolett.5b01053

95. MIKE SCHMIDT: I Cannot Breathe Asphyxia in the Process Industries, https://bluefieldsafety.com/2022/08/i-cant-breathe-asphyxia-in-the-process-industries/#:~:text=Hydrogen%2C%20a%20very%20flammable%20gas,personnel%20to%20oxygen%2Dinsufficient%20atmospheres

96. ALAGHMANDFARD, A., FARDINDOOST, S., FRENCKEN, A.L., HOORFAR, M.: The next generation of hydrogen gas sensors based on transition metal dichalcogenide-metal oxide semiconductor hybrid structures. Ceram. Int. 50, 29026–29043 (2024). https://doi.org/https://doi.org/10.1016/j.ceramint.2024.05.259

97. GAO, D., GAO, S., DENG, H., LIU, H., HOU, D., LU, Q., HE, X., HUANG, S.: Surface electronic structure modulation of PdO/SnO2 through loading Pd for superior hydrogen sensing performance. Chemical Engineering Journal. 515, 163694 (2025). https://doi.org/https://doi.org/10.1016/j.cej.2025.163694

98. impact of humidity electronics manufacturing,pdf, https://airinnovations.com/blog/humidity-impact-electronics-manufacturing/

99. HOU, W., WANG, Q., LI, Z., LYU, N., ZHONG, W., JIN, Y., LIANG, T., WEI, R.: Hydrogen sensors of Ce-doped MoS2 with anti- humidity for early warning thermal runaway in lithium-ion batteries. Sens. Actuators B Chem. 425, 136988 (2025). https://doi.org/https://doi.org/10.1016/j.snb.2024.136988

100. THOKALA, N., DMELLO, M.E., VALLE, K., VANKAYALA, K., KALIDINDI, S.B.: Advancements in porous framework materials for chemiresistive hydrogen sensing: exploring MOFs and COFs. Dalton Trans. 54, 3526–3550 (2025). https://doi.org/10.1039/D4DT02551B

101. LIU, Y., CHENG, H., CHENG, M., LIU, Z., HUANG, D., ZHANG, G., SHAO, B., LIANG, Q., LUO, S., WU, T., XIAO, S.: The application of Zeolitic imidazolate frameworks (ZIFs) and their derivatives based materials for photocatalytic hydrogen evolution and pollutants treatment. Chemical Engineering Journal. 417, 127914 (2021). https://doi.org/https://doi.org/10.1016/j.cej.2020.127914

102. DROBEK, M., KIM, J.-H., BECHELANY, M., VALLICARI, C., JULBE, A., KIM, S.S.: MOF-Based Membrane Encapsulated ZnO Nanowires for Enhanced Gas Sensor Selectivity. ACS Appl. Mater. Interfaces. 8, 8323–8328 (2016). https://doi.org/10.1021/acsami.5b12062

103. LI, J., YUAN, Z., GUO, Z., ZHOU, H., MENG, F.: Porous ordered thin film integrated with ZIF-8 gas enrichment coating for low concentration hydrogen detection. Int. J. Hydrogen Energy. 138, 109–116 (2025). https://doi.org/https://doi.org/10.1016/j.ijhydene.2025.05.127

104. MA, C., ZHOU, T., YANG, H., SU, H., WANG, X., WU, Q., GUO, X., ZENG, D.: High selectivity and response H2 sensors based on ZnO@ZIF-71@Ag nanorod arrays. Ceram. Int. 49, 19728–19736 (2023). https://doi.org/https://doi.org/10.1016/j.ceramint.2023.03.090

105. KHUDIAR, A.I., ELTTAYEF, A.K., KHALAF, M.K., OUFI, A.M.: Fabrication of ZnO@ZIF-8 gas sensors for selective gas detection. Mater. Res. Express. 6, 126450 (2019). https://doi.org/10.1088/2053-1591/ab69c2

106. MATATAGUI, D., SAINZ-VIDAL, A., GRÀCIA, I., FIGUERAS, E., CANÉ, C., SANIGER, J.M.: Chemoresistive gas sensor based on ZIF-8/ZIF-67 nanocrystals. Sens. Actuators B Chem. 274, 601–608 (2018). https://doi.org/https://doi.org/10.1016/j.snb.2018.07.137

107. NOH, S.J., YOON, S.P., HAN, J., PARK, S., KIM, J.: Synthesis and characterization of ZIF-7 membranes by in Situ method. J. Nanosci. Nanotechnol. 15, 575–578 (2015). https://doi.org/10.1166/jnn.2015.8347

108. MARTÍNEZ-SALAZAR, M., TIEMPOS FLORES, N., OBREGÓN-ZÚÑIGA, A., ARILLO-FLORES, O.I., DÁVILA-GUZMÁN, N.E., MICHAELIS, D.J., RAZIEL ÁLVAREZ, J., HERNÁNDEZ-FERNÁNDEZ, E.: DYE REMOVAL UTILIZING ZIF-71 AND HYDROPHOBIC ZIF-71(CLBR): Kinetic and Equilibrium Studies. ACS Omega. 10, 43404–43414 (2025). https://doi.org/10.1021/acsomega.4c09336

109. MORTADA, B., CHAPLAIS, G., NOUALI, H., MARICHAL, C., PATARIN, J.: Phase Transformations of Metal–Organic Frameworks MAF-6 and ZIF-71 during Intrusion–Extrusion Experiments. The Journal of Physical Chemistry C. 123, 4319–4328 (2019). https://doi.org/10.1021/acs.jpcc.8b12047

110. TROELTSCH, F.M., ENGELMANN, M., SCHOLZ, A.E., PETER, F., KAISER, J., HORNUNG, M.: Hydrogen Powered Long Haul Aircraft with Minimized Climate Impact. In: AIAA AVIATION 2020 FORUM

111. PETRESCU, R.V. V, MACHÍN, A., FONTÁNEZ, K., ARANGO, J.C., MÁRQUEZ, F.M., PETRESCU, F.I.T.: Hydrogen for aircraft power and propulsion. Int. J. Hydrogen Energy. 45, 20740–20764 (2020). https://doi.org/https://doi.org/10.1016/j.ijhydene.2020.05.253

112. HUNTER, G., XU, J., NEUDECK, P., MAKEL, D., WARD, B., LIU, C.C.: Intelligent Chemical Sensor Systems for In-Space Safety Applications. In: 42nd AIAA/ASME/SAE/ASEE Joint Propulsion Conference & Exhibit

113. RAMAIYAN, K., TSUI, L., BROSHA, E.L., KRELLER, C., STETTER, J.R., RUSS, T., DU, W., PEASLEE, D., HUNTER, G., XU, J., MAKEL, D., GARZON, F., MUKUNDAN, R.: Recent Developments in Sensor Technologies for Enabling the Hydrogen Economy. ECS Sensors Plus. 2, 45601 (2023). https://doi.org/10.1149/2754-2726/ad0736

114. LITRA, D., CHIRIAC, M., ABABII, N., LUPAN, O.: Acetone Sensors Based on Al-Coated and Ni-Doped Copper Oxide Nanocrystalline Thin Films. Sensors. 24, (2024). https://doi.org/10.3390/s24206550

115. CRETU, V., POSTICA, V., MISHRA, A.K., HOPPE, M., TIGINYANU, I., MISHRA, Y.K., CHOW, L., DE LEEUW, N.H., ADELUNG, R., LUPAN, O.: Synthesis, characterization and DFT studies of zinc-doped copper oxide nanocrystals for gas sensing applications. J. Mater. Chem. A. 4, 6527–6539 (2016). https://doi.org/10.1039/C6TA01355D

116. LUPAN, O., SANTOS-CARBALLAL, D., ABABII, N., MAGARIU, N., HANSEN, S., VAHL, A., ZIMOCH, L., HOPPE, M., PAUPORTÉ, T., GALSTYAN, V., SONTEA, V., CHOW, L., FAUPEL, F., ADELUNG, R., de Leeuw, N.H., Comini, E.: TiO2/Cu$_2$O/CuO

Multi-Nanolayers as Sensors for H_2 and Volatile Organic Compounds: An Experimental and Theoretical Investigation. ACS Appl. Mater. Interfaces. 13, 32363–32380 (2021). https://doi.org/10.1021/acsami.1c04379

117. KUTUKOV, P., RUMYANTSEVA, M., KRIVETSKIY, V., FILATOVA, D., BATUK, M., HADERMANN, J., KHMELEVSKY, N., AKSENENKO, A., GASKOV, A.: Influence of Mono- and Bimetallic PtO_x, PdO_x, $PtPdO_x$ Clusters on CO Sensing by SnO_2 Based Gas Sensors. Nanomaterials. 8, (2018). https://doi.org/10.3390/nano8110917

118. LUPAN, O., CRETU, V., POSTICA, V., ABABII, N., POLONSKYI, O., KAIDAS, V., SCHÜTT, F., MISHRA, Y.K., MONAICO, E., TIGINYANU, I., SONTEA, V., STRUNSKUS, T., FAUPEL, F., ADELUNG, R.: Enhanced ethanol vapour sensing performances of copper oxide nanocrystals with mixed phases. Sens. Actuators B Chem. 224, 434–448 (2016). https://doi.org/https://doi.org/10.1016/j.snb.2015.10.042

119. POSTICA, V., HÖLKEN, I., SCHNEIDER, V., KAIDAS, V., POLONSKYI, O., CRETU, V., TIGINYANU, I., FAUPEL, F., ADELUNG, R., LUPAN, O.: Multifunctional device based on ZnO:Fe nanostructured films with enhanced UV and ultra-fast ethanol vapour sensing. Mater. Sci. Semicond. Process. 49, 20–33 (2016). https://doi.org/https://doi.org/10.1016/j.mssp.2016.03.024

120. LUPAN, O., CHOW, L., SHISHIYANU, S., MONAICO, E., SHISHIYANU, T., ŞONTEA, V., ROLDAN CUENYA, B., NAITABDI, A., PARK, S., SCHULTE, A.: Nanostructured zinc oxide films synthesized by successive chemical solution deposition for gas sensor applications. Mater. Res. Bull. 44, 63–69 (2009). https://doi.org/https://doi.org/10.1016/j.materresbull.2008.04.006

121. QIAN, J., SUN, F., QIN, L.: Hydrothermal synthesis of zeolitic imidazolate framework-67 (ZIF-67) nanocrystals. Mater. Lett. 82, 220–223 (2012). https://doi.org/https://doi.org/10.1016/j.matlet.2012.05.077

122. JAPIP, S., XIAO, Y., CHUNG, T.-S.: Particle-Size Effects on Gas Transport Properties of 6FDA-Durene/ZIF-71 Mixed Matrix Membranes. Ind. Eng. Chem. Res. 55, 9507–9517 (2016). https://doi.org/10.1021/acs.iecr.6b02811

123. NAGPAL, R., LUPAN, C., BUZDUGAN, A., GHENEA, V., LUPAN, O.: Effect of Pd functionalization on optical and hydrogen sensing properties of ZnO: Eu films. Optik (Stuttg). 172247 (2025). https://doi.org/https://doi.org/10.1016/j.ijleo.2025.172247

124. ATTWA, M., SAID, A., ELGAMAL, M., EL-SHAER, Y., ELBASUNEY, S.: Bespoke Energetic Zeolite Imidazolate Frameworks-8 (ZIF-8)/Ammonium Perchlorate Nanocomposite: A Novel Reactive Catalyzed High Energy Dense Material with Superior Decomposition Kinetics. J. Inorg. Organomet. Polym. Mater. 34, 387–400 (2024). https://doi.org/10.1007/s10904-023-02834-2

125. SHARMA, S., CHAND, P.: Electrochemical behavior of solvothermally grown ZIF-8 as electrode material for supercapacitor applications. Mater. Today Proc. 76, 125–131 (2023). https://doi.org/https://doi.org/10.1016/j.matpr.2022.10.137

126. DUBROVKIN, JOSEPH.: Data compression in spectroscopy. Cambridge Scholars Publishing (2022)

127. BYRNE, C., MAZAJ, M., LOGAR, N.Z.: Assessing the heat storage potential of zeolitic imidazolate frameworks (ZIFs) using water and ethanol as working fluids. Mater. Chem. Phys. 332, 130143 (2025). https://doi.org/https://doi.org/10.1016/j.matchemphys.2024.130143

128. MISHRA, L., DWIVEDI, V.K., DARA, H.K., CHAKRADHARY, V.K., ITHINENI, S., PRABHUDESSAI, A.G., NEHAR, S.: Core/Shell-Like Magnetic Structure and Optical Properties in CuO Nanoparticles Synthesized by Green Route. ACS Sustainable Resource Management. 1, 2472–2481 (2024). https://doi.org/10.1021/acssusresmgt.4c00325

129. CARTER, D.A., PEMBERTON, J.E.: Raman spectroscopy and vibrational assignments of 1- and 2-methylimidazole. Journal of Raman Spectroscopy. 28, 939–946 (1997). https://doi.org/https://doi.org/10.1002/(SICI)1097-4555(199712)28:12<939::AID-JRS186>3.0.CO;2-R

130. OLANIYAN, B., SAHA, B.: Comparison of Catalytic Activity of ZIF-8 and Zr/ZIF-8 for Greener Synthesis of Chloromethyl Ethylene Carbonate by CO2 Utilization. Energies (Basel). 13, (2020). https://doi.org/10.3390/en13030521

131. LIU, J., GAO, Z., HUANG, Y., SONG, Y.: Structural changes and CO2 adsorption performance in Zn2(BDC)2DABCO metal-organic framework under high-pressure and high-temperature conditions. Can. J. Chem. 0, null. https://doi.org/10.1139/cjc-2024-0166

132. LI, J., CHANG, H., LI, Y., LI, Q., SHEN, K., YI, H., ZHANG, J.: Synthesis and adsorption performance of La@ZIF-8 composite metal–organic frameworks. RSC Adv. 10, 3380–3390 (2020). https://doi.org/10.1039/C9RA10548D

133. NARIMBI, J., BALAKRISHNAN, S., PEROVA, T.S., DEE, G., SWIEGERS, G.F., GUN'KO, Y.K.: XRD and Spectroscopic Investigations of ZIF—Microchannel Glass Plates Composites. Materials. 16, (2023). https://doi.org/10.3390/ma16062410

134. DEACON, A., BRIQUET, L., MALANKOWSKA, M., MASSINGBERD-MUNDY, F., RUDIĆ, S., HYDE, T. L., CAVAYE, H., CORONAS, J., POULSTON, S., JOHNSON, T.: Understanding the ZIF-L to ZIF-8 transformation from fundamentals to fully costed kilogram-scale production. Commun. Chem. 5, (2022). https://doi.org/10.1038/s42004-021-00613-z

135. MANI, G., KUMAR, A. V, MATHEW, S.: ZIF-8 derived ZnO: a facile catalyst for ammonium perchlorate thermal decomposition††Electronic supplementary information

(ESI) available. See DOI: https://doi.org/10.1039/d3su00256j. RSC Sustainability. 1, 2081–2091 (2023). https://doi.org/https://doi.org/10.1039/d3su00256j

136. SOLIMAN, A.I.A., ABDEL-WAHAB, A.M.A., ABDELHAMID, H.N.: Hierarchical porous zeolitic imidazolate frameworks (ZIF-8) and ZnO@N-doped carbon for selective adsorption and photocatalytic degradation of organic pollutants. RSC Adv. 12, 7075–7084 (2022). https://doi.org/10.1039/d2ra00503d

137. LIU, X., ZHANG, J., DONG, Y., LI, H., XIA, Y., WANG, H.: A facile approach for the synthesis of Z-scheme photocatalyst ZIF-8/g-C3N4 with highly enhanced photocatalytic activity under simulated sunlight. New J. Chem. 42, 12180–12187 (2018). https://doi.org/10.1039/C8NJ01782D

138. AWADALLAH-F, A., HILLMAN, F., AL-MUHTASEB, S.A., JEONG, H.-K.: On the nanogate-opening pressures of copper-doped zeolitic imidazolate framework ZIF-8 for the adsorption of propane, propylene, isobutane, and n-butane. J. Mater. Sci. 54, 5513–5527 (2019). https://doi.org/10.1007/s10853-018-03249-y

139. TIAN, F., CERRO, A.M., MOSIER, A.M., WAYMENT-STEELE, H.K., SHINE, R.S., PARK, A., WEBSTER, E.R., JOHNSON, L.E., JOHAL, M.S., BENZ, L.: Surface and Stability Characterization of a Nanoporous ZIF-8 Thin Film. The Journal of Physical Chemistry C. 118, 14449–14456 (2014). https://doi.org/10.1021/jp5041053

140. VASQUEZ, R.P.: CuO by XPS. Surface Science Spectra. 5, 262–266 (1998). https://doi.org/10.1116/1.1247882

141. QIU, J., XU, X., LIU, B., GUO, Y., WANG, H., YU, L., JIANG, Y., HUANG, C., FAN, B., ZENG, Z., LI, L.: Size-Controllable Synthesis of ZIF-8 and Derived Nitrogen-Rich Porous Carbon for CO_2 and VOCs Adsorption. ChemistrySelect. 7, e202203273 (2022). https://doi.org/https://doi.org/10.1002/slct.202203273

142. WU, Y., FANG, R., SHEN, L., BAI, H.: Dual mechanisms in hydrogen reduction of copper oxide: surface reaction and subsurface oxygen atom transfer. RSC Adv. 14, 9985–9995 (2024). https://doi.org/10.1039/D4RA01240B

143. NAGPAL RAJAT AND LUPAN, C. AND S.P. AND B.A. AND B.M. AND S.L. AND L.O.: Study on Al_2O_3/ZnO Heterostructure Based UV Detection for Biomedical Applications. In: Costin Hariton-Nicolae and Magjarević, R. and P.G.G. (ed.) Advances in Digital Health and Medical Bioengineering. pp. 178–188. Springer Nature Switzerland, Cham (2024)

144. MTANGI, W., AURET, F.D., NYAMHERE, C., JANSE VAN RENSBURG, P.J., CHAWANDA, A., DIALE, M., NEL, J.M., MEYER, W.E.: The dependence of barrier height on temperature for Pd Schottky contacts on ZnO. Physica B Condens. Matter. 404, 4402–4405 (2009). https://doi.org/https://doi.org/10.1016/j.physb.2009.09.022

145. MENG, X., BI, M., XIAO, Q., GAO, W.: Ultra-fast response and highly selectivity hydrogen gas sensor based on Pd/SnO$_2$ nanoparticles. Int. J. Hydrogen Energy. 47, 3157–3169 (2022). https://doi.org/https://doi.org/10.1016/j.ijhydene.2021.10.201

146. SHANKAR, P., RAYAPPAN, J.B.B.: Room temperature ethanol sensing properties of ZnO nanorods prepared using an electrospinning technique. J. Mater. Chem. C. 5, 10869–10880 (2017). https://doi.org/10.1039/C7TC03771F

147. GAO, C., WU, J., SHI, Q., YING, H., DONG, J.: Adsorption breakthrough behavior of 1-butanol from an ABE model solution with high-silica zeolite: Comparison with zeolitic imidazolate frameworks (ZIF-8). Microporous and Mesoporous Materials. 243, 119–129 (2017). https://doi.org/https://doi.org/10.1016/j.micromeso.2017.02.009

148. CHENG, I.-K., LIN, C.-Y., PAN, F.-M.: Gas sensing behavior of ZnO toward H2 at temperatures below 300°C and its dependence on humidity and Pt-decoration. Appl. Surf. Sci. 541, 148551 (2021). https://doi.org/https://doi.org/10.1016/j.apsusc.2020.148551

149. SUZUKI, T.T., OHGAKI, T., ADACHI, Y., SAKAGUCHI, I., NAKAMURA, M., OHASHI, H., AIMI, A., FUJIMOTO, K.: Ethanol Gas Sensing by a Zn-Terminated ZnO(0001) Bulk Single-Crystalline Substrate. ACS Omega. 5, 21104–21112 (2020). https://doi.org/10.1021/acsomega.0c02750

150. NAZPAL, R., CHIRIAC, M., SUGIHARA, M., LITRA, D., ABABII, N., MAGARIU, N., LUPAN, C., ZINICOVSCHI, V., AMELOOT, R., LUPAN, O.: Sensory Properties of CuO/Cu2O Nanostructures Coated with Zeolitic Imidazolate Frameworks. In: 2024 E-Health and Bioengineering Conference (EHB). pp. 1–4 (2024)

151. ZHOU, T., SANG, Y., WANG, X., WU, C., ZENG, D., XIE, C.: Pore size dependent gas-sensing selectivity based on ZnO@ZIF nanorod arrays. Sens. Actuators B Chem. 258, 1099–1106 (2018). https://doi.org/https://doi.org/10.1016/j.snb.2017.12.024

152. SUI, L., ZHANG, W., WANG, P., ZHAO, B., WU, H., ZHAO, D., DONG, G., YU, H., XU, Y., HUO, L.: A fast response ppb-level aniline gas sensor based on hierarchical hollow spheres of α-Fe$_2$O$_3$/α-MoO$_3$ heterostructure. Sens. Actuators B Chem. 346, 130519 (2021). https://doi.org/https://doi.org/10.1016/j.snb.2021.130519

153. REN, G., LI, Z., YANG, W., FAHEEM, M., XING, J., ZOU, X., PAN, Q., ZHU, G., DU, Y.: ZnO@ZIF-8 core-shell microspheres for improved ethanol gas sensing. Sens. Actuators B Chem. 284, 421–427 (2019). https://doi.org/https://doi.org/10.1016/j.snb.2018.12.145

154. SCANLON, D.O., MORGAN, B.J., WATSON, G.W., WALSH, A.: Acceptor Levels in p-Type Cu$_2$O Rationalizing Theory and Experiment. Phys. Rev. Lett. 103, 96405 (2009). https://doi.org/10.1103/PhysRevLett.103.096405

155. PAUL, G.K., NAWA, Y., SATO, H., SAKURAI, T., AKIMOTO, K.: Defects in Cu2O studied by deep level transient spectroscopy. Appl. Phys. Lett. 88, 141901 (2006). https://doi.org/10.1063/1.2175492

156. DE SOUZA LUCAS, F., PENG, H., JOHNSTON, S., DIPPO, P.C., LANY, S., MASCARO, L.H., ZAKUTAYEV, A.: Characterization of defects in copper antimony disulfide. J. Mater. Chem. A. 5, 21986–21993 (2017). https://doi.org/10.1039/C7TA07012H

157. NAIR, S.S., ILLYASKUTTY, N., TAM, B., YAZAYDIN, A.O., EMMERICH, K., STEUDEL, A., HASHEM, T., SCHÖTTNER, L., WÖLL, C., KOHLER, H., GLIEMANN, H.: ZnO@ZIF-8: Gas sensitive core-shell hetero-structures show reduced cross-sensitivity to humidity. Sens. Actuators B Chem. 304, 127184 (2020). https://doi.org/10.1016/j.snb.2019.127184

158. IUPAC analytical compendium.

159. PEÑA, Á., MATATAGUI, D., RICCIARDELLA, F., SACCO, L., VOLLEBREGT, S., OTERO, D., LÓPEZ-SÁNCHEZ, J., MARÍN, P., HORRILLO, M.C.: Optimization of multilayer graphene-based gas sensors by ultraviolet photoactivation. Appl. Surf. Sci. 610, 155393 (2023). https://doi.org/https://doi.org/10.1016/j.apsusc.2022.155393

160. ZHANG, X., SUN, J., TANG, K., WANG, H., CHEN, T., JIANG, K., ZHOU, T., QUAN, H., GUO, R.: Ultralow detection limit and ultrafast response/recovery of the H2 gas sensor based on Pd-doped rGO/ZnO-SnO2 from hydrothermal synthesis. Microsyst. Nanoeng. 8, (2022). https://doi.org/10.1038/s41378-022-00398-8

161. ZHOU, M., GUO, F., DUANMU, F., SHEN, Z.: Enhanced sensing performance toward alcohols using copper oxide based on exposed crystal facet driven catalytic oxidation. Journal of Materials Science: Materials in Electronics. 32, 26676–26687 (2021). https://doi.org/10.1007/s10854-021-07045-4

162. AL-HARDAN, N.H., ABDULLAH, M.J., AZIZ, A.A.: Sensing mechanism of hydrogen gas sensor based on RF-sputtered ZnO thin films. Int. J. Hydrogen Energy. 35, 4428–4434 (2010). https://doi.org/https://doi.org/10.1016/j.ijhydene.2010.02.006

163. LV, R., ZHANG, Q., WANG, W., LIN, Y., ZHANG, S.: ZnO@ZIF-8 Core-Shell Structure Gas Sensors with Excellent Selectivity to H2. Sensors. 21, (2021). https://doi.org/10.3390/s21124069

164. YAMUKYAN, M.H., MANUKYAN, KH.V., KHARATYAN, S.L.: Copper oxide reduction by hydrogen under the self-propagation reaction mode. J. Alloys Compd. 473, 546–549 (2009). https://doi.org/https://doi.org/10.1016/j.jallcom.2008.06.031

165. SCHLAICH, A., BARRAT, J.L., COASNE, B.: Theory and Modeling of Transport for Simple Fluids in Nanoporous Materials: From Microscopic to Coarse-Grained Descriptions, (2025)

166. ZHANG, K., LIVELY, R.P., ZHANG, C., CHANCE, R.R., KOROS, W.J., SHOLL, D.S., NAIR, S.: Exploring the Framework Hydrophobicity and Flexibility of ZIF-8: From Biofuel Recovery to Hydrocarbon Separations. J. Phys. Chem. Lett. 4, 3618–3622 (2013). https://doi.org/10.1021/jz402019d

167. TUAN, V.A., LI, S., FALCONER, J.L., NOBLE, R.D.: In Situ Crystallization of Beta Zeolite Membranes and Their Permeation and Separation Properties. Chemistry of Materials. 14, 489–492 (2002). https://doi.org/10.1021/cm010413e

168. GAO, C., SHI, Q., DONG, J.: Adsorptive separation performance of 1-butanol onto typical hydrophobic zeolitic imidazolate frameworks (ZIFs). CrystEngComm. 18, 3842–3849 (2016). https://doi.org/10.1039/c6ce00249h

169. GUSSONI, M., RUI, M., ZERBI, G.: Electronic and relaxation contribution to linear molecular polarizability. An analysis of the experimental values. J. Mol. Struct. 447, 163–215 (1998). https://doi.org/https://doi.org/10.1016/S0022-2860(97)00292-5

170. COUSIN SAINT REMI, J., RÉMY, T., VAN HUNSKERKEN, V., VAN DE PERRE, S., DUERINCK, T., MAES, M., DE VOS, D., GOBECHIYA, E., KIRSCHHOCK, C.E.A., BARON, G. V, DENAYER, J.F.M.: Biobutanol Separation with the Metal–Organic Framework ZIF-8. ChemSusChem. 4, 1074–1077 (2011). https://doi.org/https://doi.org/10.1002/cssc.201100261

171. BANERJEE, R., PHAN, A., WANG, B., KNOBLER, C., FURUKAWA, H., O'KEEFFE, M., YAGHI, O.M.: High-throughput synthesis of zeolitic imidazolate frameworks and application to CO2 capture. Science (1979). 319, 939–943 (2008)

172. DONG, X., LIN, Y.S.: Synthesis of an organophilic ZIF-71 membrane for pervaporation solvent separation. Chem. Commun. 49, 1196–1198 (2013). https://doi.org/10.1039/C2CC38512K

173. MÖSLEIN, A.F., TAN, J.-C.: Vibrational Modes and Terahertz Phenomena of the Large-Cage Zeolitic Imidazolate Framework-71. J. Phys. Chem. Lett. 13, 2838–2844 (2022). https://doi.org/10.1021/acs.jpclett.2c00081

174. ETHIRAJ, J., BONINO, F., LAMBERTI, C., BORDIGA, S.: H_2S interaction with HKUST-1 and ZIF-8 MOFs: A multitechnique study. Microporous and Mesoporous Materials. 207, 90–94 (2015). https://doi.org/https://doi.org/10.1016/j.micromeso.2014.12.034

175. YE, J., TAN, J.-C., YE, J., TAN, J.: High-Performance Triboelectric Nanogenerators Incorporating Chlorinated Zeolitic Imidazolate Frameworks with Topologically Tunable Dielectric and Surface Adhesion Properties. Nano Energy. (2023). https://doi.org/https://doi.org/10.1016/j.nanoen.2023.108687

176. DENG, Y., HANDOKO, A.D., DU, Y., XI, S., YEO, B.S.: In Situ Raman Spectroscopy of Copper and Copper Oxide Surfaces during Electrochemical Oxygen Evolution

Reaction: Identification of CuIII Oxides as Catalytically Active Species. ACS Catal. 6, 2473–2481 (2016). https://doi.org/10.1021/acscatal.6b00205

177. ZHANG, Y., GUTIÉRREZ, M., CHAUDHARI, A.K., TAN, J.-C.: Dye-Encapsulated Zeolitic Imidazolate Framework (ZIF-71) for Fluorochromic Sensing of Pressure, Temperature, and Volatile Solvents. ACS Appl. Mater. Interfaces. 12, 37477–37488 (2020). https://doi.org/10.1021/acsami.0c10257

178. ORTIZ, G., NOUALI, H., MARICHAL, C., CHAPLAIS, G., PATARIN, J.: Energetic Performances of "ZIF-71–Aqueous Solution" Systems: A Perfect Shock-Absorber with Water. The Journal of Physical Chemistry C. 118, 21316–21322 (2014). https://doi.org/10.1021/jp505484x

179. FARRANDO-PEREZ, J., MISSYUL, A., MARTÍN-CALVO, A., ABREU-JAUREGUI, C., RAMÍREZ-CEREZO, V., DAEMEN, L., CHENG, Y.Q., RAMIREZ-CUESTA, A.J., CALERO, S., CARRILLO-CARRIÓN, C., SILVESTRE-ALBERO, J.: Molecular recognition-induced structural flexibility in ZIF-71. J. Mater. Chem. A Mater. (2024). https://doi.org/10.1039/d4ta03813d

180. TIEMPOS-FLORES, N., HERNÁNDEZ-FERNÁNDEZ, E., RICO-BARRAGAN, A., RAZIEL ÁLVAREZ, J., JUÁREZ-RAMÍREZ, I., GARZA-NAVARRO, M.A., RODRÍGUEZ-HERNÁNDEZ, J., FONSECA-GARCÍA, A., MICHAELIS, D.J., DAVILA-GUZMAN, N.E.: Enhanced hydrophobicity of modified ZIF-71 metal-organic framework for biofuel purification. Polyhedron. 217, (2022). https://doi.org/10.1016/j.poly.2022.115736

181. LI, W., MA, T., TANG, P., LUO, Y., ZHANG, H., ZHAO, J., AMELOOT, R., TU, M.: Nanoscale Resist-Free Patterning of Halogenated Zeolitic Imidazolate Frameworks by Extreme UV Lithography. Advanced Science. 12, 2415804 (2025). https://doi.org/https://doi.org/10.1002/advs.202415804

182. SHAO, Z., DING, L., ZHU, W., FAN, C., DI, K., YUAN, R., WANG, K.: Highly selective detection and removal of mercury ions in the aquatic environment based on magnetic ZIF-71 multifunctional composites with sufficient chlorine functional groups. Science of The Total Environment. 921, 171085 (2024). https://doi.org/https://doi.org/10.1016/j.scitotenv.2024.171085

183. TU, M., XIA, B., KRAVCHENKO, D.E., TIETZE, M.L., CRUZ, A.J., STASSEN, I., HAUFFMAN, T., TEYSSANDIER, J., DE FEYTER, S., WANG, Z., FISCHER, R.A., MARMIROLI, B., AMENITSCH, H., TORVISCO, A., VELÁSQUEZ-HERNÁNDEZ, M. DE J., FALCARO, P., AMELOOT, R.: Direct X-ray and electron-beam lithography of halogenated zeolitic imidazolate frameworks. Nat. Mater. 20, 93–99 (2021). https://doi.org/10.1038/s41563-020-00827-x

184. FRANKCOMBE, T.J., LIU, Y.: Interpretation of Oxygen 1s X-ray Photoelectron Spectroscopy of ZnO. Chemistry of Materials. 35, 5468–5474 (2023). https://doi.org/10.1021/acs.chemmater.3c00801

185. RAEBIGER, H., LANY, S., ZUNGER, A.: Origins of the p-type nature and cation deficiency in Cu_2O and related materials. Phys. Rev. B. 76, 45209 (2007). https://doi.org/10.1103/PhysRevB.76.045209

186. SHAO, G.: Work Function and Electron Affinity of Semiconductors: Doping Effect and Complication due to Fermi Level Pinning, (2021)

187. WANG, J., WU, J., ZHENG, B., WANG, J., SHI, Q., DONG, J.: Adsorptive separation of butanol, acetone and ethanol in zeolite imidazolate frameworks with desirable pore apertures. Chem. Eng. Sci. 248, 117251 (2022). https://doi.org/https://doi.org/10.1016/j.ces.2021.117251

188. HOPPE, M., ABABII, N., POSTICA, V., LUPAN, O., POLONSKYI, O., SCHÜTT, F., KAPS, S., SUKHODUB, L.F., SONTEA, V., STRUNSKUS, T., FAUPEL, F., ADELUNG, R.: $(CuO-Cu_2O)/ZnO:Al$ heterojunctions for volatile organic compound detection. Sens. Actuators B Chem. 255, 1362–1375 (2018). https://doi.org/https://doi.org/10.1016/j.snb.2017.08.135

189. CHOI, Y.M., CHO, S.-Y., JANG, D., KOH, H.-J., CHOI, J., KIM, C.-H., JUNG, H.-T.: Ultrasensitive Detection of VOCs Using a High-Resolution $CuO/Cu_2O/Ag$ Nanopattern Sensor. Adv. Funct. Mater. 29, 1808319 (2019). https://doi.org/https://doi.org/10.1002/adfm.201808319

190. MALEPE, L., NDINTEH, T.D., NDUNGU, P., MAMO, M.A.: A humidity-resistant and room temperature carbon soot@ZIF-67 composite sensor for acetone vapour detection. Nanoscale Adv. 5, 1956–1969 (2023). https://doi.org/10.1039/D3NA00050H

191. Hübner, M., Simion, C.E., Tomescu-Stǎnoiu, A., Pokhrel, S., Bârsan, N., Weimar, U.: Influence of humidity on CO sensing with p-type CuO thick film gas sensors. Sens. Actuators B Chem. 153, 347–353 (2011). https://doi.org/https://doi.org/10.1016/j.snb.2010.10.046

192. SUI, N., ZHANG, P., ZHOU, T., ZHANG, T.: Selective ppb-level ozone gas sensor based on hierarchical branch-like In_2O_3 nanostructure. Sens. Actuators B Chem. 336, 129612 (2021). https://doi.org/https://doi.org/10.1016/j.snb.2021.129612

193. ZHAO, C., FU, H., HE, P., BAI, Y., CHEN, F., SHI, N., MAO, L., YANG, X., XIONG, S., AN, X.: Room-temperature sensing performance of $CuO/Cu2O$ nanocomposites towards n-butanol. Sens. Actuators B Chem. 373, 132630 (2022). https://doi.org/https://doi.org/10.1016/j.snb.2022.132630

194. CHAI, H., ZHENG, Z., LIU, K., XU, J., WU, K., LUO, Y., LIAO, H., DEBLIQUY, M., ZHANG, C.: Stability of Metal Oxide Semiconductor Gas Sensors: A Review, (2022)

195. HU, H., ZHU, J., YANG, F., CHEN, Z., DENG, M., WENG, L., LING, Y., ZHOU, Y.: A robust etb-type metal–organic framework showing polarity-exclusive adsorption of

acetone over methanol for their azeotropic mixture. Chem. Commun. 55, 6495–6498 (2019). https://doi.org/10.1039/C9CC02439E

196. BHATTACHARYYA, S., JAYACHANDRABABU, K.C., CHIANG, Y., SHOLL, D.S., NAIR, S.: Butanol Separation from Humid CO2-Containing Multicomponent Vapor Mixtures by Zeolitic Imidazolate Frameworks. ACS Sustain. Chem. Eng. 5, 9467–9476 (2017). https://doi.org/10.1021/acssuschemeng.7b02604

197. WEI, K., ZHAO, S., ZHANG, W., ZHONG, X., LI, T., CUI, B., GAO, S., WEI, D., SHEN, Y.: Controllable Synthesis of Zn-Doped α-Fe$_2$O$_3$ Nanowires for H2S Sensing. Nanomaterials. 9, (2019). https://doi.org/10.3390/nano9070994

198. NELSON, R.D., LIDE, D.R., MARYOTT, A.A.: Selected values of electric dipole moments for molecules in the gas phase. , Gaithersburg, MD (1967)

199. LIU, L., MEI, Z., TANG, A., AZAROV, A., KUZNETSOV, A., XUE, Q.-K., DU, X.: Oxygen vacancies: The origin of n-type conductivity in ZnO. Phys. Rev. B. 93, 235305 (2016). https://doi.org/10.1103/PhysRevB.93.235305

200. MESOUDY, A. EL, MACHON, D., RUEDIGER, A., JAOUAD, A., ALIBART, F., ECOFFEY, S., DROUIN, D.: Band gap narrowing induced by oxygen vacancies in reactively sputtered TiO2 thin films. Thin Solid Films. 769, 139737 (2023). https://doi.org/https://doi.org/10.1016/j.tsf.2023.139737

201. BLACKMAN, C.: Do We Need "Ionosorbed" Oxygen Species? (Or, "A Surface Conductivity Model of Gas Sensitivity in Metal Oxides Based on Variable Surface Oxygen Vacancy Concentration"). ACS Sens. 6, 3509–3516 (2021). https://doi.org/10.1021/acssensors.1c01727

202. FENG, X., CARREON, M.A.: Kinetics of transformation on ZIF-67 crystals. J. Cryst. Growth. 418, 158–162 (2015). https://doi.org/https://doi.org/10.1016/j.jcrysgro.2015.02.064

203. JOSHI, B.N., LEE, J.-G., AN, S., KIM, D.-Y., LEE, J.S., HWANG, Y.K., CHANG, J.-S., AL-DEYAB, S.S., TAN, J.-C., YOON, S.S.: Tuning crystalline structure of zeolitic metal–organic frameworks by supersonic spraying of precursor nanoparticle suspensions. Mater. Des. 114, 416–423 (2017). https://doi.org/https://doi.org/10.1016/j.matdes.2016.11.001

204. THI THANH, M., VINH THIEN, T., THI THANH CHAU, V., DINH DU, P., PHI HUNG, N., QUANG KHIEU, D.: Synthesis of Iron Doped Zeolite Imidazolate Framework-8 and Its Remazol Deep Black RGB Dye Adsorption Ability. J. Chem. 2017, 5045973 (2017). https://doi.org/https://doi.org/10.1155/2017/5045973

205. LI, G.-R., ZHAO, W.-X., BU, Q., TONG, Y.-X.: A novel electrochemical deposition route for the preparation of Zn1−xCdxO nanorods with controllable optical properties.

Electrochem. commun. 11, 282–285 (2009).
https://doi.org/https://doi.org/10.1016/j.elecom.2008.11.024

206. VIGIL, O., VAILLANT, L., CRUZ, F., SANTANA, G., MORALES-ACEVEDO, A., CONTRERAS-PUENTE, G.: Spray pyrolysis deposition of cadmium–zinc oxide thin films. Thin Solid Films. 361–362, 53–55 (2000). https://doi.org/https://doi.org/10.1016/S0040-6090(99)01061-5

207. LUPAN, O., PAUPORTÉ, T., LE BAHERS, T., CIOFINI, I., VIANA, B.: High Aspect Ratio Ternary $Zn_{1-x}Cd_xO$ Nanowires by Electrodeposition for Light-Emitting Diode Applications. The Journal of Physical Chemistry C. 115, 14548–14558 (2011). https://doi.org/10.1021/jp202608e

208. COUDERT, F.-X.: Responsive Metal–Organic Frameworks and Framework Materials: Under Pressure, Taking the Heat, in the Spotlight, with Friends. Chemistry of Materials. 27, 1905–1916 (2015). https://doi.org/10.1021/acs.chemmater.5b00046

209. KANNAKA, S., OHMIYA, A., OZAKI, C., OHTANI, M.: Thermodynamic analysis of gate-opening carbon dioxide adsorption behavior of metal–organic frameworks. Chem. Commun. 60, 4170–4173 (2024). https://doi.org/10.1039/D3CC05700C

210. ZHAO, P., LAMPRONTI, G.I., LLOYD, G.O., WHARMBY, M.T., FACQ, S., CHEETHAM, A.K., REDFERN, S.A.T.: Phase Transitions in Zeolitic Imidazolate Framework 7: The Importance of Framework Flexibility and Guest-Induced Instability. Chemistry of Materials. 26, 1767–1769 (2014). https://doi.org/10.1021/cm500407f

211. KUMARI, G., JAYARAMULU, K., MAJI, T.K., NARAYANA, C.: Temperature Induced Structural Transformations and Gas Adsorption in the Zeolitic Imidazolate Framework ZIF-8: A Raman Study. J. Phys. Chem. A. 117, 11006–11012 (2013). https://doi.org/10.1021/jp407792a

212. CHEN, S., LI, X., DONG, E., LV, H., YANG, X., LIU, R., LIU, B.: Intrinsic and Extrinsic Responses of ZIF-8 under High Pressure: A Combined Raman and X-ray Diffraction Investigation. The Journal of Physical Chemistry C. 123, 29693–29707 (2019). https://doi.org/10.1021/acs.jpcc.9b08460

213. HAO, J., BABU, D.J., LIU, Q., SCHOUWINK, P.A., ASGARI, M., QUEEN, W.L., AGRAWAL, K.V.: Mechanistic Study on Thermally Induced Lattice Stiffening of ZIF-8. Chemistry of Materials. 33, 4035–4044 (2021). https://doi.org/10.1021/acs.chemmater.1c00455

214. JAMES, J.B., LIN, Y.S.: Kinetics of ZIF-8 Thermal Decomposition in Inert, Oxidizing, and Reducing Environments. The Journal of Physical Chemistry C. 120, 14015–14026 (2016). https://doi.org/10.1021/acs.jpcc.6b01208

215. FRENTZEL-BEYME, L., KLOß, M., PALLACH, R., SALAMON, S., MOLDENHAUER, H., LANDERS, J., WENDE, H., DEBUS, J., HENKE, S.: Porous

purple glass – a cobalt imidazolate glass with accessible porosity from a meltable cobalt imidazolate framework. J. Mater. Chem. A. 7, 985–990 (2019). https://doi.org/10.1039/C8TA08016J

216. GUZMÁN-EMBÚS, D.A., VARGAS-CHARRY, M.F., VARGAS-HERNÁNDEZ, C.: Optical and Structural Properties of ZnO and ZnO:Cd Particles Grown by the Hydrothermal Method. Journal of the American Ceramic Society. 98, 1498–1505 (2015). https://doi.org/https://doi.org/10.1111/jace.13460

217. TORCHYNSKA, T., EL FILALI, B., JARAMILLO GOMEZ, J.A., POLUPAN, G., RAMÍREZ GARCÍA, J.L., SHCHERBYNA, L.: Raman scattering, emission, and deep defect evolution in ZnO:In thin films. Journal of Vacuum Science & Technology A. 38, 063409 (2020). https://doi.org/10.1116/6.0000364

218. NIZAR, B.M., LAJNEF, M., CHASTE, J., CHTOUROU, R., HERTH, E.: Highly C-oriented (002) plane ZnO nanowires synthesis. RSC Adv. 13, 15077–15085 (2023). https://doi.org/10.1039/D3RA01511D

219. STANKOVIĆ, A., STOJANOVIĆ, Z., VESELINOVIĆ, L., ŠKAPIN, S.D., BRAČKO, I., MARKOVIĆ, S., USKOKOVIĆ, D.: ZnO micro and nanocrystals with enhanced visible light absorption. Materials Science and Engineering: B. 177, 1038–1045 (2012). https://doi.org/https://doi.org/10.1016/j.mseb.2012.05.013

220. CAI, X., PENG, F., LUO, X., YE, X., ZHOU, J., LANG, X., SHI, M.: Understanding the Evolution of Cobalt-Based Metal-Organic Frameworks in Electrocatalysis for the Oxygen Evolution Reaction. ChemSusChem. 14, 3163–3173 (2021). https://doi.org/https://doi.org/10.1002/cssc.202100851

221. SUN, Y., LI, Y., TAN, J.-C.: Liquid Intrusion into Zeolitic Imidazolate Framework-7 Nanocrystals: Exposing the Roles of Phase Transition and Gate Opening to Enable Energy Absorption Applications. ACS Appl. Mater. Interfaces. 10, 41831–41838 (2018). https://doi.org/10.1021/acsami.8b16527

222. ARAÚJO JÚNIOR, E.A., NOBRE, F.X., SOUSA, G. DA S., CAVALCANTE, L.S., DE MORAIS CHAVES SANTOS, M., SOUZA, F.L., DE MATOS, J.M.: Synthesis, growth mechanism, optical properties and catalytic activity of ZnO microcrystals obtained via hydrothermal processing. RSC Adv. 7, 24263–24281 (2017). https://doi.org/10.1039/C7RA03277C

223. MOLLICK, S., ZHANG, Y., KAMAL, W., TRICARICO, M., MÖSLEIN, A.F., KACHWAL, V., AMIN, N., CASTREJÓN-PITA, A.A., MORRIS, S.M., TAN, J.-C.: Surface modulation of metal-organic frameworks for on-demand photochromism in the solid state.

224. YANG, X., JIANG, S., ZHANG, Z., LI, B., XU, M.: The preparation of ZIF-67 and its synergistic effect on fire performance of intumescent flame retardant polypropylene. J.

Therm. Anal. Calorim. 148, 9547–9560 (2023). https://doi.org/10.1007/s10973-023-12316-9

225. HU, H., LIU, S., CHEN, C., WANG, J., ZOU, Y., LIN, L., YAO, S.: Two novel zeolitic imidazolate frameworks (ZIFs) as sorbents for solid-phase extraction (SPE) of polycyclic aromatic hydrocarbons (PAHs) in environmental water samples. Analyst. 139, 5818–5826 (2014). https://doi.org/10.1039/C4AN01410C

226. BERGAOUI, M., KHALFAOUI, M., AWADALLAH-F, A., AL-MUHTASEB, S.: A review of the features and applications of ZIF-8 and its derivatives for separating CO_2 and isomers of C3- and C4- hydrocarbons. J. Nat. Gas Sci. Eng. 96, 104289 (2021). https://doi.org/https://doi.org/10.1016/j.jngse.2021.104289

227. DOU, S., DONG, C.-L., HU, Z., HUANG, Y.-C., CHEN, J., TAO, L., YAN, D., CHEN, D., SHEN, S., CHOU, S., WANG, S.: Atomic-Scale CoOx Species in Metal–Organic Frameworks for Oxygen Evolution Reaction. Adv. Funct. Mater. 27, 1702546 (2017). https://doi.org/https://doi.org/10.1002/adfm.201702546

228. SUN, M., WANG, M., GE, C., HUANG, J., LI, Y., YAN, P., WANG, M., LEI, S., BAI, L., QIAO, G.: Au-doped ZnO@ZIF-7 core-shell nanorod arrays for highly sensitive and selective NO2 detection. Sens. Actuators B Chem. 384, 133632 (2023). https://doi.org/https://doi.org/10.1016/j.snb.2023.133632

229. LI, Y., WEE, L.H., MARTENS, J.A., VANKELECOM, I.F.J.: ZIF-71 as a potential filler to prepare pervaporation membranes for bio-alcohol recovery. J. Mater. Chem. A. 2, 10034–10040 (2014). https://doi.org/10.1039/C4TA00316K

230. SCHWEINEFUß, M.E., SPRINGER, S., BABURIN, I.A., HIKOV, T., HUBER, K., LEONI, S., WIEBCKE, M.: Zeolitic imidazolate framework-71 nanocrystals and a novel SOD-type polymorph: solution mediated phase transformations, phase selection via coordination modulation and a density functional theory derived energy landscape. Dalton Trans. 43, 3528–3536 (2014). https://doi.org/10.1039/C3DT52992D

231. LIVELY, R.P., DOSE, M.E., THOMPSON, J.A., MCCOOL, B.A., CHANCE, R.R., KOROS, W.J.: Ethanol and water adsorption in methanol-derived ZIF-71. Chem. Commun. 47, 8667–8669 (2011). https://doi.org/10.1039/C1CC12728D

232. BISQUERT, J.: Inductive and Capacitive Hysteresis of Current-Voltage Curves: Unified Structural Dynamics in Solar Energy Devices, Memristors, Ionic Transistors, and Bioelectronics. PRX Energy. 3, 11001 (2024). https://doi.org/10.1103/PRXEnergy.3.011001

233. BISQUERT, J., GUERRERO, A., GONZALES, C.: Theory of Hysteresis in Halide Perovskites by Integration of the Equivalent Circuit. ACS Physical Chemistry Au. 1, 25–44 (2021). https://doi.org/10.1021/acsphyschemau.1c00009

234. RATHNASEKARA, R., MAYBERRY, G.M., HARI, P.: Deep-Level Transient Spectroscopy Studies on Four Different Zinc Oxide Morphologies. Crystals (Basel). 14, (2024). https://doi.org/10.3390/cryst14030224

235. ZHAO, X., LI, J., LI, H., LI, S.: Intrinsic and extrinsic defect relaxation behavior of ZnO ceramics. J. Appl. Phys. 111, 124106 (2012). https://doi.org/10.1063/1.4729804

236. PATWARI, G., KALITA, P.K., SINGHA, R.: Structural and optoelectronic properties of glucose capped Al and Cu doped ZnO nanostructures. Materials Science- Poland. 34, 69–78 (2016). https://doi.org/10.1515/msp-2016-0030

237. ELHAMDI, I., SOUISSI, H., TAKTAK, O., ELGHOUL, J., KAMMOUN, S., DHAHRI, E., COSTA, B.F.O.: Experimental and modeling study of ZnO:Ni nanoparticles for near-infrared light emitting diodes. RSC Adv. 12, 13074–13086 (2022). https://doi.org/10.1039/d2ra00452f

238. Kortidis, I., Lushozi, S., Leshabane, N., Nkosi, S.S., Ndwandwe, O.M., Tshilongo, J., Ntsasa, N., Motaung, D.E.: Selective detection of propanol vapour at low operating temperature utilizing ZnO nanostructures. Ceram. Int. 45, 16417–16423 (2019). https://doi.org/https://doi.org/10.1016/j.ceramint.2019.05.172

239. HUANG, H., DU, Z., WU, H.-C., GAO, F., JIANG, L., HOU, H., CHEN, S., LI, W., HU, F., YANG, W., ZHANG, D., WANG, L.: High-Temperature resistant ethanol sensing enhanced by ZnO Nanoparticles/SiC nanowire heterojunctions. Appl. Surf. Sci. 645, 158828 (2024). https://doi.org/https://doi.org/10.1016/j.apsusc.2023.158828

240. PILIAI, L., TOMEČEK, D., HRUŠKA, M., KHALAKHAN, I., NOVÁKOVÁ, J., FITL, P., YATSKIV, R., GRYM, J., VOROKHTA, M., MATOLÍNOVÁ, I., VRŇATA, M.: New Insights towards High-Temperature Ethanol-Sensing Mechanism of ZnO-Based Chemiresistors. Sensors. 20, (2020). https://doi.org/10.3390/s20195602

241. MENG, F., LI, G., JI, H., YUAN, Z.: Investigation on oxygen vacancy regulation mechanism of ZnO gas sensors under temperature modulation mode to distinguish alcohol homologue gases. Sens. Actuators B Chem. 423, 136747 (2025). https://doi.org/https://doi.org/10.1016/j.snb.2024.136747

242. YANG, X., WANG, W., XIONG, J., CHEN, L., MA, Y.: ZnO:Cd nanorods hydrogen sensor with low operating temperature. Int. J. Hydrogen Energy. 40, 12604–12609 (2015). https://doi.org/https://doi.org/10.1016/j.ijhydene.2015.07.086

243. LIU, X., CHEN, N., XING, X., LI, Y., XIAO, X., WANG, Y., DJERDJ, I.: A high-performance n-butanol gas sensor based on ZnO nanoparticles synthesized by a low-temperature solvothermal route. RSC Adv. 5, 54372–54378 (2015). https://doi.org/10.1039/C5RA05148G

244. ROUT, C.S., HARI KRISHNA, S., VIVEKCHAND, S.R.C., GOVINDARAJ, A., RAO, C.N.R.: Hydrogen and ethanol sensors based on ZnO nanorods, nanowires and nanotubes.

Chem. Phys. Lett. 418, 586–590 (2006).
https://doi.org/https://doi.org/10.1016/j.cplett.2005.11.040

245. HAZRA, S.K., BASU, S.: Hydrogen sensitivity of ZnO p–n homojunctions. Sens. Actuators B Chem. 117, 177–182 (2006). https://doi.org/https://doi.org/10.1016/j.snb.2005.11.018

246. PARK, S.: High-response and selective hydrogen sensing properties of porous ZnO nanotubes. Current Applied Physics. 16, 1263–1269 (2016). https://doi.org/https://doi.org/10.1016/j.cap.2016.07.005

247. ZHAO, R., LI, K., WANG, Z., XING, X., WANG, Y.: Gas-sensing performances of Cd-doped ZnO nanoparticles synthesized by a surfactant-mediated method for n-butanol gas. Journal of Physics and Chemistry of Solids. 112, 43–49 (2018). https://doi.org/https://doi.org/10.1016/j.jpcs.2017.08.039

248. MOMMA, K., IZUMI, F.: VESTA 3 for three-dimensional visualization of crystal, volumetric and morphology data. J. Appl. Crystallogr. 44, 1272–1276 (2011). https://doi.org/10.1107/S0021889811038970

249. JONES, I.M., TURNER, G.F., PITTS, K., POWELL, R., RIBOLDI-TUNNICLIFFE, A., WILLIAMSON, R., BOER, S., ALLEN, L., MOGGACH, S.A.: High-pressure induced guest-mediated gate opening behaviour of the Co-based framework ZIF-67. CrystEngComm. 25, 6533–6538 (2023). https://doi.org/10.1039/D3CE00979C

250. DEROUANE, E.G.: The energetics of sorption by molecular sieves: Surface curvature effects. Chem. Phys. Lett. 142, 200–204 (1987). https://doi.org/https://doi.org/10.1016/0009-2614(87)80922-3

251. XIONG, Y., XU, W., ZHU, Z., XUE, Q., LU, W., DING, D., ZHU, L.: ZIF-derived porous ZnO-Co_3O_4 hollow polyhedrons heterostructure with highly enhanced ethanol detection performance. Sens. Actuators B Chem. 253, 523–532 (2017). https://doi.org/https://doi.org/10.1016/j.snb.2017.06.169

252. POLYAKOV, V.A., BUTOVA, V. V, EROFEEVA, E.A., TERESHCHENKO, A.A., SOLDATOV, A. V: MW Synthesis of ZIF-7. The Effect of Solvent on Particle Size and Hydrogen Sorption Properties. Energies (Basel). 13, (2020). https://doi.org/10.3390/en13236306

253. KEYVANLOO, Z., NAKHAEI POUR, A., MOOSAVI, F.: Adsorption and diffusion of the H_2/CO_2/CO/MeOH/EtOH mixture into the ZIF-7 using molecular simulation. J. Mol. Graph. Model. 116, 108275 (2022). https://doi.org/https://doi.org/10.1016/j.jmgm.2022.108275

254. DU, Y., WOOLER, B., NINES, M., KORTUNOV, P., PAUR, C.S., ZENGEL, J., WESTON, S.C., RAVIKOVITCH, P.I.: New High- and Low-Temperature Phase Changes

of ZIF-7: Elucidation and Prediction of the Thermodynamics of Transitions. J. Am. Chem. Soc. 137, 13603–13611 (2015). https://doi.org/10.1021/jacs.5b08362

255. ZHANG, K., ZHANG, L., JIANG, J.: Adsorption of C1–C4 Alcohols in Zeolitic Imidazolate Framework-8: Effects of Force Fields, Atomic Charges, and Framework Flexibility. The Journal of Physical Chemistry C. 117, 25628–25635 (2013). https://doi.org/10.1021/jp409869c

256. LUPAN, O., CHOW, L., PAUPORTÉ, TH., ONO, L.K., ROLDAN CUENYA, B., CHAI, G.: Highly sensitive and selective hydrogen single-nanowire nanosensor. Sens. Actuators B Chem. 173, 772–780 (2012). https://doi.org/https://doi.org/10.1016/j.snb.2012.07.111

257. VANDEZANDE, W., JANSSEN, K.P.F., DELPORT, F., AMELOOT, R., DE VOS, D.E., LAMMERTYN, J., ROEFFAERS, M.B.J.: Parts per Million Detection of Alcohol Vapors via Metal Organic Framework Functionalized Surface Plasmon Resonance Sensors. Anal. Chem. 89, 4480–4487 (2017). https://doi.org/10.1021/acs.analchem.6b04510

258. CHOWDHURY, N.K., BHOWMIK, B.: Micro/nanostructured gas sensors: the physics behind the nanostructure growth, sensing and selectivity mechanisms. Nanoscale Adv. 3, 73–93 (2021). https://doi.org/https://doi.org/10.1039/d0na00552e

259. MOKOENA, T.P., SWART, H.C., HILLIE, K.T., TSHABALALA, Z.P., JOZELA, M., TSHILONGO, J., MOTAUNG, D.E.: Enhanced propanol gas sensing performance of p-type NiO gas sensor induced by exceptionally large surface area and crystallinity. Appl. Surf. Sci. 571, 151121 (2022). https://doi.org/https://doi.org/10.1016/j.apsusc.2021.151121

260. KAR CHOWDHURY, N., BHOWMIK, B.: Pd/TiO$_2$ nanosheet/Ti sensor towards propanol sensing: Influence of edge energy and defect states. Mater. Today Proc. 56, 984–988 (2022). https://doi.org/https://doi.org/10.1016/j.matpr.2022.03.113

261. WANG, J., YANG, J., HAN, N., ZHOU, X., GONG, S., YANG, J., HU, P., CHEN, Y.: Highly sensitive and selective ethanol and acetone gas sensors based on modified ZnO nanomaterials. Mater. Des. 121, 69–76 (2017). https://doi.org/https://doi.org/10.1016/j.matdes.2017.02.048

262. CHOUDHARY, M., SHRIVASTAV, A., SINHA, A.K., CHAWLA, A.K., AVASTHI, D.K., SARAVANAN, K., KRISHNAMURTHY, S., CHANDRA, R., WADHWA, S.: Emerging nanomaterials for hydrogen sensing: Mechanisms and prospects, (2024)

263. KIM, H.-J., LEE, J.-H.: Highly sensitive and selective gas sensors using p-type oxide semiconductors: Overview. Sens. Actuators B Chem. 192, 607–627 (2014). https://doi.org/https://doi.org/10.1016/j.snb.2013.11.005

264. MAŃKOWSKA, E., MAZUR, M., DOMARADZKI, J., MAZUR, P., KOT, M., FLEGE, J.I.: Hydrogen Gas Sensing Properties of Mixed Copper–Titanium Oxide Thin Films. Sensors. 23, (2023). https://doi.org/10.3390/s23083822

265. BALANAGIREDDY, G., NARAYANA, A., ROOPA, M.: Deployment of low-cost green synthesized SnO_2 and CuO nanoparticles bi-layer based transistor for H2S detection. Results Chem. 7, 101322 (2024). https://doi.org/https://doi.org/10.1016/j.rechem.2024.101322

266. CHEN, B.-E., WU, C.-X., TSAI, J.-H.: Resistive Hydrogen Sensor Based on Amorphous CuO Thin Film Covered With Pd Nanoparticles. IEEE Sens. Lett. 6, 1–4 (2022). https://doi.org/10.1109/LSENS.2022.3201035

267. BHAT, N., UKKUND, S.J., ASHRAF, M., ACHARYA, K., J. RAMEGOUDA, N., PUTHIYILLAM, P., HASAN, M.A., ISLAM, S., KORADOOR, V.B., PRAVEEN, A.D., KHAN, M.A.: GO/CuO Nanohybrid-Based Carbon Dioxide Gas Sensors with an Arduino Detection Unit. ACS Omega. 8, 32512–32519 (2023). https://doi.org/10.1021/acsomega.3c02598

268. NAKATE, U.T., LEE, G.H., AHMAD, R., PATIL, P., HAHN, Y.-B., YU, Y.T., SUH, E.: Nano-bitter gourd like structured CuO for enhanced hydrogen gas sensor application. Int. J. Hydrogen Energy. 43, 22705–22714 (2018). https://doi.org/https://doi.org/10.1016/j.ijhydene.2018.09.162

269. LIN, R., HU, Q., LIU, Z., PAN, S., CHEN, Z., ZHANG, W., LIU, Z., ZHANG, S., ZHANG, C.: Integrated CuO/Pd Nanospike Hydrogen Sensor on Silicon Substrate. Nanomaterials. 12, (2022). https://doi.org/10.3390/nano12091533

270. ZHAO, M., NITTA, R., IZAWA, S., YAMAURA, J. ICHI, MAJIMA, Y.: Nano-Patterned CuO Nanowire Nanogap Hydrogen Gas Sensor with Voids. Adv. Funct. Mater. (2024). https://doi.org/10.1002/adfm.202415971

271. ZHOU, T., SANG, Y., SUN, Y., WU, C., WANG, X., TANG, X., ZHANG, T., WANG, H., XIE, C., ZENG, D.: Gas Adsorption at Metal Sites for Enhancing Gas Sensing Performance of ZnO@ZIF-71 Nanorod Arrays. Langmuir. 35, 3248–3255 (2019). https://doi.org/10.1021/acs.langmuir.8b02642

272. ZHOU, Y., ZHOU, T., ZHANG, Y., TANG, L., GUO, Q., WANG, M., XIE, C., ZENG, D.: Synthesis of core-shell flower-like WO3@ZIF-71 with enhanced response and selectivity to H2S gas. Solid State Ion. 350, 115278 (2020). https://doi.org/https://doi.org/10.1016/j.ssi.2020.115278

273. ZHANG, M., LV, X., WANG, T., PEI, W., YANG, Y., LI, F., YIN, D., YU, H., DONG, X.: CuO-based gas sensor decorated by polyoxometalates electron acceptors: From constructing heterostructure to improved sensitivity and fast response for ethanol detection. Sens. Actuators B Chem. 415, 136016 (2024). https://doi.org/https://doi.org/10.1016/j.snb.2024.136016

274. RAJAT, Nagpal, SUGIHARA, M., LUPAN, C., MAGARIU, N., TJARDTS, T., MELING-LIZARDE, N., STRUNSKUS, T., JETTER. J., QIU, H., CHAKRABORTY, B., AMERI, T., QUANDT, E., ADELUNG, R., AMELOOT, R., LUPAN, O. In-situ

temperature-dependent properties of metal-organic frameworks ZIF-coated ZnO hybrid structures: structural and advanced spectroscopic insights, revised/accepted, ACS Omega, March, 2026.

ANNEX 1. Physicochemical and the corresponding gas-sensing properties of ZIF-8/CuO:Al hybrids
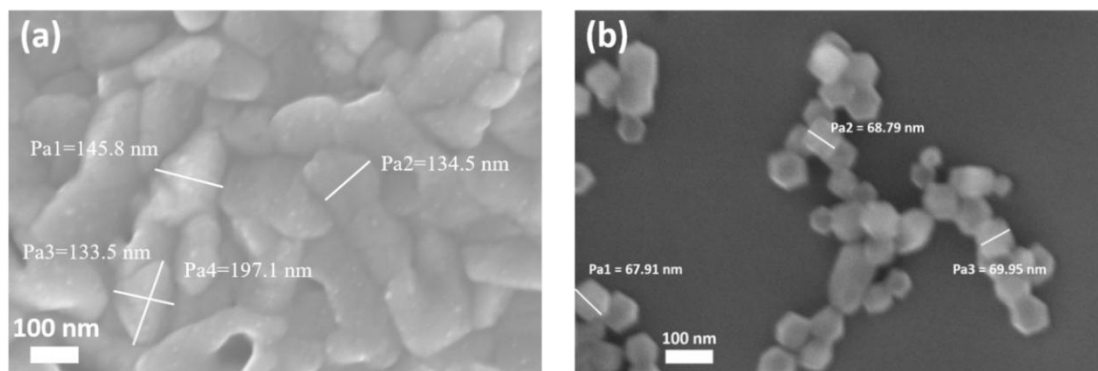
Fig. A1.1. SEM images of (a) the CuO:Al film on glass substrate, and (b) ZIF-8 nanoparticles on Si substrate showing the particle size.
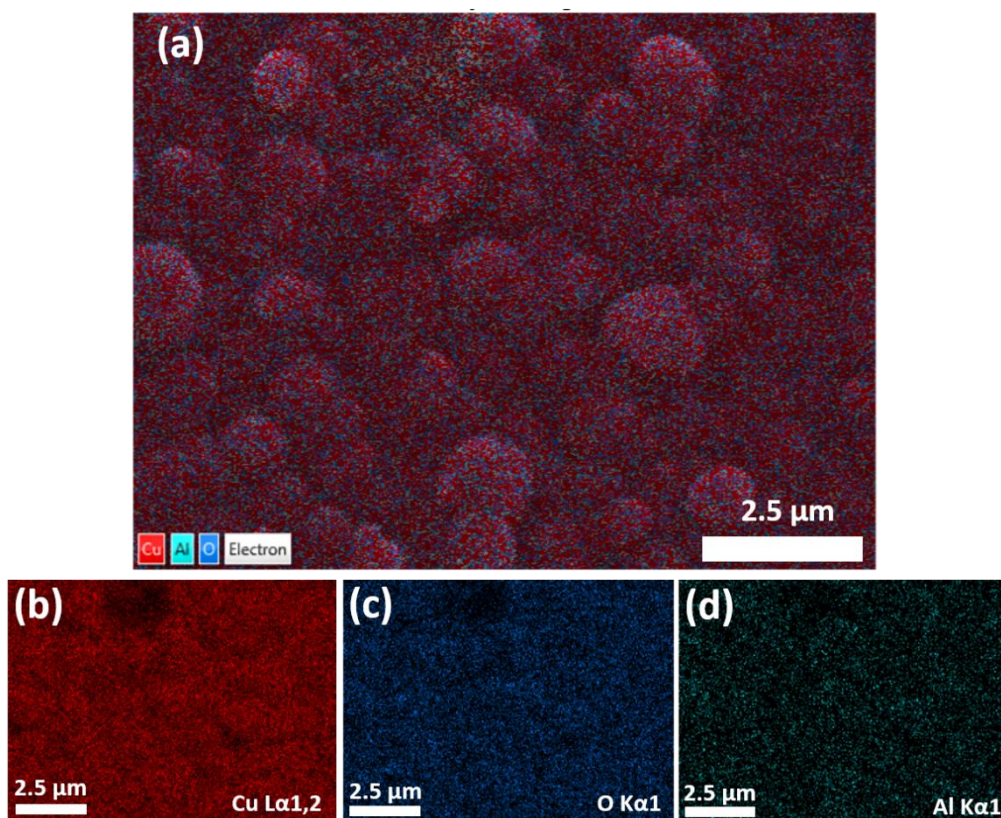

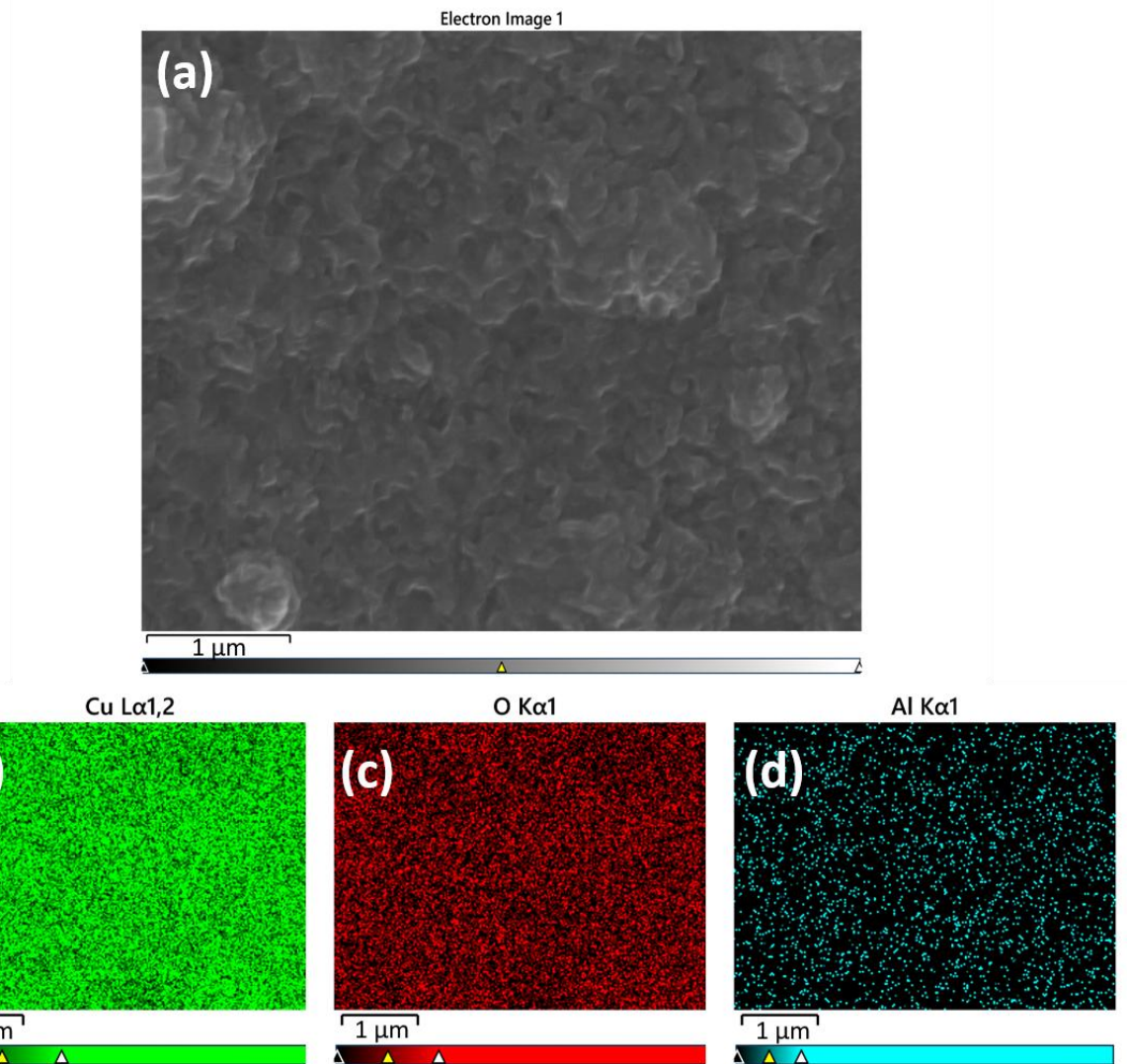**Fig. A1.2. (a) The SEM image of the investigated area in the CuO:Al film, and the composition images using EDX mapping: (b) Cu distribution, (c) O distribution, and (d) Al distribution.**
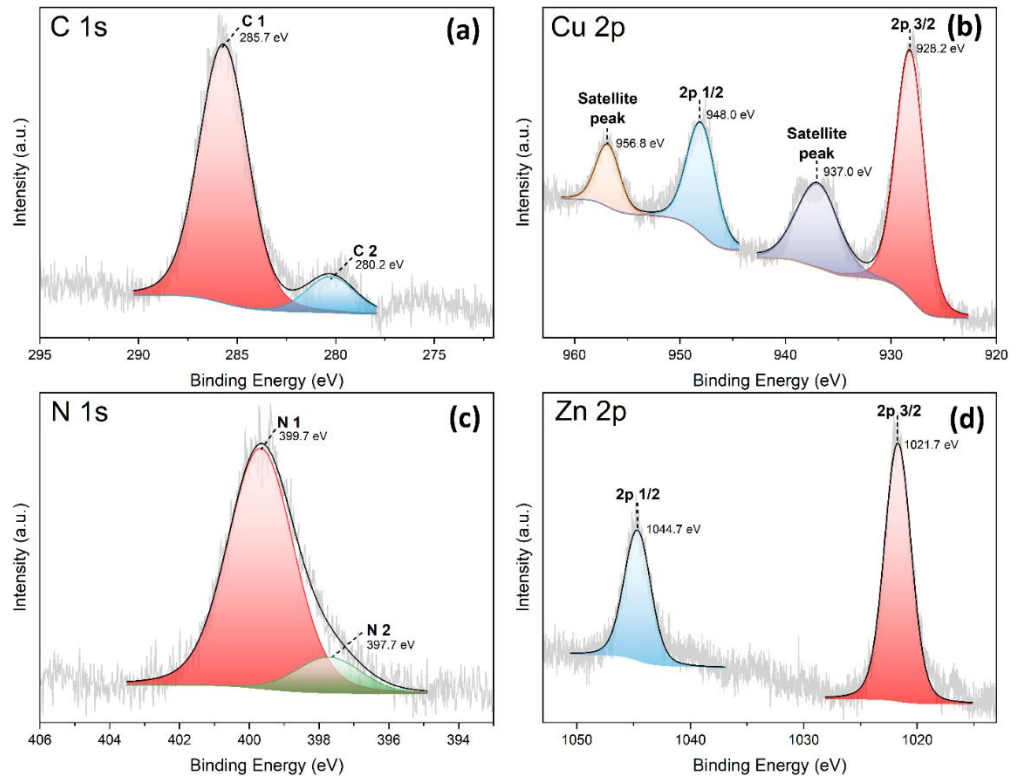
Fig. A1.3. High-resolution XPS spectra of the ZIF-8/CuO:Al (low coverage) sample: (a) C 1s, (b) Cu 2p, (c) N 1s and (d) Zn 2p spectrum.
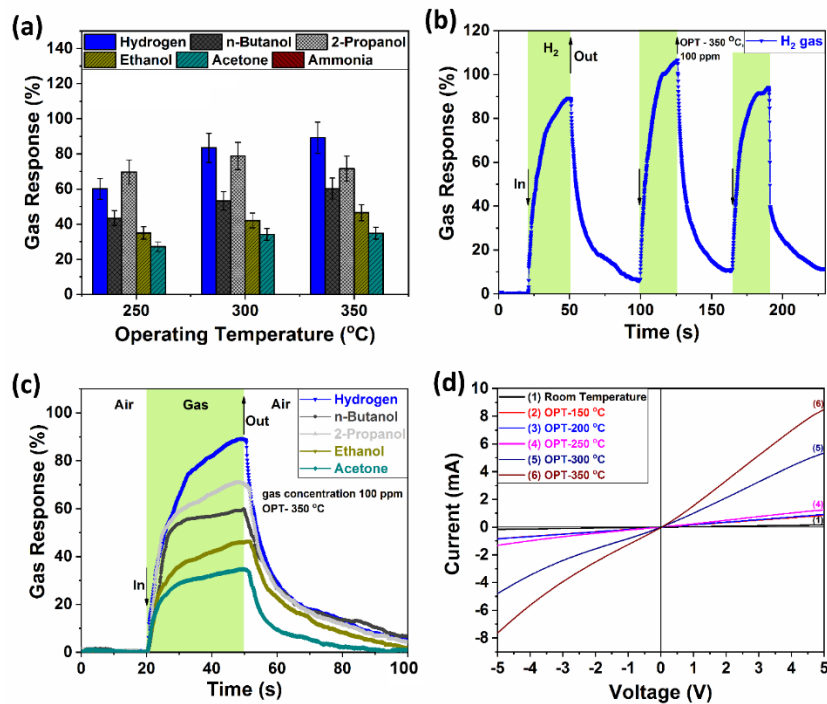
Fig. A1.4. Gas response of the CuO:Al based sensor: (a) to a series of gases with concentration of 100 ppm at 350 °C, (b) dynamic response to 100 ppm of hydrogen at 350 °C, and (c) dynamic characteristic of all the tested gases at 350 °C; (d) current-voltage (I-V) characteristics at different OPTs.
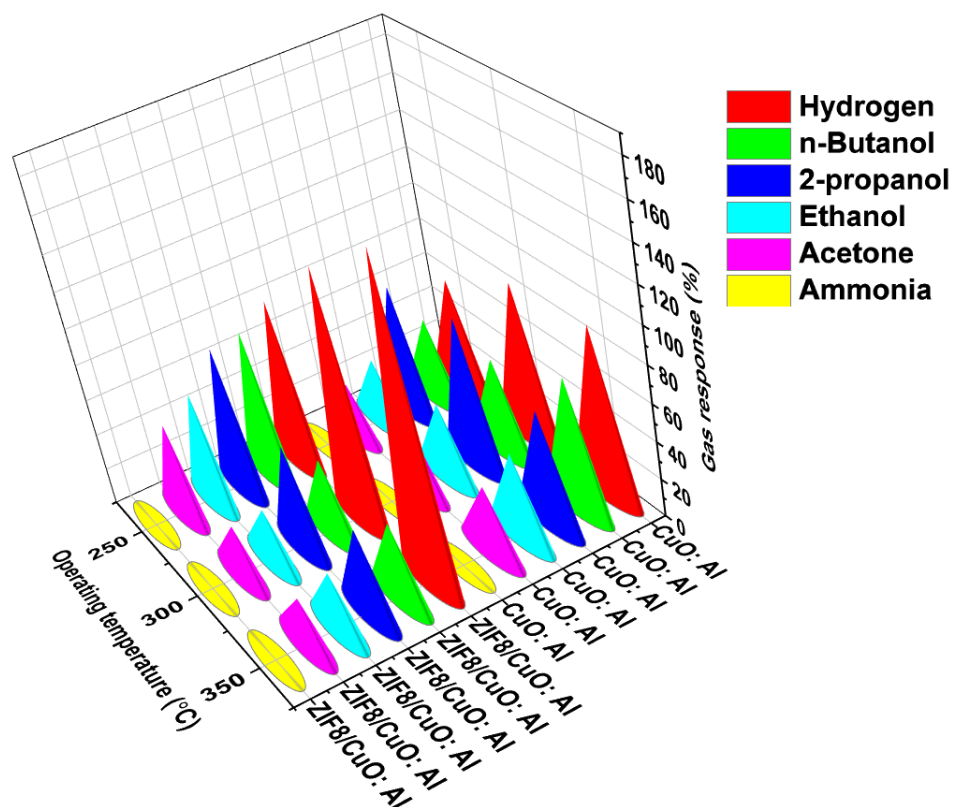
Fig. A1.5. The comparative visualization of the gas responses of the ZIF-8/CuO:Al and CuO:Al sensors to a series of gases with concentration 100 ppm at different operating temperatures.
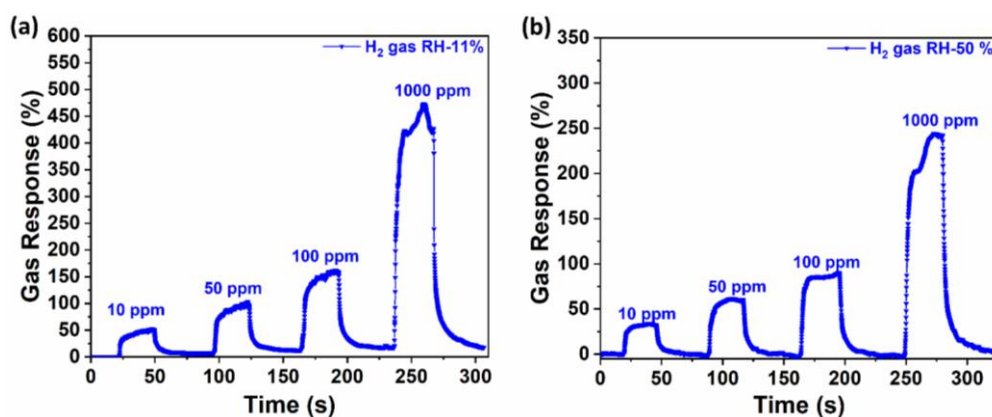
Fig. A1.6. Gas response of the ZIF-8/CuO:Al based hybrid sensor to different hydrogen concentrations and RH values (a). RH 11%, and (b). RH 50% after three weeks.
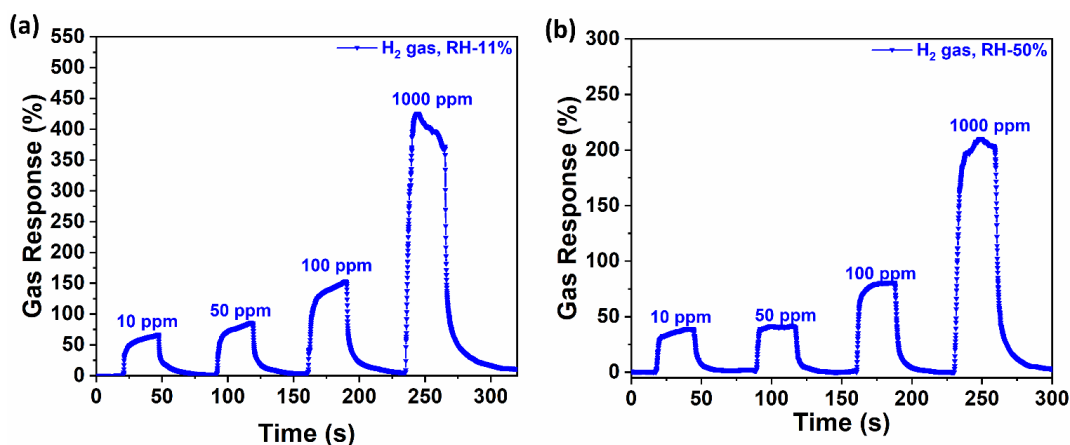
Fig. A1.7. Gas response of the ZIF-8/CuO:Al based hybrid sensor to different hydrogen concentrations and RH values (a). RH 11%, and (b). RH 50% after four weeks.

Table A1.1. A comparative study of the current work with the other reported literature.

Sensing material	OT (°C)	Target gas	Concentration (ppm)	Response (%)	RH (%)	LDL (ppb)	reference
(CuTi)O$_x$ thin film	200	H$_2$	1000	186	<10	-	[264]
ZnO:ZIF-8	270	H$_2$	50	40	-	-	[105]
SnO$_2$-CuO layer	RT	C$_2$H$_5$OH	-	65	-	-	[265]
Pd NPs/CuO	300	H$_2$	100	~125	-	-	[266]
GO/CuO	-	CO$_2$	-	~60	-	-	[267]
Nano-bitter CuO	200	H$_2$	100	~175	<30	2	[268]
Pd/CuO/Si	RT	H$_2$	1%	~10.8	-	40000	[269]
CuO NWs	300	H$_2$	5000	~259	50	-	[270]
CuO NWs	300	H$_2$	5000	~200	0	5	[270]
CuO:Al film	350	H$_2$	100	~90	11	-	This work
Z8/CuO: Al film	3350	H$_2$	100	~170	11	686	This work
Z8/CuO: Al film	250	C$_4$H$_9$OH	100	~80	11	-	This work
Z8/CuO: Al film	350	H$_2$	100	~152	50	-	This work

ANNEX 2. Physicochemical and sensing properties of ZIF-71/CuO:Al hybrids
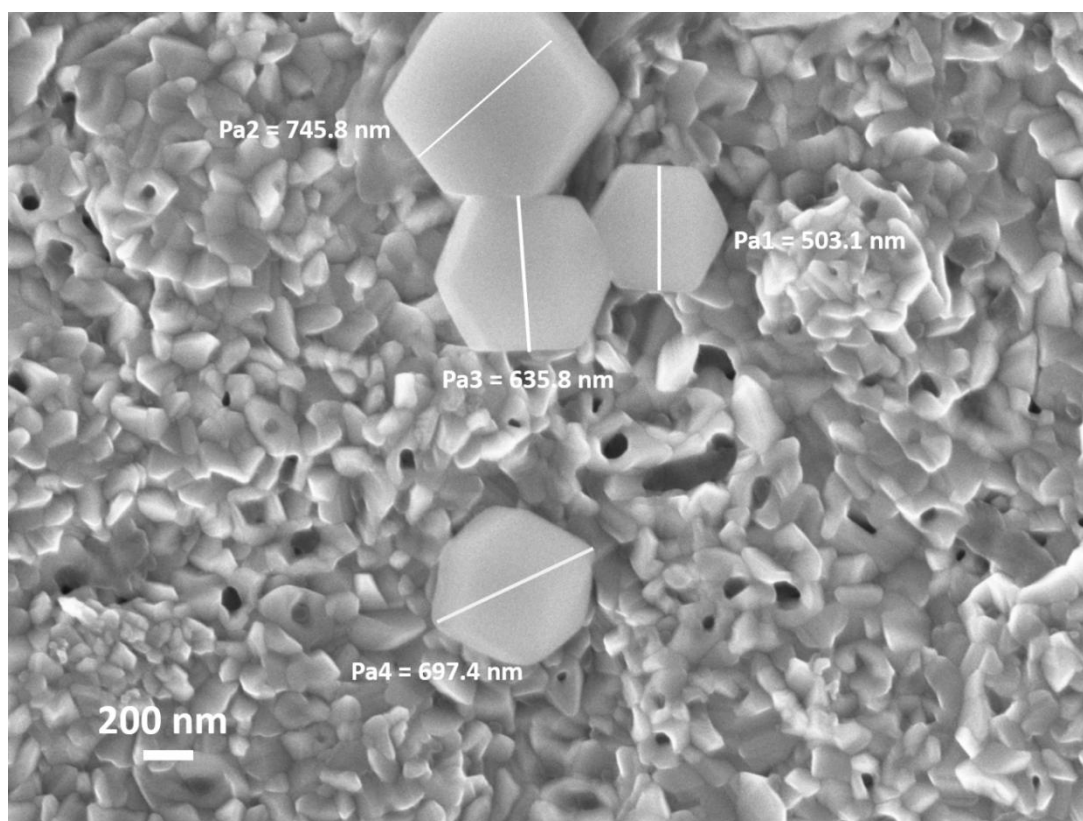
Fig. A2.1. Particle size determination of ZIF-71 particles using SEM, showing an average diameter in the range 500 to 750 nm.

Fig. A2.2. (a) The SEM image of the investigated area; and the composition images of the CuO:Al film using EDX mapping: (b) Cu distribution. (c) O distribution. (d) Al distribution.
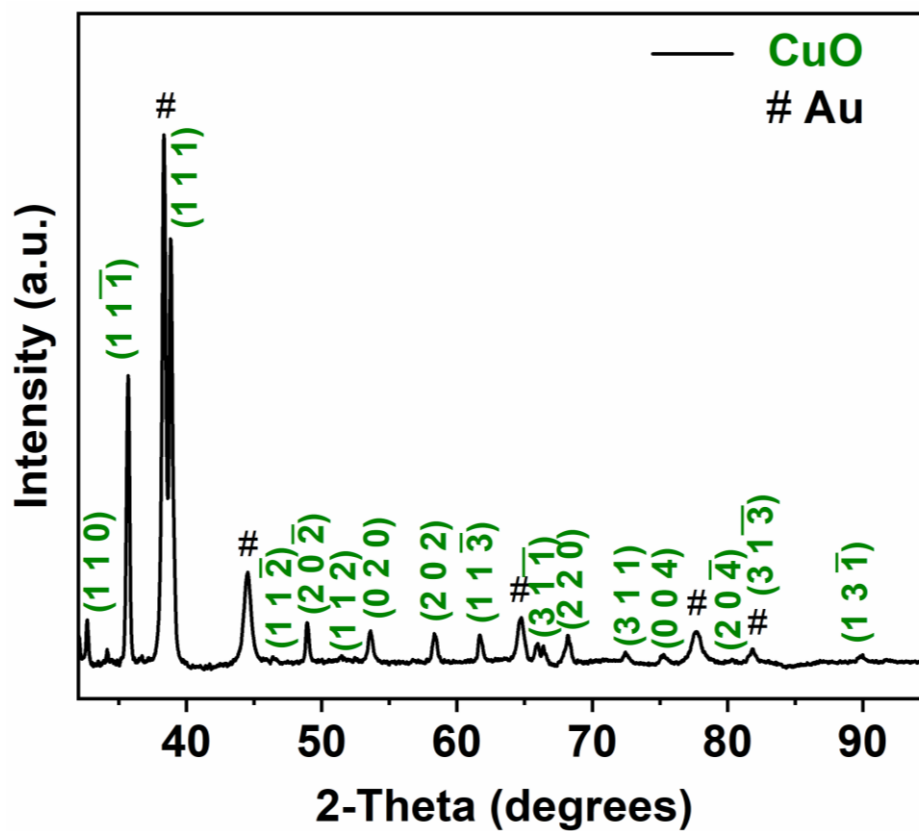
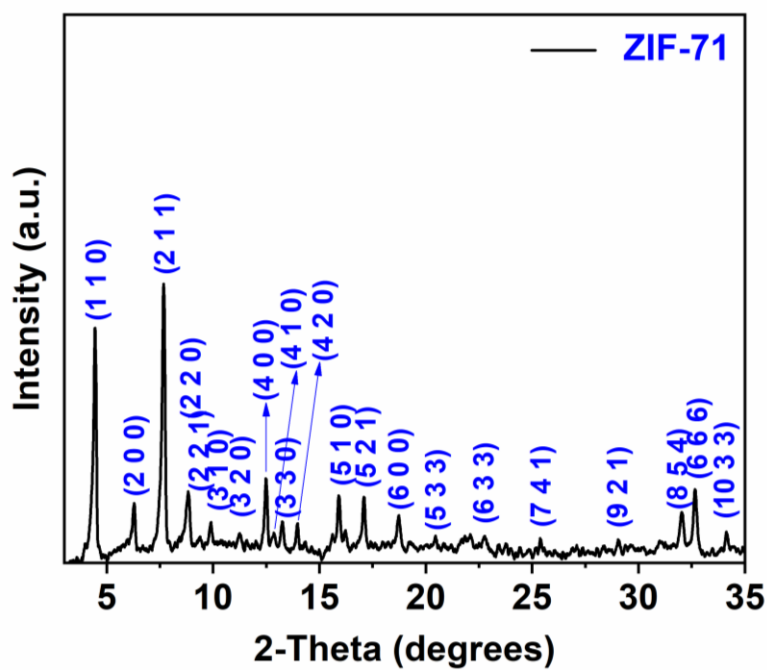**Fig. A2.3. X-ray diffraction pattern of the CuO:Al film with electrical Au contacts.**

Fig. A2.4. X-ray diffraction pattern of ZIF-71 particles.
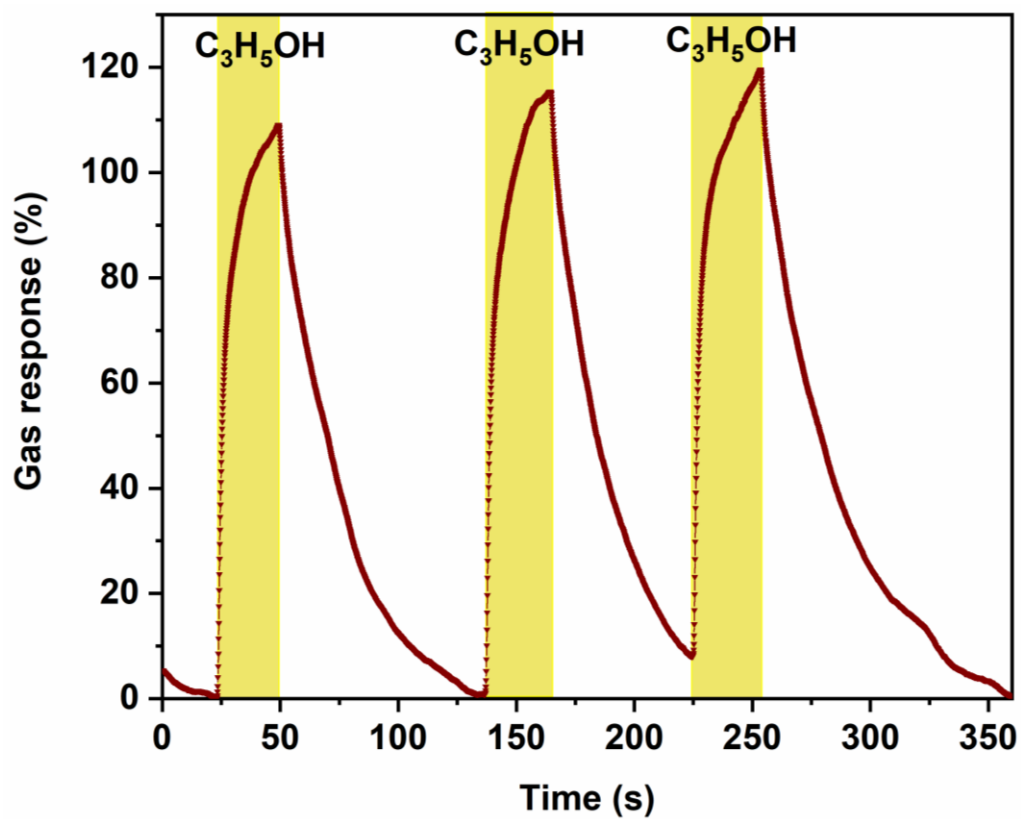
Fig. A2.5. Transient gas sensing response of the ZIF-71/CuO:Al-based MOF/MO hybrid sensor to acetone at 250 °C at RH 10%, measured 21 days after the initial measurements.
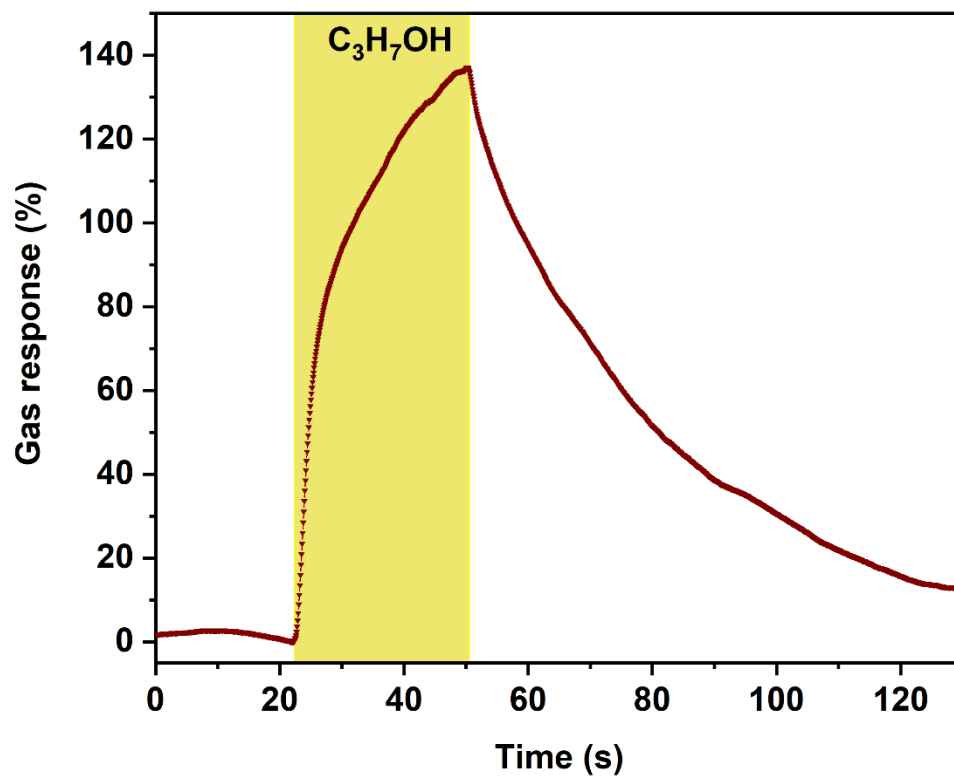
Fig. A2.6. Transient gas sensing response of the ZIF-71/CuO:Al-based MOF/MO hybrid sensor to 2-propanol at 250°C (after 21 days measurement).
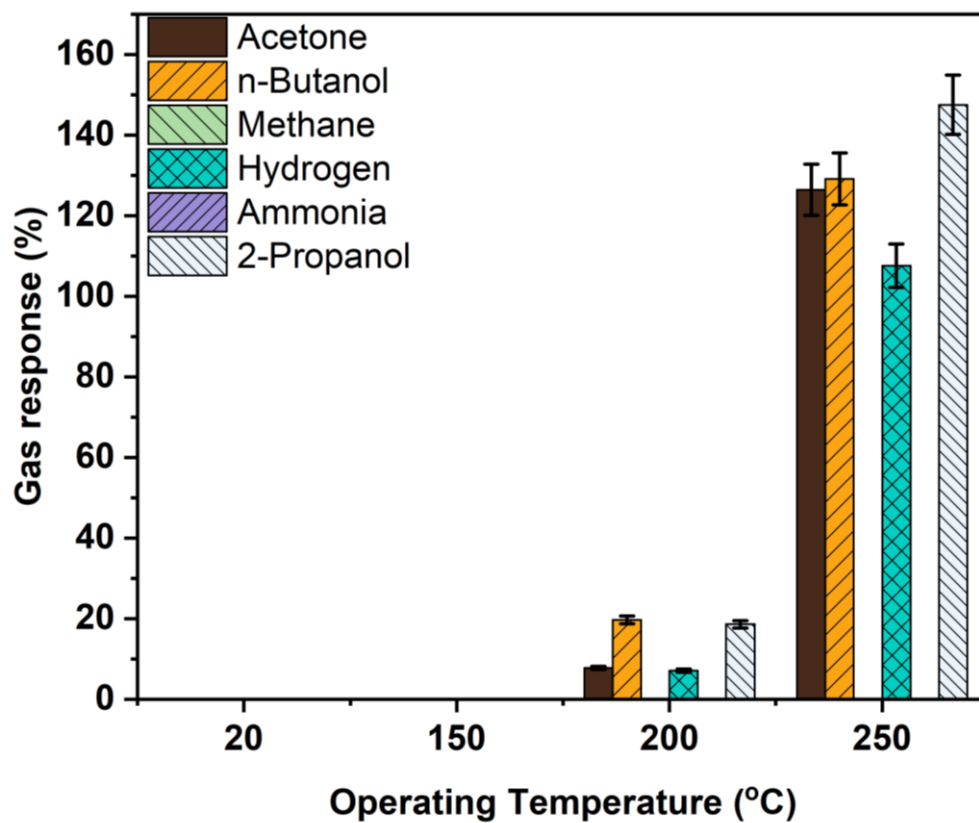
Fig. A2.7. Gas sensing response to a series of analytes at different operating temperatures from 20 to 250 °C for ZIF-71/CuO:Al films after 42 days from the initial measurements at RH 10%.
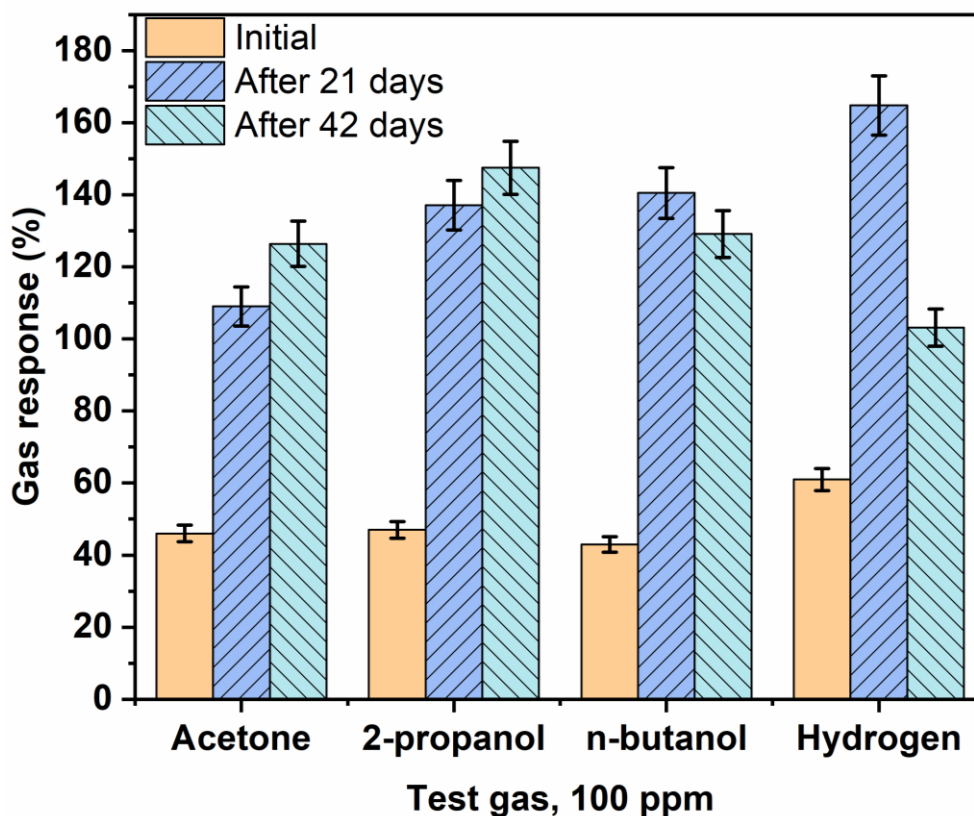
Fig. A2.8. Gas response of the ZIF-71/CuO:Al-based MOF/MO hybrid sensor to a series of gases at 250°C at RH 10%.

Table A2.1. Comparison chart of presented gas sensing results with other reported literature using a similar material combination.

Material (type) ref.	Concentration, test gas	Response value, S (%)	Enhancement in sensing response after ZIF-71 coating ($S_{\text{ZIF-71coated}}/S_{\text{uncoated}}$)	Response/recovery time (s)	Relative humidity (%)	Operating temperature (°C)
ZnO (nanorod arrays) [151]	50 ppm, hydrogen	~100	0.8	-	-	250
ZnO@ZIF-71 (nanorod arrays) [151]		~80		-	-	
ZnO (nanorod arrays) [271]	10 ppm, ethanol	2.59	~4	419.4/988.2	-	150
ZnO@ZIF-71 (nanorod arrays) [271]		13.4		194.3/442.1		
ZnO (nanorod arrays) [271]	5 ppm, acetone	20.6	~1.8	373.3/772.4	-	150
ZnO@ZIF-71 (nanorod arrays) [271]		38.9		195.9/535.5	-	

Material (type) ref.	Concentration, test gas	Response value, S (%)	Enhancement in sensing response after ZIF-71 coating ($S_{ZIF-71coated}/S_{uncoated}$)	Response/recovery time (s)	Relative humidity (%)	Operating temperature (°C)
WO$_3$ (nanorod arrays) [272]	20 ppm, ethanol	27	~6	-	-	250
WO$_3$@ZIF-71 (flower-like) [272]		163				
WO$_3$ (nanorod arrays) [272]	20 ppm, acetone	47	~2.1	-	-	250
WO$_3$@ZIF-71 (flower-like) [272]		101				
CuO/1%PMA (nanofibers) [273]	100 ppm, ethanol	66	-	5/4	30	240
CuO (nanowires) [270]	2500 ppm, hydrogen	100	-	25/14	0	300
		115		73/80	50	
CuO:Al (intergranular grains) (this work)	100 ppm, hydrogen	42	~1.4	11/14	10	250
ZIF-71/CuO:Al (rhombic dodecahedron) (this work)		61		2/11	10	
CuO:Al (intergranular grains) (this work)	100 ppm, n-butanol	~0.1	~110	-	10	200
ZIF-71/CuO:Al (rhombic dodecahedron) (this work)		11		~23/110	10	
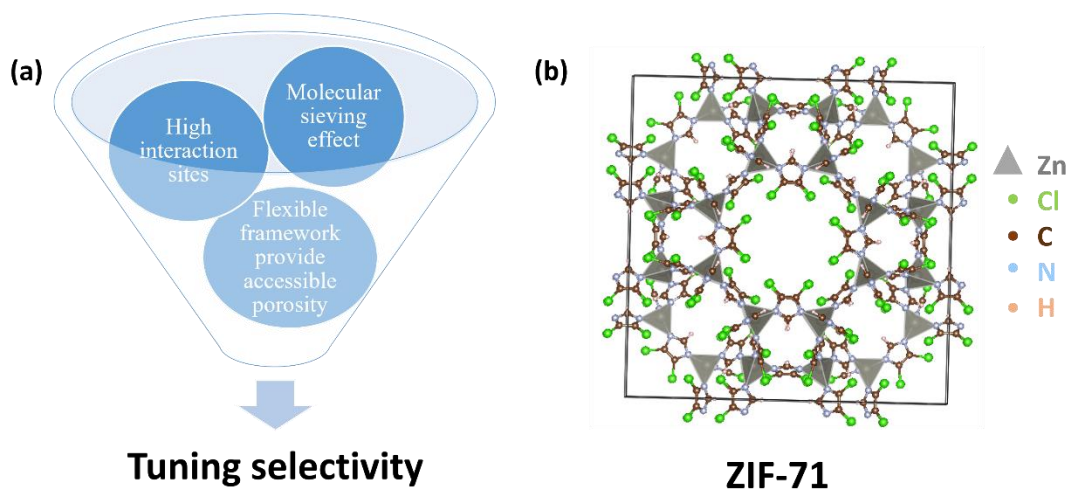
Fig. A2.9. (a) The schematic for tuning the selectivity using porous crystalline materials. (b) Crystal structure of metal-organic frameworks ZIF-71 visualized using VESTA.[248] Adapted with permission from ref. [171] Copyright 2008 Science.
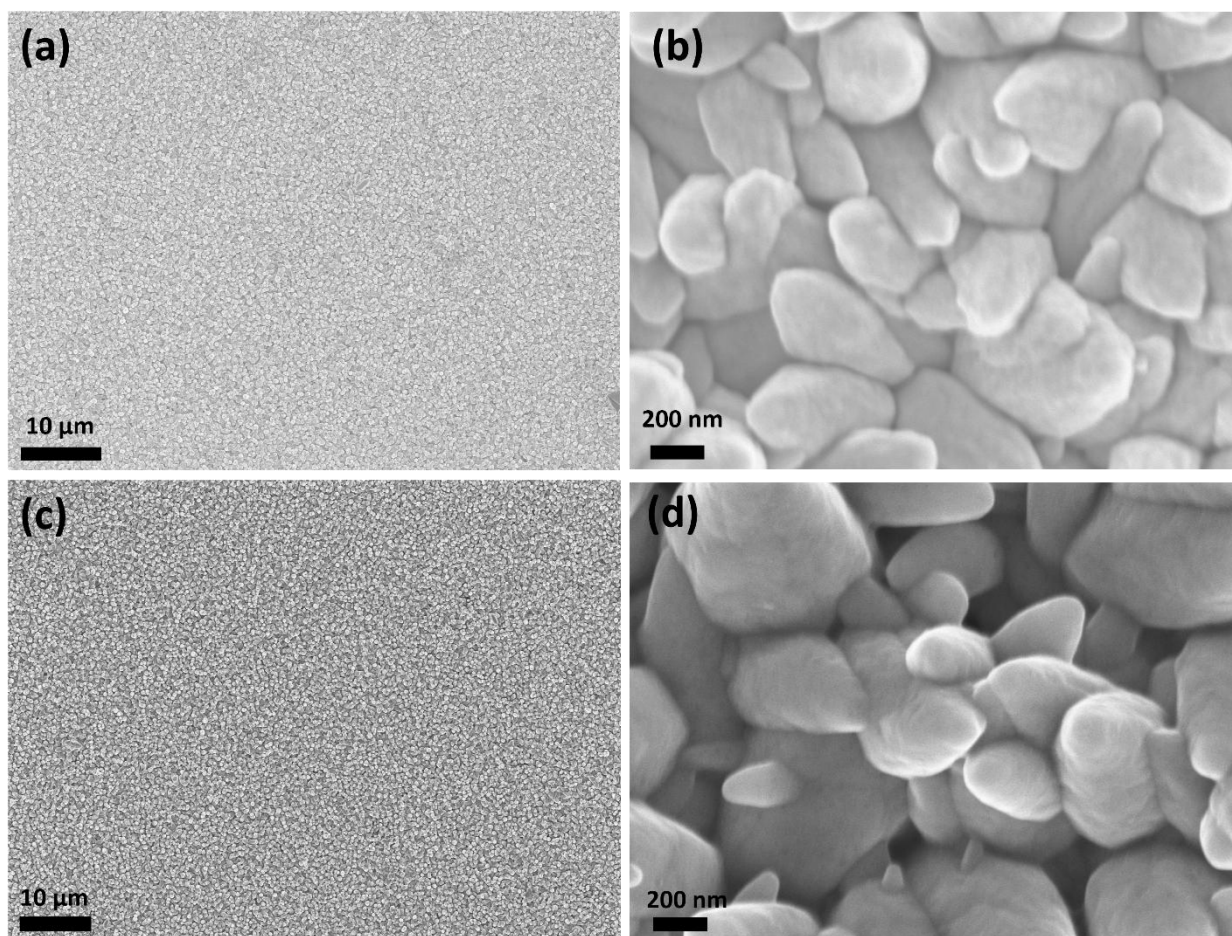
Fig. A3.1. SEM micrographs of the ZnO and Cd-doped ZnO films at lower magnification (a) and (b); and higher magnification (c) and (d), respectively.
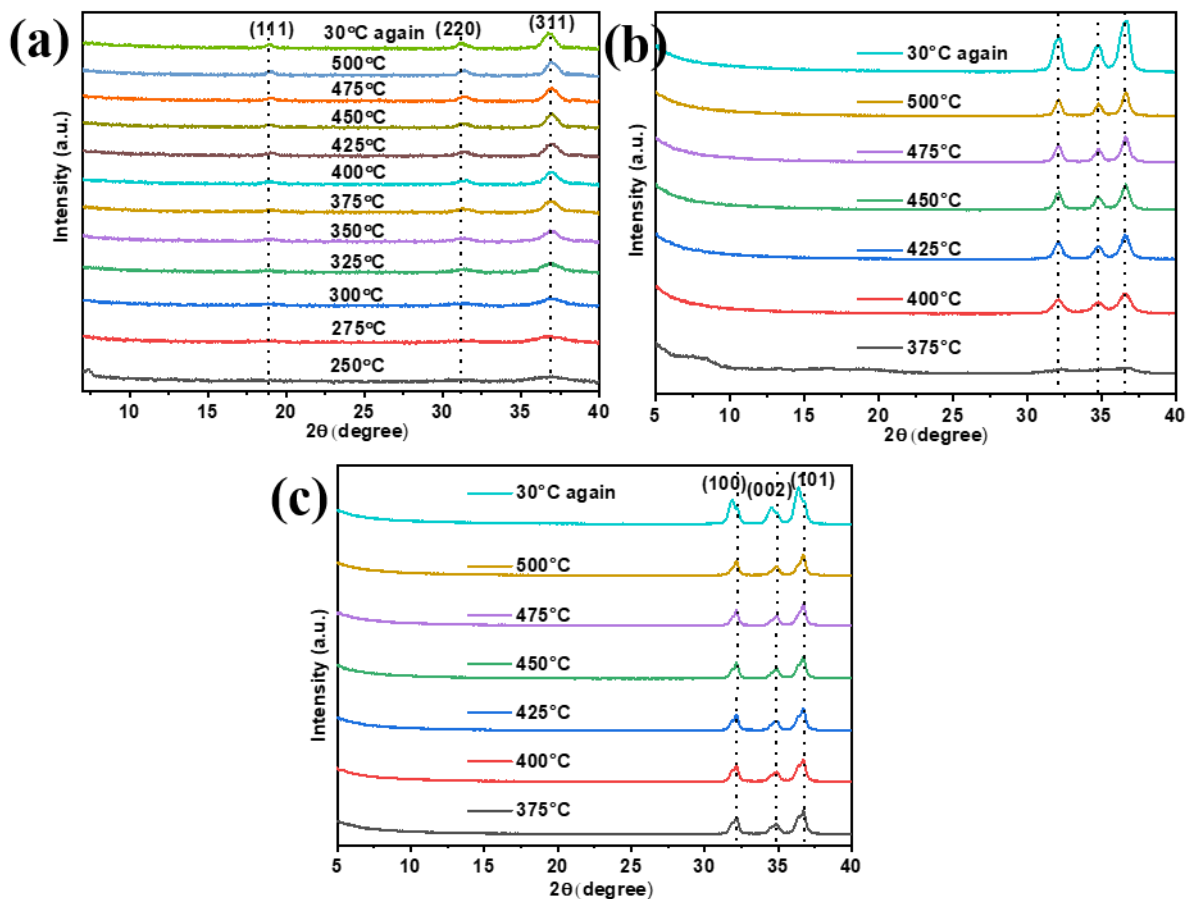
Fig. A3.2. XRD patterns of (a) ZIF-67 (b) ZIF-7 and (c) ZIF-71 on Si substrate during *in-situ* heating experiment.
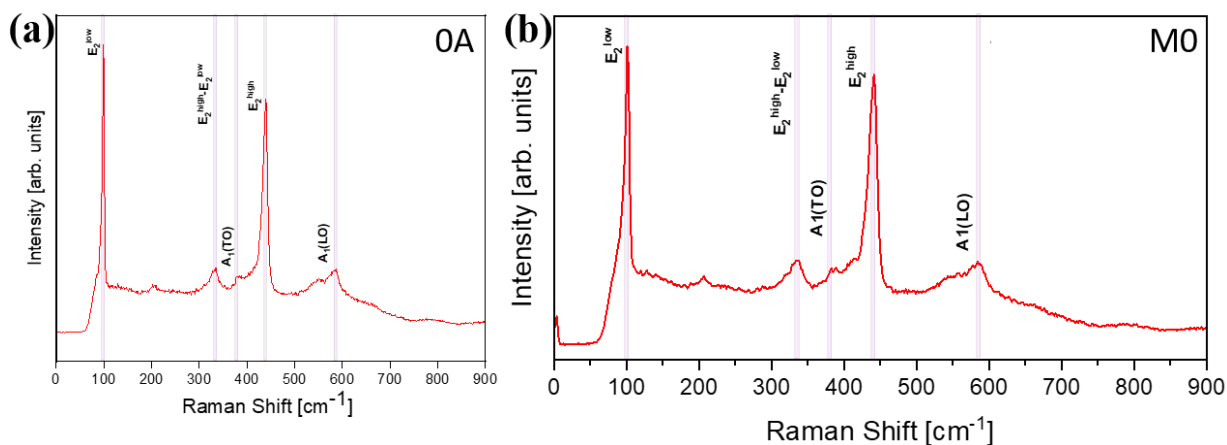
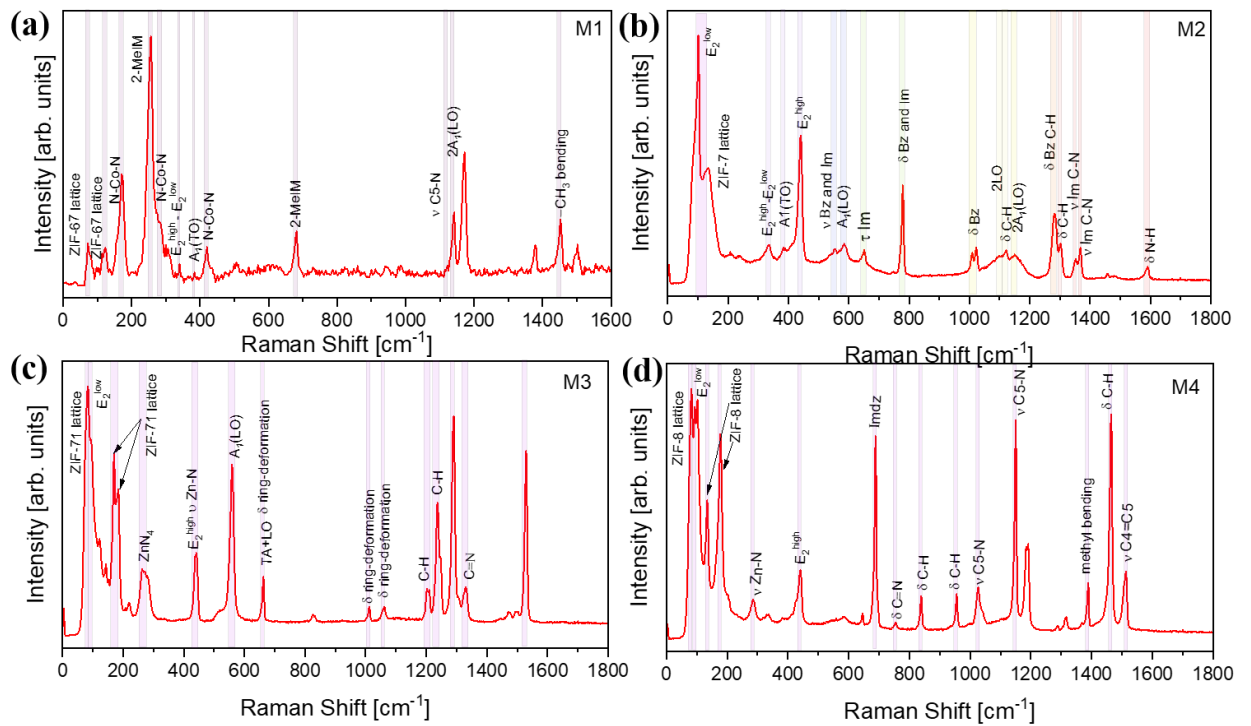**Fig. A3.3. (a) Raman spectra of the 0A sample and (b) M0 sample.**

Fig. A3.4. Raman spectra of the ZIF-coated Cd-doped ZnO samples: (a) M1; (b) M2; (c) M3; and (d) M4 sample.
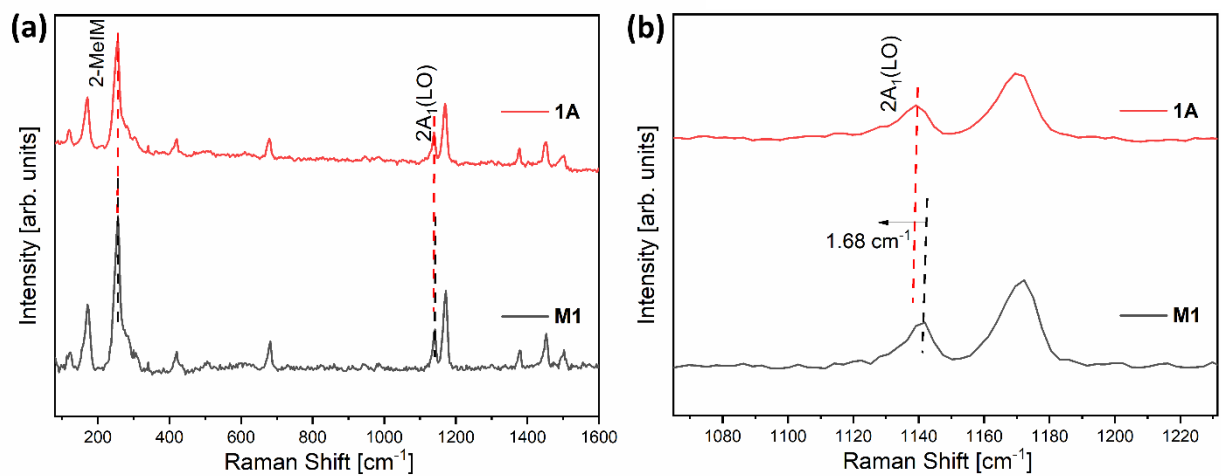

Fig. A3.5. Raman spectra of (a) 1A and M1 samples, (b) zoom-in spectra of (a) to show the peak shift due to Cd doping.

Table A3.1. Elemental composition of samples M1–M4 obtained by semiquantitative XPS analysis.

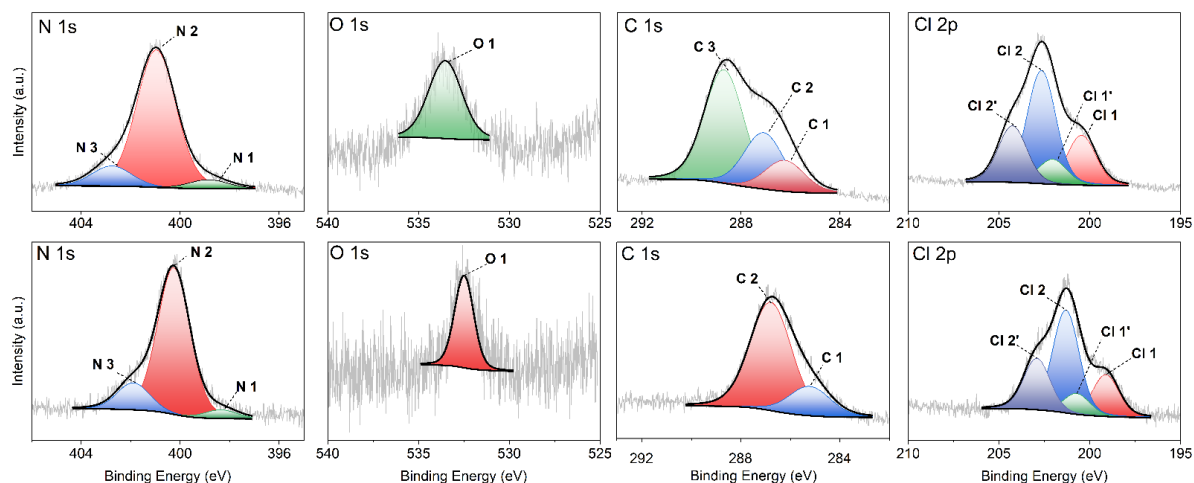| Element Composition (at%)	C - C 1s	O - O 1s	N - N 1s	Zn - Zn 2p	Cl - Cl 2p	Co - Co 2p
M1 (ZIF-67)	64.8	4.0	24.8	0.6	-	5.9
M2 (ZIF-7)	72.1	2.6	18.6	6.7	-	-
M3 (ZIF-71)	49.6	1.8	19.4	6.2	22.4	-
M4 (ZIF-8)	61.1	3.1	26.2	9.5	-	-

Fig. A3.6. Comparison of N 1s, O 1s, C 1s, and Cl 2p XPS high-resolution spectra of the M3 sample from this study and a ZIF-71-coated Al-doped CuO film from a previous study[7] after respective charge correction and fitting.

Table A3.2. Absolute E_b positions of all fitting functions used in the XPS analysis.

Element	Components	Binding Energy (eV)
M1		
C 1s	C 1	286.7
Co 2p	Co 1	781.2
Co 2p	Co 1'	796.7
Co 2p	Satellites	786.4
Co 2p	Satellites	802.4
N 1s	N 1	400.3

| Element	Components	Binding Energy (eV)
O 1s	O 1	532.3
Zn 2p	Zn 1	1020.5
Zn 2p	Zn 1'	1043.5
M2		
C 1s	C 1	286.2
C 1s	C 2	287.3
N 1s	N 1	400.6
O 1s	O 1	533.0
Zn 2p	Zn 1	1021.7
Zn 2p	Zn 1'	1044.6
M3		
C 1s	C 3	288.7
C 1s	C 2	287.1
C 1s	C 1	286.2
Cl 2p	Cl 1	200.4
Cl 2p	Cl 2	202.7
Cl 2p	Cl 1'	202.0
Cl 2p	Cl 2'	204.3
N 1s	N 3	402.8
N 1s	N 2	401.0
N 1s	N 1	398.9
O 1s	O 1	533.5
Zn 2p	Zn 1	1021.7
Zn 2p	Zn 1'	1044.6
M4		
C 1s	C 1	286.9
N 1s	N 2	400.6
N 1s	N 1	398.7
O 1s	O 1s	532.9
Zn 2p	Zn 2p 3/2	1021.7
Zn 2p	Zn 2p 1/2	1044.7
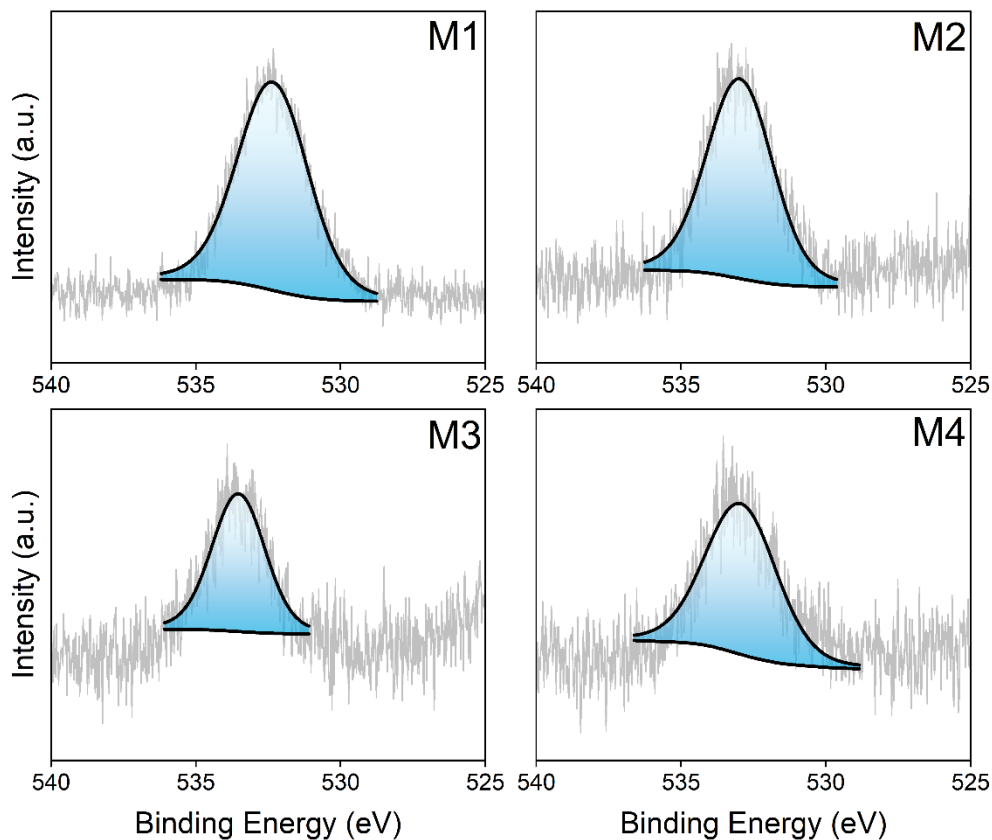
Fig. A3.7. XPS High-resolution XPS spectra of the M1, M2, M3, and M4 samples corresponding to O 1s.
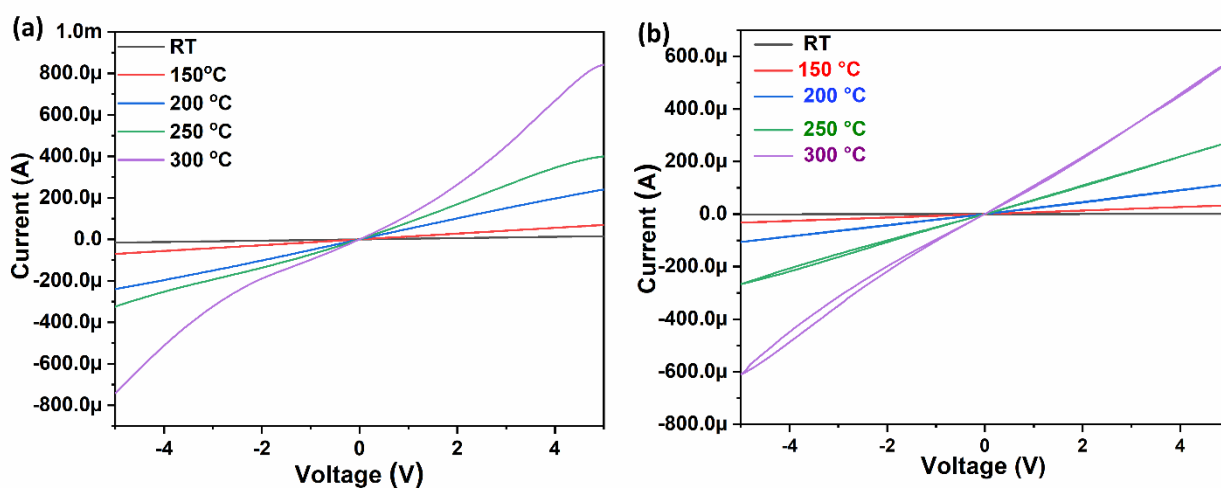

Fig. A3.8. I-V characteristics of (a) 0A and (b) M0 samples at different temperatures.
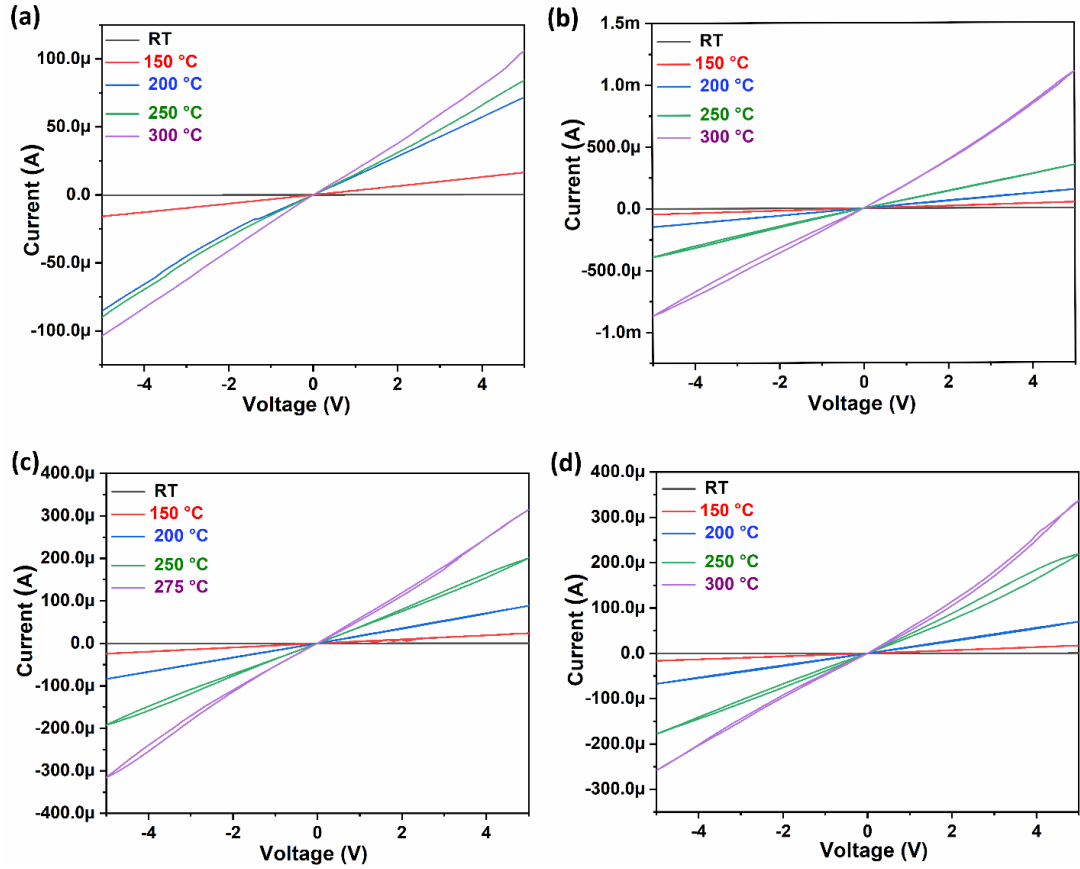
Fig. A3.9. I-V characteristics of (a) M1, (b) M2, (c) M3, and (d) M4 samples at different temperatures.
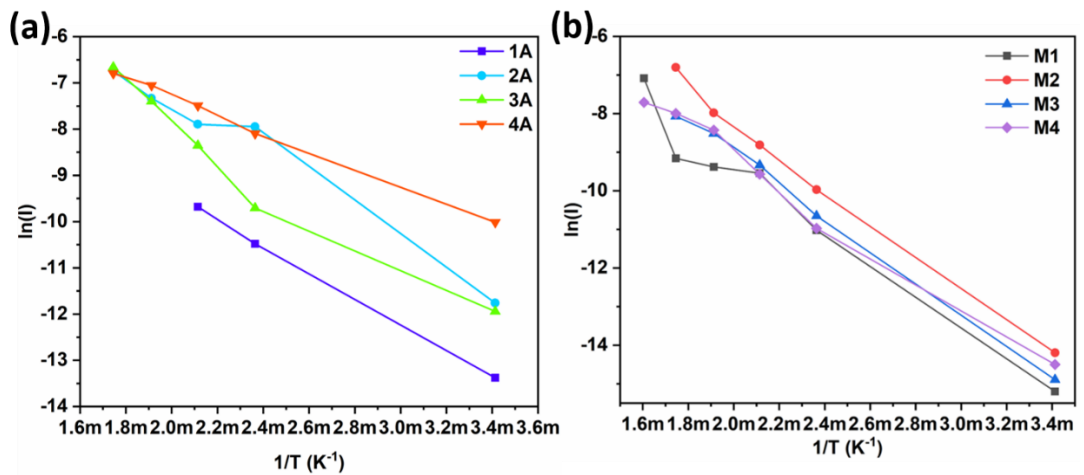

Fig. A3.10. Arrhenius plot of two different batch of samples, (a) 1A, 2A, 3A, and 4A, and (b) M1, M2, M3, and M4 samples.

Table A3.3: Values of slope of the curve and activation energy for all the eight samples.

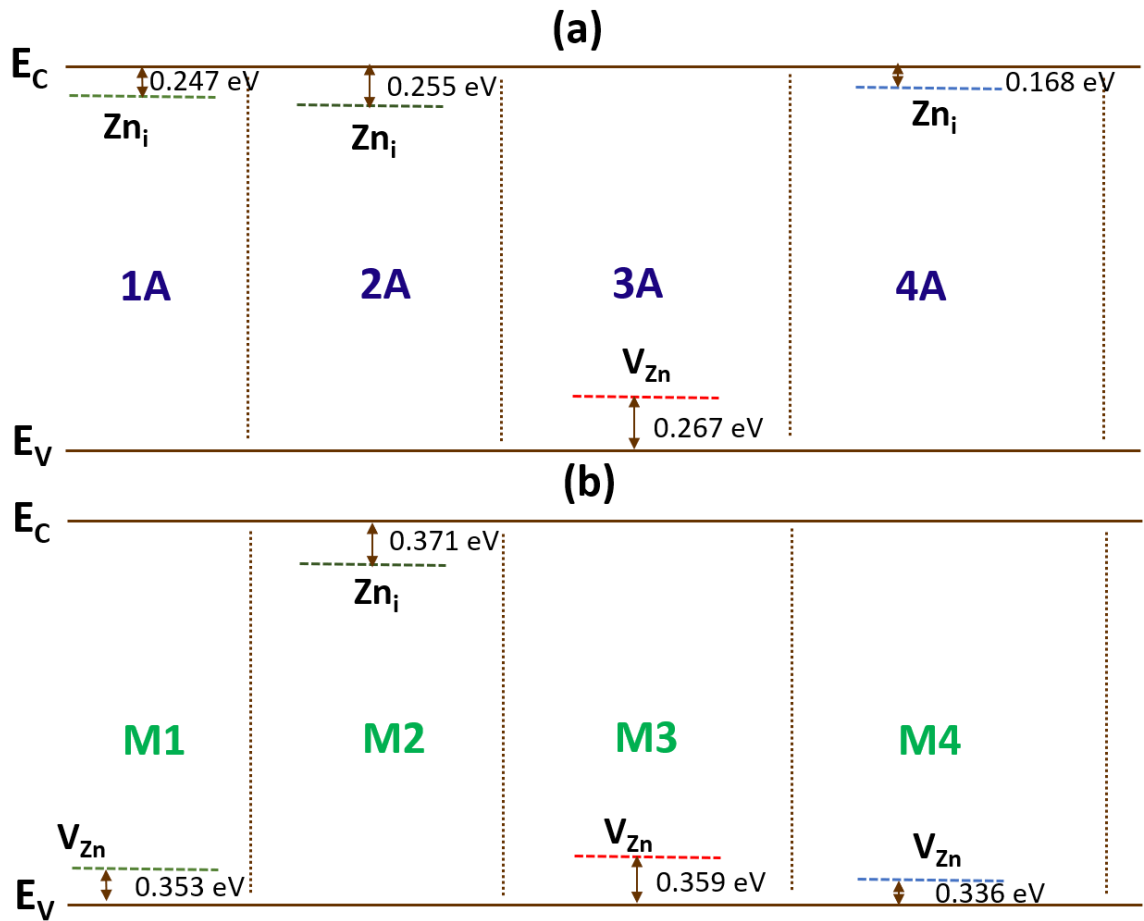| Sample name	Slope of the curve $(-E_a/k_B)$ in K	Calculated activation energy (E_a) in eV
1A	-2870.842	0.247
2A	-2964.291	0.255
3A	-3094.449	0.267
4A	-1950.181	0.168
M1	-4101.909	0.353
M2	-4301.349	0.371
M3	-4172.621	0.359
M4	-3895.565	0.336

Fig. A3.11. Trap energy states for carriers in different samples (a) 1A, 2A, 3A, and 4A and (b) M1, M2, M3, and M4.
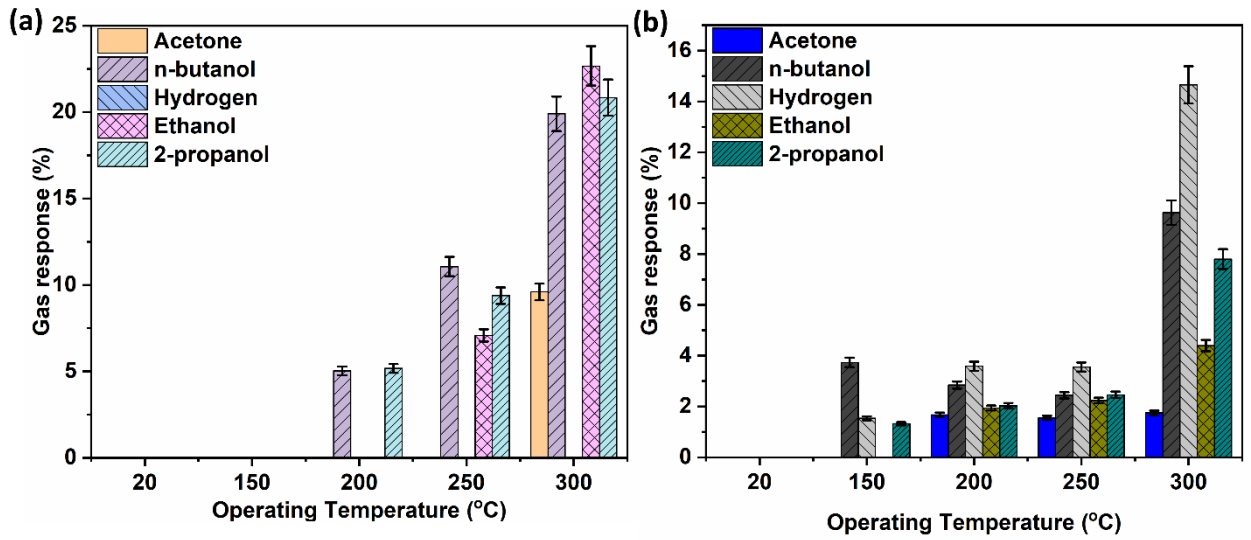
Fig. A3.12. Gas sensing results of different gases for (a) 0A and (b) M0 samples, at different operating temperatures in the range of 20 to 300 °C.

Fig. A3.13. Gas sensing results of different gases for (a) 1A, (b) 2A, (c) 3A, and (d) 4A samples, at different operating temperatures in the range of 20 to 300˚C.

Fig. A3.14. An illustration of an energy band diagrams of Co_3O_4/ZnO heterostructure: (a) in air; and (b) in the presence of ethanol.

Fig. A3.15. (a) Dynamic resistance changes and (b) Dynamic gas sensing response of the sample 1A in the presence of ethanol at 250 °C.
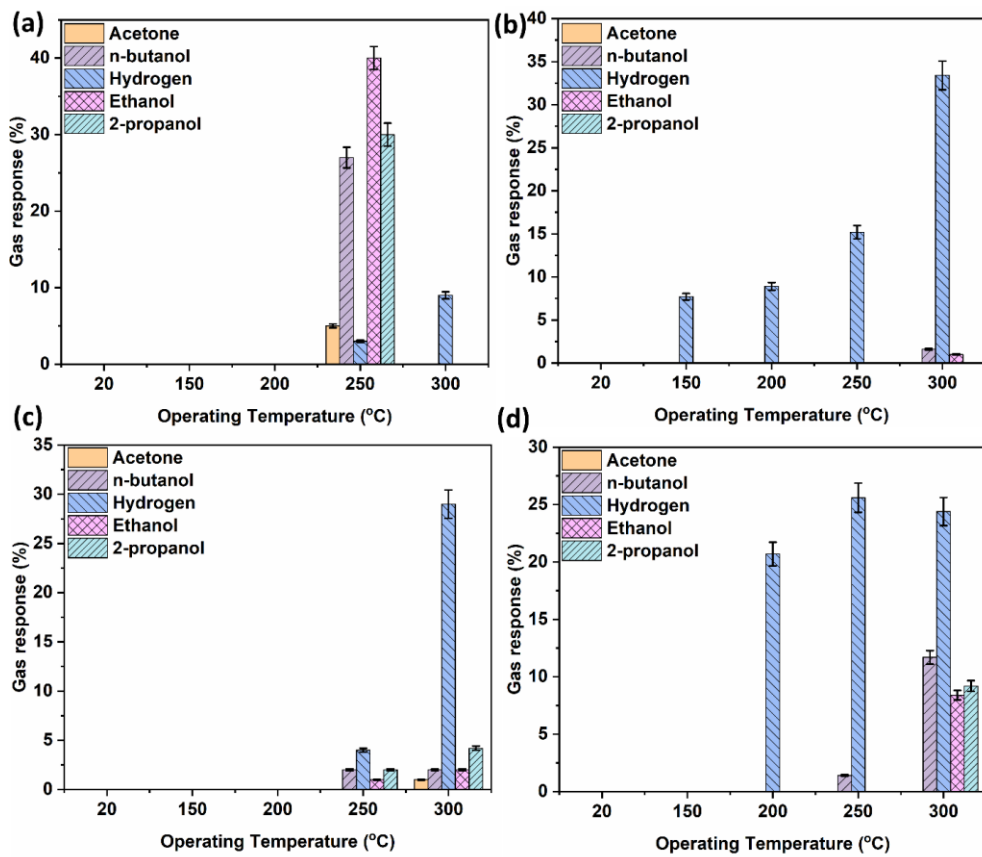
Fig. A3.16. Gas sensing results of different gases for (a) M1, (b) M2, (c) M3, and (d) M4 samples, at different operating temperatures in the range of 20 to 300 °C.
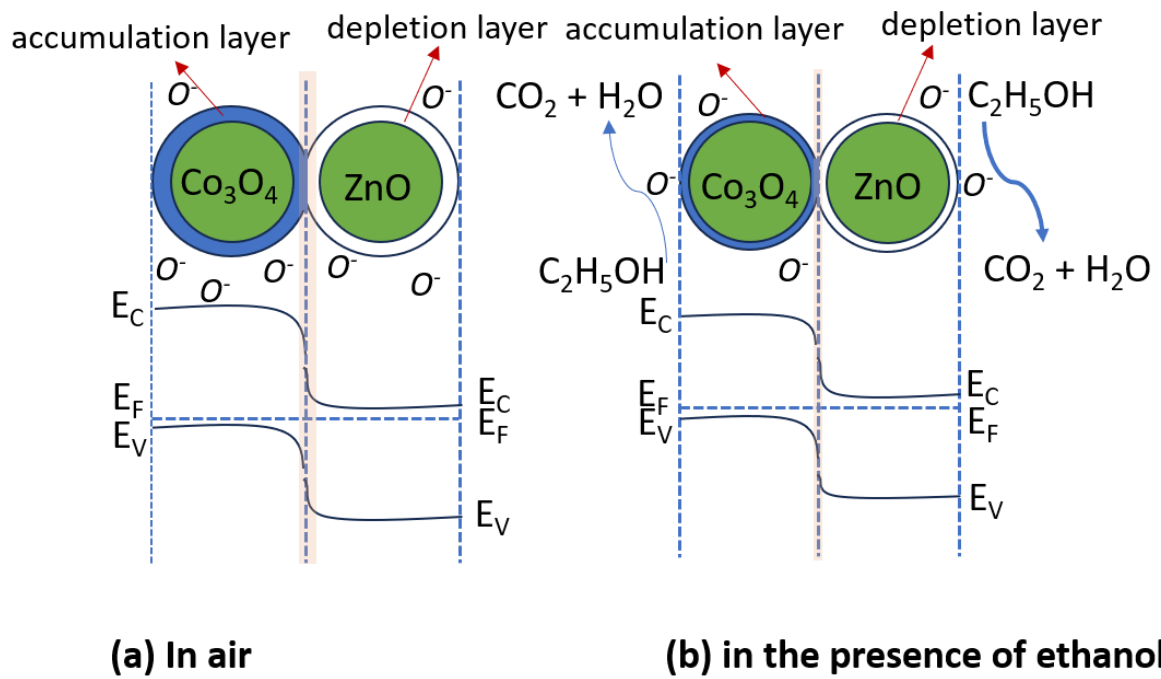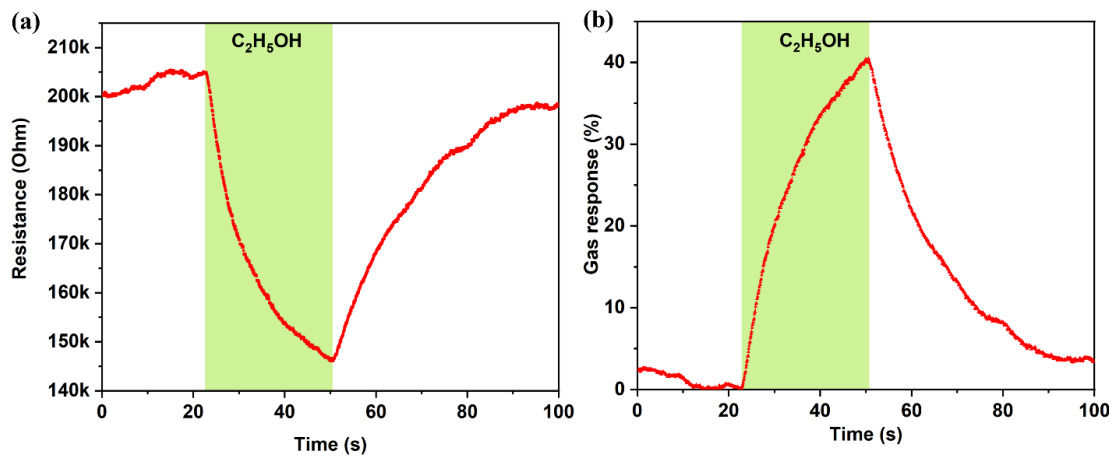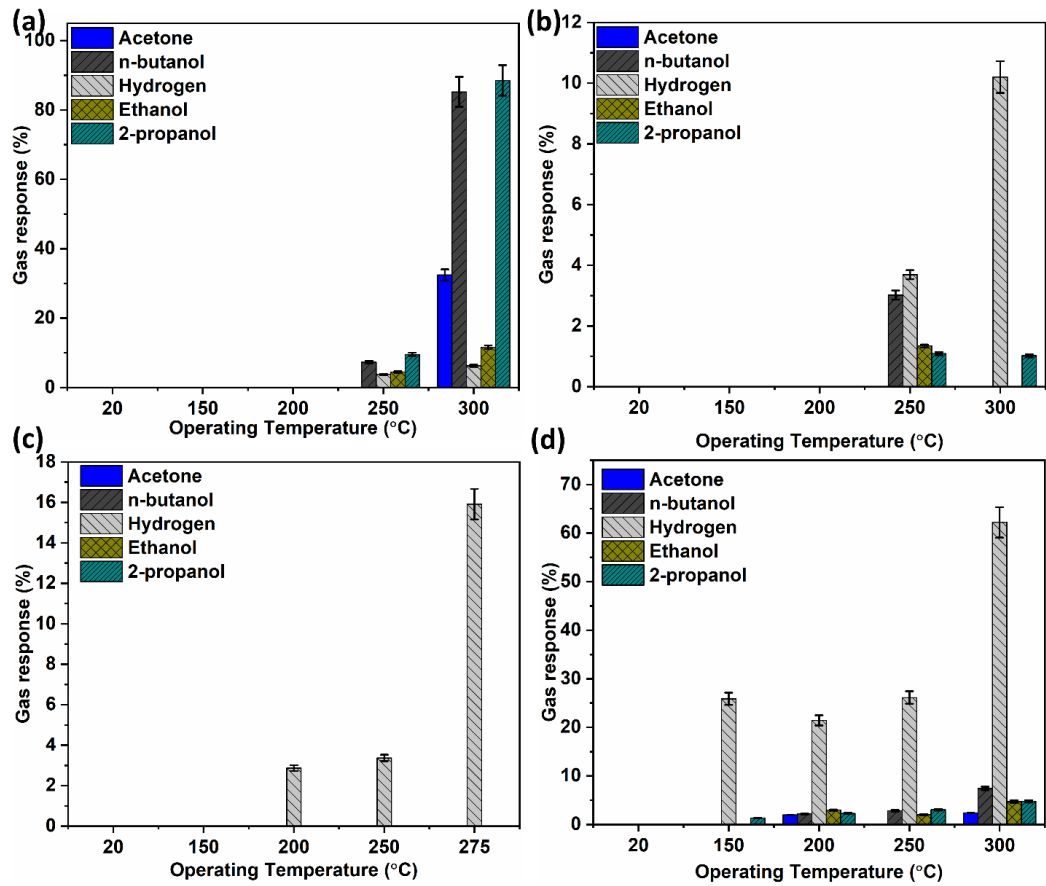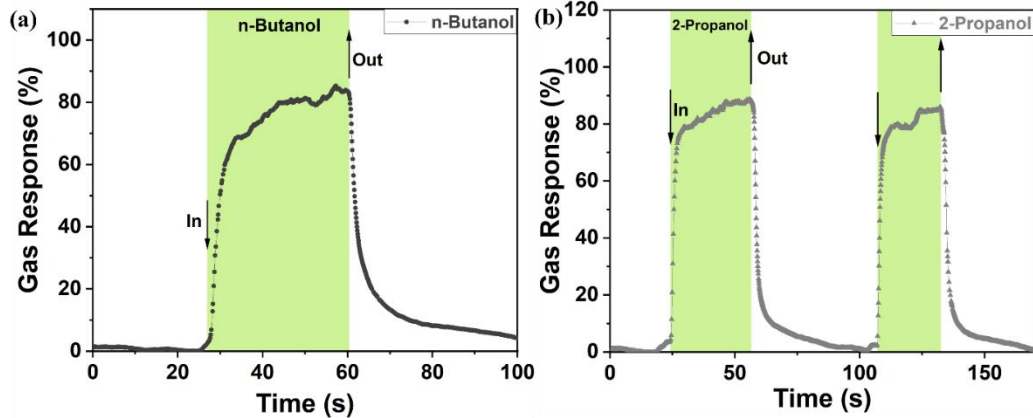

Fig. A3.17. Dynamic gas sensing response of the sample M1 in the presence of (a) n-butanol and (b) 2-propanol at 300 °C.

SALONUL INTERNAŢIONAL AL CERCETĂRII ŞTIINŢIFICE, INOVĂRII ŞI INVENTICII

PRO INVENT

EDIŢIA XXI, 25-27 OCTOMBRIE 2023
CLUJ-NAPOCA

UNIVERSITATEA TEHNICĂ

DIPLOMA DE EXCELENŢĂ
ŞI MEDALIA DE AUR

Se acordă **Rajat Nagpal, drd. (MD/INDIA); Lupan Cristian, drd. (MD); Birnaz Adrian, drd. (MD); Leonard Siebert Dr.-Ing. (DE); Lupan Oleg, prof. univ. dr. hab. (MD)**

De la **UNIVERSITATEA TEHNICĂ A MOLDOVEI**

Pentru **DETECTOARE DE ULTRAVIOLETE PE BAZA UNEI STRUCTURI DE AL2O3/ZNO**

PREŞEDINTELE SALONULUI
Prof. dr.ing. VIOREL POPA
Rector al Universităţii Tehnice din Cluj-Napoca

PREŞEDINTELE JURIULUI
Prof. dr. ing. RADU MUNTEANU

GRIGORE T. POPA UNIVERSITY OF
MEDICINE AND PHARMACY IASI

FACULTY OF
MEDICAL BIOENGINEERING

sensors

EHB 2023
9-10 NOVEMBER 2023
BUCHAREST, ROMANIA

THE SCIENTIFIC COMMITEE OF THE 11TH INTERNATIONAL CONFERENCE ON E-HEALTH AND BIOENGENEERING
has the pleasure to offer
MENTION

to

RAJAT NAGPAL

Authors:
Rajat Nagpal, Cristian Lupan, Adrian Birnaz, Philipp Schadte, Mihai Brînză, Leonard Siebert and Oleg Lupan

For their paper:
Study on Al2O3/ZnO heterostructure based UV detection for biomedical applications
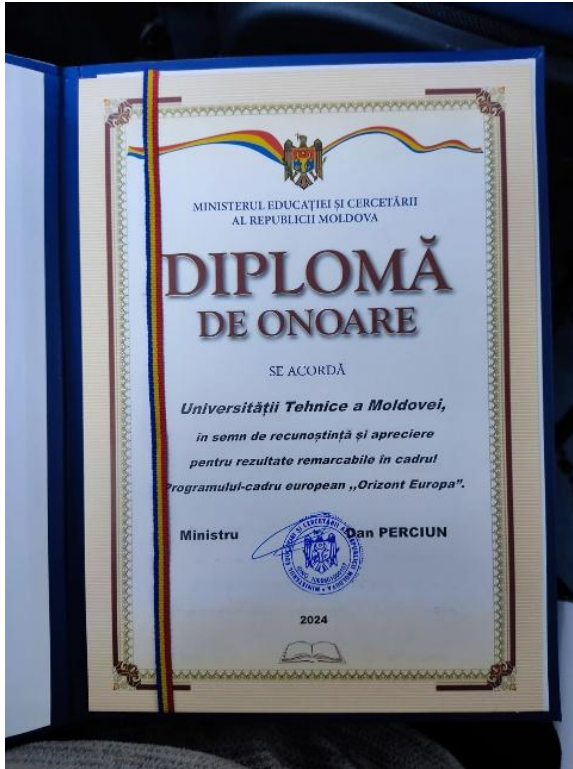
Prof. Hariton COSTIN
General Chair EHB 2023

11th International Conference on
E-HEALTH AND BIOENGINEERING
9-10th November 2023, Bucharest, ROMANIA

www.ehbconference.ro
@ehb.conference
EHB Conference

epigeum

Certificate
Number: 1594610446

This is to certify that

Rajat Nagpal
of TU Dublin

Successfully completed the course
Research Integrity: Core

Good research conduct	80%
Irresponsible research practices	80%
Planning your research	80%
Managing and recording your research	90%
Data selection, analysis and presentation	80%

as part of the Epigeum Online Course System with a score of 86%.

Dated: 23 May 2023

epigeum

Certificate
Number: 1594610446

This is to certify that

Rajat Nagpal
of TU Dublin

Successfully completed the course
Research Integrity: Core

Scholarly publication	90%
Professional responsibilities	100%
Communication, social responsibility and impact	90%

as part of the Epigeum Online Course System with a score of 86%.

Dated: 23 May 2023

epigeum

Certificate

Number: 1594610448

This is to certify that

Rajat Nagpal
of TU Dublin

Successfully completed the course
Research Integrity: Specialist

Conflicts of interest	90%
Research involving human participants	90%
The care and use of animals in research	90%
Intellectual property	80%
Export controls	80%

as part of the Epigeum Online Course System with a score of 86%.

Dated: 23 May 2023

Copyright Sage Publications 2021

SelectScience 20

This is to acknowledge that

Rajat Nagpal

Attended a one-hour webinar and Q&A session entitled

'Sniffing out quality': Analyzing volatile organic compounds (VOCs) to assess food and beverage quality throughout the supply chain

November 16th, 2023

Key Learning Outcomes

How trap-based SPME can be used to assess the freshness of harvested food products.
How combining thermal desorption with a human sensory panel can be used to assess the aroma of fruits.
How high-capacity sorptive extraction used in conjunction with a focusing trap is a compelling alternative to traditional headspace extraction.
How, using advanced preconcentration and extraction with GC×GC, time-of-flight mass spectrometry and powerful software processing can be applied to complex biological matrices for accurate terpene profiling.
How SPME–trap with enrichment significantly enhances sensitivity, providing more confident profiling of foods and beverages for their taste and odor.

Arif Butt
CEO & President
SelectScience

Dr Natasha Spadafora
Senior Product Specialist
Markes International

FAU

Friedrich-Alexander-University Erlangen-Nuremberg
Institute of Separation Science and Technology (TVT)
Egerlandstraße 3
91058 Erlangen
Germany

Rajat Nagpal
Technical university of Moldova
Department of microelectronics and Biomedical Engineering
moldova
2045 CHISINAU
Romania

Erlangen, 05.09.2025

To Whom It May Concern

Dear Sir or Madam,

We confirm that **Rajat Nagpal** participated at Erlangen-Edinburgh School of Adsorption (EESA 2025).

With best regards,

Prof. Matthias Thommes

Deutsches Elektronen-Synchrotron DESY
A Research Centre of the Helmholtz Association

DESY | DESY Photon Science User Office

M. Sc. Rajat Rajat
Christian-Albrechts-Universitaet Kiel
Technische Fakultaet
Kaiserstr. 2
24143 Kiel
Germany

10-Jul-2024

**Confirmation of planned participation in beamtime at DESY Photon Science
- not for VISA purposes -**

Dear M. Sc. Rajat Rajat,

This is to confirm that you are registered as participant for the beamtime at PETRA III
beamline P03 scheduled from 15-Jul-2024 to 22-Jul-2024 for the proposal I-20231219
by Berit Zeller-Plumhoff/Leonard Siebert.

We look forward to welcoming you at DESY for this experiment.

With best regards,
DESY Photon Science User Office

MOLDOVA STATE UNIVERSITY

HR EXCELLENCE IN RESEARCH

PARTICIPATION CERTIFICATE

This is to certify that **Rajat NAGPAL**
has participated to the national scientific conference
with international participation

INTEGRATION THROUGH RESEARCH AND INNOVATION

dedicated to the international day of science for peace and
development

Rector USM
Igor ȘAROV, PhD., Associate Professor

Chișinău, 9-10 november 2023

TECHNICAL SCIENTIFIC CONFERENCE OF UNDERGRADUATE, MASTER AND PHD STUDENTS

March 27-29, 2024
Technical University of Moldova
Chisinau, Republic of Moldova

THIRD DEGREE CERTIFICATE

This certificate is presented to

Rajat NAGPAL, Cristian LUPAN

in recognition of contributing with the excellent paper entitled

EFFECTS OF TEMPERATURE ON OPTICAL PROPERTIES OF ZnO NETWORKS

Prof. Viorel BOSTAN
Rector of TUM

Chisinau 2024

ECCO INTERNATIONAL CONFERENCE

CERTIFICATE OF APPRECIATION

Awarded to

Rajat Nagpal

For authoring and presenting the research titled

t-ZnO based sensor for optical and gas sensing applications

contributing essentially to the 13th (2024) edition of the

International Conference

ELECTRONICS, COMMUNICATIONS AND COMPUTING

This conference edition celebrates the 60th year since the founding of the Technical University of Moldova.

Assoc. professor, dr. Dumitru CIORBĂ
Conference Chairman, FCIM Dean

Assoc. professor, dr. Lilia SAVA
Conference Chairwoman, FET Dean

GRIGORE T. POPA UNIVERSITY OF MEDICINE AND PHARMACY IASI

FACULTY OF MEDICAL BIOENGINEERING

sensors

EHB 2023
9–10 NOVEMBER 2023
BUCHAREST, ROMANIA

THE SCIENTIFIC COMMITEE OF THE 11TH INTERNATIONAL CONFERENCE ON E-HEALTH AND BIOENGENEERING

has the pleasure to offer

MENTION

to

RAJAT NAGPAL

Authors:
Rajat Nagpal, Cristian Lupan, Adrian Birnaz, Philipp Schadte, Mihai Brînză, Leonard Siebert and Oleg Lupan

For their paper:
Study on Al2O3/ZnO heterostructure based UV detection for biomedical applications

Prof. Hariton COSTIN
General Chair EHB 2023

11th International Conference on
E-HEALTH AND BIOENGINEERING
9-10th November 2023, Bucharest, ROMANIA

www.ehbconference.ro
@ehb.conference
EHB Conference

biosensors

an Open Access Journal by MDPI

CERTIFICATE OF ACCEPTANCE

The certificate of acceptance for the manuscript (**biosensors-2931497**) titled:

Multifunctional 3-in-1 sensor on t-ZnO for ultraviolet, VOC and temperature sensing for bioengineering applications

Authored by:

Rajat Nagpal; Cristian Lupan; Adrian Bîrnaz; Alexandr Sereacov; Erik Greve; Monja Gronenberg; Leonard Siebert; Rainer Adelung; Oleg Lupan

was accepted in *Biosensors* (ISSN 2079-6374) on 06 May 2024

Prof. Dr. Giovanna Marrazza
Editor-in-Chief

Basel, May 2024

AUTHOR'S CONTRIBUTION TO THE RESEARCH AND DISSERTATION

- Development of hybrid structures;

- XRD: sample measurement; data interpretation and corresponding analysis;

- SEM: data interpretation and corresponding analysis;

- micro-Raman: data interpretation and corresponding analysis;

- Gas sensing results: data interpretation and corresponding analysis;

- Conceptualization, data curation, formal analysis, investigation, methodology, validation, and visualization.

ACKNOWLEDGEMENTS

partners, including **Ing. UNGETHÜM Bert** and **Ing. PONGPHAIBOON Sivapoom** from Airsense Analytics, Germany.

Most importantly, I express my deepest gratitude to my friends and family for their moral support and unconditional encouragement throughout this journey. I also thank Almighty God and bow with reverence to Lord Hanuman ji and H.H. Yoganand Ji Maharaj for spiritual guidance and blessings.

With due respect,

Rajat

Chișinău, 2026

Disclaimer

I, the undersigned, hereby declare, on my own responsibility, that the materials presented in this doctoral thesis are the result of my own original research and scientific work. I am aware that any violation of this declaration will entail consequences in accordance with the applicable legislation.

Rajat

Signature

Date

CURRICULUM VITAE

First name: Rajat

Nationality: Indian

Date of birth: 06/06/1998

EDUCATION AND TRAINING

Studies:

2004-2014: Secondary school studies, Sanjay Gandhi Memorial Public School, Yamuna Nagar, Haryan, India

2014-2016: High school studies, Mukand Lal Senior Secondary School, Yamuna Nagar, Haryana, India

2016-2019: Higher education (Bachelor's degree in science with speciality in Electronics), Mukand Lal National College affiliated to Kurukshetra University, Haryana, India

2020-2022: Master's degree in science with speciality in Physics, Indian Institute of Technology Jodhpur, Rajasthan, India

2023-2026: Joint doctorate studies, Technical University of Moldova with speciality in "Physics of Nanosystems and Nanotechnologies" and Kiel University in Materials Science engineering

Professional experience:

03.08.2022-31.03.2023: Research Associate, Department of Physics, Indian Institute of Technology Delhi, India

01.08.2025-31.10.2025: Research Intern in industry, Airsense Analytics, Schwerin, Germany

Fields of scientific activity:

Comprehensive gas sensing performance assessment by systematically investigating the underlying sensing mechanisms. Rigorous sensor testing protocols, quantitative data analysis, and implementation of quality assurance and quality control (QA/QC) protocols to ensure data reliability and reproducibility. Hands-on experience in the design and development of custom gas sensing measurement systems, integrating both electronic circuitry, and mechanical components to optimize sensor performance and measurement accuracy. Designing and implementation of a gas sensing setup with stainless-steel casing and tubings for controlled analyte exposure and testing.

Participation in national and international scientific projects:

Project 101072845, "Porous Networks for Gas Sensing", HORIZON-MSCA-2021-DN-01-01 project, 2023-2026, https://sennet-project.eu/

Articles published in ISI and SCOPUS-listed international journals:

1) **RAJAT, Nagpal**, SUGIHARA, M., MAGARIU, N., TJARDTS, T., MELING-LIZARDE, N., STRUNSKUS, T., AMERI, T., AMELOOT, R., ADELUNG, R., LUPAN, O. Humidity-tolerant selective sensing of hydrogen, and n-butanol using ZIF-8 coated CuO:Al films, *Materials Chemistry Frontiers* 2025, 9, pp. 3425-3442, https://doi.org/10.1039/D5QM00565E **(Impact Factor: 6.4)**

2) **RAJAT, Nagpal**, SUGIHARA, M., LUPAN, C., TJARDTS, T., MELING-LIZARDE, N., STRUNSKUS, T., QIU, H., ADELUNG, R., AMELOOT, R., LUPAN, O. ZIF-71 coated CuO:Al with enhanced gas sensing performance for n-butanol and hydrogen, *Applied Electronic Materials* 2025, 7, pp. 10198-10215, https://doi.org/10.1021/acsaelm.5c01659 **(Impact Factor: 4.7)**

3) **RAJAT Nagpal**, ABABII, N., LUPAN, O., Comprehensive Advances in Gas Sensing: Mechanisms, Material Innovations, and Applications in Environmental and Health Monitoring, *Material Today Electronics* 2026, 15, 100192, ISSN 2772-9494, *Accepted 10 December* 2025, https://doi.org/10.1016/j.mtelec.2025.100192 **(Impact Factor: 7.4)**

4) **RAJAT, Nagpal**, LUPAN, C., BÎRNAZ, A., SEREACOV, A., GREVE, E., GRONENBERG, M., SIEBERT, L.; ADELUNG, R.; LUPAN, O. Multifunctional Three-in-One Sensor on t-ZnO for Ultraviolet and VOC Sensing for Bioengineering Applications, *Biosensors* 2024, 14, pp. 293, https://doi.org/10.3390/bios14060293 **(Impact Factor: 5.6)**

5) **RAJAT, Nagpal**, LUPAN, C., BUZDUGAN, A., GHENEA, V., LUPAN, O. Effect of Pd functionalization on optical and hydrogen sensing properties of ZnO: Eu films, *Optik* 2025, 325, pp. 172247, https://doi.org/10.1016/j.ijleo.2025.172247 **(Impact Factor: 3.1)**

6) CHAKRABORTY, B., LITRA, D., MISHRA, A.K., LUPAN, C., **RAJAT, Nagpal,** MISHRA, S., QIU, H., RAILEAN, S., LUPAN, O., LEEUW, N.H.D., ADELUNG, R., SIEBERT, L., Ultra-selective hydrogen sensors based on CuO - ZnO hetero-structures grown by surface conversion, *Journal of Alloys and Compounds*, Volume 1002, 2024, 175385, https://doi.org/10.1016/j.jallcom.2024.175385, ISSN: 0925-8388 **Impact Factor: 5.8**

7) CHAKRABORTY, B.; TJARDTS, T.; ZELLER-PLUMHOFF, B.; SCHÜRMANN, U.; DAVYDOK, A.; WIELAND, D.; QIU, H.; REIßMANN, A.; MELING L., NAHOMY; **RAJAT, Nagpal**; STRUNSKUS, T.; SIEBERT, L.; ADELUNG, R., A Versatile Synthesis Approach and Interface Characterization of t-ZnO@metal hydroxide/oxide Heterostructures, *ACS Crystal Growth & Design* , https://doi.org/10.1021/acs.cgd.5c01604, ISSN: 1528-7483 **(Impact Factor: 3.4)**

8) **RAJAT, Nagpal**, SUGIHARA, M., LUPAN, C., MAGARIU, N., TJARDTS, T., MELING-LIZARDE, N., STRUNSKUS, T., JETTER. J., QIU, H., CHAKRABORTY, B., AMERI, T., QUANDT, E., ADELUNG, R., AMELOOT, R., LUPAN, O. *In-situ* temperature-dependent XRD and advanced spectroscopic insights and defect-mediated properties in ZIF-coated ZnO hybrid structures, submitted in *ACS Applied Nano Materials,* under review (**Impact Factor: 5.5)**

Article published in National register for specialized journals (JES)

9) **RAJAT, Nagpal,** CHIRIAC, M., SEREACOV, A., BIRNAZ, A., ABABII, N., LUPAN, C., BUZDUGAN, A., SANDU, I., SIEBERT, L., PAUPORTÉ, T., LUPAN, O., ANNEALING EFFECT ON UV DETECTION PROPERTIES OF ZnO:Al STRUCTURES, *Journal of Engineering Science*, Vol. 30 (4) 2023, pp. 45–62, https://doi.org/10.52326/jes.utm.2023.30(4).04, ISSN: 287-3474;

Participation in scientific conferences and other events (national and international):

10) **RAJAT, Nagpal,** LUPAN, C., BÎRNAZ A., LUPAN O., Al_2O_3/ZnO HETEROSTRUCTURE BASED DEVICE FOR UV DETECTION. Salonul Internaţional al Cercetării Ştiinţifice, Inovării şi Inventicii, PRO INVENT, UNIVERSITATEATEHNICĀ DIN CLUJ-NAPOCA, 25-27 Octombrie 2023, Cluj – Napoca, România (certificate attached in annexure 4 of joint doctoral thesis);

11) **RAJAT, Nagpal**, LUPAN, C., LUPAN O., Evaluation Of Sensitivity, Selectivity and Stability Of MOF- And Zeolite-Functionalized Resistive Sensors, Sensor Arrays, And Pre-Concentrators For The Detection of VOCs Mixtures. The VIIth International Fair of Innovation and Creative Education for Youth (ICE-USV) Suceava, ROMANIA, July, 07 - 09, 2023 (certificate attached in annexure 4 of joint doctoral thesis);

12) **RAJAT**, R., KUMAR, A.K., KUMAR, M. Realization of H_2S gas sensor using sol-gel processed $ZnFe_2O_4$ thin film. In: Conferinţa tehnico-ştiinţifică a studenţilor, masteranzilor şi doctoranzilor, Chișinău, Moldova, 5-7 Aprilie 2023. Available:

https://repository.utm.md/handle/5014/23772, ISBN: 978-9975-45-956-3;

13) **RAJAT, Nagpal**, LUPAN, C., LITRA, D., SCHADTE, P., BÎRNAZ, A., BRINZA M., SIEBERT, L., LUPAN, O. Study on Al_2O_3/ ZnO heterostructures based UV detection for biomedical applications. At the conference: The 11th IEEE International Conference on E-Health and Bioengineering – EHB 2023 Grigore T. Popa University of Medicine and Pharmacies Iasi, *Springer Nature*, November 9-10, 2023, Bucharest, Romania, pp. 178-188, https://doi.org/10.1007/978-3-031-62523-7_20, ISBN: 978-3-031-62523-7;

14) **RAJAT Nagpal,** BÎRNAZ A., LUPAN, C., LUPAN O., Study on ZnO network-based UV detection. UGAL INVENT, Innovation and research exhibition, November 9-10, 2023, (certificate attached in annexure 4 of joint doctoral thesis);

15) **RAJAT, Nagpal**, LUPAN, C., SANDU, I., BÎRNAZ**,** A. UV LIGHT DETECTION BASED ON ZnO NETWORKS. *At the conference: Integration through research and innovation*, State University of Moldova, Chisinau, Moldova, November 9-10, 2023, pp. 752-757, Available: https://ibn.idsi.md/vizualizare_articol/201035, ISBN: 978-9975-62-687-3;

16) BRINZA, M., **RAJAT, Nagpal,** LITRA, D., CHIRIAC, M., LUPAN, O. Gas Sensing Structure of CuO/Cu_2O Doped with Sn for Ethanol with Potential Detection in Exhaled Breath. In: Costin, HN., Magjarević, R., Petroiu, G.G. (eds) Advances in Digital Health and Medical Bioengineering. EHB 2023. IFMBE Proceedings, vol 111. *Springer Nature*, Cham., pp. 189-196, https://doi.org/10.1007/978-3-031-62523-7_21, ISBN: 978-3-031-62523-7;

17) **RAJAT, Nagpal,** LUPAN, C.**,** EFFECTS OF TEMPERATURE ON OPTICAL PROPERTIES OF ZnO NETWORKS. In: Conferinţa tehnico-ştiinţifică a studenţilor, masteranzilor şi doctoranzilor, Chişinău, Moldova, 27-29 Martie 2024, Vol 1, pp. 439-443, Available: https://ibn.idsi.md/vizualizare_articol/224337, ISBN: 978-9975-64-458-7;

18) **RAJAT, Nagpal**, SIEBERT, L., LUPAN, C., PADUNNAPPATTU, A., POSCHMANN, MIRJAM P.M., STOCK, N., ADELUNG, R., LUPAN, O. Metal Organic Framework based low powered ultraviolet signal detection. Poster presentation: *MOFSIM 2024,* Montpellier, April 10-12, 2024, pp. 90 (Book of Abstracts).Available:https://drive.google.com/file/d/10KpC8RzHq7JqZbHrqf2nRcGnRRZMFmg2/view;

19) **RAJAT, Nagpal**. Mixed metal oxide-based gas sensor. Conferinţa "NANO-2024: "Quo Vadis– Ethics of the Scientific Research, pp. 60-61, Available: https://ibn.idsi.md/vizualizare_articol/205823, ISBN: 978-9975-64-422-8;

20) **RAJAT, Nagpal,** LUPAN, C., VIANA, B., PAUPORTÉ, T., LUPAN, O., ADELUNG, R., Study on the Optical and Gas Sensing Properties of Eu-Doped ZnO, *IEEE 14th International Conference Nanomaterials: Applications and Properties)* , *IEEE Xplore*, 2024, pp. 1-4, https://doi.org/10.1109/NAP62956.2024.10739686, **ISBN:** 979-8-3503-8012-5;

21) **RAJAT, Nagpal.** t-ZnO based sensor for optical and gas sensing applications. At Conference: Oral presentation, ECCO 2024, Chisinau, Moldova, October 17-18, 2024, pp. 73-74, Available: https://ibn.idsi.md/vizualizare_articol/223189, **ISBN:** 978-9975-64-480-8;

22) **RAJAT, Nagpal**, CHIRIAC, M., SUGIHARA, M., LITRA, D., MAGARIU, N., LUPAN, C., ZINICOVSCHI, V., AMELOOT, R., LUPAN, O., Sensory Properties of CuO/Cu_2O Nanostructures Coated with Zeolitic Imidazolate Frameworks, *2024 E-Health and Bioengineering Conference (EHB)*, IASI, Romania, *IEEE Xplore*, 2024, pp. 1-4, doi: 10.1109/EHB64556.2024.10805729, **ISBN:** 979-8-3315-3214-7;

23) LUPAN, O., **RAJAT, Nagpal**, LITRA, D., BRINZA, M., SUGIHARA, M., AMELOOT, R., RAILEAN, S., AMERI, T., ADELUNG, R., SCHRODER, S., FAUPEL, F., Hybrid Nanomaterials for Biomedical Sensors, *7th International Conference on Nanotechnologies and Biomedical Engineering*, *2025*, *IFMBE Proceedings,* vol 134. *Springer Nature*, pp. 162-176, Cham. https://doi.org/10.1007/978-3-032-06494-3_18, **ISBN:** 978-3-032-06494-3;

24) LUPAN, O., BRINZA, M., LITRA, D., **RAJAT, Nagpal**, SCHRODER, S., SUGIHARA, M., STRUNSKUS, T., AMELOOT, R., AMERI, T., ADELUNG, R., FAUPEL, F., Nanomaterials for Biomedical and Industrial Hybrid Sensors, 2025 IEEE 15th International Conference on "Nanomaterials: Applications & Properties", Bratislava, Slovakia, Sept. 7-12, 2025, pp. 09nna-10 – 09nna-11 (Book of Abstracts). Available: https://ieeenap.org/data/Book_of_Abstracts_2025.pdf;

Patents issued by the State agency:

25) **RAJAT, Nagpal**, SUGIHARA, M., MAGARIU, N., TROFIM V., LUPAN, C., AMELOOT, R., Process for manufacturing hydrogen sensor based on CuO:Al-ZIF-8 nanostructures, Patent app., **entr. no.** 7587 date 23.10.2025, AGEPI.

Published scientific works: A total of 25 scientific works, including: 1 patent application; 8 peer-reviewed articles in journals listed in the ISI and SCOPUS databases; 15 papers presented and published at National and International Conferences; 1 publication in National register of specialized journals; 2 single-author publications

h-index=5+; i-10 index=3+, Number of citations on Google Scholar=67+; SCOPUS=45+, Scopus ID: 59194131400, Web of Science Researcher ID: KPA-8644-2024.

Known Languages:

Mother tongue: Hindi

Punjabi: C1 (Advanced)

English: C1 (Advanced)

Romanian: A2 (Basic)

Contact details:

Center for Nanotechnologies and Nanosensors, Department of Microelectronics and Biomedical Engineering, Technical University of Moldova, Chisinau, 9/7 Studentilor Street, Block No. 3. email: rajat@doctorat.utm.md, rajr@tf.uni-kiel.de, nagpalrajat0698@zohomail.eu, phone number +373 79453419, +91 9017183334.

LIST OF SCIENTIFIC WORKS, CONFERENCES AND PATENT ON THE TOPIC OF THESIS

Mr. Rajat, joint doctorate student at UTM and Kiel University in the full-time form of education

Speciality: 134.03 Physics of Nanosystems and Nanotechnologies

LIST OF PUBLISHED WORKS ON THE TOPIC OF THESIS

1. Articles in scientific journals

1.1. Articles in ISI and SCOPUS-listed international journals:

1. **RAJAT, Nagpal**, SUGIHARA, M., MAGARIU, N., TJARDTS, T., MELING-LIZARDE, N., STRUNSKUS, T., AMERI, T., AMELOOT, R., ADELUNG, R., LUPAN, O. Humidity- tolerant selective sensing of hydrogen, and n-butanol using ZIF-8 coated CuO:Al films, *Materials Chemistry Frontiers* 2025, 9, pp. 3425-3442, https://doi.org/10.1039/D5QM00565E (**Impact Factor: 6.4**)

2. **RAJAT, Nagpal**, SUGIHARA, M., LUPAN, C., TJARDTS, T., MELING-LIZARDE, N., STRUNSKUS, T., QIU, H., ADELUNG, R., AMELOOT, R., LUPAN, O. ZIF-71 coated CuO:Al with enhanced gas sensing performance for n-butanol and hydrogen, *Appl Elec Mater* 2025, 7, pp. 10198-10215, https://doi.org/10.1021/acsaelm.5c01659 (**Impact Factor: 4.7**)

3. **RAJAT Nagpal**, ABABII, N., LUPAN, O., Comprehensive Advances in Gas Sensing: Mechanisms, Material Innovations, and Applications in Environmental and Health Monitoring, *Material Today Electronics* 2026, 15, 100192, ISSN 2772-9494, *Accepted 10 December* 2025, https://doi.org/10.1016/j.mtelec.2025.100192 (**Impact Factor: 7.4**)

4. **RAJAT, Nagpal**, LUPAN, C., BÎRNAZ, A., SEREACOV, A., GREVE, E., GRONENBERG, M., SIEBERT, L.; ADELUNG, R.; LUPAN, O. Multifunctional Three-in-One Sensor on t-ZnO for Ultraviolet and VOC Sensing for Bioengineering Applications, *Biosensors* 2024, 14, pp. 293, https://doi.org/10.3390/bios14060293 (**Impact Factor: 5.6**)

5. **RAJAT, Nagpal**, LUPAN, C., BUZDUGAN, A., GHENEA, V., LUPAN, O. Effect of Pd functionalization on optical and hydrogen sensing properties of ZnO: Eu films, *Optik* 2025, 325, 172247, https://doi.org/10.1016/j.ijleo.2025.172247 (**Impact Factor: 3.1**)

6. **RAJAT, Nagpal**, SUGIHARA, M., LUPAN, C., MAGARIU, N., TJARDTS, T., MELING-LIZARDE, N., STRUNSKUS, T., JETTER. J., QIU, H., CHAKRABORTY, B., AMERI, T., QUANDT, E., ADELUNG, R., AMELOOT, R., LUPAN, O. *In-situ* temperature-dependent XRD and advanced spectroscopic insights and defect-mediated properties in ZIF-coated ZnO hybrid structures, submitted in *ACS Applied Nano Materials*, under review (**Impact Factor: 5.5**)

1.2. In journals from the National Register of specialized journals, indicating the category:

7. **RAJAT, Nagpal,** CHIRIAC, M., SEREACOV, A., BIRNAZ, A., ABABII, N., LUPAN, C., BUZDUGAN, A., SANDU, I., SIEBERT, L., PAUPORTÉ, T., LUPAN, O., ANNEALING EFFECT ON UV DETECTION PROPERTIES OF ZnO:Al STRUCTURES, *Journal of Engineering Science*, Vol. 30 (4) 2023, pp. 45–62, https://doi.org/10.52326/jes.utm.2023.30(4).04, ISSN: 287-3474;

2. Articles in conference proceedings and other scientific events

2.1. Articles in the proceedings of scientific events included in the Web of Science and SCOPUS databases:

8. **RAJAT, Nagpal,** CHIRIAC, M., SUGIHARA, M., LITRA, D., MAGARIU, N., LUPAN, C., ZINICOVSCHI, V., AMELOOT, R., LUPAN, O. Sensory Properties of CuO/Cu_2O Nanostructures Coated with Zeolitic Imidazolate Frameworks, *E-Health and Bioengineering Conference (EHB)*, IASI, Romania, *IEEE Xplore*, 2024, pp. 1-4, doi: 10.1109/EHB64556.2024.10805729, **ISBN:**979-8-3315-3214-7;

9. LUPAN, O., **RAJAT, Nagpal**, LITRA, D., BRINZA, M., SUGIHARA, M., AMELOOT, R., SERGHEI, R., AMERI, T., ADELUNG, R., SCHRODER, S., FAUPEL, F., Hybrid Nanomaterials for Biomedical Sensors, *7th International Conference on Nanotechnologies and Biomedical Engineering*, *2025*, *IFMBE Proceedings,* vol 134. *Springer*, pp. 162-176, Cham. https://doi.org/10.1007/978-3-032-06494-3_18, ISBN: 978-3-032-06494-3;

10. **RAJAT, Nagpal,** LUPAN, C., VIANA, B., PAUPORTÉ, T., LUPAN, O., ADELUNG, R., Study on the Optical and Gas Sensing Properties of Eu-Doped ZnO, *IEEE 14th International Conference Nanomaterials: Applications and Properties)* , *IEEE Xplore*, 2024, pp. 1-4, https://doi.org/10.1109/NAP62956.2024.10739686, **ISBN:** 979-8-3503-8012-5;

2.2. Articles in the proceedings of national conferences scientific events:

11. **RAJAT, Nagpal**, LUPAN, C., SANDU, I., BÎRNAZ**,** A. UV LIGHT DETECTION BASED ON ZnO NETWORKS. *At the conference: Integration through research and innovation*, State University of Moldova, Chisinau, Moldova, November 9-10, 2023, pp. 752-757, Available: https://ibn.idsi.md/vizualizare_articol/201035, ISBN: 978-9975-62-687-3;

2.3. In the volume of abstracts of international scientific conferences (abroad)

12. **RAJAT, Nagpal**, SIEBERT, L., LUPAN, C., PADUNNAPPATTU, A., POSCHMANN, MIRJAM P.M., STOCK, N., ADELUNG, R., LUPAN, O. Metal Organic Framework based low powered ultraviolet signal detection. Poster presentation: *MOFSIM 2024,* Montpellier, April 10-12, 2024, pp. 90 (Book of Abstracts).Available:https://drive.google.com/file/d/10KpC8RzHq7JqZbHrqf2nRcGnRRZMFmg2/view;

13. LUPAN, O., BRINZA, M., LITRA, D., **RAJAT, Nagpal** SCHRODER, S., SUGIHARA, M., STRUNSKUS, T., AMELOOT, R., AMERI, T., ADELUNG, R., FAUPEL, F., Nanomaterials for Biomedical and Industrial Hybrid Sensors, *IEEE 15th International*

Conference on "Nanomaterials: Applications & Properties", Bratislava, Slovakia, Sept. 7-12, 2025, pp. 09nna-10 – 09nna-11 (Book of Abstracts). Available: https://ieeenap.org/data/Book_of_Abstracts_2025.pdf;

3. **Patents and other intellectual property objects request (IPO):**

3.1. **Issued by the State Agency for Intellectual Property**

14. **RAJAT, Nagpal**, SUGIHARA, M., MAGARIU, N., TROFIM V., LUPAN, C., AMELOOT, R., Process for manufacturing hydrogen sensor based on CuO:Al-ZIF-8 nanostructures, Patent app., **entr. no.** 7587 date 23.10.2025, AGEPI.